THE UNIVERSITY OF HULL

Nematic Liquid Crystals for Nano-Structured Organic Photovoltaic

being a Thesis submitted for the Degree of

Doctor of Philosophy (PhD)

in the University of Hull

by

Manea S. Alkhalifah, B.Sc, M.Sc

February 2010

Acknowledgements

Great thanks and praise to God the most merciful for giving me the health, help and patience to complete this work.

This study could not have been brought to final result without the support of a number of people, to whom I owe a debt of gratitude.

First of all I would like to thank my supervisor Prof. Mary O'Neill for her advice, and support from the very early stage of my research, as well as providing me many opportunities and freedom to try different interesting things.

I would like to thank my colleagues at the University of Hull for the wonderful working atmosphere especially Gordon Sowersby, whose help and technical advice was most valuable. I thank Prof. Steve Kelly for his valuable ideas and discussion in our group meetings.

I would like to thank Dr. Stuart P. Kitney for the synthesis of the liquid crystals investigated in this work. I also thank the previous members of organophotonics group especially Dr Wing Chung Tsoi, for being the first person who taught me how to work in the lab, and Dr. C. H. Lei for sharing the ideas and lab experience together.

I wish to express my gratitude to my parents, for their prayers for me to complete my study successfully, encouraging me to follow my own path and for being always there to help and support me in every aspect of my life.

I would like to express my warm feeling and offer special thanks to my wife, Umm Sulaiman, who sacrificed so much for me, to my beloved son Sulaiman, and my much loved daughters Norah, Noaf and Lyan, my thanks also to my father-in-law and mother-in-law. Thanks to my brothers, sisters and friends for their prayers for me.

Abstract

A range of novel liquid crystals and amorphous organic conjugated semiconductors were synthesised by the chemistry branch of the Organophotonics group at Hull University. These compounds are studied electrochemically and optically to investigate the suitability of these materials as good donor/acceptor with suitable pairs energy levels for use in organic photovoltaic devices. Liquid crystal compounds with a fluorene-thiophene structure were identified as potential electron donors in combination with perylene based compounds as electron acceptors.

Time-of-flight was used to study the charge transport of organic semiconductors in this thesis. The nature of the functional groups of the molecules was found to have a significant influence on the charge carrier mobility. The incorporation of a reactive end group with spacer affected the charge carrier mobility of electron donors negatively, suggesting that the mobility depends on the intermolecular separation. Based on the need to correlate the charge transport of the donor/acceptor blends with photovoltaic devices, the electron and hole mobility were studied for blends. For all blends the hole mobility is lower than that of the pure electron donor. The electron mobility of the blends is much higher than that of the pure electron acceptor. The thermal activation of charge transport in the liquid crystals is investigated by applying the Gill model. The result shows that charge transport in the liquid crystals is thermally activated and the activation energy is field dependent. The Gaussian disorder model and correlated disorder model were used to analyze the mobility data of four liquid crystals compounds with the same conjugated core and different end groups.

We show that the thin film nanoscale morphology and the phase separation of the donors/acceptors blends depend on the chemical structures of donors and acceptors, the casting solvents and the annealing temperature of the film. The functional groups of the perylene bisimide are found to influence the roughness. The surface roughness of the blended thin film is minimum and its phase separation finest when the electron donors component has short terminal aliphatic groups rather than long polymerisable chains. Chlorobenzene shows the best performance as coasting solvent. The annealing temperature is significant in controlling the nanoscale morphology and the phase separation of an intermixed network of the blends.

We successfully demonstrate photovoltaic performance using blends of our novel donors and acceptors. The annealing temperature is very important to optimise the solar cell performance by optimisation of the phase separation. The perylene based liquid crystals have disappointing performance as electron acceptors. The donor with the shortest terminal end group gives the best result. The device performance fully correlates with the blend nanoscale morphology of the blends; the blend with the smallest domains gives best power conversion efficiency; the best device has a value of 1.1%.

Table of Contents

1. INTRODUCTION

1.1. Motivation

The worldwide energy consumption will on average continue to increase by 2% per year according to both the American Energy Information Administration (EIA) and the International Energy Agency(IEA)[1]. (Figure 1-1) shows the actual values of energy consumption from 1980 until 2005 in blue and the prediction of the energy consumption until year 2030 in red.

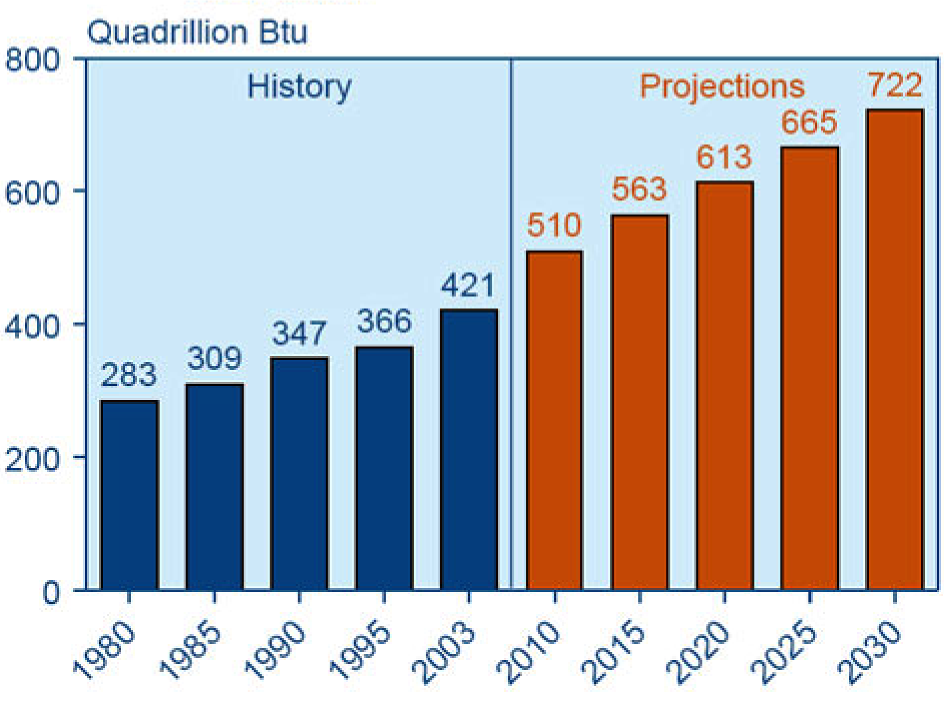

Figure 1-1: The world market energy consumption, between 1980-2030.[1]

Fossil fuels are the main energy source today, which include coal, oil, and natural gas. As an example figure 1-2 shows the energy sources used in the USA during 2008, where fossil fuels supply more than 80% of the energy consumption. However all these resources are limited and are going to disappear. Also, the byproducts of these resources have a harmful effect on the environment, especially carbon dioxide, which contributes heavily to the green house effect which appears to be the cause of global warming. Nuclear energy is one of the alternative sources. However the waste produced by this source is hazardous and the disposal of it can cause major environmental problems.

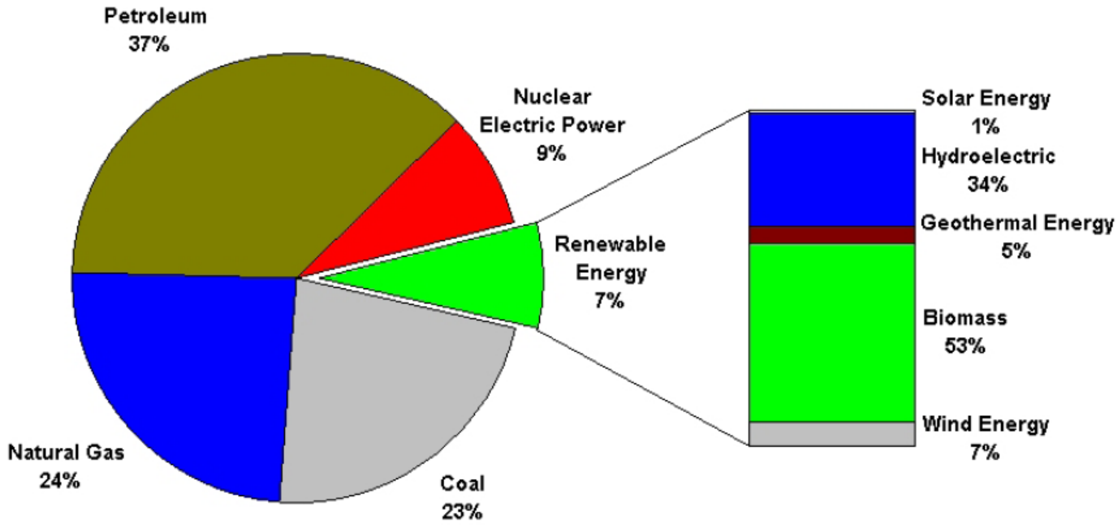

Figure 1-2: The USA energy supply in 2008 of the Renewable energy[2].

The ideal energy source should be clean with no by-product and can be used without depleting earth resources. This type of energy is classed as renewable, and as illustrated in figure 1-2, the most popular renewable sources are biomass, hydroelectric, geothermal energy, wind energy, and solar energy. The sun supplies the earth with $3x10^{24}$ Joules/year, which is about 10,000 times more than human energy requirements[3]. Several ways have been used to employ this huge amount of solar energy, one of them is converting the solar light energy to electrical energy via the photovoltaic effect (PV). The PV industry is going through a rapid period of growth and is considered to be one of the most promising renewable energy sources. A 30% annual growth in the production of solar cells was expected, based on the growth during the period of 1988 to 2002[4]. However by 2008 the contribution of the solar photovoltaic to the world demand for electricity reached 5.95 GW, as shown in figure1-3 with a growth of 110% over the previous year, with much higher growth in some countries, such as Spain where it rose very rapidly to reach 285%[5]. However, solar energy production is still less than 1% of the total world production of energy. There is need for a big effort to improve the power conversion efficiency of the solar cells and to bring the cost down, which is very high compared to the fossil fuels.

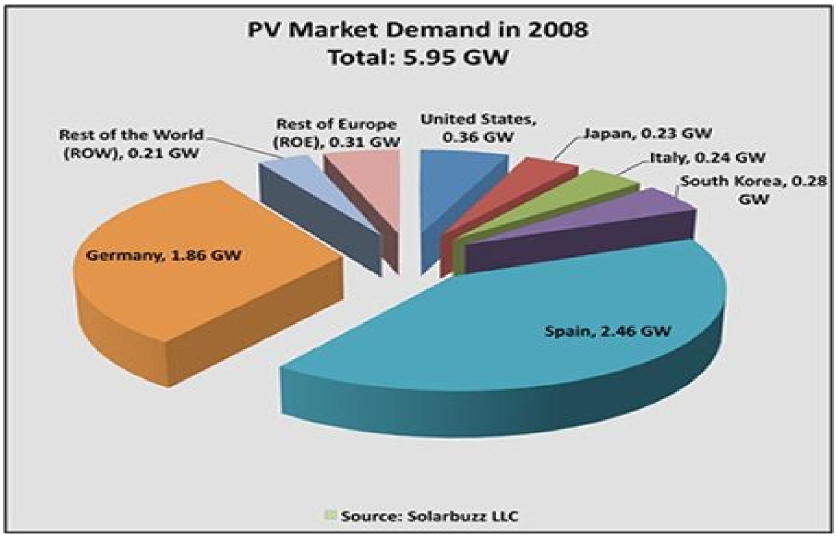

Source: Solarbuzz LLC

Figure 1-3: The world PV market demand in 2008, of total electricity production of 5.95GW[5].

Among the most promising new energy sources are solar cells based on organic materials, where inorganic semiconductors have been replaced with conjugated organic semiconductors. The organic materials have significant advantages compared to inorganic materials, but big improvements need to be done. Recently, 5% power conversion efficiency has been achieved based on small molecule materials and conjugated polymers[6,7]and 6.5% for tandem solar cells[8]. The growth of the plastic solar cells results from the developments in organic synthesis and device fabrication technologies.

1.2. The Photovoltaic Effect

The photovoltaic effect (PV) is the conversion of light energy (electromagnetic waves) in a one step process to electrical energy. The explanation of this effect given by the quantum theory of Albert Einstein in 1905 is that the electromagnetic waves of frequency ν incident on a metal surface consist of packets of energy called quanta or photons. The energy E of the photon depends only on v as[9]

$$\mathbf{E} = \mathbf{h\nu} \tag{1-1}$$

wher h is Planck's constant.

Visible light is enough to excite the bound electrons in solids up to higher energy levels, so they can move freely within the material. However, the excited electrons relax back to the ground state (recombination between the electrons and holes) within a short period called the relaxation time. The photovoltaic architecture exploits the variation in the electrical properties of the semiconductor materials to create a potential difference and electric field, giving a driving force to separate the excited electrons and holes and drive them to the external circuit before they recombine as illustrated in figure 1-4[10].

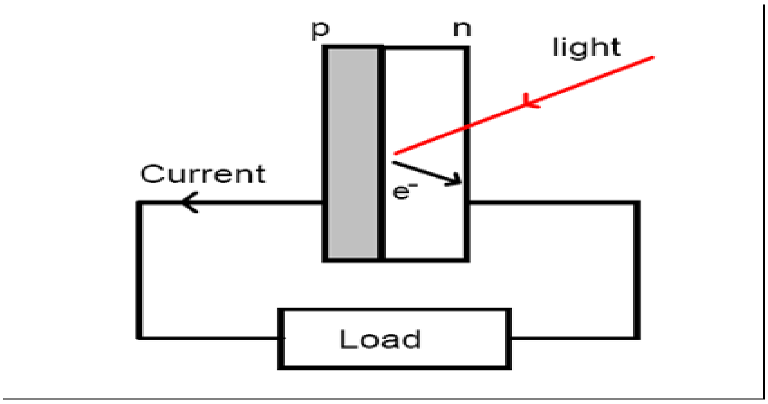

Figure 1-4: The photovoltaic effect in a solar cell, which requires special construction to pull the excited electrons to the external circuit[10].

1.3. The Basics of Electronics Semiconductors Materials and Devices

There are two main groups of semiconductors, conventional inorganic semiconductors (IS) and organic semiconductors (OS). Although the latter is our target, understanding the origin of the optical and electrical properties and the basic device architectures of the IS is a substantial step to understanding the OS, although, the physical properties of the organic and inorganic are different. For example, photoexcitation of the electrons in the OS results in the creation of bound electron-hole pairs (excitons) with small diffusion lengths (10-20 nm)[8], instead of the creation of free carriers as in the IS. The OS molecules form a weak non-covalent van der Waals intermolecular interaction, which result in low intermolecular orbital overlapping, and low dielectric constant compared to the strong covalent bonds of the IS atoms which have high orbital overlapping and high dielectric constant. As a consequence the OS have a low charge carrier mobility compared to the IS.

1.3.1. Inorganic Semiconductors

Electrons under the influence of the attractive potential around widely separated and independent atoms move in atomic orbitals separated by energy gaps. However, when the atoms are brought together in a solid, each atomic orbital splits into a very large number of levels (equals to the number of atoms), so close together in energy that they form what are known as bands of allowed levels. Each band has a limited bandwidth and the energy levels distribution within the band is quasi-continuous. Bands are occupied or not based on the occupation of the original molecular orbitals of the atoms. The highest occupied band is called the valence band (VB), which contains the atomic valence electrons. The lowest unoccupied band is called the conduction band (CB). The lowest level of the CB, and the highest energy level of the VB are the most important energy levels. These two levels are known as the conduction energy level E_c, and the valence energy level E_v respectively. Between these energy bands there lies a range of energy values that cannot be occupied called the bandgap (E_g) as shown in figure1-5 [10,11,12].

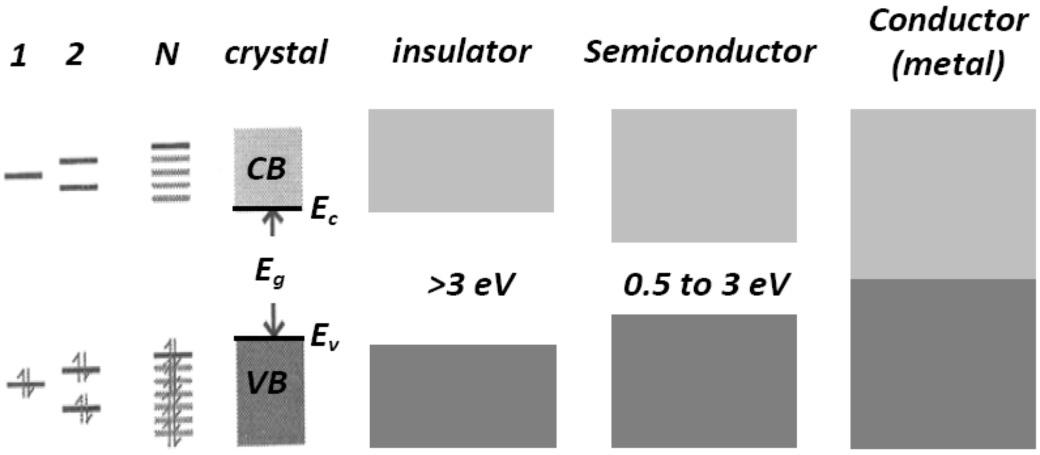

Figure 1-5: The formation of the energy band of the atomic orbitals, and the energy bands of the insulators, semiconductors, and conductors.

The band gap between VB and CB is responsible for the optical and electrical properties of the solids. As illustrated in figure 1-5 the solid materials can be classified based on the size of their energy bands gap. In conductors (such as metals) the VB and CB overlap in energy, so the electron is free to move because of the availability of empty states at similar energies, which allows good heat conduction and electrical current flow. In the case of the insulator the VB is fully occupied and separated from the CB by a bandgap, typically, of more than 3 eV. This large energy causes these materials to be poor conductors of heat and electricity. Semiconductors have bandgaps lying between conductors and insulators, with energy separations in the range of 0.5 to 3 eV [9,10, 13].

At absolute zero temperature, a pure semiconductor, which is called an intrinsic semiconductor, is unable to conduct heat or electricity since all the electrons occupy the VB and there are no electrons in the CB to participate in charge conduction. However, as the temperature is raised, some electrons in the VB gain enough energy to be promoted to the CB leaving vacancies in the VB known as holes. This operation is termed thermal excitation. The excited electrons in the CB are able to move and transport charge and energy through the material. The holes in the VB also participate in the conduction process. In intrinsic semiconductors the concentration of electrons n and holes p is equal, $n = p = n_i$

The conductivity of the intrinsic semiconductors can be increased by adding certain impurities to control the carrier concentration. This is doping, and the doped semiconductor then becomes an extrinsic semiconductor. Impurities are split into two types which produce extrinsic semiconductors with characteristics as shown in figure 1-6. N-type semiconductors are doped to increase the density of electrons relative to the holes. Thus the electrons are majority carriers and the holes are the minority carriers. This type of impurity is called a donor atom because it donates an extra electron to the semiconductor lattice. These electrons occupy an energy level just below the conduction band, known as the donor level, with a small energy separation of around 0.01 eV from the CB as shown in figure 1-6. The donor level electrons are thermally excited into the CB and participating in the electrical conductivity of the semiconductors. For example silicon and germanium have a tetravalent lattice; therefore the impurity needs to be any element with five valence electrons (group V elements) such as phosphorus. P-type is the second type of extrinsic semiconductor, which has been doped to increase the density of the holes relative to the electrons. The holes are now the majority carriers and the electrons are the minority carriers. This type of impurity atom, called an acceptor impurity, has fewer valence electrons than the bonds it need to correctly fit the semiconductor lattice, which is equivalent to saying that there is a hole created at the site of the impurity atom. For example the tetravalent silicon or germanium needs an impurity of elements with three valance electrons (group III elements) such as the boron.

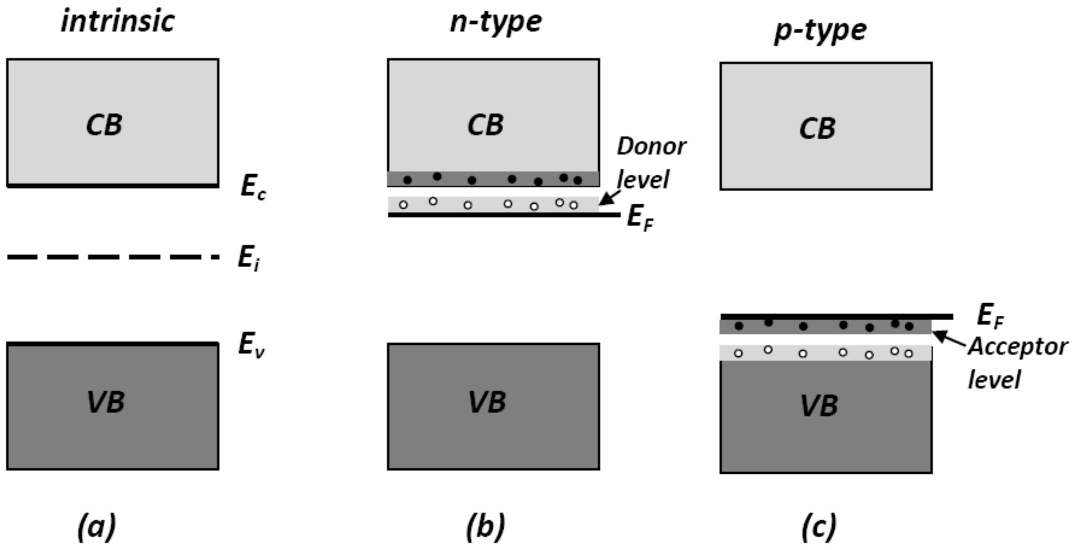

Figure 1-6: (a) The Fermi level and energy levels in intrinsic semiconductors. Impurity levels and Fermi level in (b) n-type semiconductors, and (c) p-type semiconductors.

Typically, the energy band diagram has two more important energy levels besides the E_c and E_v. These are the Fermi level E_F and the intrinsic Fermi level E_i as illustrated in figure 1-6(a). The intrinsic Fermi level is equal to the Fermi level when the concentration of electrons and holes is equal in the material, which is the case with intrinsic semiconductors. Usually E_i is approximately in the middle of the band gap. The doping of the intrinsic semiconductors shift the Fermi level up or down away from the centre of the bandgap based on the type of the impurity, up towards E_c in n-type materials, and down towards E_v in p-type materials[10,14,15].

Under illumination extra electrons are excited to the CB in addition to the thermally excited and doping electrons. A driving force is needed for the extraction of these excited electrons. The force can be provided using special composition of the two types of materials to offer a spatial variation in the electronic environment. The p-n junction is the most important and widely used structure for solar cells to provide the required force. The p-n junction is built by doping some parts of a single and continuous intrinsic semiconductor crystal with n-type (donor) materials giving a high Fermi level, while the other part is doped by p-type (acceptor) material giving a low Fermi level. An interface is produced between the donor and acceptor doped material. Because of the difference of the Fermi levels (carrier concentration) in both sides, the electrons in the material with higher Fermi level (n-type) find unoccupied energy states in the material with the lower Fermi level (p-type), and start diffusing to fill these states, which also means that the holes diffuse in the opposite direction. As a result of the carrier diffusion, the regions close to the junction interface on both sides ends up without any free electrons or holes (depleted). Each diffused carrier crossing the junction leaves behind a charged atom (ion), the electrons leaving positive ions in the n region and holes leave negative ions in the p region. Therefore a space charge region is built up on both sides of the junction which is called depletion region. Space charge builds up an electrostatic field which increasingly attenuates the diffusion across the junction until it reaches an equilibrium, when the diffusion of the majority carrier across the junction is in balance with the drifting of the minority carriers back across the junction. At this point the Fermi level is the same on both sides as illustrated in figure 1-7.

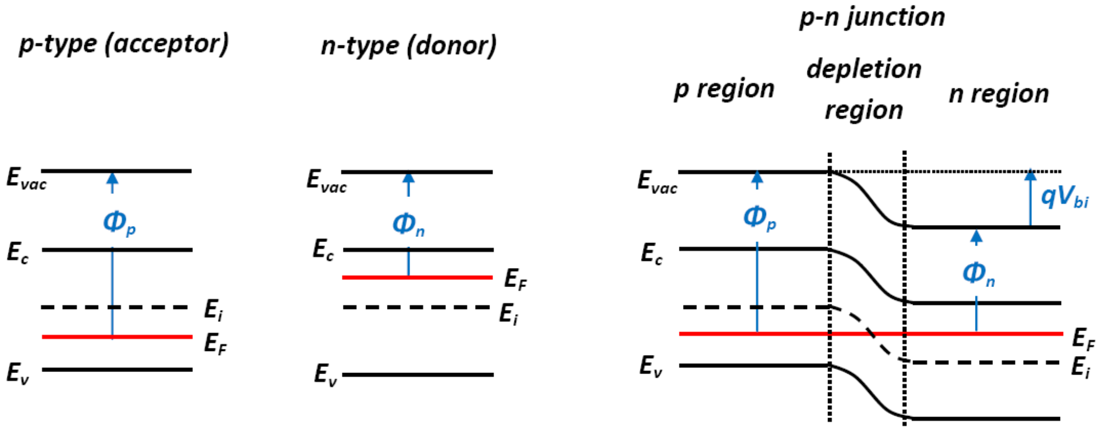

Figure 1-7: Energy band diagram for p-type and n-type semiconductors, before and after forming the p-n junction.

In the equilibrium state of the p-n junction, the difference between the work functions of the n and p type (Φ_n, Φ_p) is qV_{bi} , where V_{bi} is the built-in bias, Therefore[10]

$$V_{bi} = \frac{1}{q}\left(\Phi_n - \Phi_p\right) = \frac{1}{q}\left[(E_i - E_F)_{p\,side} - (E_i - E_F)_{n\,side}\right] \tag{1-2}$$

Illumination of the p-n junction increases the population of the holes in the p side and the electrons in the n side changing the charge distribution in the three regions and splitting the Fermi level back into two levels as illustrated in figure 1-8, where in the p region the Fermi level shifts toward the VB, forming the hole quasi Fermi level E_{Fp}. In the n region it shifts up towards the CB forming the electron quasi Fermi level E_{Fn}, and within the depletion region; E_{Fp} and E_{Fn} remain relatively constant. For solar cells it is required to split the Fermi level ($E_{Fp} \neq E_{Fn}$) [10,16].

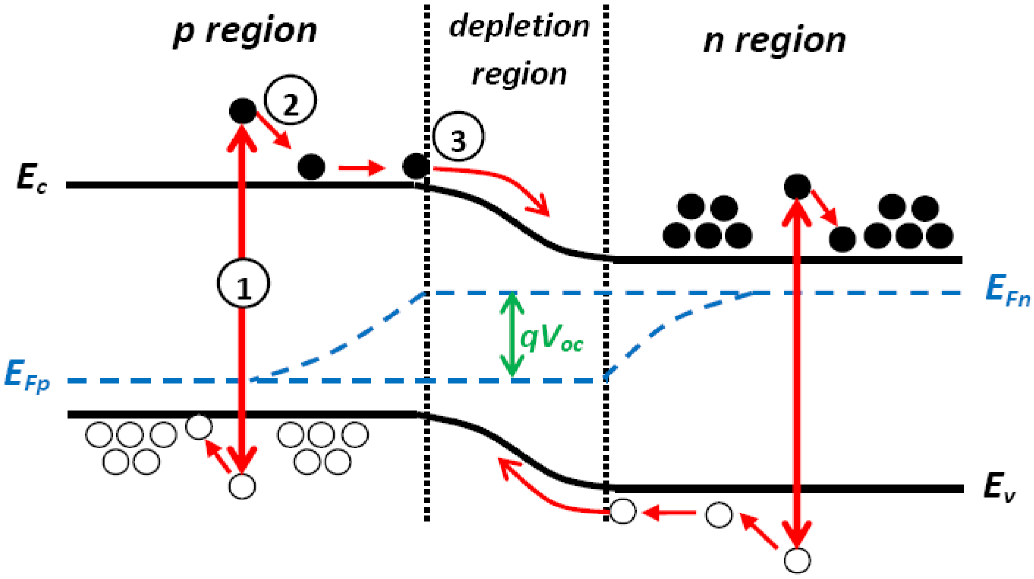

Figure 1-8: Energy band diagram of the p-n junction under illumination.

A combination of drift and diffusion of the carriers results in the carrier transport inside the semiconductors. As shown in figure 1-8, photogeneration of the holes and electrons in each region is followed by thermalization of the holes and electrons to the top of the VB and the bottom of the CB respectively. Away from the depletion region (junction) the minority carriers (electrons in p-region and holes in n-region) diffuse to the junction. Within the junction the minority carriers drift under the influence of the junction potential to the other side of the junction where they become majority carriers. The collected charges give rise to a photocurrent (in a short circuit), I_{sc} or photovoltage (in open circuit), V_{oc} , where the energy difference between the quasi Fermi level's energy determines the maximum open circuit voltage[8].

1.3.2. Organic Conjugated Semiconductors

Organic materials have been considered as electrical insulators in many applications until the seventies. In 1977 Heeger, Shirakawa and MacDiarmid (Nobel Prize for Chemistry 2000) discovered the increase of the conductivity of the conjugated polymer polyacetylene by several orders of magnitude via the doping with iodine[17].

Organic conjugated materials show the mechanical properties of conventional plastics in addition to the semiconducting properties allowing use as active layers in optoelectronics. The electronic properties of organic semiconductors are quite different from conventional inorganic semiconductors. The main feature of organic semiconductors is the alternation of single and double carbon-carbon bonds as shown in figure 1-9, where molecules with this structure are known as "conjugated".

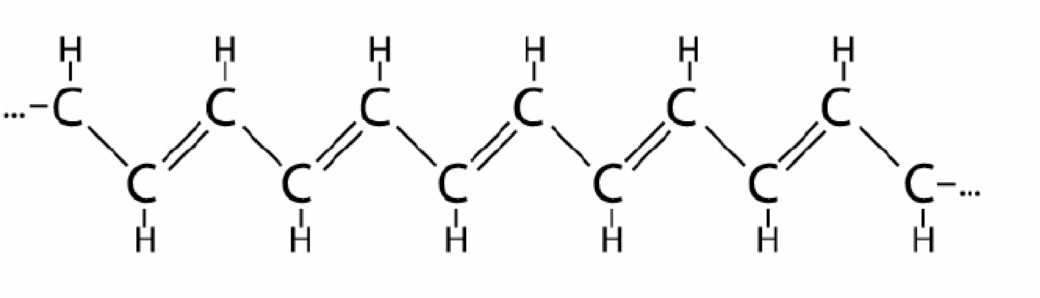

Figure 1-9: Schematic diagram of the simplest conjugated polymer molecule, Polyacetylene[18].

A basic understanding of carbon bonding is required in order to understand the origin of semiconductivity in conjugated materials[19,20,18,21,22]. The ground state configuration of carbon atom is $1s^2\ 2s^2\ 2p_x^1\ 2p_y^1$, which suggest a carbon would form only two bonds with its neighbours using the two unpaired electrons of $2p_x^1\ 2p_y^1$, since the *2s* shell is filled. However it is known that carbon atom forms four bonds, this can be clarified via what is known as the hybridization. The atomic orbitals may be considered to be mixed together to form hybrid orbitals of sp^1, sp^2, sp^3configuration depending upon the number of orbitals that are combined. One of the $2s$ electrons of the carbon atom is promoted to a $2p$ orbital forming a configuration $1s^2\ 2s^1\ 2p_x^1\ 2p_y^1\ 2p_z^1$, with four unpaired electrons in separated orbitals. In semiconducting conjugated organic materials the potential to transport electronic current and to absorb light is due to the *sp^2-hybridization*, where the one *s* orbital pairs with two the *p* orbitals to form 3 sp^2 hybrid orbitals leaving the p_z orbital unhybridized as illustrated in figure 1-10.

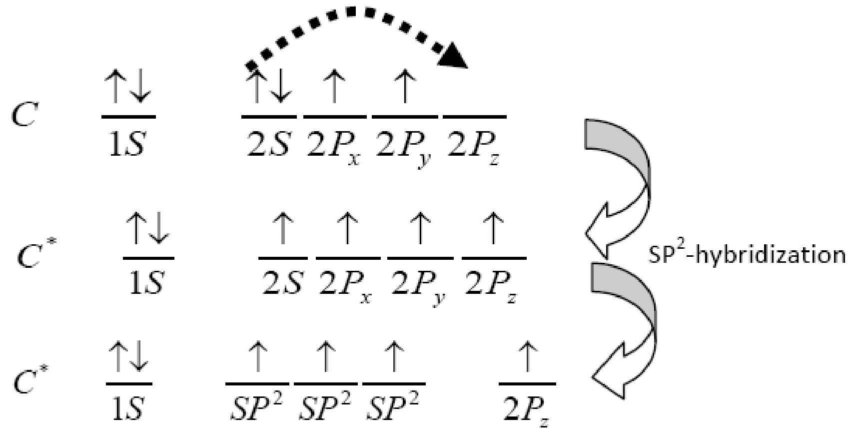

Figure 1-10: Formation of the *sp^2 hybridization* in the carbon atom

Two of the sp^2 hybrid orbitals form σ-bonds with the neighbouring carbon atoms, while the third forms a σ-bond with hydrogen or any substituent. These covalent bonds are very strong and stable because they have fully paired electrons in their bonding states and empty antibonding states. The unhybridized p_z orbital, which lies perpendicular to the internuclear axis, forms π-bonds with the unhybridized p_z orbital of the adjacent carbon atom in the linear chain of *sp^2-hybridized* carbon atoms, therefore; this leads to an alternating single and double bond along the chain (dimerization) giving the unique structure of conjugated organic materials as illustrated in figure1-11.

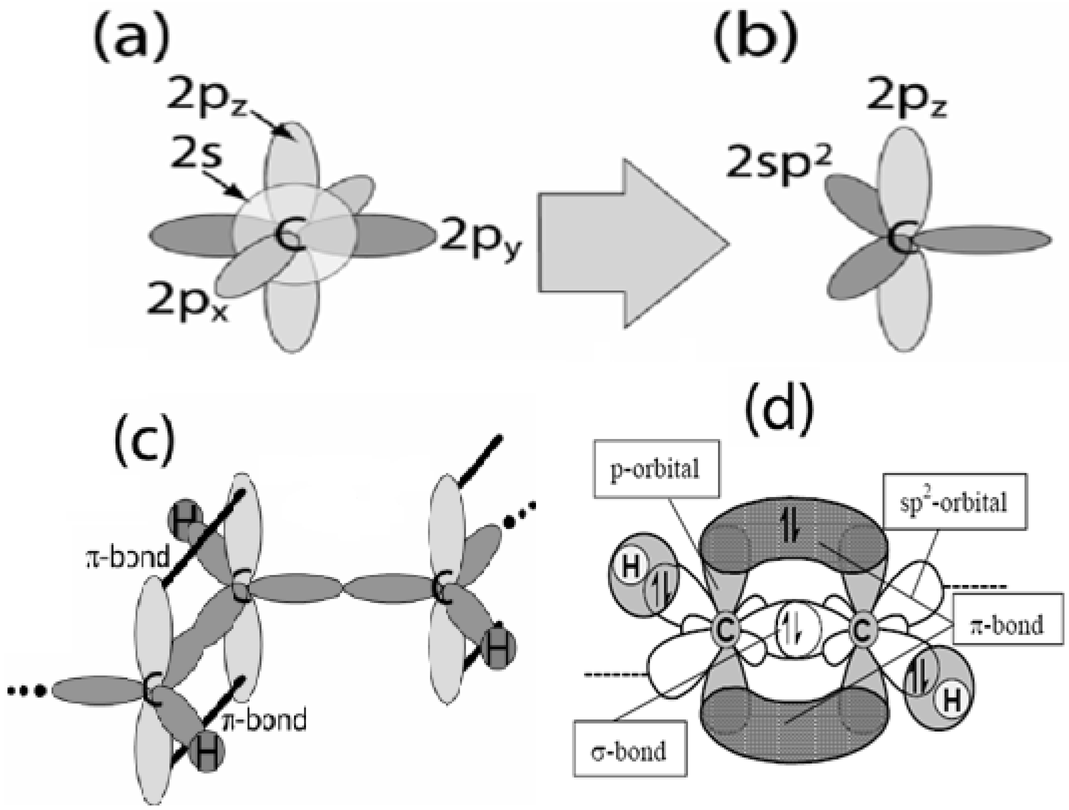

Figure 1-11: Formation of σ-bonds and π-bonds in organic conjugated materials[18].

The π-bonds are loose bonds and significantly weaker than σ-bond. Therefore π-electrons are able to move from atomic site to atomic site and are effectively delocalized among the atoms in the molecule, and so are responsible for the electrical and optical properties of organic conjugated materials.

For isolated molecules, each carbon atom on average brings one π-electron (half filled state) filling discrete energy levels known as molecular π-orbitals. The π-orbitals are split into two types, filled π-orbitals (bonding orbitals), and empty π^*-orbital (antibonding orbital). These two groups are thus an analogue of the valence (VB) and conduction (CB) bands of conventional semiconductors. However conjugated organic materials have extremely narrow bands since the charge delocalization is only over part or all of a single molecule. The frontier states of these groups are the two most important molecular orbitals, namely the highest occupied molecular orbital (HOMO) of π-orbitals, and the lowest unoccupied molecular orbital (LUMO) of π^*-orbital as illustrated in figure 1-12. The π-electrons are the origin of the light absorption and emission as well as charge generation and transport properties of all conjugated organic semiconductors. The lowest electronic excitation of conjugated molecules is the π-π*-transition, which is known as the optical band gap (E_g = HOMO - LUMO) with an energy gap typically between 1.5-3 eV leading the materials to absorb and emit light in the visible spectral range[23]. The HOMO and the LUMO energies can be measured experimentally using cyclic voltammetry technique as discussed in chapter 3.

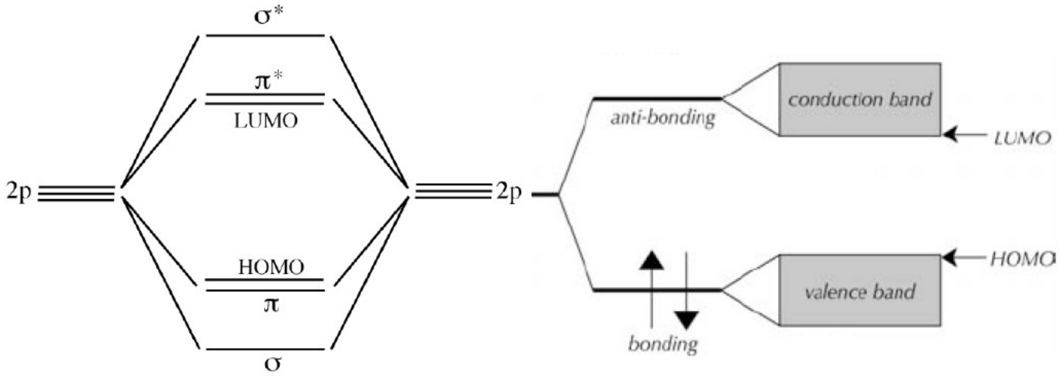

Figure 1-12: Energy level splitting of orbitals in a conjugated materials according molecular orbital theory.

Charge excited states are formed by the addition or removal of charges from the molecule or promoting charges to higher energy levels as illustrated in figure 1-13. Excitons, polarons and bipolarons are different excited states. The electronic structure of an organic semiconductor is strongly coupled with the lattice; any addition, removal of charge or its promotion to a higher energy level induces a lattice deformation creating a local distortion of the molecular structure. Excitation of the molecule creates one electron and a hole interacting with each other via coulomb attraction forming a bound electron-hole pair, called an exciton. The addition (removal) of one electron to (from) the molecule creates a negative (positive) polaron. A bipolaron is formed when two electrons are added or removed to (from) the molecule.

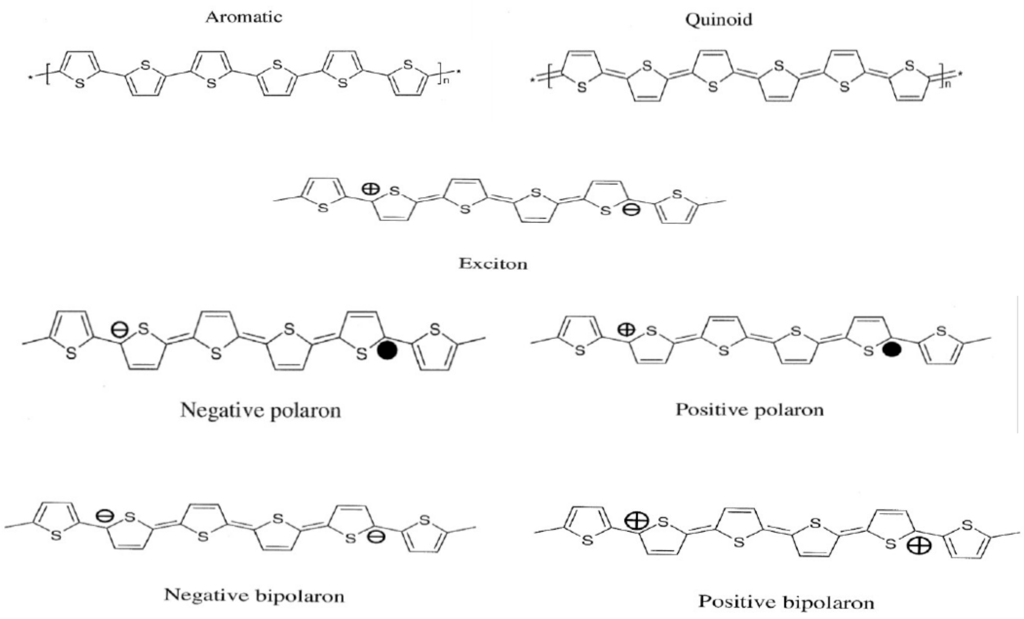

Figure 1-13: The ground states (aromatic, quinoid) and the excited states of polythiophene[24].

The donor/acceptor heterojunction (DA-HJ) is the general structure of an organic photovoltaic devices, which was first introduced by Tang in 1986 [25]. A DA-HJ consists of two organic semiconductors of electron donor properties (ED) and electron acceptor properties (EA), brought together to form a ED/EA interface, where the electron donating materials (ED) has higher HOMO/LUMO energy level relative to the acceptor materials (EA) as illustrated in figure 1-14. The ED/EA interface gives rise to dissociation of the excitons, and has an equivalent function to the junction in inorganic solar cells. The photocurrent extraction process is explained in detail in section 1.5.

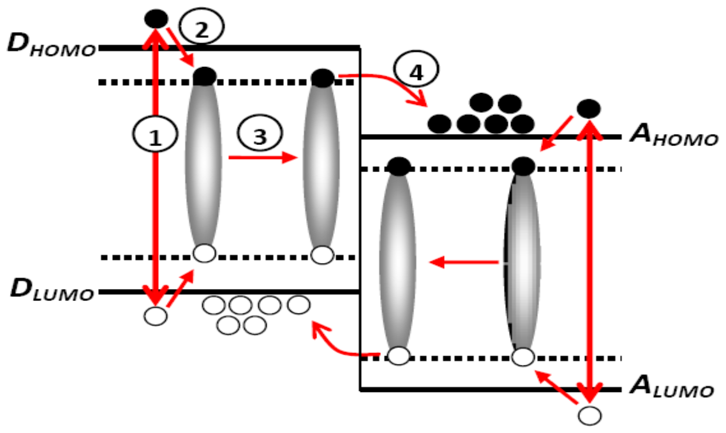

Figure 1-14: Energy level diagram of the organic DA-HJ under illumination

1.4. Characterization of solar cells

1.4.1. Ideal Solar Cells Parameters and Equivalent Circuit Diagram

Most photovoltaic devices act like diodes when there is no illumination. Therefore they have a rectifying behaviour; admitting much larger current when forward biased (V>0) than under reverse bias (V<0) which is almost zero as shown in the JV characteristics in figure 1-15. This behaviour results from the asymmetric junction, which is needed for charge separation. The current which flows across the device under the applied voltage V in the dark is called the dark current $I_d(V)$, which increases exponentially with the positive voltage. Therefore, the dark current density $J_d(V)$ of the ideal diode varies like[10,21,26,27]

$$\mathbf{J_d(V) = J_o\left(e^{eV/k_BT} - 1\right)} \tag{1-3}$$

where J_o is a constant called the saturation current density, e is the electron charge, k_B is Boltzmann's constant and T is temperature.

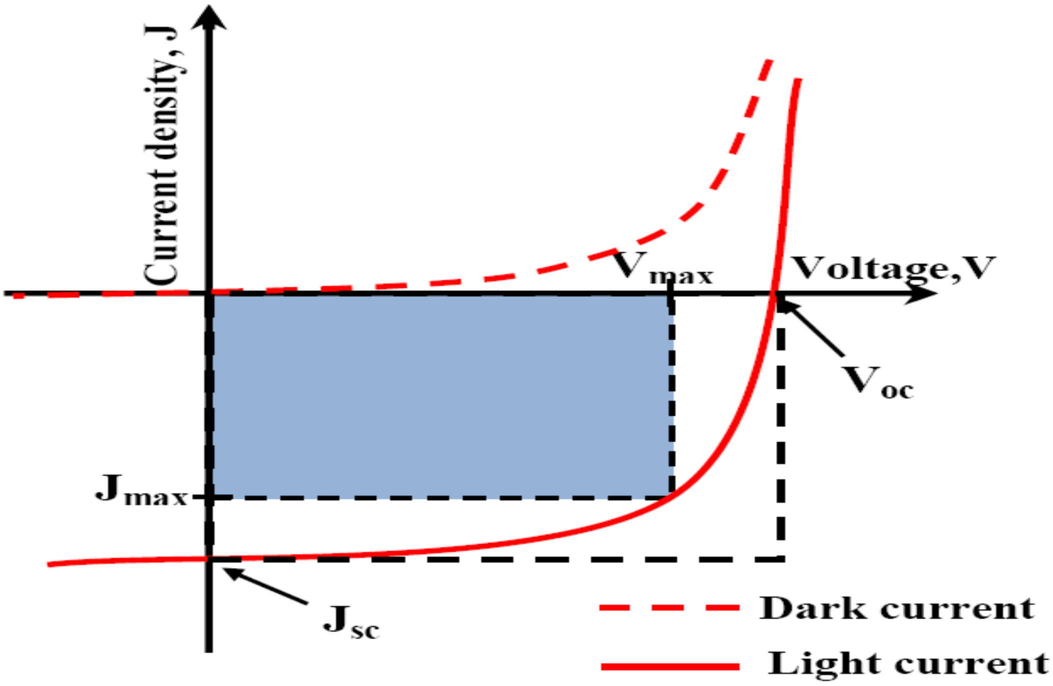

Figure 1-15: I-V characteristic of an organic solar cell under dark, and under illuminated condition.

The ideal solar cell behaves like a current generator in parallel with a diode, as illustrated in the equivalent circuit in figure 1-16, when a solar cell is illuminated; a potential difference develops between its electrodes. The photocurrent generated as a result of the potential difference flows in the opposite direction to the dark current through the external load.

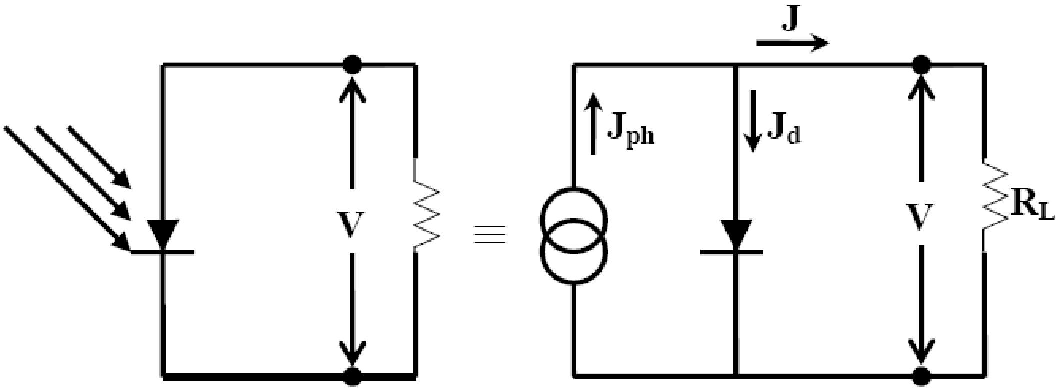

Figure 1-16: The equivalent circuit ideal solar cell under illumination.

The net current density of the solar cell J (V) under illumination, which flows through the load resistance, can be approximated from its IV characteristic as the sum of the dark current and the photocurrent, which can be given as

$$\mathbf{J(V) = J_o(e^{eV/k_BT} - 1) - J_{ph}} \tag{1-4}$$

In the case of an open circuit, the current density goes to zero (J(V) = 0), and the potential difference has a maximum value which is called the open circuit voltage (V_{oc}). Substituting these values of current density and potential in eq.1-4 give a quantitative value for V_{oc}

$$\mathbf{V_{oc} = \frac{k_BT}{e} \ln\left(\frac{J_{ph}}{J_o} + 1\right)} \tag{1-5}$$

As shown in eq.1-4 and the IV characteristic figure 1-15, if the applied voltage goes to zero (as with zero Ohm load resistance) the net current through the load resistance is known as the short circuit current density, J_{sc}, which is the maximum output current of the solar cell.

1.4.2. Non-Ideal Solar Cells Parameters and Equivalent Circuit Diagram

Real solar cells divert from the ideal because of the power losses as a result of the presence of some kind of resistances. The cell power is influenced by two types of resistance, the load resistance (R_L) externally, and the diode (solar cell) resistance internally. Therefore it is divided between the two resistances in a ratio; which depends on the value of the load resistance and the level of illumination. Moreover the diode resistance, known as the parasitic resistance has two components, the series resistance R_s and shunt resistance R_{sh}. The series resistance R_s is in series with the cell, and has to be minimized. R_s depends on the material's resistivity, the electrodes' resistivity, and the metal organic interfaces at the electrodes. The shunt resistance R_{sh} is a parallel resistance to the cell, which need to be maximized as it causes loss of the current via the leakage and shorts around the sides of the devices, and structure defects such as pinholes in the film, or the recombination centres of impurities. The equivalent circuit of the solar cell including series and shunt resistance is shown in figure 1-17.

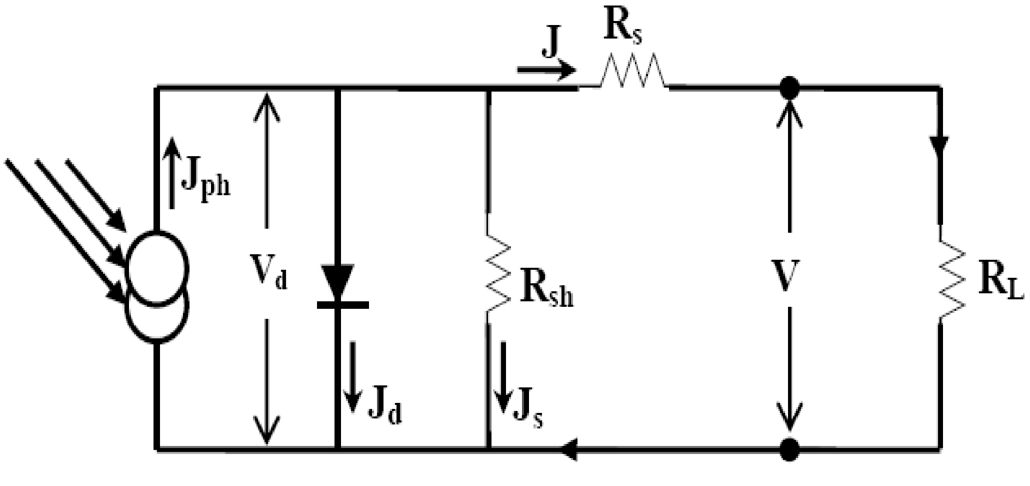

Figure 1-17: Scheme for real equivalent cell under illumination. R_s is the series resistance and R_{sh} is the shunt resistance R_L is the load resistance.

The current voltage dependence of solar cells is quantified by the ideality factor, *n,* which is equal to one in the ideal diode case where $R_s = 0$, and $R_{sh} = \infty$. The diode dark current is given by the Shockley equation[16]

$$\mathbf{J_d = J_o(e^{eV/nk_BT} - 1)} \qquad (1\text{-}6)$$

Solving for the equivalent circuit, using Shockley equation and the Kirchhoff's Laws provides the analytical relation for the IV characteristics for a cell of area A as[8,28]

$$\mathbf{J(V) = \frac{1}{1+R_s/R_{sh}}\left[J_o\left(e^{\frac{e(V-JAR_s)}{nk_BT}} - 1\right) - \left(J_{ph} - \frac{V}{AR_{sh}}\right)\right]} \qquad (1\text{-}7)$$

From eq.1-7 and using the condition of the open circuit voltage V_{oc} and short circuit current density J_{sc}, the equation of each can be derived as

$$\mathbf{V_{oc} = \frac{nk_BT}{e}\ln\left[1 + \frac{J_{ph}}{J_o}\left(1 - \frac{V_{oc}}{J_{ph}R_{sh}A}\right)\right] \approx \frac{nk_BT}{e}\ln\left[1 + \frac{J_{ph}}{J_o}\right]} \qquad (1\text{-}8)$$

$$\mathbf{J_{sc} = \frac{1}{1+R_s/R_{sh}}\left[J_{ph} - J_o\left(e^{\frac{e(|J_{sc}|AR_s)}{nk_BT}} - 1\right)\right] \approx -J_{ph}} \qquad (1\text{-}9)$$

For truly efficient rectifying devices the series resistance R_s should be as small as possible, and the shunt resistance R_{sh} should be as high as possible (several KΩ). The effects of increasing the R_s and decreasing the R_{sh} on the I-V curve are illustrated in figure 1-18. Increasing the R_s reduces the J_{sc} and the fill factor FF of the cell, defined in eq.1-12. The V_{oc} is not influenced since the current flow through R_s is zero at V_{oc}. Decreasing the R_{sh} reduces the V_{oc} and the fill factor FF of the cell. The J_{sc} is not influenced by the change in R_{sh} because R_{sh} is still much larger than R_s and therefore the current through R_{sh} can be neglected. The value of R_s can be found from the inverse slope of the straight line in the 2nd quadrant around $V = V_{oc}$ and $J = 0$. R_{sh} can be found from the inverse slope of the straight ling in the 4th quadrant around $V = 0$, $J = J_{sc}$.

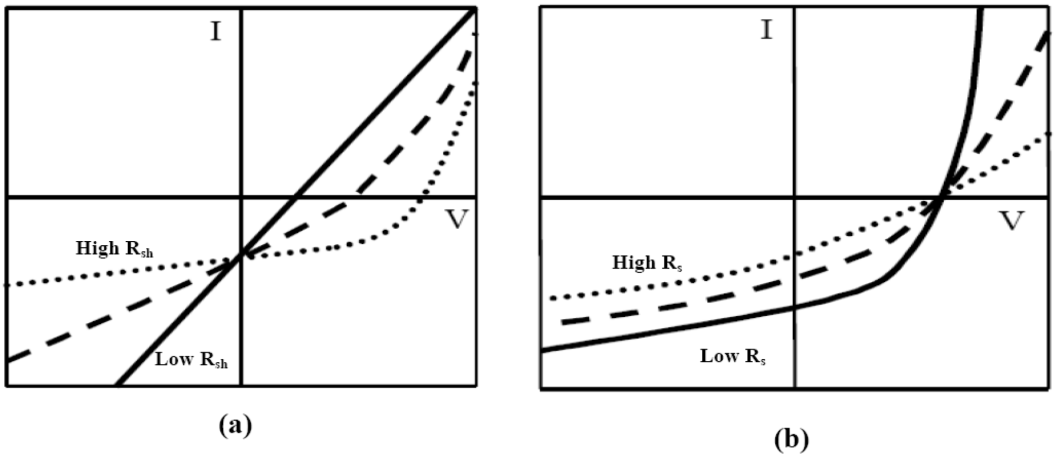

Figure 1-18: (a) The effect of the shunt resistance on the shape of the I-V characteristic. The fill factor area decreases with the decrease of the shunt resistance. (b) The effect of the series resistance on the shape of the I-V characteristic. The fill factor area decreases with the increase of the series resistance[29].

1.4.3. Fill Factor, Power Conversion Efficiency and External Quantum Efficiency

The output power density of the cell is given by

$$\mathbf{P = JV} \tag{1-10}$$

The cell power output reaches its maximum at an operation point known as the maximum power point P_{max}. This point refers to the voltage V_{max} located between zero and the open circuit voltage ($0< V_{max}<V_{oc}$) and the corresponding current density J_{max} located between zero and the short circuit current ($0> J_{max}>J_{sc}$) as shown in figure 1-15, so that

$$\mathbf{P_{max} = J_{max}V_{max}} \tag{1-11}$$

Note that the photovoltaic effect occurs only in forward bias ($V>0$), where the cell generates power when the product of the current and the voltage is negative, so the power conversion can be obtained between 0 and V_{oc}. However the other regions of the IV characteristic are suitable for other devices, $V>V_{oc}$ is the region where a light emitting diode operates, and $V<0$ is the region where the device acts as a photodetector.

The practical parameters that can be used to characterize the solar cell are the fill factor FF, the power conversion efficiency PCE, and the external quantum efficiency EQE[10,26,30]. The fill factor (FF) is the ratio between the maximum power density delivered to the external circuit P_{max} and the potential power density of the device as

$$\mathbf{FF} = \frac{J_{max}V_{max}}{J_{sc}V_{oc}} \qquad (1\text{-}12)$$

From figure 1-15; the fill factor can be defined as the ratio between the dark small rectangular area and the white large one. The maximum power conversion efficiency (PCE) is defined as the ratio between the maximum power density delivered to the external circuit P_{max} and the incident light power density P_o

$$\mathbf{PCE} = \frac{J_{max}V_{max}}{P_o} = \frac{J_{sc}V_{oc}FF}{P_o} \qquad (1\text{-}13)$$

Eq.1-13 shows that J_{sc}, V_{oc}, FF and PCE are key parameters to monitor the performance of solar cells and all of them should be defined at a specific power density of the incident light. Also the two resistances have an influence on all of these parameters.

In addition, the spectral response of the solar cell's materials is another important way of characterising solar cells. By illuminating the solar cell using monochromatic light source the photocurrent is measured as a function of the wavelength. Hence, the cell efficiency versus wavelength can be calculated. The external quantum efficiency (EQE) also can be used to study the spectrum response, which is defined as the number of electrons generated (n_e) per incident photons (n_{ph}):

$$\mathbf{EQE} = \frac{n_e}{n_{ph}} = \frac{J_{sc}}{P_o}\frac{hc}{\lambda e} = \frac{J_{sc}}{P_o}\frac{1240}{\lambda} \qquad (1\text{-}14)$$

where h is Planck's constant, c is the speed of light, λ is the wavelength of the light, e is the electrical charge. The internal quantum efficiency is also used to characterize solar cells, this being the ratio of the photocurrent to the actual photons absorbed.

1.5. Work Principles of Organic Photovoltaic

For DA-HJ organic solar cells PCE depends on four steps as illustrated in figure 1-14 and figure 1-19 [31,32,33]

$$\mathbf{PCE} = \boldsymbol{\eta}_{\mathbf{A}}(\boldsymbol{\lambda})\boldsymbol{\eta}_{\mathbf{ED}}\boldsymbol{\eta}_{\mathbf{CD}}(\mathbf{V})\boldsymbol{\eta}_{\mathbf{CC}}(\mathbf{V}) \tag{1-15}$$

Where, η_A is the light absorption and exciton formation efficiency of the various layers of the device, η_{ED} is the efficiency of the exciton diffusion, which is the percentage of photogenerated excitons that diffuse to a DA interface, η_{CD} the fraction of the electron-hole pairs that are dissociated into holes in the donor side and electrons in the acceptor side, where the electron-hole pair is still coulomb bound and called a geminate or polaron pair, and finally η_{CC} the fraction of charges that reach the electrodes.

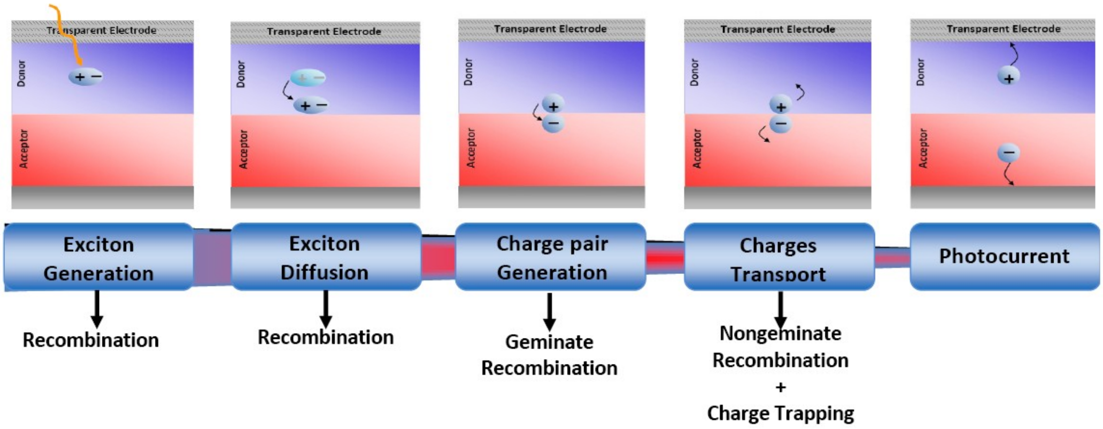

Figure 1-19: The work principles of organic solar cells.

The working principles of the conversion of the light energy to electrical energy using the organic semiconductors are discussed in more detail in the following points:

1.5.1. Light Absorption

The DA active layer of the DA-HJ is considered the core of the PV operation, where the absorption of the photon with an average energy larger than the optical band gap on either side of the DA-HJ results in the transfer of an electron from the HOMO energy level to the LUMO energy level leaving a hole as the first step of the OPV operation. It is important to absorb as many photons as possible in the active organic layer which is dependent upon the optical absorption coefficient, the optical energy gap of the organic material, and the thickness of the active layer. Most organic materials possess high absorption coefficients of $\propto > 10^5 cm^{-1}$ [31]. However, most of the organic devices absorb small fractions of the incident light for the following reasons: (i)The mismatch between the active materials absorption and the solar spectrum; most OS materials have bandgaps higher than 2 eV (<600nm), while over 60% of the total solar spectrum is at wavelengths longer than 600 nm with almost 50% in the red and near infrared spectrum, which limits the absorption of photons by the organic materials as illustrated in figures1-20. Here the photon flux is shown, which is the percentage of the photons available for a material with a certain band gap. A band gap of 1.1eV (1100 nm) is required to absorb 77% of the solar radiation on earth[21,34]. (ii) As discussed in detail below, the exciton diffusion length (10-20nm) limits the thickness of the organic layer, which should be of the order of 100nm. However, the absorption coefficient of organic material is much higher than silicon, so a 100nm thickness is enough to absorb between 60 and 90% if a reflective back contact is used[21,35]. Therefore, to overcome these limitations the chemists should invent new OPV materials which absorb further into the red and infrared spectrum by lowering the energy gap[36,37], this will be one of the aims of chapter two. The absorption coefficient of the organic dyes is better than that of polymers; so the absorption of the light can be increased by mixing the polymers with dye; which should transfer the absorbed energy to the polymers[35].

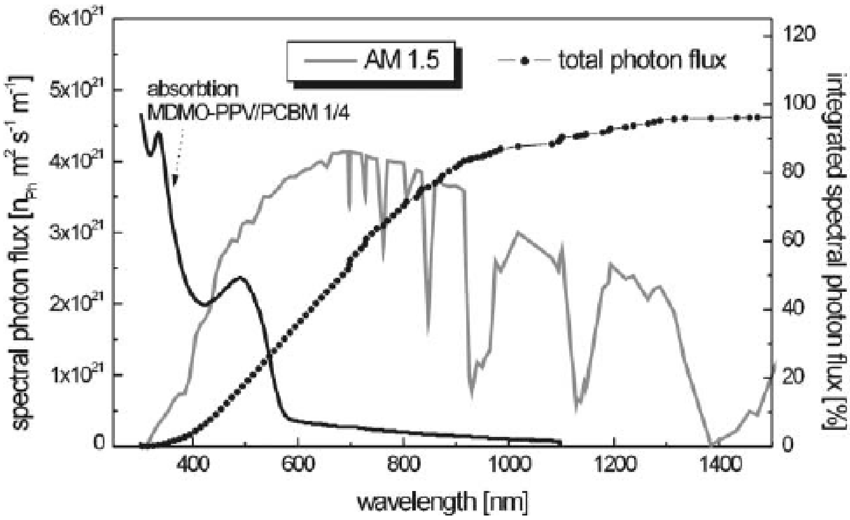

Figure 1-20: Spectral photon flux of the AM1.5 solar spectrum in comparison with the absorption profile of the MDMO-PPB: PCB M 1:4 film. Dotted line shows the total photon flux[38].

1.5.2. Excitation Generation

The promotion of an electron to the LUMO level leaving a hole in the HOMO level is followed by thermalization and formation of excitons as shown in step two of figure 1-14, where the electron and hole remain bound to each other by a Coulombic force, which will be discussed in more detail in chapter two. The exciton binding energy in the OS materials is of the order of a few tenth of eV to as high as 1.5 eV compared with few meV in the IS materials. The former is too large for the exciton to be ionised thermally at room temperature, such an energy is twenty times or more the thermal energy at room temperature (k_BT= 26 meV)[8,39,40]. An exciton rather than free charges is created because: (i) the screening length is large by reason of the small dielectric constant of typically (3-4)[41], which is low compared to inorganic materials. Therefore the Coulomb attraction force between the opposite charges is much higher in the OS materials. (ii) The weak non-covalent electronic interaction between organic molecules gives localised state with negligible band width[41].

1.5.3. Exciton Diffusion and Dissociation

To reach higher efficiency most of the photogenerated excitons should diffuse and reach the dissociation region where the excitons are separated into free negative and positive polarons (electrons and holes). Excitons are neutral species, so they diffuse via random hops without any influence of the electric field[8]. The dissociation region is usually located at the interface between two materials with different electronic properties such as workfunction, electron affinity, or ionization potential. Exciton generation can happen in any part of the semiconductor so that the layer thickness should equal the diffusion length, the distance over which the exciton moves before recombination. Generally the diffusion length of the exciton in organic semiconductors is small, around 10-20 nm. The diffusion length depends on the structure of the materials and the dielectric constant[28,40]. There is an intermediate status between excitons and the fully separated charges. This so called charge pair is a Coulombic bound pair of a negative and positive charges in different molecules as shown in figure 1-19.

1.5.4. Charge Transport

The separated charges should move toward the respective electrode. The charge transport is limited by the low charge mobility of the organic materials. Typically the mobility of the hole transporting materials is 10^{-7} $cm^2V^{-1}s^{-1}$ up to 10^{-3} $cm^2V^{-1}s^{-1}$; and the electron transporting materials have usually lower mobility than the holes as will be detailed in chapter three. Transport is also affected by the recombination of the electrons and holes especially if the same material is used as the transporting medium for both electrons and holes. The trapping by impurity and defects also participates in lowering the efficiency of the charge transportation. Materials with ordered phases, e.g. liquid crystals, have higher mobilities[42,21].

1.5.5. Charge Collection

Not all the electrons or holes approaching the electrodes will get into the outer circuit. Electrons and holes may have to overcome the potential barrier of a thin oxide layer. The metal may also form a block contact at the interface with the semiconductor. This is a function of geometry, topology, and interface formation. [21,30]

1.6. Organic Photovoltaic Materials

The simplest molecular structure of organic conjugated materials consists of carbon chain with alternating double and single bonds and hydrogen atoms at the remaining bond as illustrated in figure 1-9. The molecular structure and properties of the materials can be modified via replacement of some carbon atoms with some atoms of *sp^2-hybridized* electronic structure such as nitrogen, oxygen, sulphur, or replacement of hydrogen with an organic group. The conjugated organic materials are divided into small molecules and polymers[18].

1.6.1. Small Molecules

Organic conjugated materials are denoted small molecules if they have a low molecular weight (a few 100u). Small molecules like Buckminsterfullerene (C_{60}) are mostly processed by sublimation under vacuum (dry process) and have high glass transition temperatures (T_g) to avoid crystallisation of materials during device operation. Some are processed via wet solution methods such as PCBM (1-(3-methoxycarbonyl) propyl-1-phenyl[6,6]C61) and all the compounds used in this thesis which are illustrated in table 2-1. Figure 1-21 shows the chemical structure of some organic small molecules commonly used in organic photovoltaic.

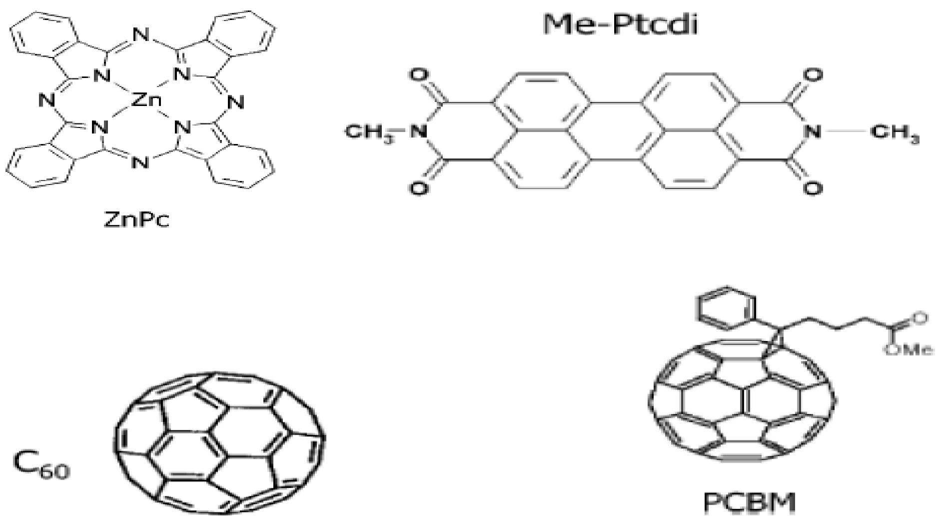

Figure 1-21: Chemical structure of some commonly used small molecules in the organic photovoltaic: ZnPc (zinc-phthalocyanine), Me-Ptcdi (N,N'-dimethylperylene- 3,4,9,10-dicarboximide), and the buckminster fullerene C60, and a soluble derivative of C60, PCBM (1-(3-methoxycarbonyl) propyl-1-phenyl[6,6]C61).[43]

1.6.2. Conjugated Polymers

Polymers are made of large numbers of identical repeated units, which are called monomers (small molecules with reactive end groups). The chemical structures of some commonly used monomers are shown in figure 1-22. Between ten to tens of thousands of monomers can be linked together by covalent bonding in a linear way to form long chains, branched structure, or in networks. If the monomers have two reactive groups the final result is a linear chain, while if the monomers have more than two reactive groups the form is a polymer network. The molecule is known as copolymers when more than one type of monomer is linked. The wet process is used to deposit conjugated polymers in thin films because they are soluble in various solvents. It is not possible to use the dry process because of their high molecular weight and low thermal stability.

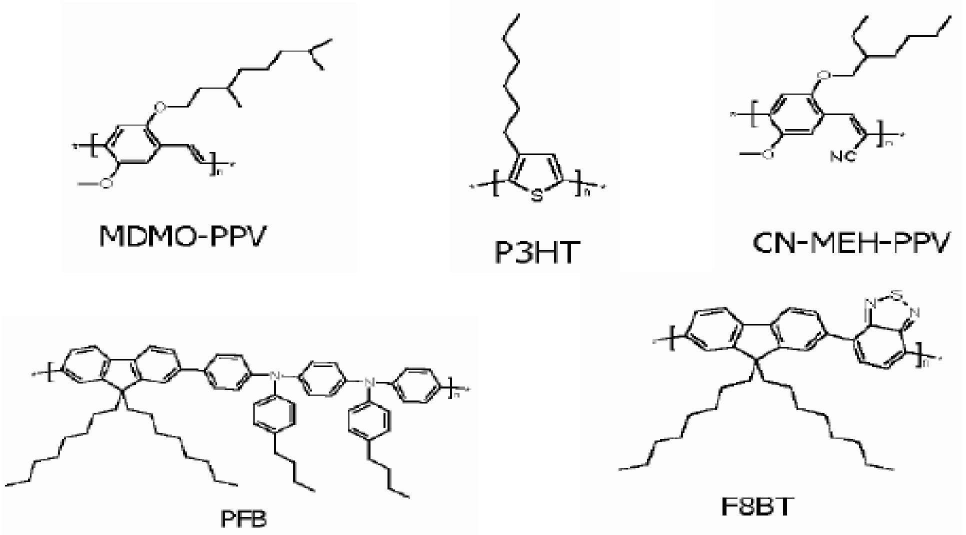

Figure 1-22: Chemical structure of some common conjugated monomers used in organic solar cells. the p-type hole-conducting donor polymers: MDMO-PPV (poly[2-methoxy-5-(3,7-dimethyloctyloxy)]-1,4-phenylenevinylene), P3HT (poly(3-hexylthiophene-2,5-diyl) and PFB(poly(9,9'-dioctylfluorene-co-bis-N,N'-(4-butylphenyl)-bis-N,N'-phenyl-1,4-phenylenediamine). The electron-conducting acceptor polymers: CN-MEH-PPV (poly-[2-methoxy-5-(2'-ethylhexyloxy)-1,4-(1-cyanovinylene)-phenylene) and F8TB (poly(9,9'-dioctylfluoreneco-benzothiadiazole).[44]

Oligomers are small of polymers chain with a finite number of monomers linked together linearly (2-10 monomers). Long oligomers exhibit all the essential electrical and optical properties of the polymers[45]. The dendrimer is made of monomers linked together by covalent bonds in a three dimensional way forming a network[45,46]. The molecular structure is arranged in many branches and subbranches starting from the centre of the molecule as in figure 1-23. The absorption spectrum of the dendrimer can be controlled by selection of the core of the dendrimer. In addition; the solubility can be controlled by the selection of the surface groups.

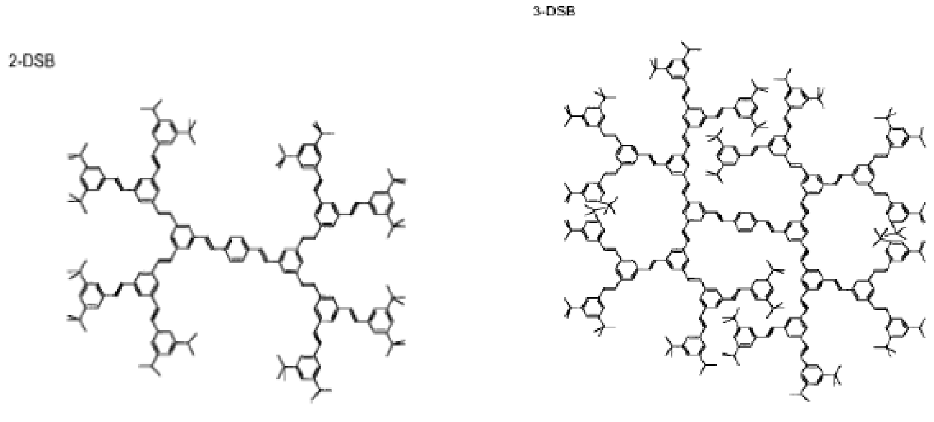

Figure 1-23: Chemical structure of some conjugated dendrimers : 2DSB ,and 3DSB[46].

1.7. Photovoltaic Device Design and Fabrication

Charge separation and transport are the key elements in the construction of the photovoltaic devices. These require a driving force, which should be built into our device. The driving force can be provided by the spatial variation in the electronic environment; a junction between electronically different materials creates an internal electric field on the order of 10^6-10^7 V/m[32,47]. This electric field provides an electrostatic force, which drives the electrons and the holes towards the respective electrodes. These requirements are controlled by three main factors: material selection, material growth technique, and device architecture. As the first two factors were discussed elsewhere, in this section we are going to discuss some different types of architectures used as photovoltaic devices.

1.7.1. Monolayer Diode

The monolayer diode is known as the simplest organic semiconductor device[21,32,42,48]. It consists of only one layer of organic semiconductor sandwiched between two electrodes of different workfunction, one of them, such as indium tin oxide (ITO) has a high workfunction and the other, such as Al, Ca or Mg has a low workfunction as shown in figure 1-24.

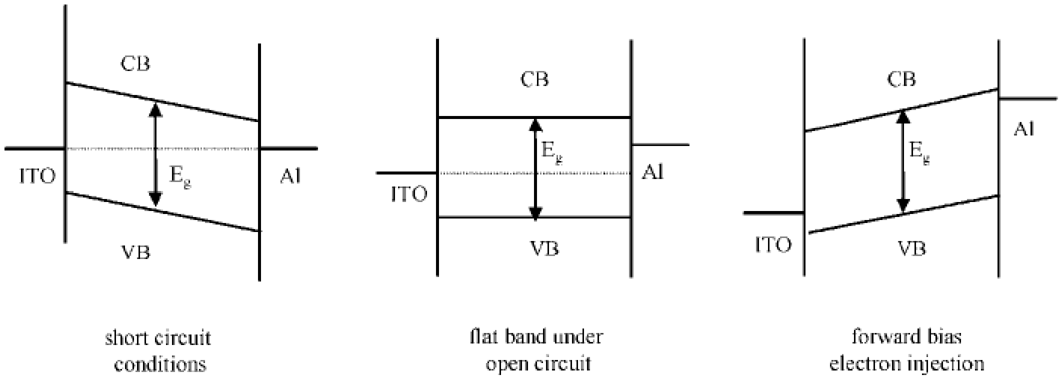

Figure 1-24: Diagram of the energy level of the single layer device under flat band condition , and under short circuit condition, and forward bias[48].

The junction results from the equalization of the chemical potential of the electron (Fermi level in the organic semiconductors) with the two different contacts. Consider the work function W_f, the ionization potential of the metal, and IP the equivalent for the organic semiconductor, IP is taken as the HOMO energy. The action of charges at the metal semiconductor contacts depends on the difference between W_f and IP: (i) if $W_f > IP$ the electron diffuse from the semiconductor to the metal. No barrier forms at the interface and the contact is ohmic. (ii) If $W_f < IP$ the electrons diffuse from metal to the semiconductor. The resistance at the interface increases rapidly creating the depletion region W and the contact is rectifying (Schottky) as shown in figure 1-25[21].

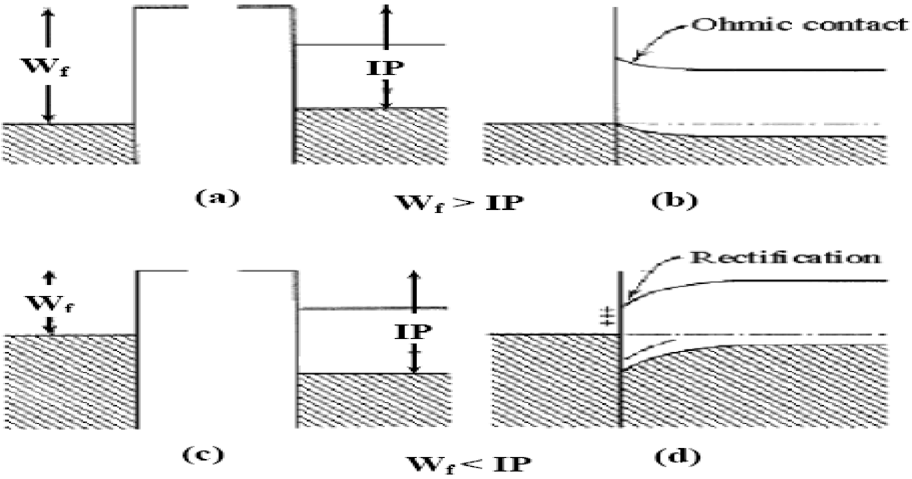

Figure 1-25: Energy levels of a metal-semiconductor contact before and after contact for Wf>IP (a),(b) and Wf<IP (c),(d)[21].

The monolayer organic photovoltaic is often known as a Schottky diode since the exciton dissociation occurs at the Schottky junction with one electrode, the other electrode should have an ohmic contact with the organic layer.

Typically monolayer solar cells have external quantum efficiency (EQE) less than 1% and power conversion efficiency (PCE) less than 0.1%. Only one material is used so that the absorption range of the optical spectrum is limited. The photovoltaic active region is very narrow because of the short exciton diffusion length (~10nm). Both positive and negative charges travel through the same material, so that recombination losses are high[49].

1.7.2. Bilayer Planar Heterojunction

The bilayer heterojunction is the simplest structure of the donor/acceptor heterojunction (DA-HJ) shown in section 1-3-2. This has a planar interface between two organic materials of different electron affinities (E_{EA}) and ionisation potentials (E_{IP}) as shown in figure 1-14 and figure 1-26(a), as reported originally by Tang in 1986[25]. This provides a high potential drop between the two layers so that exciton dissociation is favourable at the interface. The electron is accepted by the material with the large electron affinity; so it is called the electron acceptor (EA). The hole is accepted by the material with the lower ionization potential, which is called the electron donor (ED).

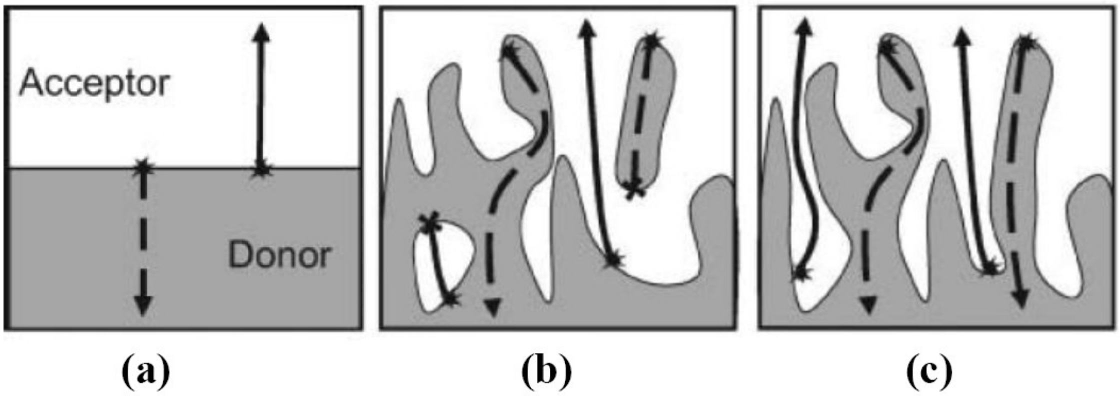

Figure 1-26: The DA-HJ interfaces architecture possibilities: (a) bilayer planar HJ, (b) bulk HJ illustrating the loss possibility via dead end ways, (c) diffuse bilayer HJ[31].

For the exciton in the donor (acceptor) material, the condition for dissociation is satisfied if the difference in the energy of the lowest unoccupied (highest occupied) molecular orbital of the two materials, ΔE_{LUMO} (ΔE_{HOMO}), exceeds the donor (acceptor) exciton binding energy, $E_{B,D}$ ($E_{B,A}$) as [31,47]

$$\mathbf{E_{B,D} < \Delta\, E_{LUMO}} \tag{1-16}$$

$$\mathbf{E_{B,A} < \Delta\, E_{HOMO}} \tag{1-17}$$

An alternative criterion for exciton separation is that:

$$\mathbf{E}_{\mathbf{HOMO,D}} - \mathbf{E}_{\mathbf{LUMO,A}} < h\boldsymbol{\nu}_{\mathbf{min}} \qquad (1\text{-}18)$$

where $h\nu_{min}$ is the minimum absorption energy of the exciton in the device.

The bilayer is sandwiched between two electrodes matching the donor HOMO and the acceptor LUMO with their workfunctions W_f, for efficient extraction of the corresponding charge carrier[32].

The exciton dissociates much more efficiently in the organic bilayer heterojunction interfaces than in the organic-metal interfaces of the monolayer devices. The probability of recombination between the electron and the hole is small (it may happen with high trap densities) because the electrons and holes travel in separate materials, acceptor and donor respectively. The limitation of this device is that the useful active length of the devices to their separate electrodes is small; which is the exciton diffusion length (~10 nm) at both sides of the interface. This is about 10% of the thickness which is necessary to absorb a significant proportion of sunlight[21]. Excitons generated outside this useful length recombine before dissociation.

1.7.3. Bulk Heterojunction

The revolutionary development in organic photovoltaic devices came in the mid 1990s by introduction of the bulk heterojunction independently by Yu et al.[50] and Hall et al.[51] to overcoming the limitation of the bilayer heterojunction. The bulk heterojunction is a mix of the donor and acceptor materials in a bulk volume. Therefore, each donor-acceptor interface is ideally within a distance less than the exciton diffusion length of each absorbing site. Each photogenerated exciton in either site material is more likely to diffuse to the interface and dissociate into its components. If each material has a continuous path between the interface and the respective electrode, the separated charges can be delivered to the external circuit as shown in figure 1-26 [32,42].

The limitation of the BHJ technique is the dead-ends to the respective electrodes, which result on increasing the charges recombination within the bulk.

Techniques used to prepare a bulk heterojunction include (i) co-deposition of donor and acceptor small molecules; (ii) spin coating of the donor-acceptor blends. The highest efficiency device today of 5% power conversion efficiency has been achieved based on small molecule materials and conjugated polymers[6,52].

1.7.4. Diffuse Bilayer Heterojunction

The diffuse bilayer heterojunction was invented to overcome the limitation of the bilayer and bulk heterojunction devices by enlarging the interface between the donor and the acceptor; and limiting the interruption of the pathway, i.e. dead-ends to the respective electrodes. The diffused bilayer device consists of the acceptor on top of the donor material as shown in figure 1-26(c), but with a large interface cross-section up to 20-30nm.

There are different ways to make this kind of device: (i) by spin coating the second layer using a solvent that partially dissolves the first layer without removing it, which modify the roughness of the first layer[32,53], (ii) Using a mixture of more than one solvent when depositing acceptor onto donor. The mixture dissolves the second layer and one of its components dissolves the first layer whereas the other does not. Hence the effect of the mixture on the first layer can be controlled by changing the ratio of the two solvents[54]. (iii) By heating the bilayer device up to near the glass transition temperature before depositing the top electrode , this method allows the two layers to diffuse into each other[32,55]. (iv) Using the gel technique, which involves spin coating the first layer of a mixture of a cross linkable donor material and a non cross linkable one, followed by photo-induced cross linking to form an insoluble polymer network. Washing this layer with a suitable organic solvent dissolves and removes the non-cross linkable material and leaves the cross-linkable one with roughened surface. After that the acceptor material is spin coated on top forming a large interface area[56].

This device technique is expected to obtain high fill factor values and high efficiency in the device, because of the good condition of the charge collection and transport. So far 2% of power conversion efficiency has been reported for the laminated polymer-polymer device under standard solar spectrum simulated AM1.5[32].

1.7.5. Tandem Devices

As we discussed before, the thickness of the layers is limited by the small diffusion length of the excitons, which limits the absorption of the solar spectrum. In order to overcome this limitation tandem devices have been invented. These are made by stacking solar cells, which use materials with different absorption spectra, and of small thickness to allow a large fraction of the excitons to diffuse to the dissociation region. Stacked devices are also thick enough to absorb a high proportion of the solar spectrum. Each subcell can be a bilayer or trilayer organic and each two subcells are separated by a thin metallic nanocluster layer[30,57,58].

The structure and the mechanism of the tandem device are illustrated in figure 1-27. The two cells (PV1, PV2) are sandwiched between an indium tin oxide (ITO) as anode and silver (Ag) as cathode, and are separated by Ag nanocluster layer. The dissociated hole in the donor layer of the PV1 and the electron in the acceptor layer of the PV2 are collected at the electrode. The electron in the acceptor layer of PV1 and the hole in the donor layer of the PV2 are diffused to the metal nanocluster layer and recombine, which prevents the build-up of the charge within the cells[57].

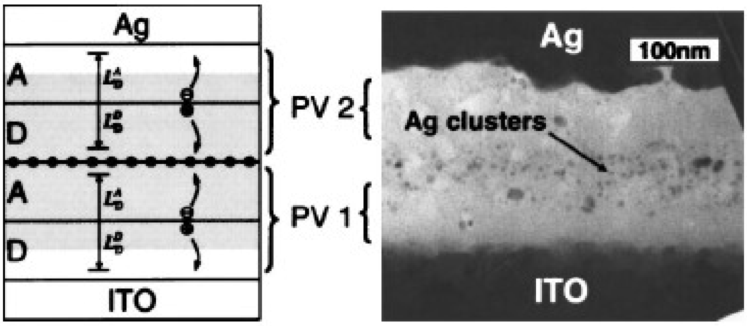

Figure 1-27: Cross section of a tandem bilayer device, schematic (left) and transmission electron micrograph (right)[57]

The tandem devices enhance the power conversion efficiency by enhancement of the open circuit voltage (V_{oc}). The charge recombination is also enhanced, which increases the photocurrent of the cell[30,32,57-59]. 5.7% power conversion efficiency under 1sun AM1.5G solar illumination has been reported by Xue and co-workers[58], and up to 6.1% at 200 mW/cm^2 has been reported by Kim and co-worker[60].

1.8. Liquid Crystals

1.8.1. Introduction and Historical Overview

The first discovery of the liquid crystal was in 1988 by the Austrian botanist Friedrich Reinitzer; when he noted that cholesteryl benzoate exhibits two distinct melting points. In 1889 the German physicist Otto Lehmann found that some materials would not melt directly to a liquid but first go through a phase where the material flows like a liquid and exhibits the optical properties of a solid crystal at the same time. He named the phase “flowing crystal”, then “crystalline fluid”, and finally “liquid crystal”. In the 20th century the liquid crystal received little attention from scientists until the late 1960s when liquid crystals started to be used in display applications due to the discovery of their optoelectronic properties. The twisted-nematic mode used for liquid crystal displays (LCDs) was discovered independently by M. Schadt, W. Helfrich and E. P. Raynes in 1970. In 1973 G. Gray of the University of Hull achieved the first stable, room temperature nematic LCs to be used for display purposes[30,61,62]. In 1969, S. Kusabayashi et al discovered the PV effect in smectic LCs. In 1972, H. Kamei et al discovered an ionic PV effect of nematic LCs. In 1990, the photoconduction property of a liquid crystal was reported by Warman et al. and Haarer et al[30,63].

Liquid crystals are a phase of matter between the isotropic liquid (I) and the solid crystal (Cr) phases known as mesophases. In the solid crystal the molecules exhibit positional and orientational order, meaning that the molecules are fixed in a specific position in lattice, unable to rotate or realign their axes, which in most cases leads to anisotropy of the physical properties such as mechanical, electrical, magnetic, and optical properties. On the other hand the molecules in the liquid phase (isotropic liquid) exhibit no positional and orientational order, so they can move randomly in different directions. Between these phases the molecules can still move around, much like a conventional liquid but can possess degrees of orientational and often positional order, both short and long range, which can lead to physical properties of high anisotropy.

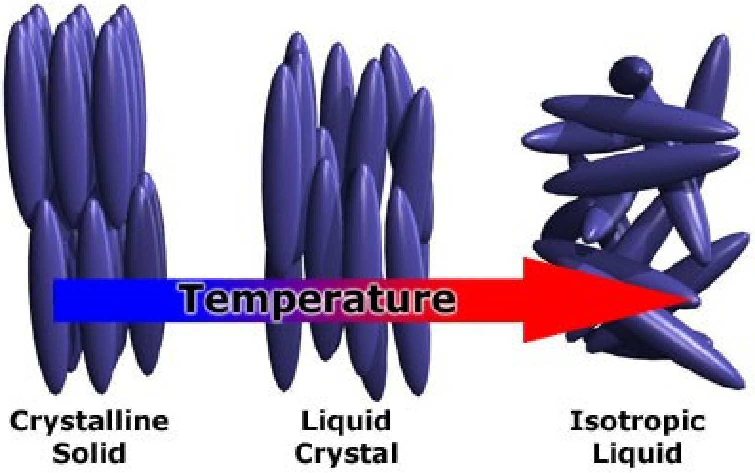

Figure 1-28: The states of matter, illustrating the LCs phase as a transition phase between the crystalline solid and isotropic liquid[64].

The degree of long-range of orientational order is defined by the so-called order parameter or anisotropy factor S, see figure 1-29,

$$\mathbf{S = \frac{1}{2}\langle 3\cos^2\theta - 1\rangle} \tag{1-19}$$

where θ is the angle between the molecular axis and the mean direction of the orientation (director) for each domain. The brackets denote the average for the material. Therefore S is zero for a completely isotropic liquid; for a perfectly aligned crystalline solid it is equal to one, and for a liquid crystal S is in the range $0.4 < S < 0.6$[30,65,66].

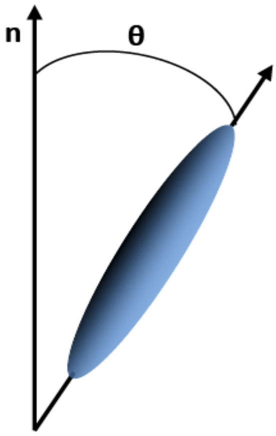

Figure 1-29: The director and orientational order.

1.8.2. Liquid Crystal Materials

Liquid crystal materials consist of molecules called mesogens, whose shape gives rise to the liquid crystal properties while the chemical structure of their aromatic core (chromophore) affects the optical and electrical properties which can be controlled and tailored via chemical synthesis. The mesogens must generally be rigid for at least some portion of their length and have a specific shape to form a liquid crystal. In order to produce interactions that favour alignment they must be uniaxial, different in one direction than in the orthogonal ones, most LCs are rod or disc shaped [30,66,67]. Here we focus on rod shaped LCs.

In general the liquid crystals materials are divided into two categories depending on their molecular structure, monomer liquid crystals (MLCs), and polymer liquid crystals (PLCs)[61,68]. The MLC has a low-molar-mass and consists of an aromatic core with one or more aliphatic terminal groups. Figure1-30 (a) shows the terthiophene, 8-TTP-8, as an example of a MLC and for PLC the 9,9-dioctyl polyfluorene PFO is shown in figure 1-30(b).

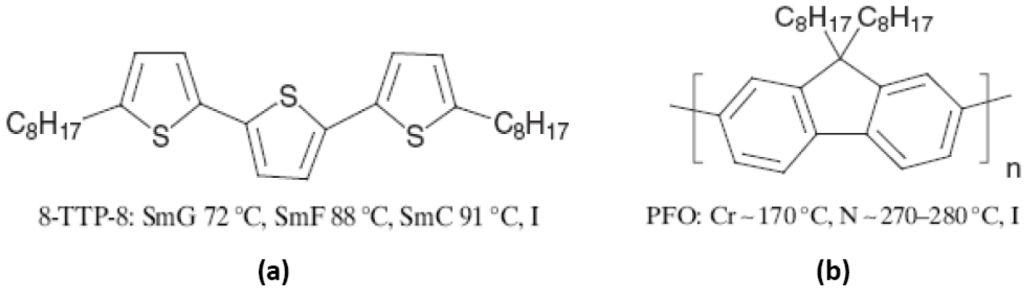

8-TTP-8: SmG 72 °C, SmF 88 °C, SmC 91 °C, I

PFO: Cr ~ 170 °C, N ~ 270–280 °C, I

Figure 1-30: (a) The terthiophene, 8-TTP-8, as an example of MLC and (b) The 9,9-dioctyl polyfluorene PFO as an example for PLC[69].

The aromatic core and terminal groups can be modified to control mesophase morphology and physical properties of the liquid crystal to meet the need of some applications; such as control of the transition temperature and solubility[65,66]. Reactive end groups can be incorporated into terminal chains so that the mesogens can be polymerised as shown in figure 1-31.

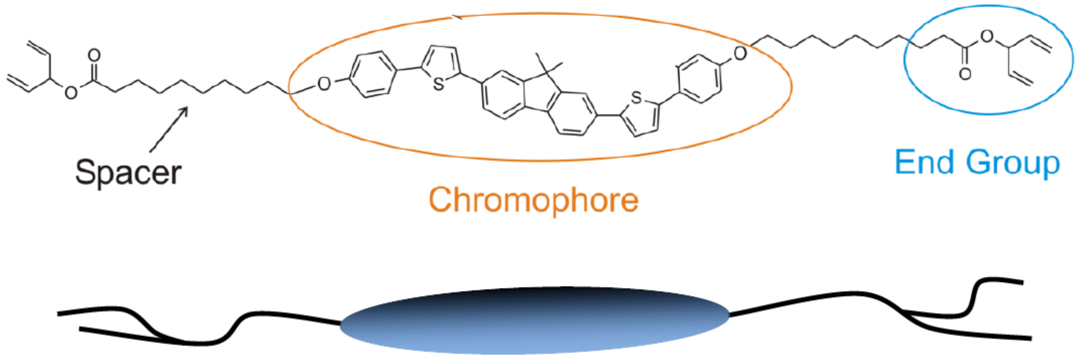

Figure 1-31: Example of the chemical structure of a monomer liquid crystal.

If the MLC mesogens are connected together via polymerisation of one of the end groups they will continue to keep the liquid crystal properties thus forming a polymer liquid crystal (PLC). One of the most important characteristics of the PLC is its ability to freeze the liquid crystal ordering of the material into a glassy state. The monomers can be attached together to form a polymer in different ways. If the monomers are attached to one another side by side to form one single chain this is called main chain polymer, as shown in figure 1-32(a). If the monomers form extended branches away from the polymer backbone a side chain polymer is formed as shown in figure 1-32(b). The polymers can also be formed as a network when the monomers have two polymerisable end groups as shown in figure 1-32(c)[61,65,68,70,69].

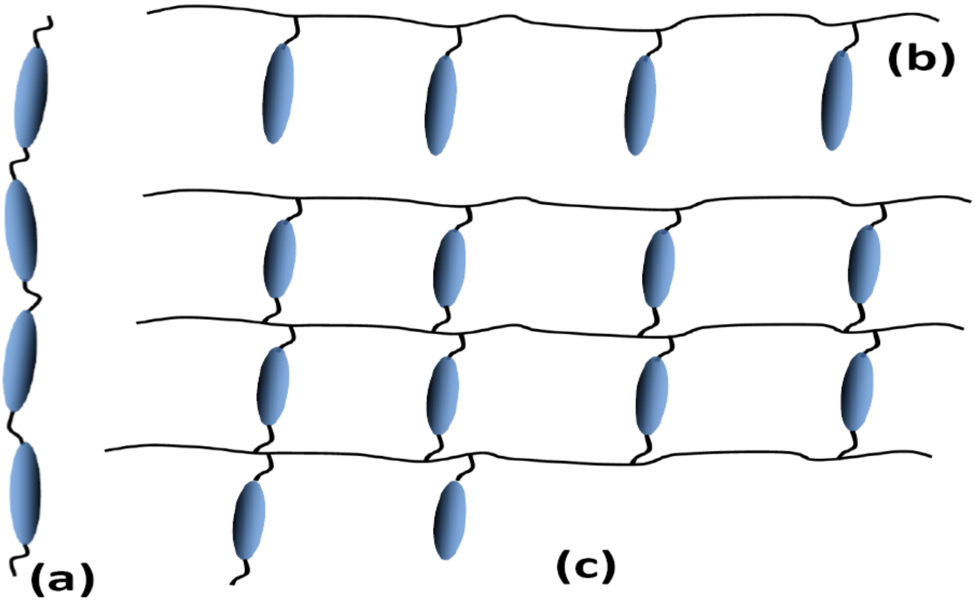

Figure 1-32: The different ways of attaching the MLC to form the PLC, (a) main chain polymer, (b) side chain polymer, (c) polymer network.

1.8.3. Classification of Liquid Crystals

The classification of the liquid crystal materials depends on the mechanism of the mesophase formation, molecular structure, the liquid crystal phases formed and their symmetry. The liquid crystal phases can be classified into two large groups: (i) lyotropic liquid crystals, and (ii) thermotropic liquid crystals. The lyotropic liquid crystals are mesogens which exhibit the liquid crystal properties when dissolved in an appropriate solvent with a certain concentration. The thermotropic liquid crystal where the LC phase is temperature dependent is detailed in the next section, and is the one used for electronic devices, at least in this thesis.

1.8.3.1. Thermotropic Liquid Crystal

Most research and development for optical and electrical applications focus on this branch of liquid crystal mesophases. If thermal energy is pumped into a crystalline material with highly ordered molecules (Cr), vibration of the molecules within the lattice increases in proportion to the increase of the thermal energy injected to the system. Above a certain temperature there is a complete breakdown of the intermolecular force between the molecules that maintains the crystalline nature of the material. This leads to the loss of the long-range orientational and positional order. However some order is maintained in the LC phases. Thermotropic mesophases exist only over well defined temperature ranges.

Thermotropic materials fall into two main branches based on the molecular structure of the mesogen. Rod-like and disk-like molecules, which can be formed by both MLC and PLC materials[30,66,67].

1.8.3.1.1. Rod-Like Liquid Crystal:

Calamitic liquid crystals describe the rod-like liquid crystals, which have long and short axes, and orientational order based on their long axis. The typical structures of the rod-like liquid crystal materials are shown in figure 1-31. Calamitic liquid crystal form different phases, the most common mesophases formed are the Smectic, Nematic, and Cholesteric.

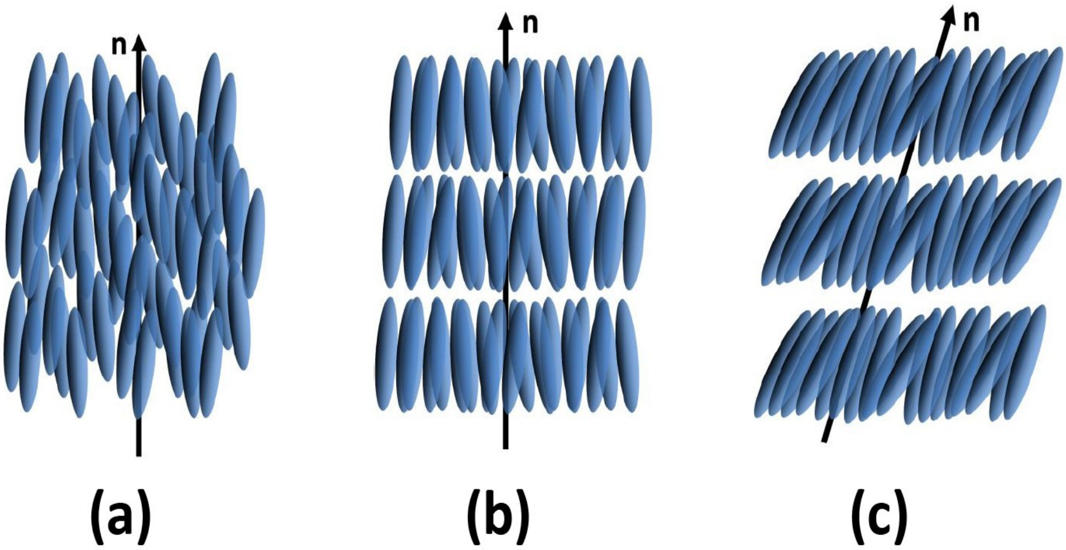

Figure 1-33: The liquid crystal arrangement in the pases; (a) Nematic, (b) Smectic A phase, and (c) Smectic C phase.

Nematic Phase (N)

The Nematic phase is the simplest liquid crystal phase. It is much more mobile and disordered than the Smectic phase described below. The molecules diffuse through the sample in different directions; however, they retain a preferred orientation. Therefore, the nematic phase has an orientational order and no positional order. This is the phase which is used in many liquid crystal devices, because the average orientation may be controlled with an electric field, and the plane of light polarization will follow the molecular orientation as it changes through a cell.

Smectic Mesophase (Sm)

Smectic mesophases are characterized by both the orientational and positional order and are the most ordered of calamitic mesophases. Here the molecules are free to move around quite randomly, but they tend to point along the director and arrange themselves in layers with an average thickness comparable with the length of molecules. There are many smectic mesophases with different packing of the layers between the director and the layer plane, see figure 1-33.

Cholesteric Phase

The cholesteric is considered as a special form of the Nematic phase and called chiral nematic phase (N*). This phase shows nematic ordering but the director rotates following a helical path throughout the sample. The helix results from doping of the nematic with a chiral molecule or incorporating a chiral centre in the LC molecule. The axis of this rotation is perpendicular to the director as shown in figure 1-34. The chiral nematic phase is characterised by the pitch, which is the distance along the helix over which the director rotates 360^o.

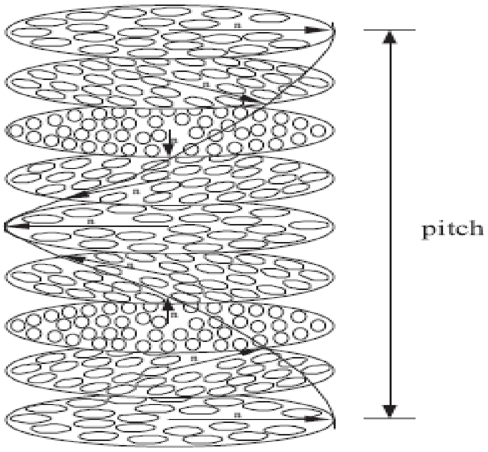

Figure 1-34: The liquid crystal arrangement in a cholesteric phase[69].

1.8.3.1.2. Discotic Liquid Crystal:

Disk-like or discotic mesogens have disk shaped molecules with long and short axes. There are two discotic sub-phases, the discotic nematic phase and the columnar phase.

Discotic Nematic

The molecules distribute themselves randomly throughout the material but they tend to be oriented in one direction in the discotic nematic mesophases.

Discotic Columnar

In the columnar mesophases, the molecules tend to arrange themselves into columns. The columns can be randomly arranged relative to each other or they can order themselves in groups forming a two dimensional lattice of columns, such as a hexagonal or rectangular lattice.

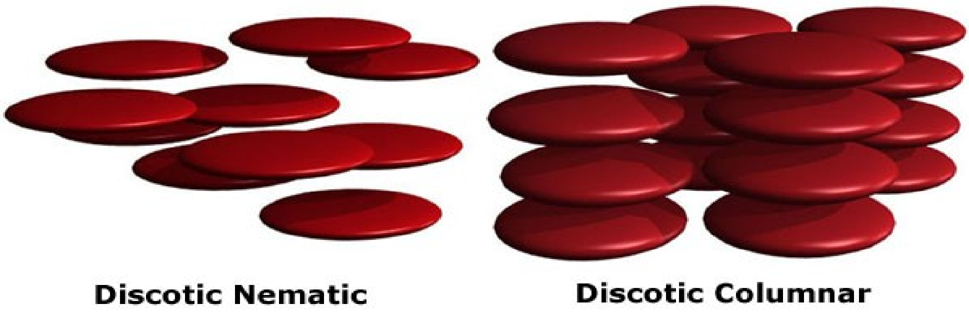

Figure 1-35: The liquid crystal arrangement in the discotic phases[64].

1.8.3.2. LCs Transition Temperature

The liquid crystal phases appear over a fixed range of temperature. The most common techniques to identify the material phases are optical polarising microscopy and differential scanning calorimetry (DSC). The most accurate one is X-ray diffraction. At the various transition temperatures the LC changes phase, as shown in figure 1-36 [65].

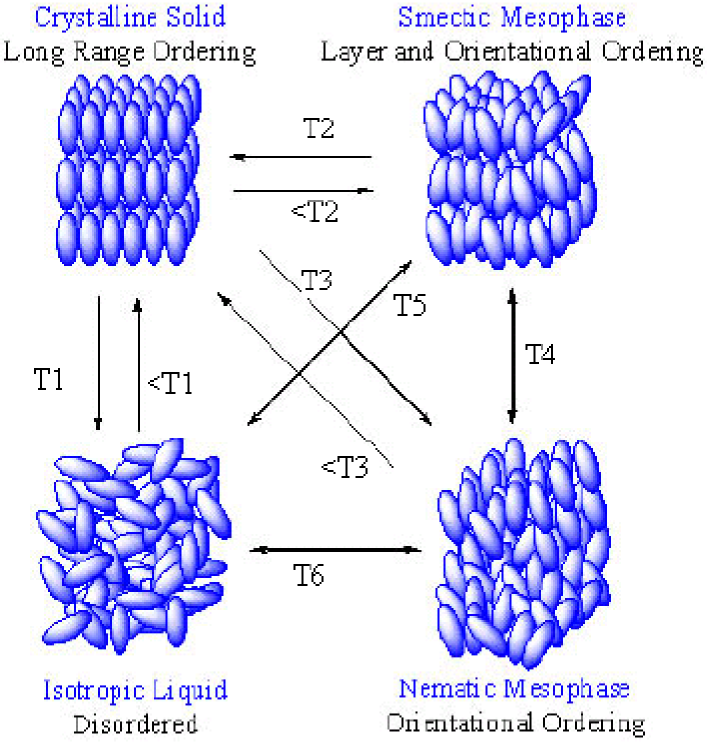

Figure 1-36: Possible transition temperature sequences for the liquid crystal materials

Because of the asymmetry of the molecules shape in the rod-like material there are two strong intermolecular forces to hold the molecules together. The lateral intermolecular force, which is responsible for the interaction between molecules through the long molecular axes and the terminal intermolecular force, which is responsible of the interaction between the ends of the molecules. These two intermolecular forces can be overcome when the material is heated above a specific temperature.

As shown in figure 1-36 T_1 is the melting point where the crystalline solid material (Cr) loses positional and orientational order to give an isotropic liquid phase (I) of highly disordered molecules where both the intermolecular forces are overcome. This step of phase transfer does not commonly occur in most LCs, which go through some other phases between the crystalline (Cr) and isotropic (I) phase. Some LCs melt and only show LC phases on cooling.

T_2 is the transition temperature from crystalline solid to Smectic phase (Cr-Sm): at this temperature the lateral intermolecular forces are stronger than the terminal ones. So the material tends to arrange itself into layers.

T_3 is the transition temperature from crystalline solid to Nematic phase (Cr-N): some materials go directly to the nematic phase where both intermolecular forces in the crystalline solid become weak simultaneously so the molecules move randomly but still keep their orientation to one direction.

T_4 is the transition temperature from Smectic to Nematic phase (Sm-N). At this temperature the lateral intermolecular force are overcome so that molecules lose their layer orientation and move randomly but still keep their long range orientation.

T_5, T_6 is the transition temperature of (Sm-I) and (N-I) respectively: these temperatures are known as clearing points. The material loses its orientational and positional (for Sm-I) order and the molecules move randomly in different directions. These temperatures give some indication of the material's thermal stability, where the higher the clearing point the greater the thermal stability of the material[66].

1.8.4. Liquid Crystal Alignment

LCs can align with respect to the substrate surface either orthogonally to the substrate surface, homeotropic alignment, or parallel to the substrate surface, planar alignment, as shown in figure 1-37. The alignment of the LCs can be achieved and controlled using an alignment layer composed of a material such as hexamethyldisilazane (HMDS), or rubbed polymide[71,72,73,74].

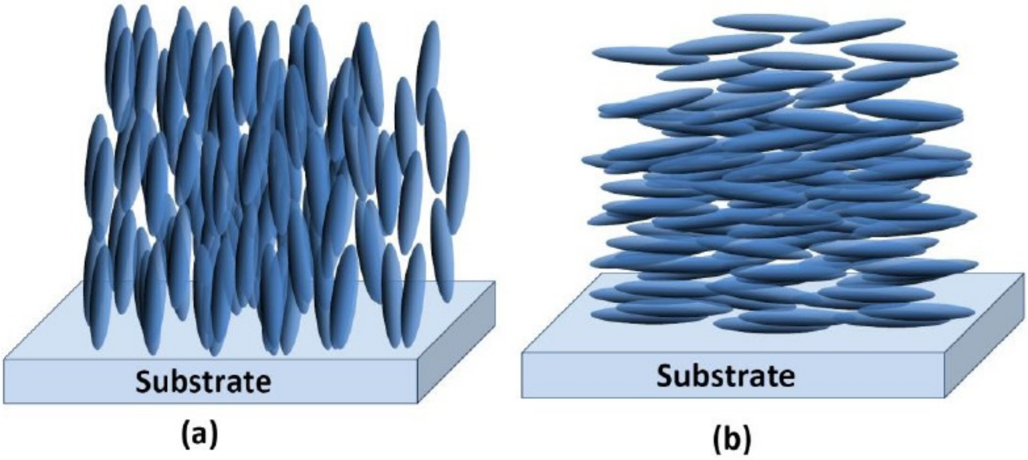

Figure 1-37: LCs alignments configurations, (a) Homeotropic, (b) Planar.

1.8.5. Charge Transport in Liquid Crystals

The charge carrier mobility of the amorphous material is limited by molecular disorder to be in the order of 10^{-3} $cm^2V^{-1}S^{-1}$ or less[69,75], which has large influence on the organic devices performance. The discovery of the conjugated discotic and calamitic liquid crystal conductivity in 1993 and 1995 respectively helps to overcome this limitation with self-molecular alignment improving the mobility to be larger than 10^{-3} $cm^2V^{-1}s^{-1}$ up to 0.1 $cm^2V^{-1}s^{-1}$ [76,77].

Liquid crystal mesophases provide large self organized domains with highly ordered and close packed structures, which improves the overlap of the intermolecular π orbitals, and support the hopping mechanism of the charge carrier between the closely spaced molecules (hopping sites)[78]. However the liquid crystals mesophase usually occur above room temperature, which means cooling down to room temperature fragments the large organized domains to small polycrystalline domains separated by grain boundaries, which increase the charge trapping and attenuate the charge carrier mobility, the cross linking of the liquid crystals is one of the suggested solutions to overcome this limitation.

1.8.6. Crosslinking of Liquid Crystals

To retain liquid crystals mesophase properties at room temperature reactive mesogens have been introduced[69,71,75]. These contain aromatic cores with semiconducting properties attached to two photoreactive polymerizable end groups via aliphatic spacers as shown is figure 1-31 and figure 1-38. The irradiation of thin films materials with a UV lamp or laser at the mesophase temperature cross-links the mesogens to form an insoluble crosslinked polymer network, which retains the molecular alignment on cooling. Some semiconducting reactive mesogens are nematic at room temperature. Others form nematic glasses on cooling from the nematic phase and can be cross-linked at room temperature.

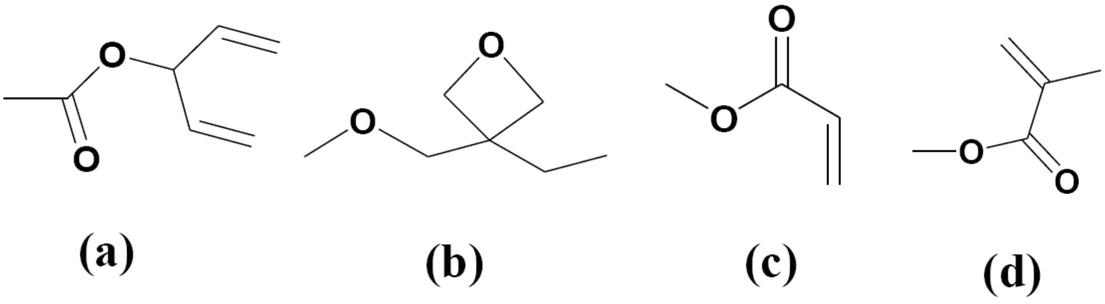

Figure 1-38: Some example of reactive end groups: (a) diene, (b) oxetane (c) acrylate, (d) methacrylate.

The additional advantage of the crosslinking is the formation of insoluble polymer networks, which can be used in the production of multilayer devices such as bilayer organic solar cells and RGB pixellated OLEDs using solution processing techniques [56,74,79].

Crosslinking can be induced using different techniques, chemical crosslinking with some suitable initiator, thermal crosslinking, or photochemical crosslinking via light irradiation (UV light is the most common used). For photochemical crosslinking a UV laser was used at the mesophase temperature, which retains the molecular orientational and positional alignment.

1.9. Thesis Outline

This thesis aims to search for novel organic semiconductors to be used as active materials (EDs/EAs) in bulkheterojunction photovoltaic devices.

In chapter two, we describe the design rules for molecular engineering of materials for organic solar cells based on the energy levels (HOMO/LUMO) of the organic semiconductor. We describe the cyclic voltammetry technique which has been used to estimate the energy levels, and apply this technique to study 31 home synthesised compounds of different chemical structures and active groups. Finally we discuss the influence of the chemical structure and the different active groups and elements on the energy levels ending by recommending EDs and EAs.

In chapter three we study the charge transport mechanism in organic semiconductors. We describe the time of flight (TOF) technique and use it to measure the charge carriers mobility and study the charge transport in six EAs and four EDs. Some models of charge transport in organic semiconductors are applied to analyse the measurements. The charge transport in the ED/EA blends is also investigated.

In chapter four we investigate the nanoscale morphology of the top surface of the active layer of the OPV and try to correlate it to the performance of solar cells. Atomic force microscope (AFM) is used in the investigation. The data is analysed using the roughness analysis parameters of root mean square (rms), height distribution and variation, and power spectral density (PSD). Four EDs and four EAs are studied for the OPV.

In chapter five, the nominated EDs and EAs active materials are used in BHJ solar cells and their performance analysed.

Finally, chapter 6 gives the conclusion of this work and suggests some ways of improvement and possibilities for future work.

1.10. References

1 http://timeforchange.org/prediction-of-energy-consumption.

2 http://www.eia.doe.gov/cneaf/alternate/page/renew_energy_consump/rea_prereport.html.

3 M. Gratzel, "Photoelectrochemical cells," Nature **414** (6861), 338-344 (2001).

4 G. Dennler, C. Lungenschmied, H. Neugebauer et al., "Flexible, conjugated polymer-fullerene-based bulk-heterojunction solar cells: Basics, encapsulation, and integration," Journal of Materials Research **20** (12), 3224-3233 (2005).

5 http://www.solarbuzz.com/Marketbuzz2009-intro.htm.

6 M. Reyes-Reyes, K. Kim, and D. L. Carroll, "High-efficiency photovoltaic devices based on annealed poly(3-hexylthiophene) and 1-(3-methoxycarbonyl)-propyl-1-phenyl-(6,6)C-61 blends," Applied Physics Letters **87** (8) (2005).

7 B. P. Rand, J. Li, J. G. Xue et al., "Organic double-heterostructure photovoltaic cells employing thick tris(acetylacetonato)ruthenium(III) exciton-blocking layers," Advanced Materials **17** (22), 2714-+ (2005).

8 B. Kippelen and J. L. Bredas, "Organic photovoltaics," Energy & Environmental Science **2** (3), 251-261 (2009).

9 Atam P. Arya, *Elementary modern physics*. (Reading, Mass., etc.: Addison-Wesley, 1974), pp.pp. xii, 548. 525 cm.

10 Jenny Nelson, *The physics of solar cells*. (Imperial College Press, London, 2003), pp.xix, 363 p.

11 Jean-Pierre Colinge and C. A. Colinge, *Physics of semiconductor devices*. (Kluwer Academic, Boston, Mass. ; London, 2002), pp.xiii, 436 p.

12 Jasprit Singh, *Smart electronic materials : fundamentals and applications*. (Cambridge University Press, Cambridge, 2005), pp.xxii, 408 p.

13 John C. Eng M. I. E. E. Seymour, *Physical electronics: an introduction to the physics of electron devices*. (London: Pitman, 1972), p.ix. 438 p. 422 cm.

14 Robert F. Pierret, *Advanced semiconductor fundamentals*, 2nd ed. ed. (Prentice Hall ; London : Pearson Education, Upper Saddle River, N.J., 2003), pp.x, 221 p.

15 Charles Kittel, *Introduction to solid state physics*, 7th ed. ed. (Wiley, New York ; Chichester, 1996), pp.xi,673p.

16 S. M. Sze and Kwok Kwok Ng, *Physics of semiconductor devices*, 3rd ed. / S.M. Sze and Kwok K Ng. ed. (Hoboken), pp.x, 815 p.

17 C. K. Chiang, C. R. Fincher, Y. W. Park et al., "Electrical-Conductivity in Doped Polyacetylene," Physical Review Letters **39** (17), 1098-1101 (1977).

18 A. Rockett, *Materials science of semiconductors*. (Springer, New York ; London, 2008), pp.xvi, 622 p.

19 P. W. Atkins and Julio De Paula, *Atkins' physical chemistry*, 8th ed. ed. (Oxford University Press, Oxford, 2006), pp.xxx, 1064 p.

20 R. Farchioni and Giuseppe Grosso, *Organic electronic materials : conjugated polymers and low molecular weight organic solids*. (Springer, Berlin, 2001).

21 J. M. Nunzi, "Organic photovoltaic materials and devices," Comptes Rendus Physique **3** (4), 523-542 (2002).

22 S. Chasteen, University of California, 2005.

23 Wolfgang Brütting, *Physics of organic semiconductors*. (Wiley-VCH, Weinheim ; [Chichester], 2005), pp.xviii, 536 p.

24 C. J. Brabec, V. Dyakonov, J. Parisi et al., *Organic photovoltaics : concepts and realization*. (Springer, Berlin, 2003).

25 C. W. Tang, "Two-layer organic photovoltaic cell," Applied Physics Letters **48** (2), 183-185 (1986).

[26] S. M. Sze, *Semiconductor devices, physics and technology*, 2nd ed. (Wiley, New York, 2002), p.564p.

[27] N Mwiinga, "Conservation of Solar Cell Optoelectronic Parameters," Journal of Electron Devices **3**, 71-84 (2005).

[28] K. Petritsch, Technical University of Graz, 2000.

[29] M. Drees, Virginia Polytechnic Institute and State University, 2003.

[30] Sam-Shajing Sun and Niyazi Serdar Sariciftci, *Organic photovoltaics : mechanisms, materials, and devices*. (Taylor & Francis, Boca Raton, Fla. ; London, 2005), pp.xxi, 629 p., [628] leave of plates.

[31] B. P. Rand, J. Genoe, P. Heremans et al., "Solar cells utilizing small molecular weight organic semiconductors," Progress in Photovoltaics **15** (8), 659-676 (2007).

[32] H. Hoppe and N. S. Sariciftci, "Organic solar cells: An overview," Journal of Materials Research **19** (7), 1924-1945 (2004).

[33] C Deibel, "Notes on Disordeed Matter," http://blog.disorderedmatter.eu/ (2009).

[34] B. P. Rand, J. G. Xue, F. Yang et al., "Organic solar cells with sensitivity extending into the near infrared - art. no. 200508," Applied Physics Letters **87** (23) (2005).

[35] C. Winder, Johannes Kepler University, 2001.

[36] R. F. Bailey-Salzman, B. P. Rand, and S. R. Forrest, "Near-infrared sensitive small molecule organic photovoltaic cells based on chloroaluminum phthalocyanine," Applied Physics Letters **91** (1) (2007).

[37] L. J. A. Koster, V. D. Mihailetchi, and P. W. M. Blom, "The optimal band gap for plastic photovoltaics," SPIE Newsroom (2007).

[38] C. Winder and N. S. Sariciftci, "Low bandgap polymers for photon harvesting in bulk heterojunction solar cells," Journal of Materials Chemistry **14** (7), 1077-1086 (2004).

[39] P. Wurfel, "Photovoltaic principles and organic solar cells," Chimia **61** (12), 770-774 (2007).

[40] M. Knupfer, "Exciton binding energies in organic semiconductors," Applied Physics a-Materials Science & Processing **77** (5), 623-626 (2003).

[41] V. I. Arkhipov, P. Heremans, and H. Bassler, "Why is exciton dissociation so efficient at the interface between a conjugated polymer and an electron acceptor?," Applied Physics Letters **82** (25), 4605-4607 (2003).

[42] J. Nelson, "Organic photovoltaic films," Current Opinion in Solid State & Materials Science **6** (1), 87-95 (2002).

[43] H. Hoppe, M. Niggemann, C. Winder et al., "Nanoscale morphology of conjugated polymer/fullerene-based bulk-heterojunction solar cells," Advanced Functional Materials **14** (10), 1005-1011 (2004).

[44] H. Hoppe, Nanomorphology - Efficiency Relationship in Organic Bulk Heterojunction Plastic Solar Cells, Ph.D. thesis, Linz Institute for Organic Solar Cells (LIOS) , Johannes Kepler University 2004.

[45] J.-M. Nunzi, "Organic photovoltaic materials and devices," C. R. Physique **3**, 523-542 (2002).

[46] H. Mounir, N.G.P. Jonathan, D. W. Samuel Ifor et al., "Conjugated Dendrimers for Light-Emitting Diodes: Effect of Generation " Advanced materials **11** (5), 371-374 (1999).

[47] P. Peumans and S. R. Forrest, "Separation of geminate charge-pairs at donor-acceptor interfaces in disordered solids," Chemical Physics Letters **398** (1-3), 27-31 (2004).

[48] C. J. Brabec, N. S. Sariciftci, and J. C. Hummelen, "Plastic solar cells," Advanced Functional Materials **11** (1), 15-26 (2001).

[49] C. J. Brabec, "Organic photovoltaics: technology and market," Solar Energy Materials and Solar Cells **83** (2-3), 273-292 (2004).

[50] G. Yu, J. Gao, J. C. Hummelen et al., "Polymer Photovoltaic Cells- Enhanced Efficincies via A network of Internal Donor-Acceptor Hetrojunctions," Science **270** (5243), 1789-1791 (1995).

[51] J. J. M. Halls, C. A. Walsh, N. C. Greenham et al., "Efficient Photodiodes from Interpenetrating Polymer Networks," Nature **376** (6540), 498-500 (1995).

[52] J. G. Xue, B. P. Rand, S. Uchida et al., "A hybrid planar-mixed molecular heterojunction photovoltaic cell," Advanced Materials **17** (1), 66-+ (2005).

[53] C. J. Brabec, A. Cravino, D. Meissner et al., "The influence of materials work function on the open circuit voltage of plastic solar cells," Thin Solid Films **403**, 368-372 (2002); L. C. Chen, D. Godovsky, O. Inganas et al., "Polymer photovoltaic devices from stratified multilayers of donor-acceptor blends," Advanced Materials **12** (18), 1367-1370 (2000).

[54] D. Godovsky, L. C. Chen, L. Pettersson et al., "The use of combinatorial materials development for polymer solar cells," Adv. Mater. Opt. Electron. **10** (2), 47-54 (2000).

[55] M. Drees, K. Premaratne, W. Graupner et al., "Creation of a gradient polymer-fullerene interface in photovoltaic devices by thermally controlled interdiffusion," Applied Physics Letters **81** (24), 4607-4609 (2002).

[56] W. C. Tsoi, M. O'Neill, M. P. Aldred et al., "Distributed bilayer photovoltaics based on nematic liquid crystal polymer networks," Chem. Mat. **19** (23), 5475-5484 (2007).

[57] B. P. Rand, P. Peumans, and S. R. Forrest, "Long-range absorption enhancement in organic tandem thin-film solar cells containing silver nanoclusters," Journal of Applied Physics **96** (12), 7519-7526 (2004).

[58] J. G. Xue, S. Uchida, B. P. Rand et al., "Asymmetric tandem organic photovoltaic cells with hybrid planar-mixed molecular heterojunctions," Applied Physics Letters **85** (23), 5757-5759 (2004).

[59] T. Ameri, G. Dennler, C. Lungenschmied et al., "Organic tandem solar cells: A review," Energy & Environmental Science **2** (4), 347-363 (2009).

[60] J. Y. Kim, K. Lee, N. E. Coates et al., "Efficient tandem polymer solar cells fabricated by all-solution processing," Science **317** (5835), 222-225 (2007).

[61] A. A. Collyer, *Liquid crystal polymers : from structures to applications*. (Elsevier Applied Science, London, 1992), pp.xvi,474p.

[62] H. Kawamoto, "The history of liquid-crystal displays," Proceedings of the Ieee **90** (4), 460-500 (2002).

[63] R. J. Bushby and O. R. Lozman, "Photoconducting liquid crystals," Current Opinion in Solid State & Materials Science **6** (6), 569-578 (2002).

[64] Christoper J. Barrett, "The web site of Barrett Research group " http://barrett-group.mcgill.ca/main.htm (2009).

[65] Peter J. Collings and Michael Hird, *Introduction to liquid crystals*. (Taylor & Francis, London, 1997), p.298p.

[66] V. G. Chigrinov, *Liquid crystal devices : physics and applications*. (Artech House, Boston ; London, 1999), pp.xiv, 357p.

[67] The Free Encyclopedia Wikipedia, "Liquid crystal," http://en.wikipedia.org/wiki/Liquid_crystal (2009).

[68] E. T. Samulski, "MACROMOLECULAR STRUCTURE AND LIQUID CRYSTALLINITY," Faraday Discussions **79** (79), 7-20 (1985).

[69] M. O'Neill and S. M. Kelly, "Liquid crystals for charge transport, luminescence, and photonics," Advanced Materials **15** (14), 1135-1146 (2003).

70 Peter J. Collings, *Liquid crystals : nature's delicate phase of matter*. (Hilger, Bristol, 1990), p.222p.

71 I. McCulloch, W. M. Zhang, M. Heeney et al., "Polymerisable liquid crystalline organic semiconductors and their fabrication in organic field effect transistors," Journal of Materials Chemistry **13** (10), 2436-2444 (2003).

72 S. Droge, M. S. Al Khalifah, M. O'Neill et al., "Grazing Incidence X-ray Diffraction of a Photoaligned Nematic Semiconductor," Journal of Physical Chemistry B **113** (1), 49-53 (2009).

73 S. Droge, M. O'Neill, A. Lobbert et al., "A new approach to photoalignment: photo-addition to a self-assembled monolayer," Journal of Materials Chemistry **19** (2), 274-279 (2009).

74 A. E. A. Contoret, S. R. Farrar, P. O. Jackson et al., "Polarized electroluminescence from an anisotropic nematic network on a non-contact photoalignment layer," Advanced Materials **12** (13), 971-+ (2000).

75 R. J. Baldwin, T. Kreouzis, M. Shkunov et al., "A comprehensive study of the effect of reactive end groups on the charge carrier transport within polymerized and nonpolymerized liquid crystals," J. Appl. Phys. **101** (2), 10 (2007).

76 M. Funahashi and J. Hanna, "Impurity effect on charge carrier transport in smectic liquid crystals," Chemical Physics Letters **397** (4-6), 319-323 (2004).

77 K. L. Woon, M. P. Aldred, P. Vlachos et al., "Electronic charge transport in extended nematic liquid crystals," Chem. Mat. **18** (9), 2311-2317 (2006).

78 W. Pisula, M. Zorn, J. Y. Chang et al., "Liquid Crystalline Ordering and Charge Transport in Semiconducting Materials," Macromolecular Rapid Communications **30** (14), 1179-1202 (2009).

79 M. P. Aldred, A. E. A. Contoret, S. R. Farrar et al., "A full-color electroluminescent device and patterned photoalignment using light-emitting liquid crystals," Advanced Materials **17** (11), 1368-+ (2005).

2.

ELECTRICAL AND OPTICAL PROPERTIES OF ORGANIC CONJUGATED SMALL MOLECULES

2.1. Energy Levels and Electronic Devices

Organic polymers and small molecules have been used as the active components in electronic and optoelectronic devices including organic photovoltaics (OPVs), organic light emitting diodes (OLEDs), and organic field effect transistors (OFETs). However, the devices performance is still low, so they need to be further improvement of device architectures, and development of new efficient electron donors (ED)/ acceptors (EA). It is essential to know the HOMO and LUMO energy levels of the EDs and the EAs and the energy gap between them as illustrated in figure 2-1 for understanding materials and designing organic devices. In this chapter we study the energy levels of 34 compounds and investigate their suitability to be used as EDs and EAs for the OPV. Also we study the effect of substituting different chemical groups on the optical and electrical properties of the materials.

2.2. Designing Rules of Energetic Interfaces for an Optimal Organic Solar Cell

Models to estimate the performance of the solar cells have been reported[1,2,3,4]. These models were based on controlling the energetic interfaces of the EDs/EAs via designing and synthesizing new and efficient organic materials following some energetic rules.

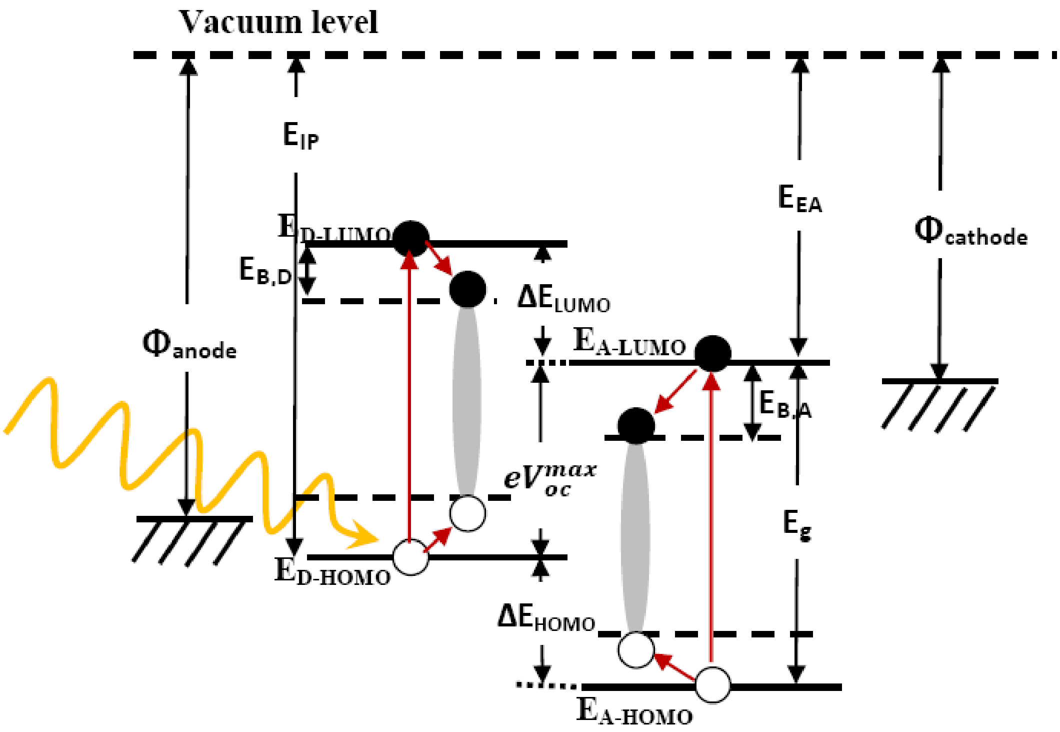

Figure 2-1: Schematic diagram of the energy levels of the organic solar cells showing the main electronic parameters.

Firstly, it is important for the organic material to be air stable for easy handling and processing. The acceptor materials are more air stable than the donor materials where the origin of the instability of the donor material come from the instability of the organic anions, which are easily oxidized in contact with air (oxygen) or water. Therefore, the HOMO energy level of these materials needs to be below the air oxidation threshold which is -5.27 eV or 0.57 V vs. SCE[1, 3,5].

Secondly, the short circuit current, I_{sc}, is one of the main parameters of the solar cells performance; the more photons absorbed by the EDs and EAs, the higher I_{sc}. Figure 2-2 shows the solar spectral irradiance and number of photons as a function of the wavelength. The energy band gap E_g between the HOMO and the LUMO energy levels of the donor and acceptor are key parameters for optimizing the photon absorption. Reducing the band gap of the organic materials leads to more photon harvesting and higher I_{sc}. However, the absorption spectrum ideally needs to be broad covering most of the solar spectrum as illustrated in figure 2-2.

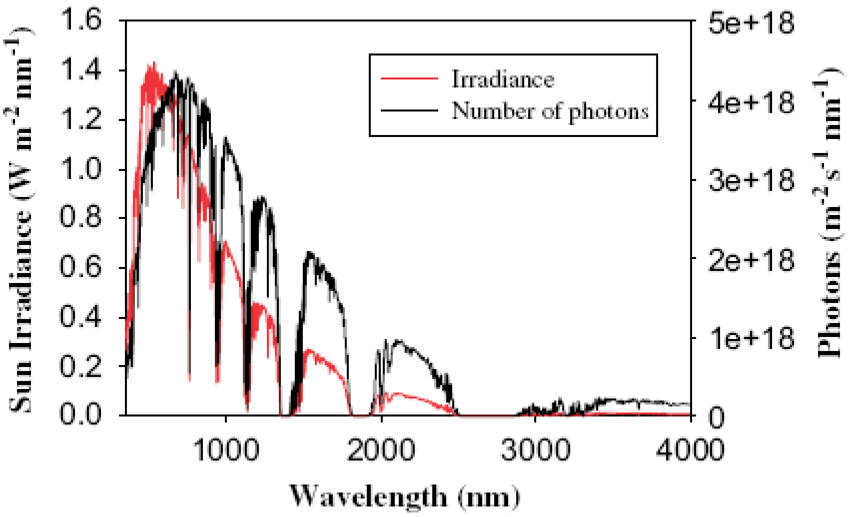

Figure 2-2: Solar spectral irradiance and number of photons as function of the wavelength[6].

Low band gap organic materials are defined as those with a band gap below 2 eV, which absorb light with wavelength longer the 620 nm[7,6]. Small band gap organic materials can be designed using chemical manipulation. There are two approaches to decrease the band gap, extending the conjugation length, or linking covalently electron donor and electron acceptor fragments[8,9,10].

Thirdly, the open circuit voltage V_{oc} of the solar cell is another important parameter of solar cells, where the maximum value of V_{oc} is found to be related to the donor HOMO energy and the acceptor LUMO energy level. There is a big debate about relating V_{oc} to the energy difference ($E_{D\text{-}HOMO} - E_{A\text{-}LUMO}$) [2,11,12,13,14], Scharber et al.[2] report that the V_{oc} of conjugated polymer: PCBM BHJ solar cells could be estimated as

$$\mathbf{V_{oc}} = \left({}^{\mathbf{1}}\!/_{\mathbf{e}}\right)\left(\left|\mathbf{E_{D,HOMO}}\right| - \left|\mathbf{E_{PCBM,LUMO}}\right|\right) - \mathbf{0.3V} \qquad (2\text{-}1)$$

Rand et al.[12] reported that the energy difference is equal to the maximum open circuit voltage V_{oc}^{max}, which is not always observed under typical conditions because it varies with factors such as nanoscale morphology, temperature and light intensity. Therefore the V_{oc} can be estimated to be

$$\mathbf{V_{oc} \leq (1/e)(|E_{D,HOMO}| - |E_{A,LUMO}|)} \tag{2-2}$$

Fourthly, the LUMO (HOMO) energy level of the donor must be positioned above the LUMO (HOMO) energy level of the acceptor to ensure efficient electron transfer from donor to acceptor. The difference between the LUMO (HOMO) energy level of the donor and the LUMO (HOMO) energy level of the acceptor is known as the frontier orbital energy offset ΔE_{LUMO} (ΔE_{HOMO}) as shown in figure 2-1. The ΔE_{LUMO} and ΔE_{HOMO} is desirable to be larger than the exciton binding energy of donor materials ($E_{B,D}$), and acceptor materials ($E_{B,A}$) respectively[15,16], which is the minimum energy to overcome the coulomb attraction force and separate the exciton into separated free electrons and holes. Its assignment is controversial with values ranging between 0.1-2 eV[17], and for organic semiconductors it typically varies between 0.2 to 1 eV[15]. The estimate of the most efficient offset varies between 0.2-0.4 eV [1,3,7]. If the energy offset is too small or too large the efficiency of the charge separation becomes less. In addition a large offset reduces the open circuit voltage V_{oc}[3,16,17]. Therefore, it is essential to analyse the donor/acceptor energy offsets in order to achieve efficient charge separation.

Fifthly, the alignment of donor/acceptor energy levels with the electrodes' work functions is important for efficient charge extraction. The requirement is

$$\mathbf{E_{D,HOMO} \sim \Phi_{anode}} \tag{2-3}$$

$$\mathbf{E_{A,LUMO} \sim \Phi_{cathode}} \tag{2-4}$$

Where Φ_{anode}, $\Phi_{cathode}$ is the work function of the cathode and the anode respectively[14,18,19,20].

Many of these requirements are contrary so that trades-off have to be made in the design of real solar cells.

2.3. HOMO/ LUMO vs. Ionization Potential/Electron Affinity

The ionization potential E_{IP} is defined chemically for molecules as the energy required to remove an electron from the highest occupied molecular orbital (HOMO) of the neutral molecule to the vacuum level. The electron affinity E_{EA} is the energy gained by an original neutral molecule when an electron is added to the lowest unoccupied molecular orbit (LUMO)[21,22], as shown in figure 2-1 and figure 2-3 where HOMO and LUMO levels in molecular semiconductors are equivalent to valence and conduction band-edges in inorganic semiconductors .

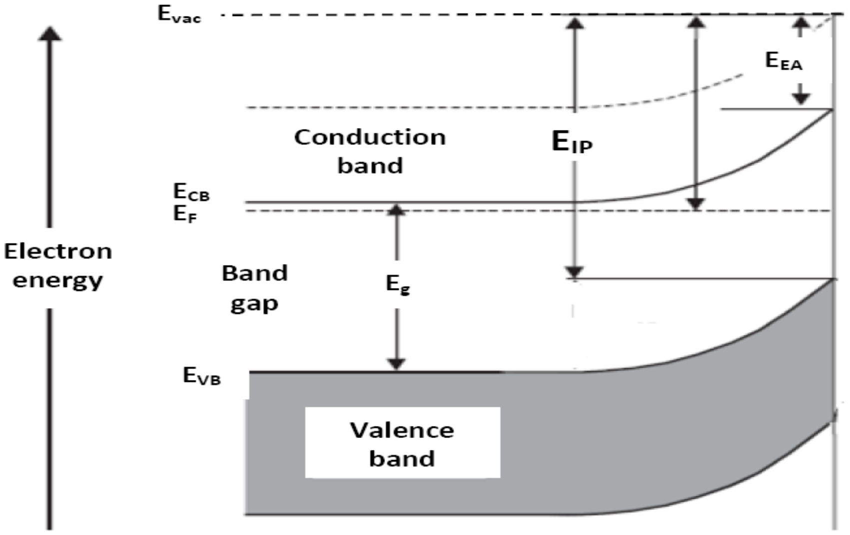

Figure 2-3: Energy band diagram of a semiconductor near its surface[21]

Unlike the non-molecular electronic solids, molecules can be considered as small N-electron system with mostly localized charge carriers. The addition or removal of an electron has a significant effect on the geometry and electronic energies. Therefore the E_{IP} and E_{EA} for a system with N electrons is defined as[21,23]

$$\mathbf{E_{IP} = E(N-1) - E(N)} \tag{2-5}$$

$$\mathbf{E_{EA} = E(N) - E(N+1)} \tag{2-6}$$

The energy levels E_{HOMO} and E_{LUMO} for organic materials can be correlated to the E_{IP} and E_{EA} based on the Koopman's theorem (KT), which equates the E_{IP} and E_{EA} to the negative value of the orbital energies as[24,25,26]

$$\mathbf{E_{IP}} = -\mathbf{E_{HOMO}} \tag{2-7}$$

$$\mathbf{E_{EA}} = -\mathbf{E_{LUMO}} \tag{2-8}$$

The E_{IP} and E_{EA} can be measured with different techniques such as ultraviolet photoemission spectroscopy (UPS), inverse photoemission spectroscopy (IPES), electrochemical voltage spectroscopy (EVS), and cyclic voltammetry (CV).

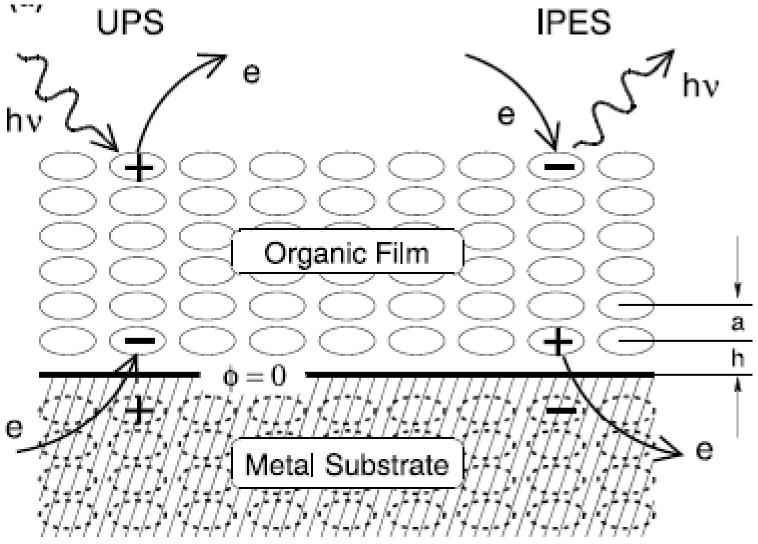

Figure 2-4: Schematic representation of charge generation processes in a molecular film, where UPS/IPES generates a cation/anion at the outer surface, while charge injection from the substrate involves the layer next to the metal.[27]

As shown in figure 2-4, UPS[25,21,27] involves the absorption of ultraviolet light at the surface of a thin film sample. An electron is ejected leaving a molecular cation in the outer surface. The electron kinetic energy is measured. The sum of the absolute value of the maximum electron kinetic energy and the orbital potential energy is equal to the photon energy.

In the IPES[21,27] technique, the surface is irradiated with low energy electrons, which are captured by the surface forming molecular anions and emitting photons. The photon energy is measured to find the LUMO and the E_{EA} as shown in figure 2-4.

The UPS and IPES measure the E_{IP} and E_{EA} more accurately than cyclic voltammetry (CV). However the former techniques are more expensive and more complicated and the result of these techniques are slightly different. D'Andrade et al. report that the oxidation potential obtained from CV can be correlated to the E_{HOMO} of the organic film measured by UPS using an empirical relation[25].

2.4. Cyclic Voltammetry

2.4.1. Introduction

Cyclic voltammetry is a versatile electroanalytical measurement technique serving a wide range of scientific fields. The electrochemical study of the electronic properties of electroactive materials is an example. Primarily cyclic voltammetry provides practical information about the redox (oxidation and reduction) properties of the target materials. It is a very important tool for the organophotonic research because it helps to estimate the energy levels of the organic compounds. The ionization potential E_{IP} can be considered as the HOMO for the material, and the electron affinity E_{EA} can be considered as the LUMO of the material as illustrated in eq. 2-7 and eq. 2-8. From these results we can decide the best materials as EDs and EAs.

2.4.2. The Instrumentation

There are three basic components of the electroanalytical system for cyclic voltammetry; the electrochemical cell, the computer, and the electronic hardware for generating the voltage, controlling it and measuring the current as shown in figure 2-5

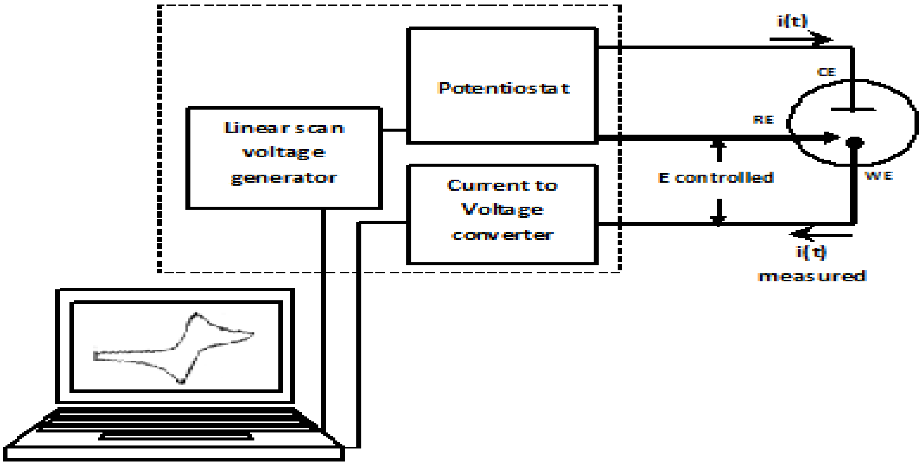

Figure 2-5: Experimental arrangement for cyclic voltammetry experiment.

The electrochemical cell is the core of the voltammetry operation[28,29,30,31], which typically consists of a glass container covered with a plastic cover as shown in figure 2-6. The cover is made of a durable material such as the PTFE to be resistant to the solvents and the materials used in the experiment. It has four holes, three for the electrodes and one for the purging of the solution with an inert gas such as N_2 or Ar to remove the dissolved Oxygen in the solution. This has a cathodic signal that can interfere with the observed current response. The three electrodes are the reference electrode (RE), working electrode (WE) and counter (auxiliary) electrode (CE) and are immersed in the sample dissolved in a solvent and an ionic electrolyte. The most commonly used REs are Silver/silver chloride (Ag/AgCl) electrode or saturated calomel electrode (SCE). The WE is consists of various geometries and materials, ranging from small Hg drops to flat disks of platinum, gold or glassy carbon. Mostly the CE consists of a thin wire of Pt or Au and sometimes graphite can be used.

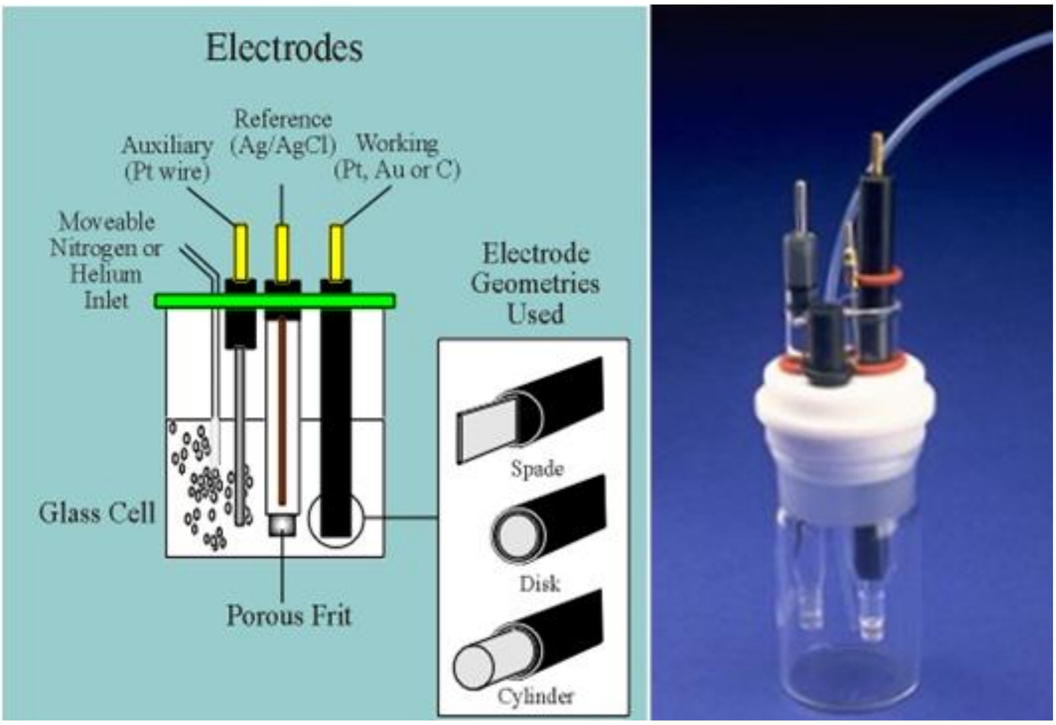

Figure 2-6: Schematic diagram and photo image of the electrochemical cell and its components.

The potentiostat, linear scan voltage generator (signal source), and current-to-voltage convertor are the main electronic hardware required to control a three electrode cell. They are interfaced with a computer, which controls the instruments with a special software package. As the schematic in figure 2-5 shows the linear scan voltage generator produces the excitation electrical signal through the potentiostat to the RE of the electrochemical cell. At the same time it adjusts the voltage between the WE and CE to maintain the potential difference between the WE and the RE, and to ensure the WE is not influenced by the electrochemical reactions which take place. The current-to-voltage converter measures the resulting current at the WE. The data is transferred to the computer to be stored and analyzed more effectively[28,29,30,31,32].

2.4.3. Reaction Mechanism

The electrochemical reactions which take place at the WE are the target of cyclic voltammetry experiments[28,29,30,31,32,33,34]. Electrolysis of the solute (oxidation, reduction) occurs by placing the solution in contact with the electrode surface, which is sufficiently positive or negative in voltage, so that current is measured when either the solute gains electrons from the surface or transfers electrons to the surface. These are known as cathodic current and anodic current respectively.

A cyclic linear potential scan is applied to the WE with respect to the RE. The resulting current-potential plot is termed a cyclic voltammogram which shown in figure 2-7(b). The electrode potential increases linearly with time, from an initial potential value (E_i) to the switching potential (E_s), where the direction of the scan is reversed down linearly to the final potential (E_f). The variation of the potential with the time is called the excitation waveform, and has a triangular waveform as shown in figure 2-7(a).

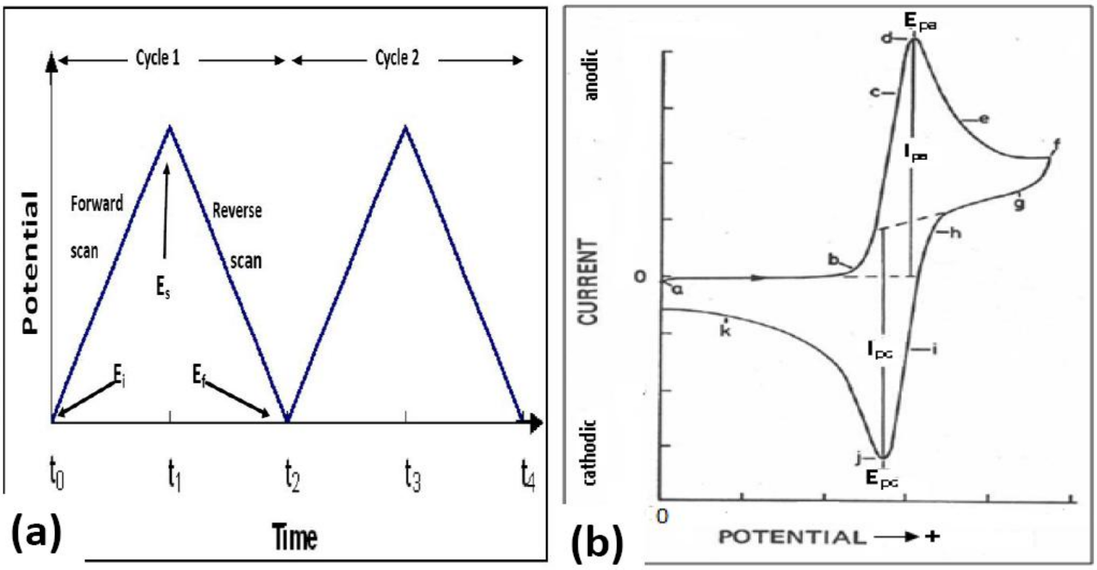

Figure 2-7: (a)The cyclic voltammetry excitation waveform, (b) plot of cyclic voltammogram[31].

We interpret the unique shape of the cyclic voltammogram from compound X shown in figure 2-7(b) and link it to the electrochemical reactions at the WE. The forward scan of the potential is in the positive direction (a). When the potential reaches a sufficiently positive potential at (b) the anodic current starts due to the oxidation

$$\mathbf{X \rightarrow X^{+} + e} \qquad (2\text{-}9)$$

The anodic current increases rapidly (b-d) until the concentration of the X^+ at the electrode surface becomes large and the X concentration is depleted near the electrode surface causing the current to peak at (d), and start decaying at (d-g). The direction of the scan is switched to negative at (f) for the reverse scan. The anodic current continues to reduce even after switching the potential to scan in the negative direction.

When the potential reaches a sufficiently negative value for reduction at (h), the accumulated X^+ around the electrode can now be reduced back to the original material by the electrode process

$$\mathbf{X^+ + e \rightarrow X} \qquad (2\text{-}10)$$

The cathodic current increases rapidly in the positive direction during (i to j), until the concentration of the X^+ is decreased around the electrode surface causing the current to decay from j to k as the solution around the electrode surface is depleted of X^+ back to X. The first cycle is completed when the potential returns back to the initial potential E_i.

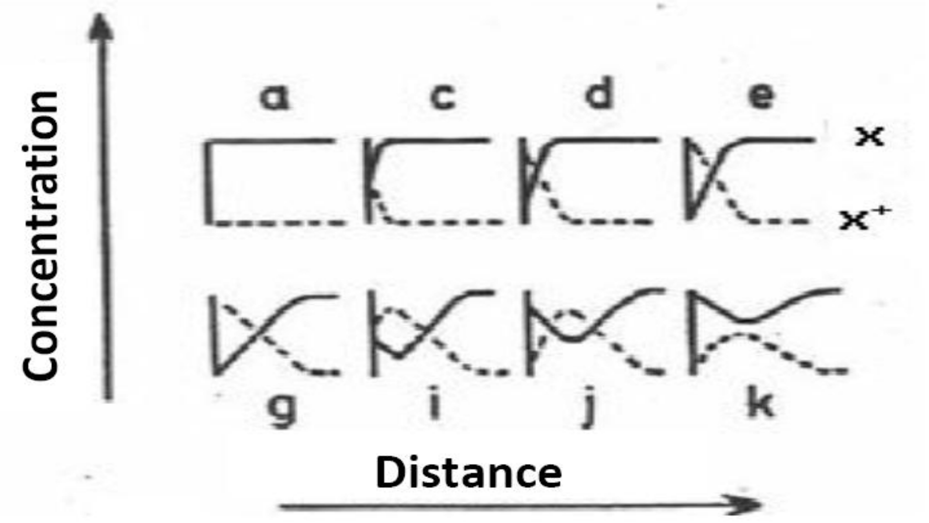

Figure 2-8: Concentration-distance profile C-x profile of the solution components from the electrode surface, at different points of the potential scan selected in the cyclic voltammogram in the previous figure.

Figure 2-8 illustrates the solution concentration-distance profile (C-*x*) profile for selected points, where *x* is the distance from the electrode surface. The C-*x* profile can be used to clearly understand the change of the current with the potential change during the scan. The current is proportional to the slope of the C-x profile $\left(\frac{\partial C}{\partial x}\right)_{x=0}$ at the electrode surface as described by Fick's Law of Diffusion[31,30,35,36]

$$\mathbf{I = nFAD\left(\frac{\partial C}{\partial x}\right)_{x=0} = K\left(\frac{\partial C}{\partial x}\right)_{x=0}} \qquad (2\text{-}11)$$

Where I is the current in A, n is the number of electrons transferred per ion in equivalents/mole, F is the faraday, A is the electrode area in cm^2, D is diffusion coefficient in cm^2/s, C is the concentration in mol/cm^3.

The slope of the profile at (a) is zero so I = 0. As the potential becomes more positive, $\left(\frac{\partial C}{\partial x}\right)_{x=0}$ starts changing at (b) and increases rapidly at (c-d) with the anodic current increasing correspondingly. However, after (d), $\left(\frac{\partial C}{\partial x}\right)_{x=0}$ decreases as shown in the profiles (e) and (g) as a result of the depletion of X close to the electrode surface; the current decreases also. When the potential is reversed to the negative direction the oxidation of X continues until the potential reaches a sufficiently negative value for reduction of X^+ to X. $\left(\frac{\partial C}{\partial x}\right)_{x=0}$ then changes rapidly as shown in the profile (i) and (j) causing the current to peak at (j) when the concentration of X^+ is depleted around the electrode.

The cycle is called the oxidation reaction because it starts with an oxidation reaction of X to X^+ and gives an anodic current by scanning in the positive direction as shown in figure 2-9. If we scan in the negative direction the reaction is called the reduction reaction because it start with reduction reaction of X to X^- and gives a cathodic current by the electrode process

$$\mathbf{X + e \rightarrow X^-} \qquad (2\text{-}12)$$

$$\mathbf{X^- \rightarrow X + e} \qquad (2\text{-}13)$$

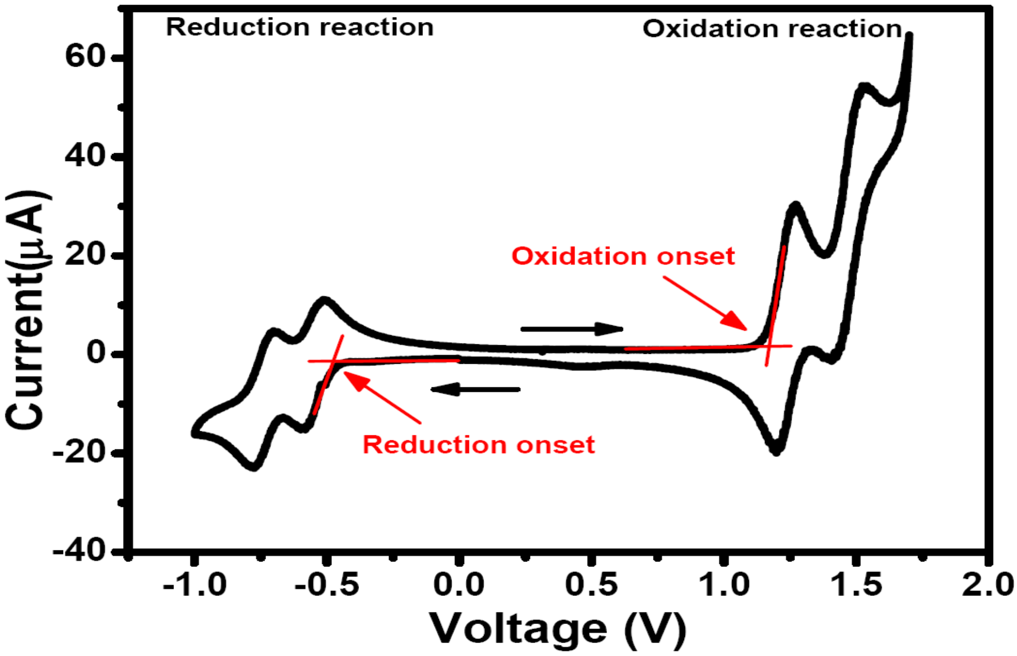

Figure 2-9: cyclic voltammogram illustrating both the oxidation and the reduction reactions for compound 13.

2.4.4. Data Interpretation

Cyclic voltammetry is characterized by several important parameters as shown in the cyclic voltammograms figure 2-7 and figure 2-9, the cathodic and anodic peak potentials (E_{pc} , E_{pa}), the cathodic and anodic peak currents (i_{pc} , i_{pa}) and the oxidation and reduction onset of the first peak (E_{ox}^{onset} , E_{red}^{onset}). These can be used to evaluate the energy levels, and reversibility and stability of the studied material.

2.4.4.1. The HOMO/LUMO Study

The E_{ox}^{onset} is used to estimate the E_{IP}, and the E_{red}^{onset} is used to estimate the E_{EA}. E_{ox}^{onset} (E_{red}^{onset}) can be estimated from the intersection of the two tangents drawn at the rising (descending) oxidation (reduction) current and background current in the cyclic voltammogram[37] as shown in figure 2-9.

The potentials recorded experimentally are relative to the reference electrode used, namely the Ag/AgCl, and need to be correlated to the vacuum level in order to obtain the E_{IP} and E_{EA} values for the compounds. These potentials values can be correlated to the vacuum level when given with respect to the normal hydrogen electrode NHE, since the potential of the NHE (E_{NHE}) is typically specified to be 4.5 V (±0.1V)[32,38] with respect to the vacuum level. The potential of the Ag/AgCl electrode $E_{Ag/AgCl}$ with respect to the NHE electrode is +0.197 V[32,30], as illustrated in figure 2-10, where the vacuum level is assumed to be $E_{vac} = 0$V. Then, all the measured potentials can be shifted appropriately as

$$\mathbf{E_{Ag/AgCl} = E_{NHE} + 0.197 = 4.7\ V} \qquad (2\text{-}14)$$

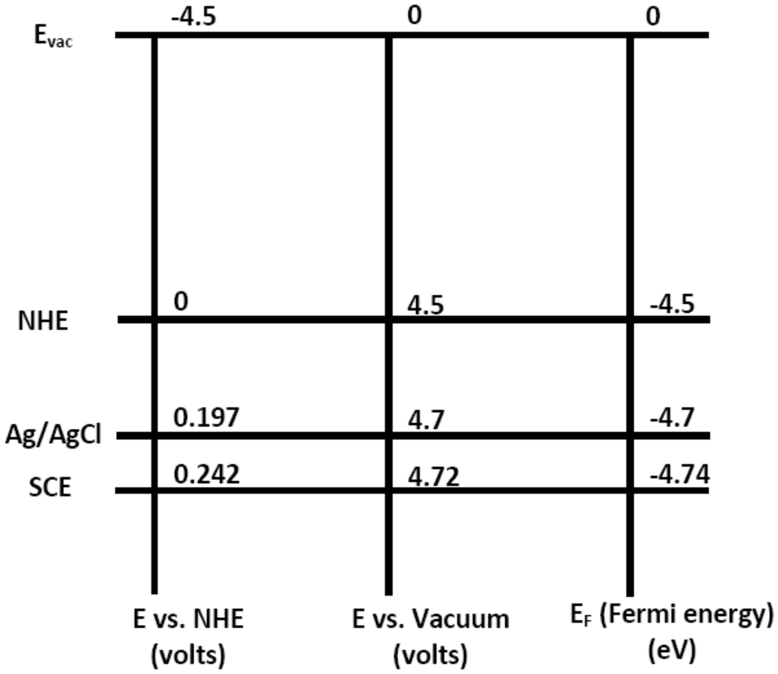

Figure 2-10: Diagram relating potentials of SCE, and Ag/AgCl electrodes with reference to the potential on NHE, the potential on the absolute scale versus vacuum, and the Fermi energy correspond to each of the indicated potential.[32]

Therefore the experimentally recorded oxidation and reduction onset E_{ox}^{onset} and E_{red}^{onset} relative to the Ag/AgCl electrode can be related to the vacuum level (E_{ox},E_{red})

$$\mathbf{E_{ox} = E_{ox}^{onset} + E_{Ag/AgCl} = E_{ox}^{onset} + 4.7} \qquad (2\text{-}15)$$

$$\mathbf{E_{red} = E_{red}^{onset} + E_{Ag/AgCl} = E_{red}^{onset} + 4.7} \qquad (2\text{-}16)$$

The actual oxidation and reduction onset potential need to be calibrated, which is typically achieved by measuring a standard reference material with a known potential.

The ferrocene/ferrocenium (Fc/Fc$^+$) couple is often used for calibrating redox reactions, since it is soluble and stable in many solvents, and it has a reversible reaction[32].

The study by V. V. Pavilishchuk and A. W. Addison[39] shows that the collection of the Fc/Fc$^+$ half-wave potential $E_{Fc}^{1/2}$ measured versus different reference electrodes shows large variations which is a significant annoyance in reporting and discussing literature data. We decided to use the average of the 31 Fc/Fc$^+$ half-wave potential measurements $E_{Fc}^{1/2}$ that we obtained during this research as our reference point. This is 0.425 V vs. Ag/AgCl electrode. Therefore we add a correction factor to eq. 2-15 and eq. 2-16 which becomes

$$\mathbf{E_{ox} = E_{ox}^{onset} + 4.7 + \boldsymbol{\delta}} \tag{2-17}$$

$$\mathbf{E_{red} = E_{red}^{onset} + 4.7 + \boldsymbol{\delta}} \tag{2-18}$$

where $\delta = 0.425 - E_{Fc}^{1/2}$ and $E_{Fc}^{1/2}$ is the half-wave potential of FC/FC$^+$ from our measurement after each materials measurement.

Finally, we correlate the E_{IP} and E_{EA} to the oxidation and reduction onset to be

$$\mathbf{E_{IP} = eE_{ox}} \tag{2-19}$$

$$\boldsymbol{E}_{\mathbf{EA}} = \mathbf{eE_{red}} \tag{2-20}$$

In some cases only one of the redox reactions can be obtained. Therefore, in this case we can relate the E_{IP} and E_{EA} to each other using the optically measured energy gap $E_{g,op}$ as

$$\mathbf{E_{IP} = E_{EA,cv} + E_{g,op}} \tag{2-21}$$

$$\mathbf{E_{EA} = E_{IP,cv} - E_{g,op}} \tag{2-22}$$

The optical energy gap $E_{g,op}$ can be estimated from the energy of the optical absorption onset. This is obtained from the material absorption spectrum as shown in figure 2-11; the onset is the intersection of the two tangents drawn at the rising maximum absorption and background absorption[37,40].

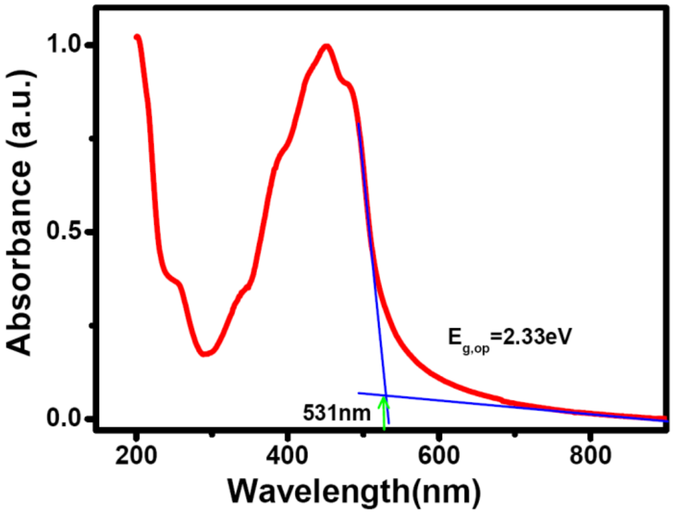

Figure 2-11: Normalized absorption spectrum of compound 1, with an illustration of the energy gap measurement.

The difference between the E_{IP}(E_{ox}) and E_{EA}(E_{red}) is known as the electrochemical band gap $E_{g,ec}$[20,12,14]

$$\mathbf{E_{g,ec} = E_{IP} - E_{EA}} \tag{2-23}$$

The energy difference ΔE_g between $E_{g,op}$ and $E_{g,ec}$ is going to be investigated.

2.4.4.2. Material Stability and Reversibility Study

The cyclic voltammetry peak potentials (E_{pc} , E_{pa}) and peak currents (i_{pc} , i_{pa}) can be used to estimate the stability of the materials, which is linked to the reversibility of the redox reaction (chemical reversibility, electrochemical reversibility).

The CV redox reactions are a diffusion-controlled reaction, where the rate of electrons transfer is controlled by the rate of the supply of materials to the electrode by diffusion. The redox reaction is considered to be electrochemically reversible if the electron transfer process between both the redox coupled species and the working electrode is fast compared with the diffusion. With the slowing of electron exchange the reaction becomes electrochemically irreversible.

The redox reaction can be considered chemically reversible if the reverse electrochemical reaction produces the original material depleted by the forward reaction with no new reaction or side chemical products appears. The reaction is chemically irreversible if the reverse cycle leads to a different electrode reaction and side products.[41]

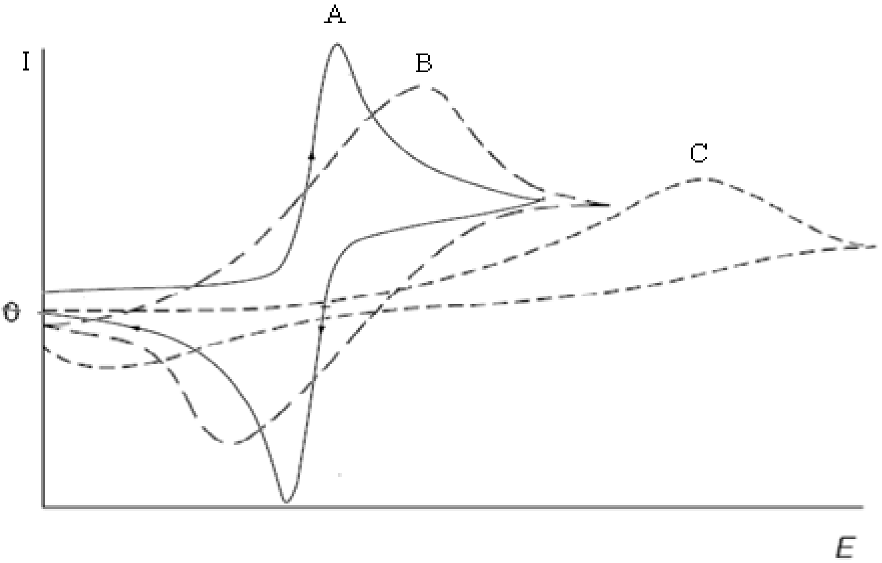

Figure 2-12: Cyclic voltammogram for (A)reversible, (B) quasi-reversible, and (C) irreversible redox processes.[35]

Both chemical and electrochemical reversibility can be identified by measurement of the potential difference ΔE_p between the potential of the two peaks in forward and reverse direction. This is related to the number of electrons transferred in the electrode reaction n[28,29]

$$\mathbf{\Delta E_p = |E_{pa} - E_{pc}| \approx \frac{0.059}{n}} \qquad (2\text{-}24)$$

Therefore, for a reversible redox reaction ΔE_p should be about 59 mV for one electron transfer. Actually, the cell resistance slows the electron transfer rate which makes it difficult to get this result, leading to an increase in ΔE_p. Therefore ΔE_p is often 60-70 mV for a reversible electron transfer.[28]

For reversible reaction, the peak current in the forward scan of the first cycle is related to the material concentration by Randles-Sevcik equation

$$\mathbf{I_p = (2.69X10^5)n^{3/2}AD^{1/2}Cv^{1/2}} \qquad (2\text{-}25)$$

where I_p is the peak current, n is electron stoichiometry, A is electrode area (cm^2), D is diffusion coefficient (cm^2/s), C is the concentration (mol/cm^3) and v is scan rate (V/s). For reversible reaction the values of I_{pa} and I_{pc} should be identical so

$$\mathbf{\frac{I_{pa}}{I_{pc}} \approx 1} \qquad (2\text{-}26)$$

A ratio of 1 is a good indication for chemical reversibility since side chemical reactions have a significant influence on the ratio of current peaks.

In this thesis abbreviated symbols are used to provide information about the reversibility of the compounds. R stands for reversible, which mean that both forward and reversible processes are fast enough to maintain equilibrium conditions at the electrode surface. IR stands for irreversible, which indicate that only the forward reaction is significant. QR stand for quasi-reversible, which mean both the forward and reversible reactions are there but not fast enough to maintain the equilibrium condition. An example for each one of these process is illustrated in figure 2-12.

2.4.5. Experimental procedure

The experimental set-up and instrumentation is fully explained in section 2-4-2. The WE was a glassy carbon electrode (area = $0.07cm^2$), Silver/silver chloride electrode (Ag/AgCl, sat. 3M NaCl) was used as the RE and a platinum wire was used as the CE. A potentiostat (Solartron 1285) functioned as wave generator, potentiostat and current to voltage converter. The software Corrware and Corrview were used to control and record the experiments respectively.

5ml dichloromethane (DCM) (purity > 99%, water content < 0.05%) was used as the solvent to dissolve the materials being tested. 0.3M Tetrabutylammonium hexafluorophosphate ($TBAHFP_6$) (purity > 98%) was recrystalized two times and used as a supporting electrolyte to improve the electrical conductance. 1mM of the materials to be tested were added to the solvent. 1mM Fc was added at the end of the experiments as an internal standard. Nitrogen purging was necessary for a few minutes before starting the scan. The purging was then stopped to form a blanket of nitrogen over the cell to maintain a stationery state during the experiment.

The measurement was first run with the solvent and supporting electrolyte only to check whether it had the required flat current response. Then, it was run on addition of the test material and finally with the addition of Fc. A typical scan rate of 20mV/s was used. Two scans were performed to check the repeatability.

A UV/VIS spectrometer (Lambda 40, Perkin Elmer) was used to measure the optical absorption spectra, for the optical energy gap $E_{g,op}$ measurement as shown in figure 2-11. The absorption spectrum was measured in solid state, where the sample material was spin-coated onto a transparent or nearly transparent substrate (quartz) as thin film.

2.5. Results and discussion

2.5.1. Materials Used in this Thesis

Table 2-1: Materials used in this thesis with illustration of chemical structures, transition temperatures, ionization potential E_{IP}, electron affinity E_{EA}, optical energy gap $E_{g,op}$, electrical energy gap $E_{g,ec}$, the different between the two energy gaps ΔE_g. ^{O} indicate an oxidation reaction, ^{R} a reduction reaction, R means reversible material, QR quasi reversible material, IR means irreversible material to electron transfer.

Mate.	Structure	
1	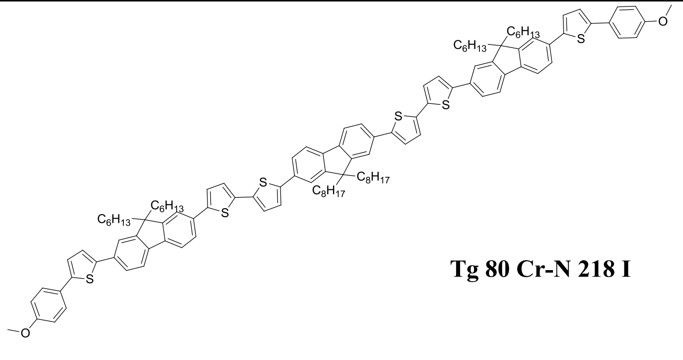 Tg 80 Cr-N 218 I	E_{IP} E_{EA} $E_{g,op}$ (eV) ^{O} 5.52 , 3.19, 2.33 (R) SPK516

2	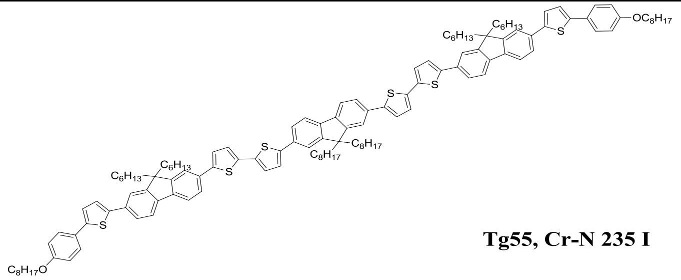 **Tg55, Cr-N 235 I**	**Similar to compound 3** **PV316**
3	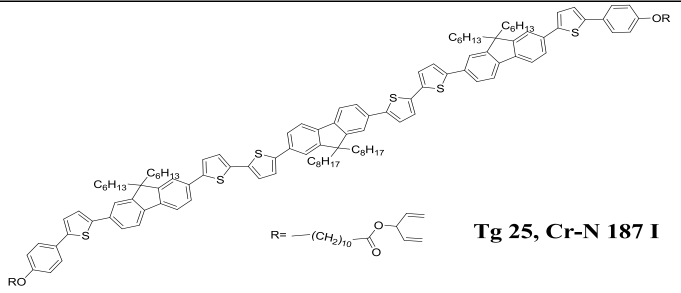 **Tg 25, Cr-N 187 I**	**E_{IP} E_{EA} $E_{g,op}$ (eV)** o **5.52 , 3.15 , 2.37 (R)** **PV318**
4	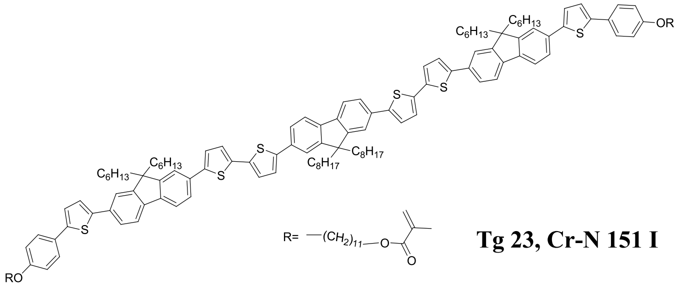 **Tg 23, Cr-N 151 I**	**E_{IP} E_{EA} $E_{g,op}$ (eV)** o **5.51, 3.13, 2.38 (QR)** **SPK394**
5	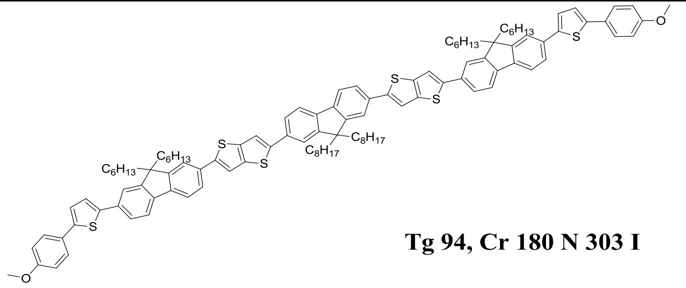 **Tg 94, Cr 180 N 303 I**	**E_{IP} E_{EA} $E_{g,op}$ (eV)** o **5.53 , 3.1 , 2.43(R)** **SPK523**
6	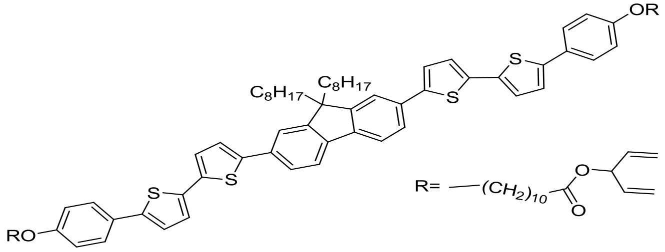 **Tg 0, Cr 53 N 143 I**	**E_{IP} E_{EA} $E_{g,op}$ (eV)** o **5.5 , 3.07 , 2.43 (IR)** **PV237**
7	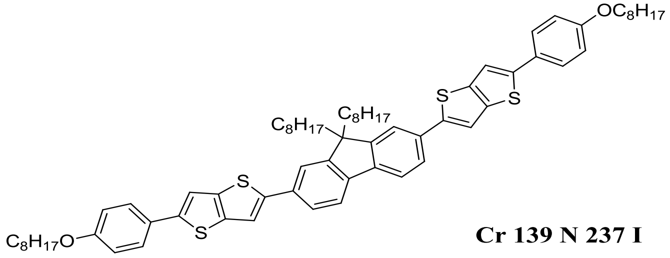 **Cr 139 N 237 I**	**E_{IP} E_{EA} $E_{g,op}$ (eV)** o **5.55 , 3.08 , 2.47 (IR)** **SPK382**

8	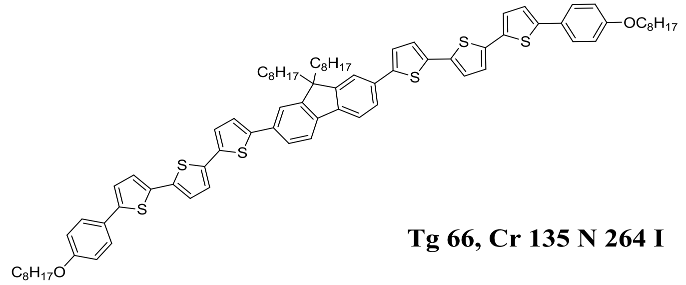 **Tg 66, Cr 135 N 264 I**	**$\underline{E_{IP}}$ $\underline{E_{EA}}$ $\underline{E_{g,op}}$ (eV)** **^{O} 5.42 , 3.11 , 2.31 (R)** **SPK388**
9	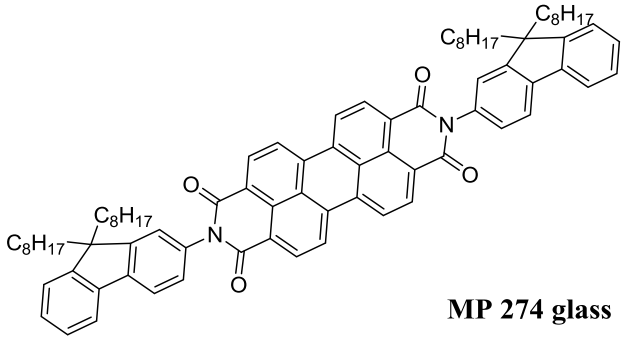 **MP 274 glass**	**$\underline{E_{IP}}$ $\underline{E_{EA}}$ $\underline{E_{g,op}}$ (eV)** **^{R} 6.31, 4.19, 2.12 (IR)** **MPA340**
10	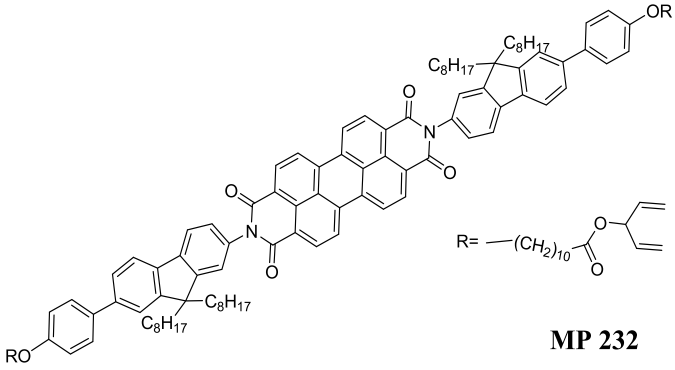 **MP 232**	**$\underline{E_{IP}}$ $\underline{E_{EA}}$ $\underline{E_{g,op}}$ (eV)** **^{O} 5.94 , 3.82, 2.12 (R)** **^{R} 6.33 , 4.21 , 2.12 (R)** **$E_{g,ec}$ ΔE_g** **1.73 , 0.39** **SPK290**
11	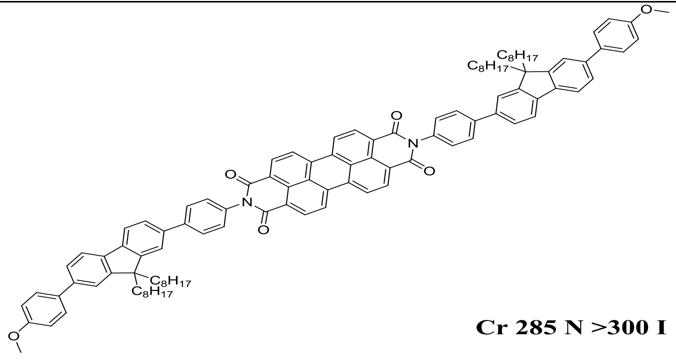 **Cr 285 N >300 I**	**$\underline{E_{IP}}$ $\underline{E_{EA}}$ $\underline{E_{g,op}}$ (eV)** **^{O} 5.89 , 3.77, 2.12 (R)** **^{R} 6.37 , 4.25 , 2.12 (R)** **$E_{g,ec}$ ΔE_g** **1.64 , 0.48** **SPK309**
12	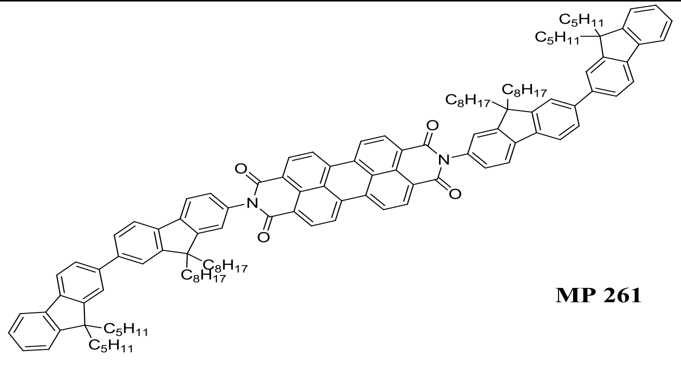 **MP 261**	**$\underline{E_{IP}}$ $\underline{E_{EA}}$ $\underline{E_{g,op}}$ (eV)** **^{O} 5.98 , 3.86, 2.12 (QR)** **^{R} 6.33 , 4.21 , 2.12 (QR)** **$E_{g,ec}$ ΔE_g** **1.77 , 0.35** **SPK318**

13	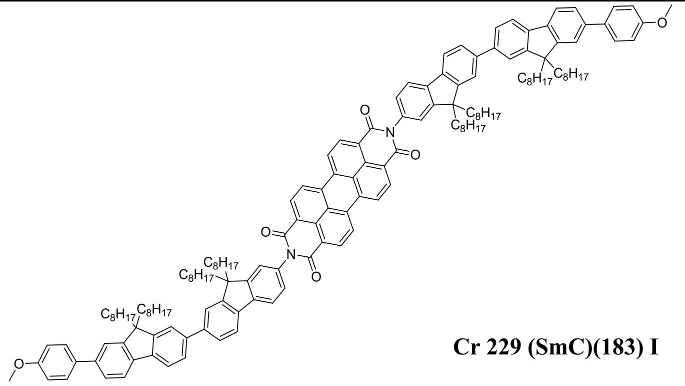 **Cr 229 (SmC)(183) I**	**E_{IP} E_{EA} $E_{g,op}$ (eV)** **O 5.85 , 3.73, 2.12 (R)** **R 6.32 , 4.2 , 2.12 (QR)** **$E_{g,ec}$ ΔEg** **1.65 , 0.47** **SPK326**
14	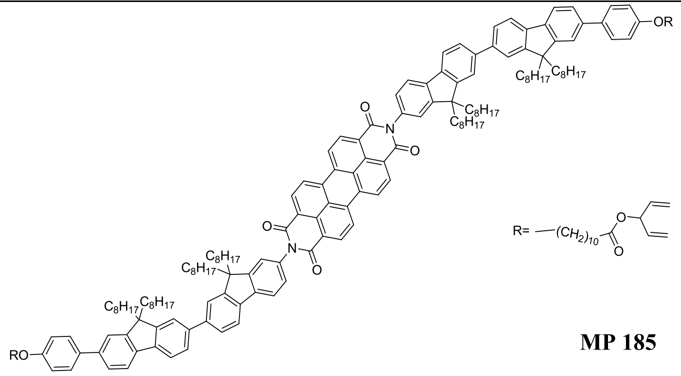 **MP 185**	**E_{IP} E_{EA} $E_{g,op}$ (eV)** **O 5.82 , 3.72, 2.1 (R)** **R 6.32 , 4.22 , 2.1 (QR)** **$E_{g,ec}$ ΔEg** **1.6 , 0.5** **SPK339**
15	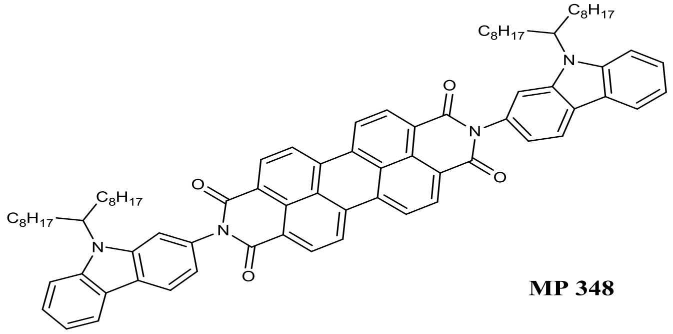 **MP 348**	**E_{IP} E_{EA} $E_{g,op}$ (eV)** **O 5.55 , 3.49, 2.06 (R)** **R 6.29 , 4.23 , 2.06 (QR)** **$E_{g,ec}$ ΔEg** **1.32 , 0.74** **SPK370**
16	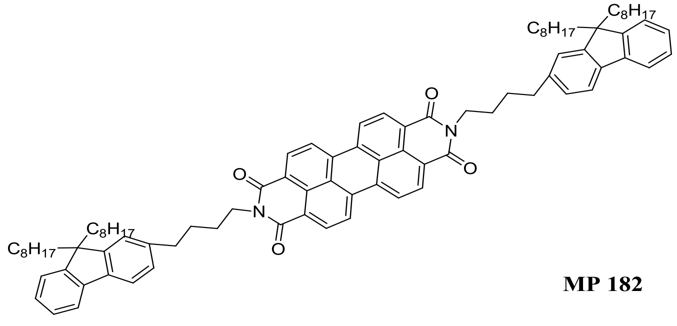 **MP 182**	**E_{IP} E_{EA} $E_{g,op}$ (eV)** **O 6.19 , 4.09, 2.1 (IR)** **R 6.32 , 4.22 , 2.1 (QR)** **$E_{g,ec}$ ΔEg** **1.97 , 0.13** **SPK417**
17	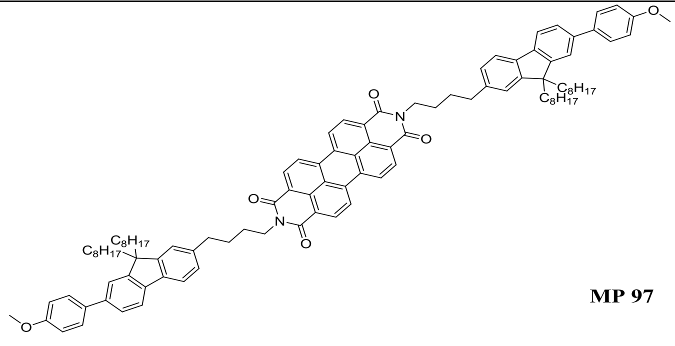 **MP 97**	**E_{IP} E_{EA} $E_{g,op}$ (eV)** **O 5.87 , 3.74, 2.13 (R)** **R 6.31 , 4.18, 2.13 (QR)** **$E_{g,ec}$ ΔEg** **1.69 , 0.44** **SPK452**

18	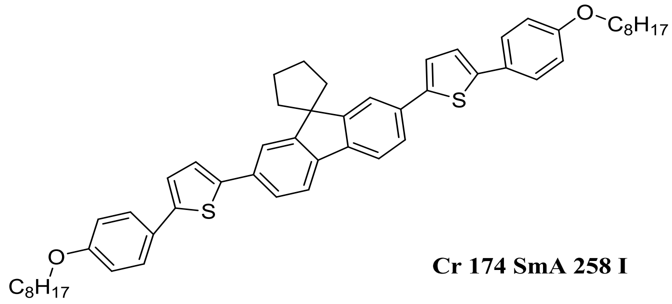 **Cr 174 SmA 258 I**	**E_{IP} E_{EA} $E_{g,op}$ (eV)** o **5.56 , 2.83, 2.73 (IR)** **KK045**
19	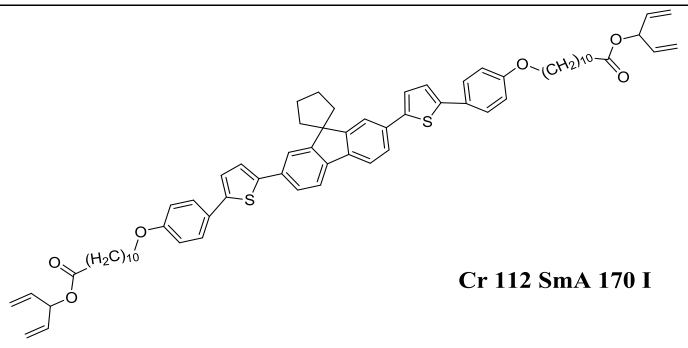 **Cr 112 SmA 170 I**	**E_{IP} E_{EA} $E_{g,op}$ (eV)** o **5.53 , 2.82, 2.71 (R)** **KK041**
20	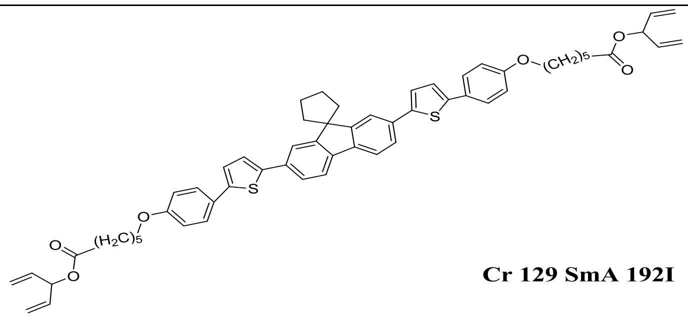 **Cr 129 SmA 192I**	**E_{IP} E_{EA} $E_{g,op}$ (eV)** o **5.54 , 2.82, 2.72 (IR)** **KK054**
21	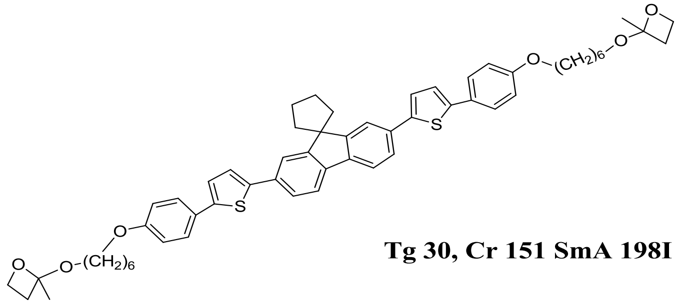 **Tg 30, Cr 151 SmA 198I**	**E_{IP} E_{EA} $E_{g,op}$ (eV)** o **5.54 , 2.82, 2.72 (R)** **KK050**
22	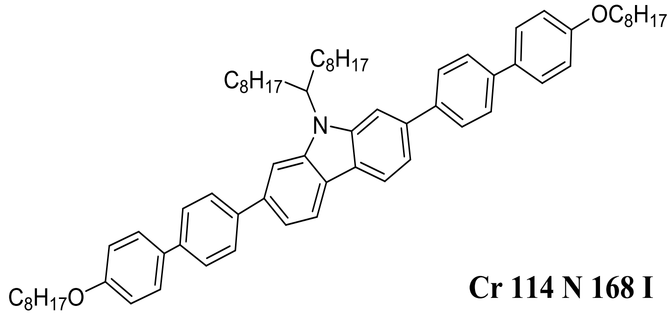 **Cr 114 N 168 I**	**E_{IP} E_{EA} $E_{g,op}$ (eV)** o **5.78 , 2.86, 2.92 (IR)** **MK024**

23	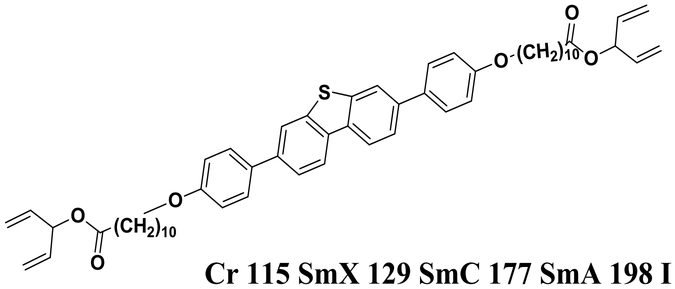 **Cr 115 SmX 129 SmC 177 SmA 198 I**	**E_{IP} E_{EA} $E_{g,op}$ (eV)** o **5.78 , 3.86 , 2.65 (R)** **MD029**
24	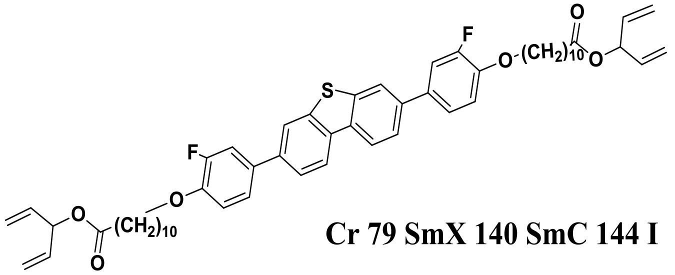 **Cr 79 SmX 140 SmC 144 I**	**E_{IP} E_{EA} $E_{g,op}$ (eV)** o **5.97 , 3.25, 2.72 (R)** **MD039**
25	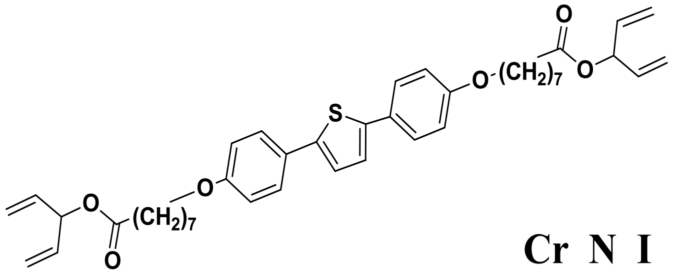 **Cr N I**	**E_{IP} E_{EA} $E_{g,op}$ (eV)** o **5.5 , 2.82 , 2.68 (R)** **MD062**
26	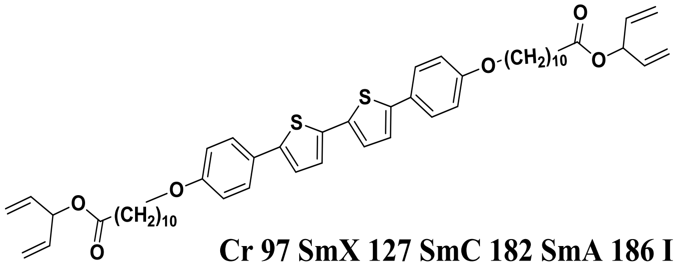 **Cr 97 SmX 127 SmC 182 SmA 186 I**	**E_{IP} E_{EA} $E_{g,op}$ (eV)** o **5.48 , 2.85, 2.63 (R)** **MD068**
27	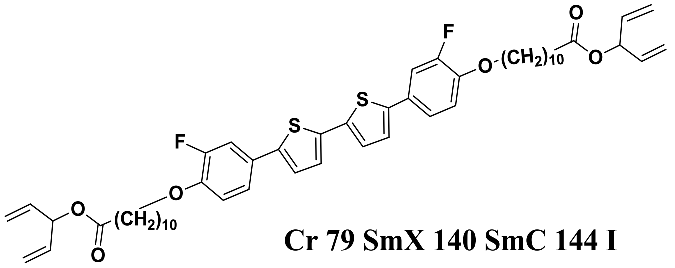 **Cr 79 SmX 140 SmC 144 I**	**E_{IP} E_{EA} $E_{g,op}$ (eV)** o **5.59 , 2.93, 2.66 (R)** **MD075**
28	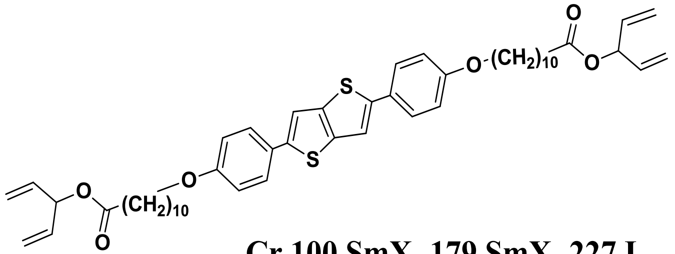 **Cr 100 SmX$_1$ 179 SmX$_2$ 227 I**	**E_{IP} E_{EA} $E_{g,op}$ (eV)** o **5.54 , 2.62, 2.92 (R)** **MD087**

29	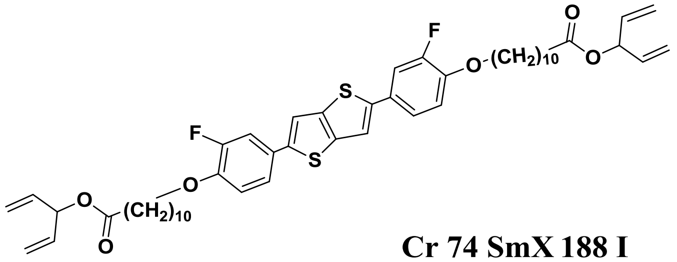 **Cr 74 SmX 188 I**	**E_{IP} E_{EA} $E_{g,op}$ (eV)** **O 5.67 , 2.72, 2.95 (R)** **MD093**
30	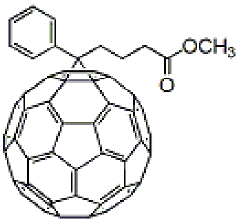	**E_{IP} E_{EA} $E_{g,op}$ (eV)** **R 5.96 , 4.14 , 1.82 (R)** **PCBM C61**
31*[1]	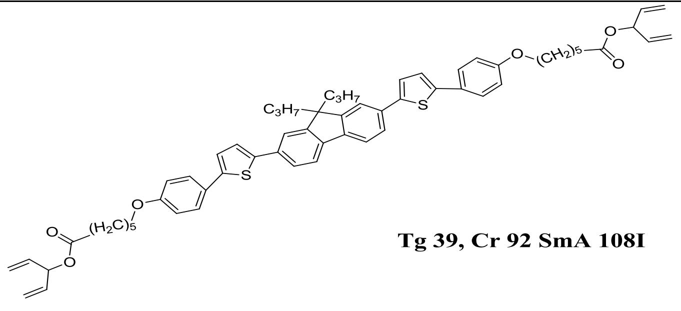 **Tg 39, Cr 92 SmA 108I**	**E_{IP} E_{EA} $E_{g,op}$ (eV)** **O 5.58 , 2.91, 2.67 (R)** **GJR130**
32*	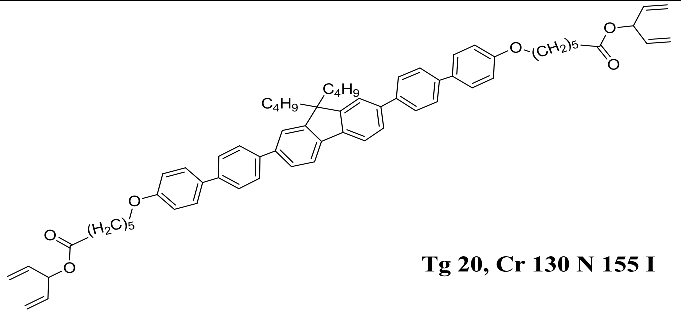 **Tg 20, Cr 130 N 155 I**	**E_{IP} E_{EA} $E_{g,op}$ (eV)** **O 5.86 , 2.76, 3.1 (IR)** **MPA043**
33*	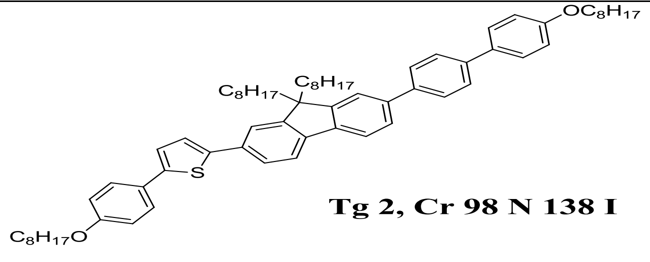 **Tg 2, Cr 98 N 138 I**	**E_{IP} E_{EA} $E_{g,op}$ (eV)** **O 5.62 , 2.8, 2.82(QR)** **PV202**

---

[1] * Indicates that experimental measurements were made by Dr. W. C. Tsoi. Analysis was done by me.

34*	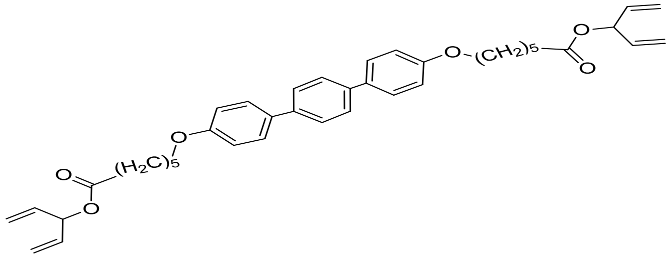	**E_{IP} E_{EA} $E_{g,op}$ (eV)** **O 5.87 , 2.45, 3.42 (R)** **MPA364**

2.5.2. Molecular Engineering for Optimum Electrical and Optical Properties of n-type Organic Semiconductors

Compounds **9** to **17** are nine perylene bisimides based compounds which have been synthesized and studied as new electron acceptors with good chemical, electrical and optical properties. As table 2-1 shows, compounds **11** and **13** have high temperature liquid crystalline phases.

In this study **9** has been used as our reference because it shows good acceptor properties and it has the simplest structure in the group. As shown in table 2-1 this compound has three components, the perylene bisimide in the middle and two 9,9-dioctyl-9H-fluorene groups on each side as functional group. Starting from **9**, the functional group structure has been changed and each time we try to monitor the effect of that change on the optical and electrical properties.

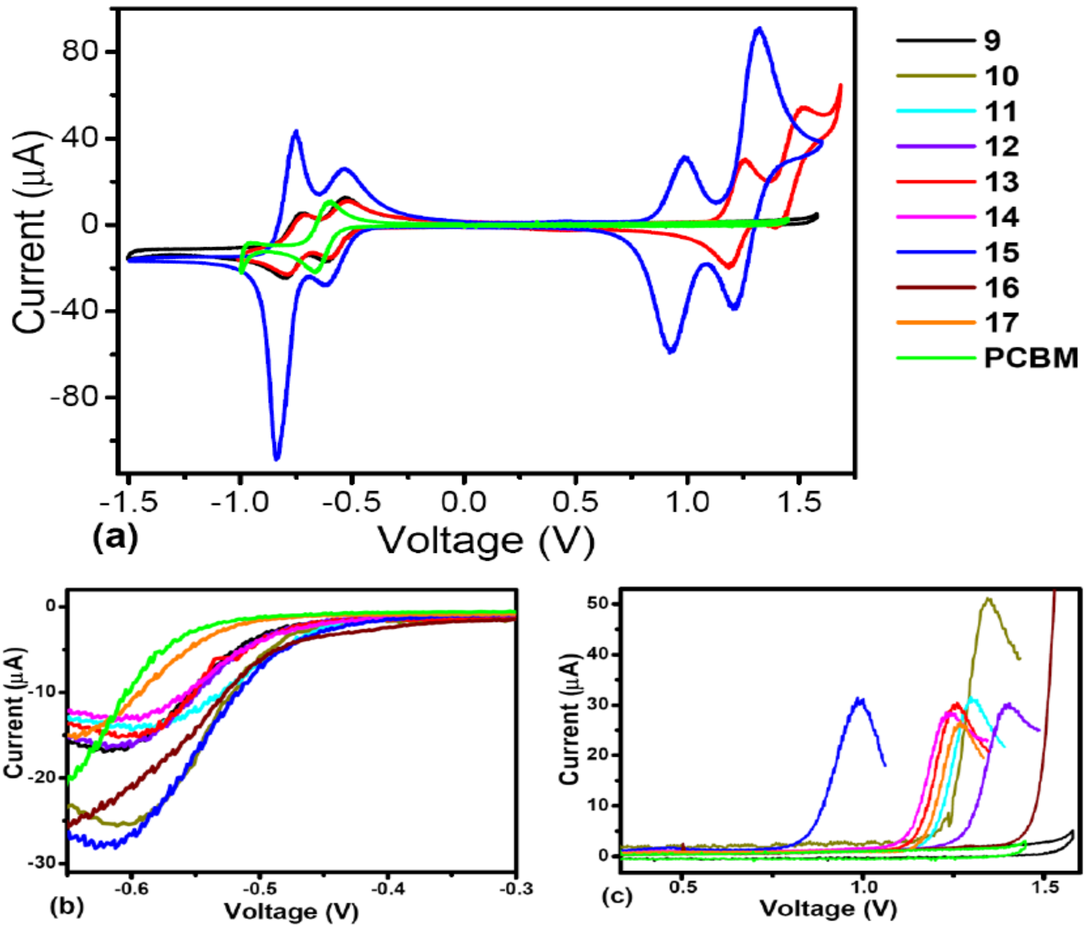

Figure 2-13: (a) Cyclic voltammogram of 9,13,15 and PCBM, (b) magnification of the reduction onset, (c) magnification of oxidation onset.

Figure 2-13 shows that all compounds show both oxidation and reduction reactions using CV apart from **9**, which only shows the reduction reaction. This means the E_{IP}/E_{EA} (HOMO/LUMO) measurement is attainable in two different ways as explained in section 2.4.4.1. The HOMO (oxidation) and the LUMO (reduction) indicates that the HOMO and LUMO energies were obtained directly from CV and measured from the oxidation onset and the reduction onset respectively. HOMO (reduction) and LUMO (oxidation) are obtained using absorption data and eq. 2-21 and eq. 2-22.

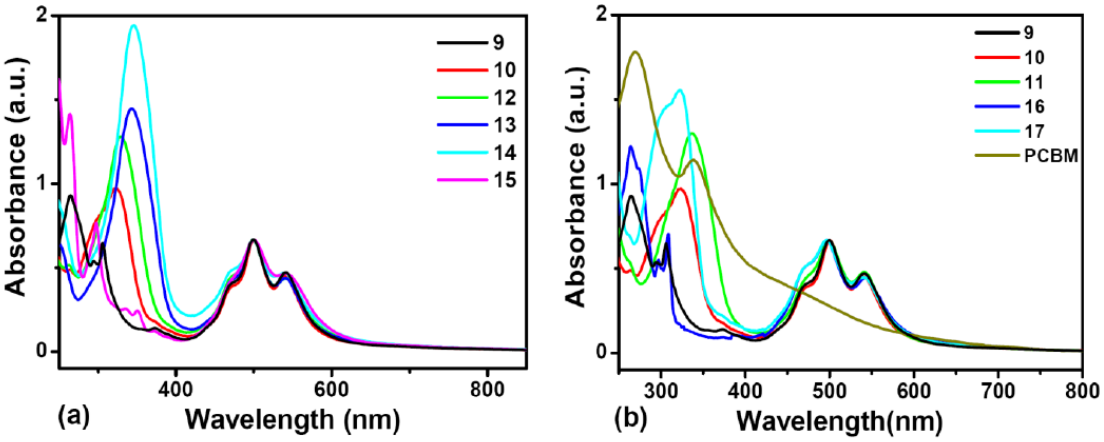

Figure 2-14: The absorption spectrum of the compound 9 to 17, and the PCBM.

The absorption spectra of all the nine compounds are shown in figure 2-14 and can be split into two spectral regions, wavelengths less than 400nm and wavelengths more than 400nm. The first region is affected by the change of the chemical structure of the side functional group, the second region relates to the perylene bisimide central core. In the latter region the spectrum is virtually independent of changes in the chemical structure of the two outer functional groups. The second region is our measurement target where we can get the absorption edge and use it to measure the optical energy gap $E_{g,Op}$ of these compounds.

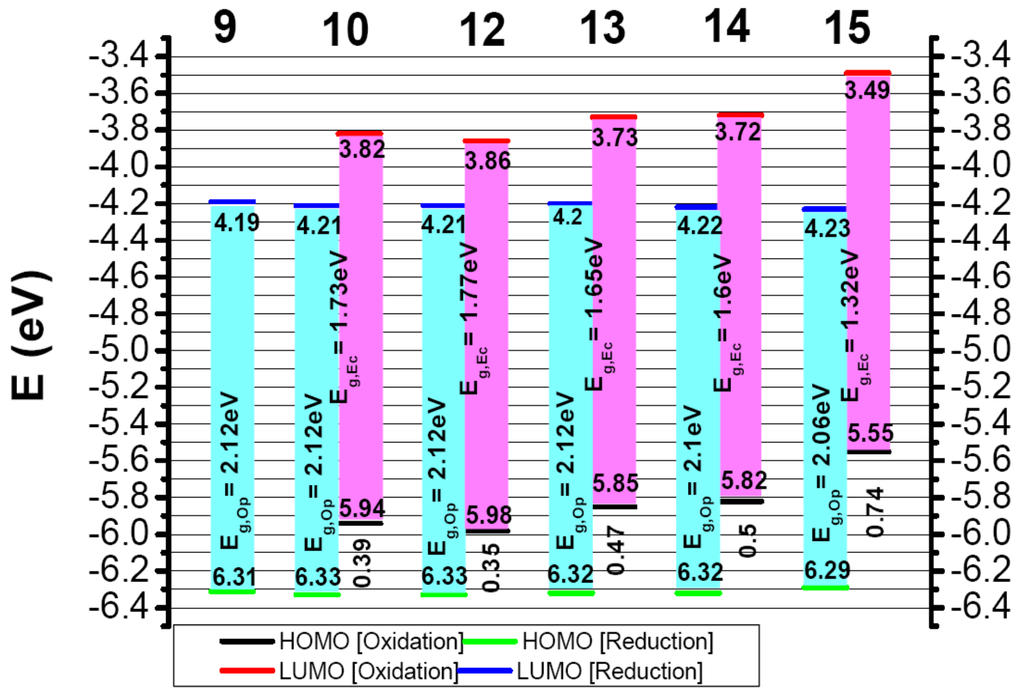

Figure 2-15: The energy levels of compounds 9,10,12,13,14, and 15 using both oxidation and reduction reactions.

Figure 2-15 shows the energy levels of the compounds obtained using electrochemical and optical methods. The two methods give different results with variations in the difference between the two energy gap measurements. This is because oxidation and reduction occur at completely different sites in the molecules. The LUMO (reduction) energy is approximately equal for all compounds because the same perylene bisimide group is used. The HOMO (oxidation) depends on the two aromatic end groups and vary accordingly. Hence the compounds apart from **9**, can be considered as donor-acceptor materials, where the HOMO wavefunction occupy different regions (phenyl and fluorene moieties) than the LUMO wavefunction perylene component as illustrated in figure 2-16.

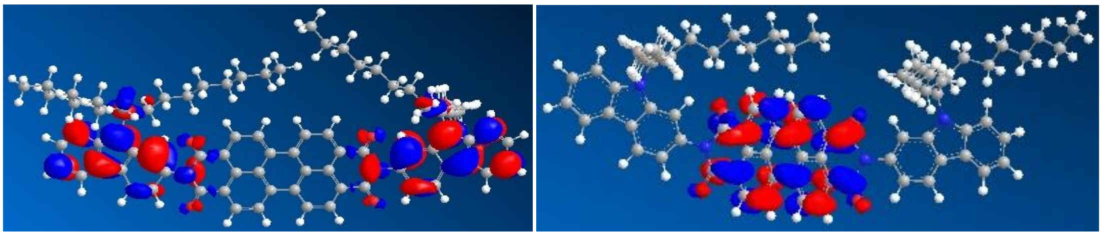

Figure 2-16: Molecular orbital contour plot of compound 15, HOMO (left) and LUMO (right), Chem-draw software was used for energy minimization with (MM2+AM1) method and orbital calculation.

In the next sections we emphasize that the electrochemical and optical properties change significantly as a function of the chemical structure of the functional group.

2.5.2.1. Double Fluorene Groups

As illustrated in table 2-1 the variation of the chemical structure between **9** and **12,** and between **10** and **14** is the single fluorene functional group in the former compound and double groups in the latter for each set. Optically doubling the number of fluorene groups has a significant effect on the short wavelength region (<400nm), where the peak is shifted toward the red for the two groups studied as illustrated in figure 2-14(a). For the region of wavelength longer than 400nm the effect is insignificant, therefore the optical energy gap $E_{g,Op}$ have similar values.

Electrochemically, the doubling of the groups has an insignificant effect on the reduction reaction but increases the HOMO (oxidation) energy and so lowers the electrical energy gap $E_{g,Ec}$ as illustrated in figure 2-13 and figure 2-15. The energy gap difference ΔE_g of the optical and electrical energy gap is increasing also, which for comparison is 0.39 eV and 0.5 eV for **10** and **14** respectively.

The addition of the second fluorene group agrees with the literature which shows a reduction in the energy gap with an increase of the chain length[9,42].

2.5.2.2. Carbazole Group

Compound **15** has the carbazole functional group instead of the fluorene group in **9** as shown in table 2-1. In the long wavelength region (>400nm) of the absorption spectrum there is a small reduction in the optical energy gap $E_{g,OP}$, by 0.06 eV as shown in figure 2-14(a) and figure 2-15. However on the short wavelength region (<400nm) the effect was insignificant.

Electrochemically, the substitution of carbazole affects both the oxidation and reduction reactions and reduces the electrical energy gap $E_{g,Ec}$ via reducing the E_{ox}^{onset} and increasing E_{Red}^{onset} as illustrated in figure 2-13 and figure 2-15; the oxidation side changes more the reduction one. The energy gap difference ΔE_g is the highest as shown in figure 2-15. Also the carbazole substitution has a strong effect on the reversibility of the reactions; it gives an irreversible reaction.

Changes in the optical and electrical properties can be related to the influence of the CN electron withdrawing group of carbazole[6], where both carbon and nitrogen have high electron negativity of 2.6, and 3 respectively[22].

2.5.2.3. Alkoxyphenyl Group and Phenyl Group

The phenyl group is an important aromatic structure in the field of organic semiconductors. As shown in table 2-1 there are three examples to investigate the effect of the alkoxyphenyl group and phenyl group itself on the optical and electrical properties. Compound **10** has alkoxyphenyl groups next to the fluorene groups in contrast to **9,** and **11** has an extra phenyl group on the other side of the fluorene group. Also compound **13** has alkoxyphenyl groups next to the fluorene groups in contrast to **12**.

Optically the alkoxyphenyl group and phenyl group have a significant affect in the short wavelength region (<400nm), with the peak of **10**, **11** and **13** shifted toward the longer wavelength and its amplitude increasing relative to spectra of **9** and **12**, as illustrated in figure 2-14(a,b). For the region of wavelength longer than 400nm the effect was insignificant, therefore the optical energy gap $E_{g,Op}$ have similar values.

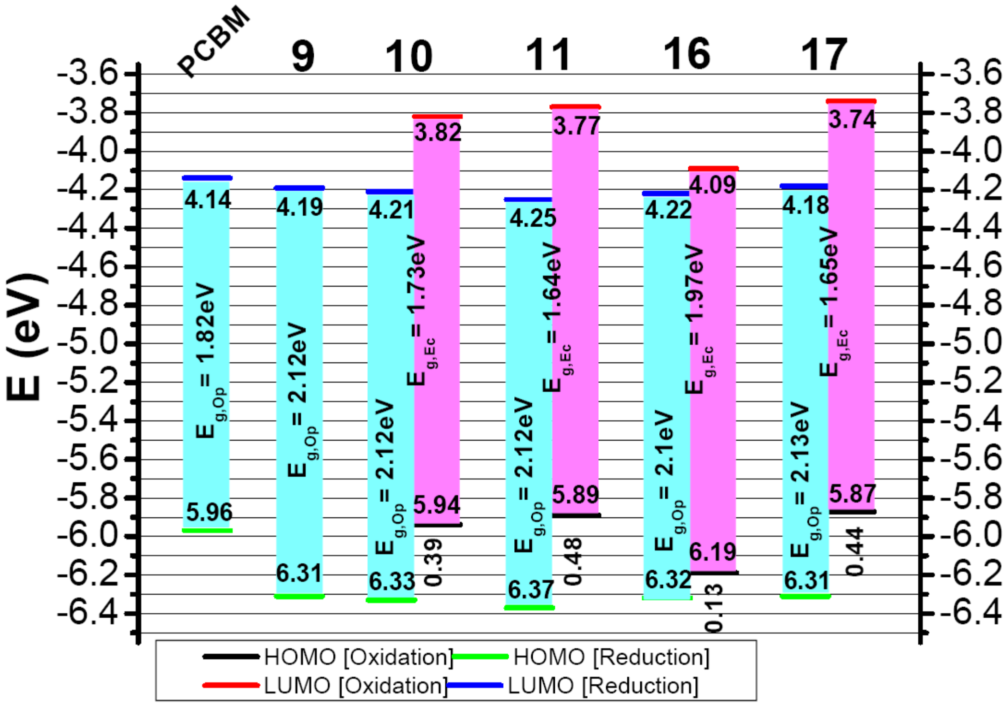

Figure 2-17: The energy levels of compounds 9, 10, 11, 16, 17 and PCBM using both oxidation and reduction reactions, and showing the optical and electrical energy gaps and the difference in the energy gap.

Electrochemically, the addition of alkoxyphenyl group has no affect on the reduction reaction, however the insert of the second phenyl ring in compound **11** reduces the value of the LUMO (reduction) by 0.04 eV compared to that of **10**. The HOMO (oxidation) also increases from -5.94 eV to -5.89 eV as illustrated in figure 2-13, figure 2-15 and figure 2-17. However the alkoxyphenyl group has an even bigger affect: HOMO (oxidation) of **9** is too low to be measured (<-6.25 eV) while that of **10** is only -5.94 eV.

Similarly as illustrated in figure 2-15 and figure 2-17 the HOMO (oxidation) energy levels of **13** is 0.13 eV higher than that of **12**. As a result the electrical energy gap $E_{g,Ec}$ decreases and the difference of energy gaps ΔE_g increases as illustrated in figure 2-15 and figure 2-17.

2.5.2.4. Spacing the Functional Group of Perylene Bisimide Core

The addition of different functional groups may inhibit the good EA properties of the perylene bisimide. Therefore we separate the functional groups from the perylene bisimide with C_3 alkyls chain. Compound **16** has a spaced fluorene group in contrast to **9**, and **17** has spaced the fluorene and alkoxyphenyl group as side group in contrast to **10** as shown in table 2-1. A similar compound with a similarly spaced benzene ring as side group shows high mobility and good stability in the air[43].

The E_{ox}^{onset} decrease for both compounds increasing the HOMO (oxidation) energy. The E_{Red}^{onset} only changes by about 0.03 V by spacing the substituent. Therefore the $E_{g,Ec}$ is slightly reduced increasing the difference of energy gaps ΔE_g as shown in figure 2-17.

2.5.3. Molecular Engineering for Optimum Electrical and Optical Properties of p-type Organic Semiconductors

In this section we investigate how changes in the chemical structure of p-type semiconducting liquid crystals affect the optical and electrochemical properties of the material. All the compounds in this section only show the oxidation reactions. This indicates that only HOMO (oxidation) is obtained directly from CV and measured from oxidation onset whereas LUMO (oxidation) is obtained using absorption data.

2.5.3.1. End Groups

Compound **1**, **3**, and **4** have the same aromatic core. However each has a different end group, being a methoxy group, alkyl chain with a terminal photoreactive diene-ester group and alkyl chain with photoreactive terminal methyl methacrylate respectively. Compounds **18**, **19**, **20**, and **21** have also the same aromatic core with different end groups as shown in table 2-1.

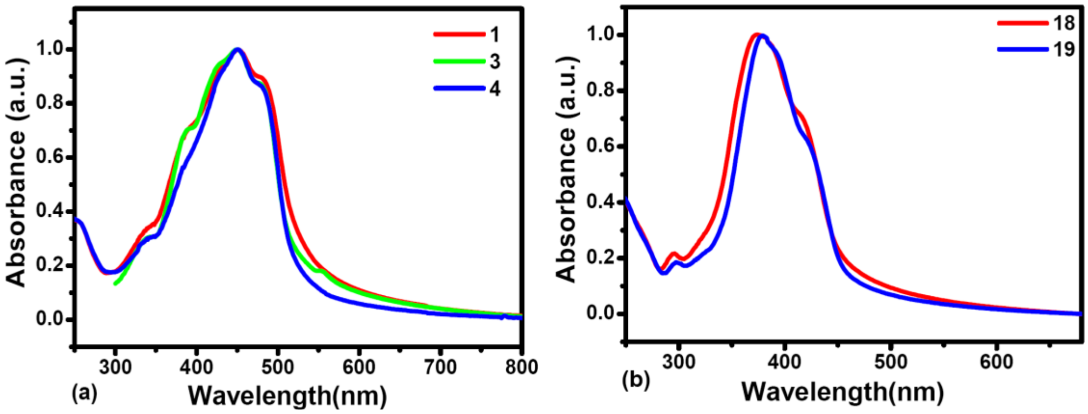

Figure 2-18: Normalized absorption spectrum of compounds a) 1, 3, and4, b) 18, 19.

The thin film absorption spectra of compounds **1**, **3**, and **4**, and **18** and **19** are shown in figure 2-18(a,b). There is no shift in the peak position. However there is some variation in the two sides of the peaks, which provide small differences in the absorption wavelength edge and optical energy gap $E_{g,op}$. This may be related to differences in intermolecular interactions and molecular backing which depend on the film morphology and are influenced by the side chains[6,44].

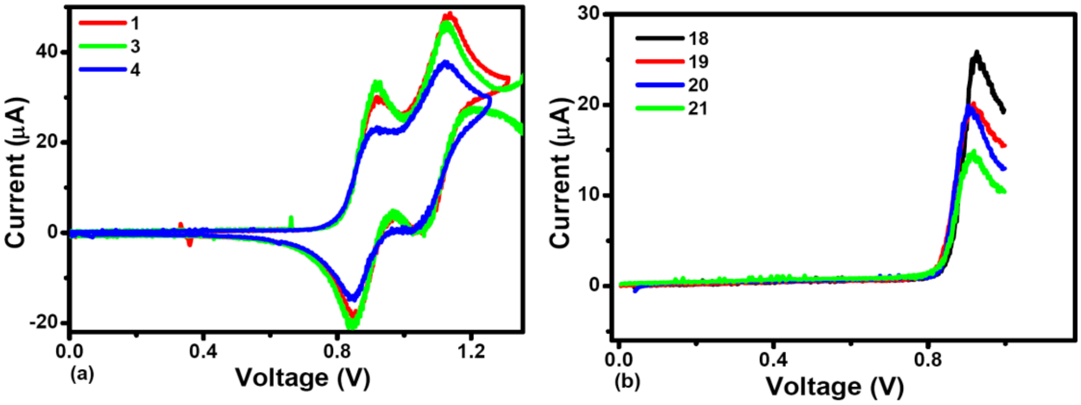

Figure 2-19: :(a) cyclic voltammogram of the compounds 1, 3, and 4. (b) cyclic voltammogram onset of compounds 18,19,20, and 21, where all calibrated with Fc/Fc$^+$.

Figure 3-19 shows no significant effect of the side groups on the oxidation potential onset E_{ox}^{onset} , which indicate that the aromatic core is primarily responsible for the optical and electrical properties of the compound.

Hence, the substantial part of the molecule is the aromatic core, while the end groups have no significant effect on HOMO/LUMO levels apart from small errors in obtaining the LUMO level because of the sensitivity of the optical energy gap to intermolecular interactions.

2.5.3.2. Sulphur Atoms Position

As illustrated in table 2-1, the aromatic core of compound **34** has three benzene rings. Its middle benzene ring is substituted by different aromatic groups with sulphur atoms at different positions. For compounds **23**, **25**, **26**, and **28**, the substitutions are dibenzothiophene, one thiophene ring, two thiophene rings, and a fused thiophene ring respectively. The substitutions were to investigate the influence of the sulphur atoms in different position and number on the optical and electrical property of the organic semiconductors as EDs.

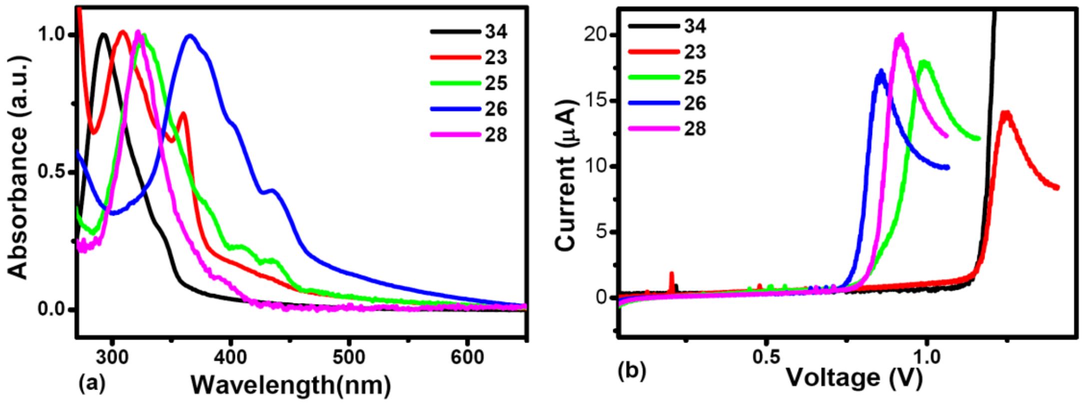

Figure 2-20:(a) Normalized absorption spectrum of the compounds 23,25,26, 28, and 34. (b) cyclic voltammogram onset of the same compounds, which calibrated with Fc/Fc$^+$.

Figure 2-20(a) shows that all the four compounds with sulphur atoms show a shift of the absorption spectrum toward longer wavelengths compared with **34** which indicates a decrease in the optical energy gap $E_{g,Op}$. The shift depends on the number of sulphur atoms and their position in the aromatic core. The shift increases in the order: dibenzothiophene, a single thiophene ring, and double thiophene rings. However when the two thiophene are fused the shift is slightly smaller than for the dibenzothiophene and other groups as will be investigated in section (2.5.3.4).

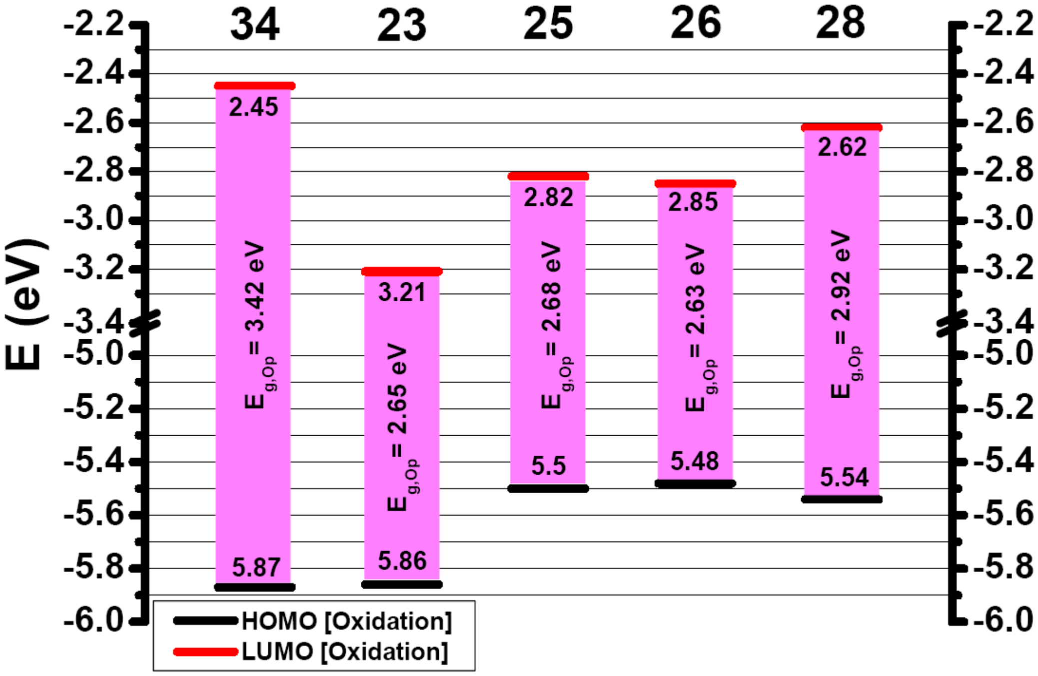

Figure 2-21: HOMO/LUMO energy levels for compounds 35, 23, 25, 26, 28 measured from oxidation onset and optical energy gap.

As shown in figure 2-20(b) and figure 2-21 the oxidation potential onset E_{ox}^{onset} and HOMO (oxidation) vary as a function of the number and position of the sulphur atoms. The dibenzothiophene has no effect on the oxidation potential, but reduces LUMO (oxidation) significantly because of the reduced optical band gap. The thiophene groups have a significant reduction of the HOMO (oxidation), the influence decreases in the order double thiophene, single thiophene and finally fused thiophene.

The LUMO (oxidation) values are reduced in the same order for the thiophene groups, but the dibenzothiophene reduce more. The thiophene rings push both HOMO/LUMO levels closer. The importance of the thiophene and fused thiophene groups encourage us to further investigate them in the next two sections.

2.5.3.3. Thiophene Ring Population

The thiophene is an important active group in organic semiconductors, for example the polythiophene has been used widely for low band gap polymers, and is one of the most environmentally and thermally stable materials[6,45,46]. In this section we investigate the effect of the number of thiophene groups population on the optical and electrical properties of the ED compounds.

As shown in table 2-1 the aromatic core of compound **32** consists of a fluorene with two benzene rings on either side of it. We compare its optical and electrical properties with those of compound **33** where one benzene ring on one side is replaced with one thiophene ring. In compounds **31**, **6** and **8** the benzene ring on each side is replaced with one two and three thiophene rings respectively.

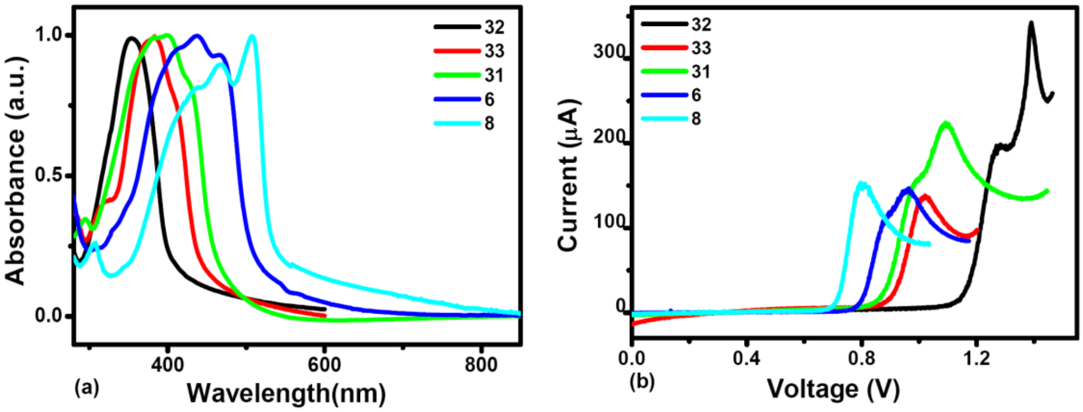

Figure 2-22: (a) Normalized absorption spectrum of the compounds 6, 8, 31, 32 and 33. (b) cyclic voltammogram onset of same compounds, calibrated with Fc/Fc$^+$

Figure 2-22(a) shows the influence of the substitution of the benzene ring with the thiophene ring on the absorption spectrum and the absorption edge of compounds **32, 33**, **31**, **6**, and **8**. The incorporation of a thiophene ring gives a red shift of the absorption peak with some difference in the absorption regions before and after the peak and at the absorption edge. The red shift increases and the optical energy gap $E_{g,Op}$ decreases with the increase in the number of the thiophene rings.

Figure 2-22(b) shows that the oxidation potential onset E_{ox}^{onset} decreases with the substitution of the benzene ring with thiophene ring. As the number of the thiophene rings increases the shift toward lower potential values increases.

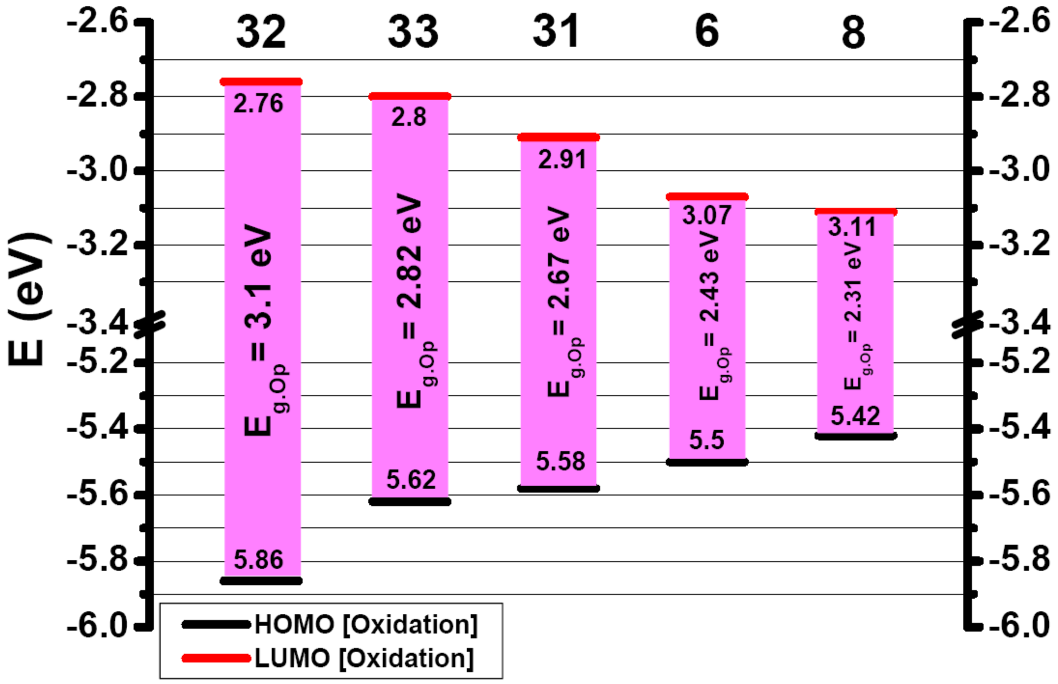

Figure 2-23: HOMO/LUMO energy levels for compounds 6, 8, 31, 32, 33 measured from oxidation onset.

Similarly as figure 3-23 shows, an increase in the number of thiophene rings increases the HOMO energy and decreases the LUMO energy, providing lower optical energy gap $E_{g,Op}$.

2.5.3.4. Fused Thiophene

In this section we study the influence of replacing two thiophene rings with a fused one on the electrical and optical properties of organic semiconductors.

Compounds **1** and **5**, compounds **6** and **7**, compounds **26** and **28**, and finally compounds **27** and **29** are four pairs to investigate the influence of the fused thiophene on the optical and electrical properties of the organic semiconductors. The chemical structure of the former compound in each group includes two thiophene rings next to each other which are substituted by fused thiophene in the latter compounds as illustrated in table 2-1.

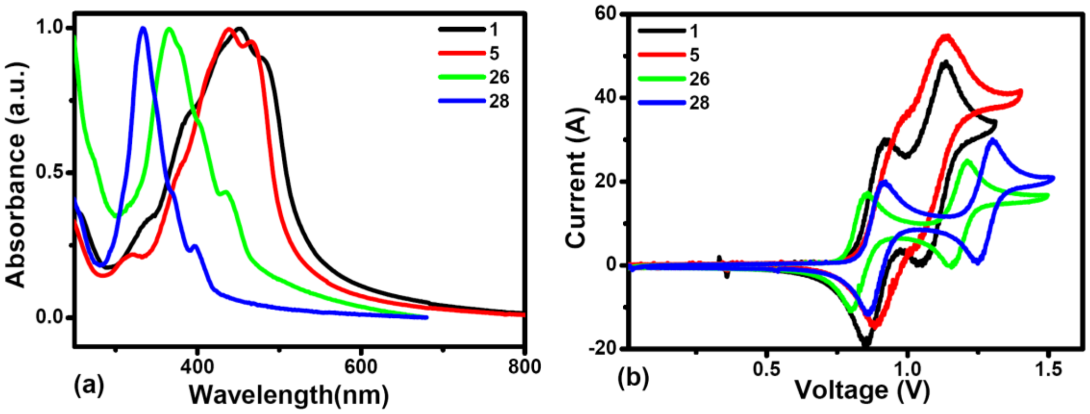

Figure 2-24: (a) Normalized absorption spectrum of the compounds 1, 5, 26, and 28. (b) cyclic voltammogram of the same compounds, which calibrated with Fc/Fc$^+$

Figure 2-24(a) shows the influence of the replacement of double thiophene rings with fused thiophene on the absorption spectra of compounds **1, 5**, and **26**, **28**. The absorption edge blue shifts and the peak narrows. The optical energy gap $E_{g,Op}$ increases with the fused thiophene replacements. Figure 2-24(b) shows that the oxidation potential onset E_{ox}^{onset} increases slightly with the fused thiophene substitution.

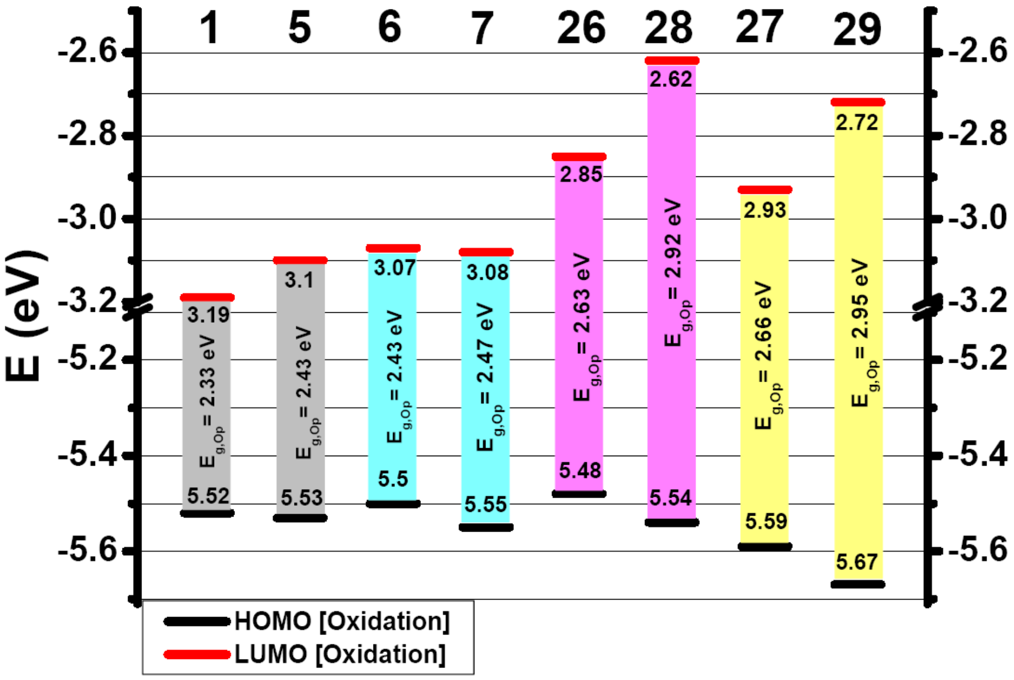

Figure 2-25: HOMO/LUMO energy levels for compounds 1, 5, 6, 7, 26, 28, 27, 29 measured from oxidation onset, and optical energy gap.

Similarly figure 3-25 illustrates that the HOMO (oxidation) energy decreases and the LUMO (oxidation) energy increases on substitution with the fused group for three of the four pairs indicating an increase in the optical energy gap $E_{g,op}$. Our result agrees with that found by E. Lim, and coworkers[47].

2.5.3.5. Fluorination

Fluorination is suggested as a solution for the poor stability of organic semiconductors against oxygen attack, and it also known to affect the electrical and optical properties[48]. The high electronegativity of the fluorine atoms of 4 together with electronegativity of 2.6 for the carbon atoms result in an electron withdrawing fluoro-carbon substituent, which has been investigated to lower the energy of the unoccupied orbitals producing n-type semiconductors[48,49]. In this section we investigate the influence of the fluorination on the energy levels of the organic semiconductors.

Compounds **23** and **24**, compounds **26** and **27**, and finally compounds **28** and **29**, are three pairs used to investigate the influence of the fluorine atoms on the optical and electrical properties of the organic semiconductors. The chemical structure of the aromatic core of the two compounds in each group is identical apart from two fluorine atoms in the second compound of each group as shown in table 2-1.

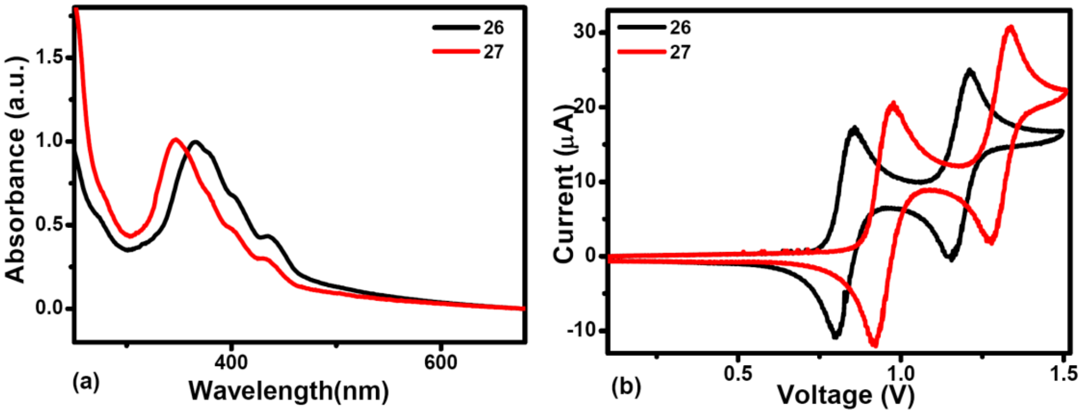

Figure 2-26: (a) Normalized absorption spectrum of the compounds 26, and 27. (b) cyclic voltammogram of the same compounds, which calibrated with Fc/Fc$^+$.

Using 26, 27 as an example figure 2-26(a) shows that fluorination blue shifts the absorption spectra, which increases the optical energy gap $E_{g,Op}$. Figure 2-26(b) shows that the oxidation potential onset E_{ox}^{onset} is increased with the addition of the fluorine atoms.

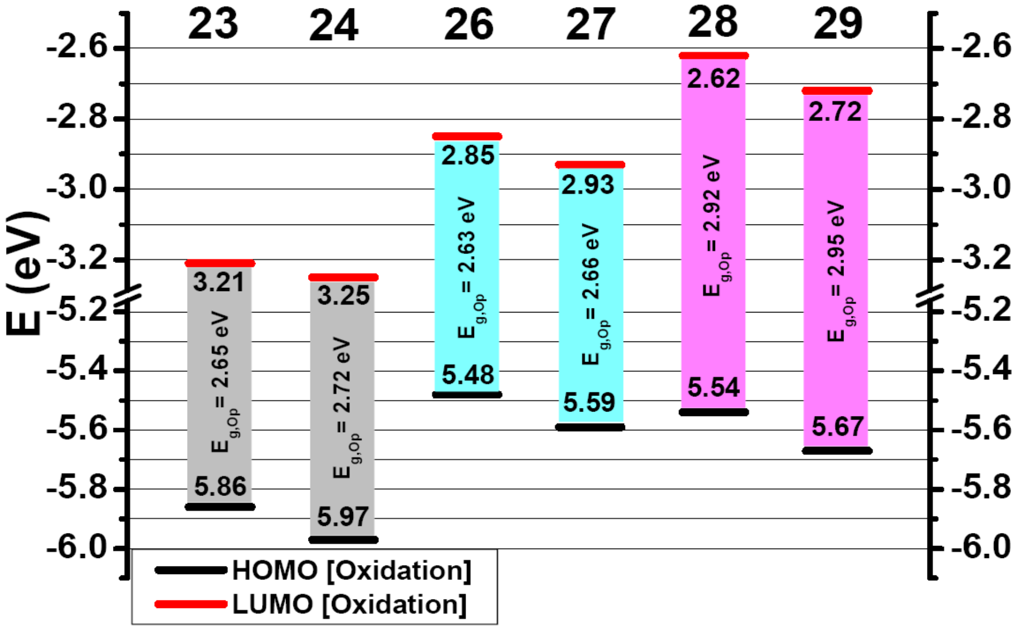

Figure 2-27: HOMO/LUMO energy levels for compounds 23, 24, 26, 27, 28, and 29 measured from oxidation onset, and optical energy gap.

Figure 3-27 shows the energy levels of the three investigated groups, and confirming that fluorination decreases both the HOMO and LUMO energies by different amount increasing the optical energy gaps $E_{g,op}$.

2.5.3.6. Effect of Nitrogen Atoms (Carbazole Group)

The fluorene group in the middle of compound **32** is replaced by the carbazole group in compound **22** as shown in table 2-1.

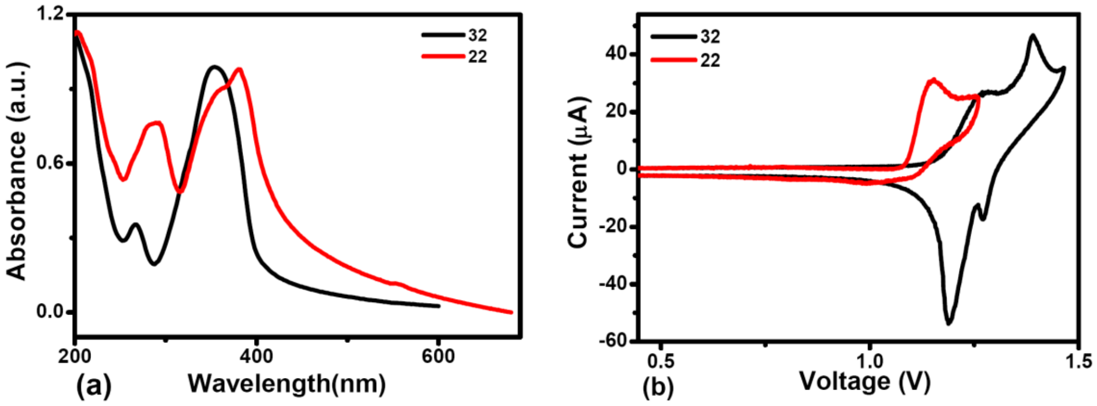

Figure 2-28: Normalized absorption spectrum of the compounds 22, and 33. (b) cyclic voltammogram onset of the same compounds, which calibrated with Fc/Fc$^+$.

As a result of this replacement the absorption spectrum shifts toward a longer wavelength which leads to a decrease of the optical energy gap $E_{g,Op}$ as shown in figure 2-28(a). Figure 2-28(b) shows a reduction in the oxidation potential onset E_{ox}^{onset} for **22**.

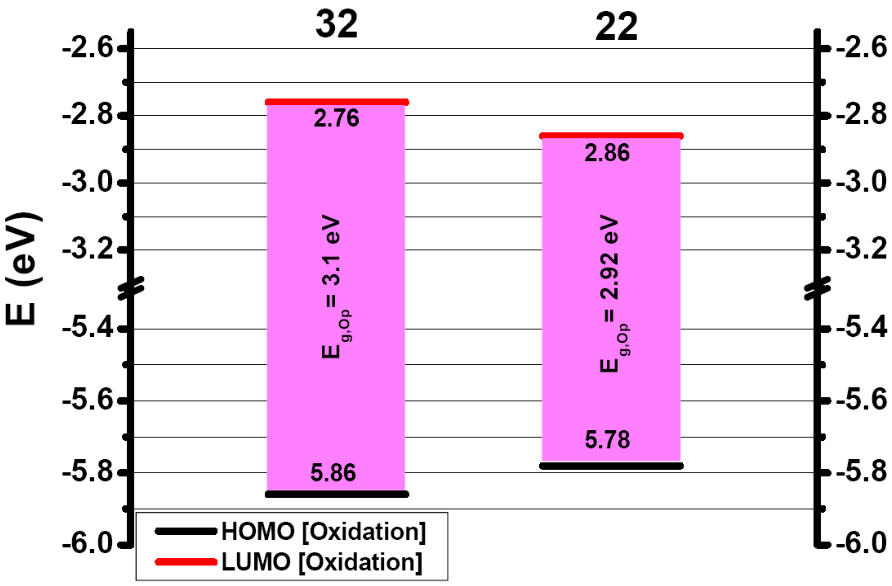

Figure 2-29: HOMO/LUMO energy levels for compounds 32, and 22 measured from oxidation onset.

In summary the nitrogen atoms in carbazole shift the HOMO/LUMO energy levels towards the centre of the energy gap lowering the optical energy gap $E_{g,Op}$ as shown in figure 2-29.

2.6. Conclusion

A range of novel semiconducting liquid crystals and perylene based compounds were synthesised by the chemistry branch of the Organophotonics group at the University of Hull, These have been studied electrochemically and optically to investigate the suitability of these materials as EDs and EAs for organic photovoltaic devices. The absorption spectra of these materials were studied to show how the incorporation of different aromatic groups modifies the optical energy gap $E_{g,op}$. The oxidation and reduction potentials measured using the CV experiment were used to estimate the HOMO/LUMO energy levels of these materials. The alteration of the chemical structure is correlated to the variation of the energy levels.

Based on the optical and electrical properties we nominate liquid crystals with a fluorene-thiophene structure of **1**, **2**, **3** and **4** as EDs in combination with the nine perylene based compounds of **9** to **16** as EAs. The latter set shows, smaller energy gap and good energy interfaces with the EDs. TOF mobility and AFM surface measurements discussed in the next two chapters will select the best compounds from the list of 4 EDs and 9 EAs to be applied in solar cells.

2.7. References

[1] B. C. Thompson, Y. G. Kim, and J. R. Reynolds, "Spectral broadening in MEH-PPV : PCBM-based photovoltaic devices via blending with a narrow band gap cyanovinylene-dioxythiophene polymer," Macromolecules **38** (13), 5359-5362 (2005).

[2] M. C. Scharber, D. Wuhlbacher, M. Koppe et al., "Design rules for donors in bulk-heterojunction solar cells - Towards 10 % energy-conversion efficiency," Advanced Materials **18** (6), 789-+ (2006).

[3] N. Blouin, A. Michaud, D. Gendron et al., "Toward a rational design of poly(2,7-carbazole) derivatives for solar cells," J. Am. Chem. Soc. **130** (2), 732-742 (2008).

[4] G. Dennler, M. C. Scharber, T. Ameri et al., "Design rules for donors in bulk-heterojunction tandem solar cells-towards 15 % energy-conversion efficiency," Advanced Materials **20** (3), 579-+ (2008).

[5] D. M. deLeeuw, M. M. J. Simenon, A. R. Brown et al., "Stability of n-type doped conducting polymers and consequences for polymeric microelectronic devices," Synthetic Metals **87** (1), 53-59 (1997).

[6] E. Bundgaard and F. C. Krebs, "Low band gap polymers for organic photovoltaics," Solar Energy Materials and Solar Cells **91** (11), 954-985 (2007).

[7] L. J. A. Koster, V. D. Mihailetchi, and P. W. M. Blom, "The optimal band gap for plastic photovoltaics," SPIE Newsroom (2007).

[8] D. F. Perepichka and M. R. Bryce, "Molecules with exceptionally small HOMO-LUMO gaps," Angewandte Chemie-International Edition **44** (34), 5370-5373 (2005).

[9] J. L. Bredas, R. Silbey, D. S. Boudreaux et al., "Chain-Length Dependence of Electronic and Electrochemical Properties of Conjugated Systems: Polyacetylene, Polyphenylene, Polythiophene, and Polypyrrole," Journal of the American Chemical Society **105** (22), 6555-6559 (1983).

[10] I. Imae and Y. Kawakami, "Modification of thermal property and LUMO level of disilane by phenyl-substitution," Science and Technology of Advanced Materials **6** (5), 443-446 (2005).

[11] F. B. Kooistra, J. Knol, F. Kastenberg et al., "Increasing the open circuit voltage of bulk-heterojunction solar cells by raising the LUMO level of the acceptor," Organic Letters **9** (4), 551-554 (2007).

[12] B. P. Rand, D. P. Burk, and S. R. Forrest, "Offset energies at organic semiconductor heterojunctions and their influence on the open-circuit voltage of thin-film solar cells," Physical Review B **75** (11) (2007).

[13] T. Yamanari, T. Taimaa, J. Sakaib et al., "Origin of the open-circuit voltage of organic thin-film solar cells based on conjugated polymers " Solar Energy Materials and Solar Cells (in press, available online 5 November 2008).

[14] Sam-Shajing Sun and Niyazi Serdar Sariciftci, *Organic photovoltaics : mechanism, materials, and devices*. (Taylor & Francis, Boca Raton, Fla, 2005), p.629p.

[15] B. P. Rand, J. Genoe, P. Heremans et al., "Solar cells utilizing small molecular weight organic semiconductors," Progress in Photovoltaics **15** (8), 659-676 (2007).

[16] S. S. Sun, "Optimum energy levels and offsets for organic donor/acceptor binary photovoltaic materials and solar cells," Materials Science and Engineering B-Solid State Materials for Advanced Technology **116** (3), 251-256 (2005).

[17] P. Peumans and S. R. Forrest, "Separation of geminate charge-pairs at donor-acceptor interfaces in disordered solids," Chemical Physics Letters **398** (1-3), 27-31 (2004).

[18] H. Frohne, S. E. Shaheen, C. J. Brabec et al., "Influence of the anodic work function on the performance of organic solar cells," Chemphyschem **3** (9), 795-+ (2002).

[19] J. S. Kim, J. H. Park, J. H. Lee et al., "Control of the electrode work function and active layer morphology via surface modification of indium tin oxide for high efficiency organic photovoltaics," Applied Physics Letters **91** (2007).

[20] Y. F. Li, Y. Cao, J. Gao et al., "Electrochemical properties of luminescent polymers and polymer light-emitting electrochemical cells," Synthetic Metals **99** (3), 243-248 (1999).

[21] D. Cahen and A. Kahn, "Electron energetics at surfaces and interfaces: Concepts and experiments," Advanced Materials **15** (4), 271-277 (2003).

[22] P. W. Atkins and Julio De Paula, *Atkins' physical chemistry*, 8th ed. ed. (Oxford University Press, Oxford, 2006), pp.xxx, 1064 p.

[23] Alessio Filippetti, "Electron affinity in density-functional theory in the local-spin-density approximation," Physical Review A **57** (2), 914 (1998).

[24] D. Danovich, "NDDO semiempirical approximations coupled with Green's function technique - a reliable approach for calculating ionization potentials," Theochem-Journal of Molecular Structure **401** (3), 235-252 (1997).

[25] B. W. D'Andrade, S. Datta, S. R. Forrest et al., "Relationship between the ionization and oxidation potentials of molecular organic semiconductors," Organic Electronics **6** (1), 11-20 (2005).

[26] D. P. Piet, D. Danovich, H. Zuilhof et al., "Ionization potentials of porphyrins and phthalocyanines. A comparative benchmark study of fast improvements of Koopman's Theorem," Journal of the Chemical Society-Perkin Transactions 2 (8), 1653-1661 (1999).

[27] E. V. Tsiper, Z. G. Soos, W. Gao et al., "Electronic polarization at surfaces and thin films of organic molecular crystals: PTCDA," Chemical Physics Letters **360** (1-2), PII S0009-2614(0002)00774-00771 (2002).

[28] David K. Gosser, Cyclic voltammetry : simulation and analysis of reaction mechanisms. (VCH, Germany, 1993), p.154.

[29] Frank A. Settle, *Handbook of instrumental techniques for analytical chemistry*. (London : Prentice Hall PTR ; Prentice-Hall International (UK), Upper Saddle River, N.J., 1997), pp.xxi, 995.

[30] Douglas A. Skoog, F. James Holler, and Timothy A. Nieman, *Principles of instrumental analysis*, 5th ed / Douglas A. Skoog, F. James Holler, Timothy A. Nieman. ed. (Saunders College Publishing, Philadelphia ; London, 1998), pp.xv, 849, [893]p.

[31] P. T. Kissinger and W. R. Heineman, "Cyclic Voltammetry," J. Chem. Educ. **60** (9), 702-706 (1983).

[32] Allen J. Bard and Larry R. Faulkner, *Electrochemical methods : fundamentals and applications*, 2nd ed. ed. (John Wiley, New York ; Chichester, 2001), pp.xxi, 833 p.

[33] Peter T. Kissinger and William R. Heineman, *Laboratory techniques in electroanalytical chemistry*, 2nd ed. (Marcel Dekker, Inc., New York, 1996), p.986p.

[34] G. A. Mabbott, "AN INTRODUCTION TO CYCLIC VOLTAMMETRY," J. Chem. Educ. **60** (9), 697-702 (1983).

[35] Joseph Wang, *Analytical electrochemistry*, 3rd ed. ed. (Wiley ; Chichester : John Wiley [distributor], Hoboken, N.J., 2006), pp.xvi, 250 p.

[36] W. C. Tsoi, University of Hull, 2006.

[37] L. Micaroni, F. C. Nart, and I. A. Hummelgen, "Considerations about the electrochemical estimation of the ionization potential of conducting polymers," Journal of Solid State Electrochemistry **7** (1), 55-59 (2002).

[38] S. Trasatti, "The absolute electrode potential- an explanatory note (recommendations 1986)," Pure and Applied Chemistry **58** (7), 955-966 (1986).

[39] V. V. Pavlishchuk and A. W. Addison, "Conversion constants for redox potentials measured versus different reference electrodes in acetonitrile solutions at 25 degrees C," Inorganica Chimica Acta **298** (1), 97-102 (2000).

[40] F. Crespilho, V. Zucolotto, and J. Siqueira Jr, "Using Electrochemical Data to Obtain Energy Diagrams Layer-By-Layer Films from Metallic Phthalocyanines," Int. J. Electrochem. Sci. **1**, 151-159 (2006).

[41] Cynthia G. Zoski, *Handbook of electrochemistry*. (Elsevier, Amsterdam ; Oxford, 2007), pp.xx, 892 p., [819] p. of plates.

42 J. L. Bredas, A. J. Heeger, and F. Wudl, "Towards organic polumers with very small intrinsic band gaps.1. electronic-structure of polyisothianphthene and derivatives.," Journal of Chemical Physics **85** (8), 4673-4678 (1986).

43 M. M. Ling, P. Erk, M. Gomez et al., "Air-stable n-channel organic semiconductors based on perylene diimide derivatives without strong electron withdrawing groups," Advanced Materials **19** (8), 1123-1127 (2007).

44 J. Gierschner, J. Cornil, and H. J. Egelhaaf, "Optical bandgaps of pi-conjugated organic materials at the polymer limit: Experiment and theory," Advanced Materials **19** (2), 173-191 (2007).

45 S. Koyuncu, I. Kaya, F. B. Koyuncu et al., "Electrochemical, optical and electrochromic properties of imine polymers containing thiophene and carbazole units," Synthetic Metals **159** (11), 1034-1042 (2009).

46 K. Oyaizu, T. Iwasaki, Y. Tsukahara et al., "Linear ladder-type pi-conjugated polymers composed of fused thiophene ring systems," Macromolecules **37** (4), 1257-1270 (2004).

47 E. Lim, B. J. Jung, and H. K. Shim, "Synthesis and characterization of a new light-emitting fluorene-thieno[3,2-b]thiophene-based conjugated copolymer," Macromolecules **36** (12), 4288-4293 (2003).

48 F. Brovelli, B. L. Rivas, J. C. Bernede et al., "Electrochemical and optical studies of 1,4-diaminoanthraquinone for solar cell applications," Polymer Bulletin **58** (3), 521-527 (2007).

49 S. E. Koh, B. Delley, J. E. Medvedeva et al., "Quantum chemical analysis of electronic structure and n- and p-type charge transport in perfluoroarene-modified oligothiophene semiconductors," Journal of Physical Chemistry B **110** (48), 24361-24370 (2006).

3. TRANSPORT OF CHARGE CARRIERS IN ORGANIC SEMICONDUCTORS

3.1. Introduction

Over the last few decades a new academic and industrial research area based on organic conjugated materials has emerged. These materials are used as semiconductor materials for a wide range of applications such organic light emitting diodes (OLED), field effect transistors (OFET), and photovoltaics (OPV). Charge transport is one of the key factors determining the performance of these applications. For organic photovoltaics, as discussed in chapter one, the power conversion efficiency of the solar cells depends on three steps; the first and second steps are the light absorption to create excitons, and the exciton diffusion and dissociation at the ED/EA interface forming electrons and holes in the EA and ED moieties respectively. The third step is the transport of the charge carriers through the respective material to the right electrode, which is our investigation in this chapter.

3.2. Mobility

In semiconductors; charge carriers (electron, holes) move randomly in the absence of net applied electric field E, which give an average drift velocity of $\langle v \rangle = 0$ over a period of time, and average momentum p of zero so that $\langle \frac{dp}{dt} \rangle = 0$. However if there is an applied electric field E, the charge carriers accelerate with time either in the same or opposite direction to the applied electric field according to their charge and this leads to a linear increase of the momentum. The charge carriers are not always accelerated but may decelerate due to the scattering events caused by impurities, defects, phonons (lattice vibrations), and some other causes. The relation of the average velocity to the field in the steady state condition can be correlated to an average momentum loss per unit time and an average distance travel per unit time $\left(\frac{d\langle\Lambda\rangle}{dt}\right)$ as[1]

$$-\langle\frac{\mathbf{dp}}{\mathbf{dt}}\rangle = \boldsymbol{\beta}\frac{\mathbf{d}\langle\boldsymbol{\Lambda}\rangle}{\mathbf{dt}} = \mathbf{m}\frac{\langle\mathbf{v}\rangle}{\boldsymbol{\tau}} \qquad (3\text{-}1)$$

where β can be expressed as the ratio of a effective mass m and a relaxation time τ. For a charged particle the change of the momentum in an electric field E is

$$\langle\frac{\mathbf{dp}}{\mathbf{dt}}\rangle = \mathbf{eE} \qquad (3\text{-}2)$$

where e is the elementary charge. Therefore

$$\langle\mathbf{v}\rangle = \frac{\mathbf{e}}{\mathbf{m}}\boldsymbol{\tau}\mathbf{E} \qquad (3\text{-}3)$$

The magnitude of the average drift velocity per unit electric field is known as the carrier mobility μ,

$$\boldsymbol{\mu} = \frac{\langle v\rangle}{E} = \frac{e}{m}\boldsymbol{\tau} \qquad (3\text{-}4)$$

The mobility is the essential electronic charge transport quantity, which can be used to characterize the charge transport property of semiconductor materials. The electronic conductivity of the material for each charge carrier is given by[2,3]

$$\boldsymbol{\sigma}_{\mathbf{e}} = \mathbf{ne}\boldsymbol{\mu}_{\mathbf{e}} \ \ , \ \boldsymbol{\sigma}_{\mathbf{h}} = \mathbf{pe}\boldsymbol{\mu}_{\mathbf{h}} \qquad (3\text{-}5)$$

where n and p are the concentration of the electrons and holes respectively. The total electronic conductivity of the material is

$$\boldsymbol{\sigma} = (\mathbf{ne}\boldsymbol{\mu}_{\mathbf{e}} + \mathbf{pe}\boldsymbol{\mu}_{\mathbf{h}}) \qquad (3\text{-}6)$$

3.3. Electronic States and Transport Mechanisms

Several models have been developed to study the charge carrier transport mechanisms in semiconductors. For all of these models the charge carrier mobility and its variation with temperature, doping, or electric field are the central issues. Generally these models are classified according to two main mechanisms: band transport, and hopping transport. These two mechanisms can be characterized and distinguished according to the magnitude of the mobility and its temperature dependence.

3.3.1. Extended (Delocalized) States and Band Transport

The charge carrier transport and electronic structure of crystalline and weakly disordered semiconductors is well described by the band theory and band transport model. The charge carriers move as a highly delocalized plane wave in an energy band of large width with a relatively large mean free path and very high mobility of $\mu >> 1$ $cm^2/V.s$. The hole motion of the carriers in Ge can be considered as an example for this type, where the valence bandwidth is approximately 3 eV, the scattering time $\tau \approx 10^{-3}$s and the mean free path (at T=300K) is ≈1000 Å, which is very large compared to the inter-atomic distance (2.45 Å)[4,5].

It has been found that when the atoms are widely separated and independent of each other the electrons in the attractive potential of each atom occupy bound states separated by forbidden energy gaps. However, when the atoms move sufficiently close to each other they interact; each energy level is split into a very large number of energy levels (equals to the number of atoms), which are called bands. Each band has a band width and the energy levels distribution within the band is quasi-continuous when the number of atoms is large. Between the energy bands there is a range of energy values which cannot be occupied called bandgaps as shown in figure 3-1.[6,7]

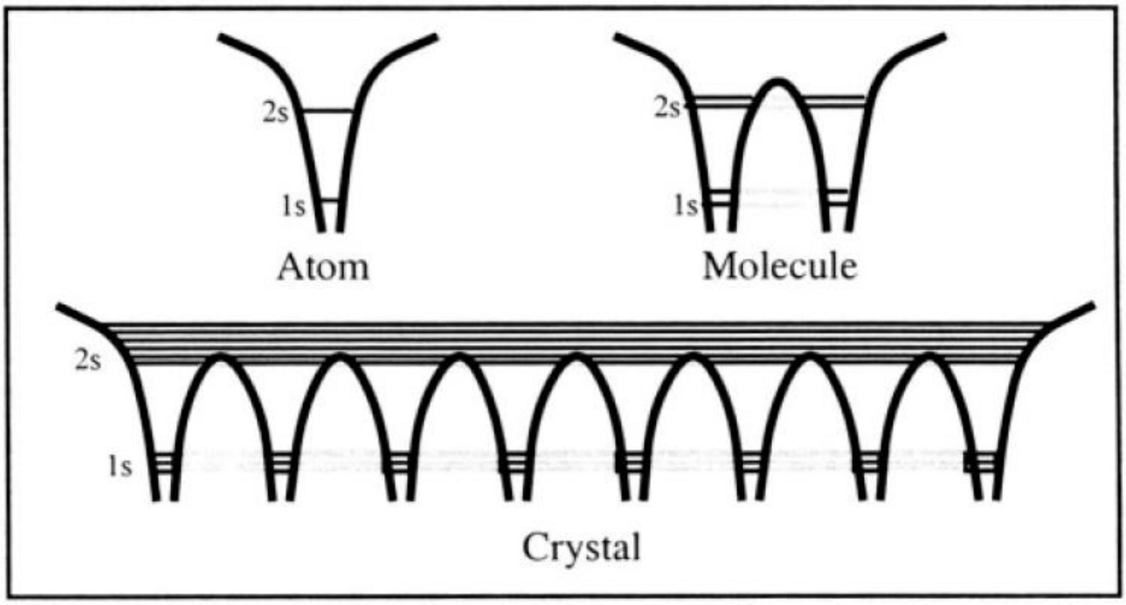

Figure 3-1: Allowed energy levels of an atom, hypothetical molecule and crystal[6].

Potential wells are generated by the nuclei of the equally spaced atoms over the crystalline sample. The electrons which occupy energy levels close to the nucleus are strongly bound. Those in higher energy levels are less bound to the nucleus so that the electrons can overcome the nuclear attraction and move throughout the crystal; those energy bands can be considered as extended (delocalized) states. Therefore, electronic transport in crystalline and weakly crystalline semiconductors can be described using the concept of almost free quasi-particles (Bloch waves), where the wavefunctions of the electrons do not undergo significant attenuation in the perfect periodic potential. However the atoms in the crystal at temperature above absolute zero have enough thermal energy to cause them to vibrate around their lattice points (phonon) leading to a disturbance of the perfect periodic potential as shown in figure 3-2 causing scattering and attenuation of the movement of electrons.

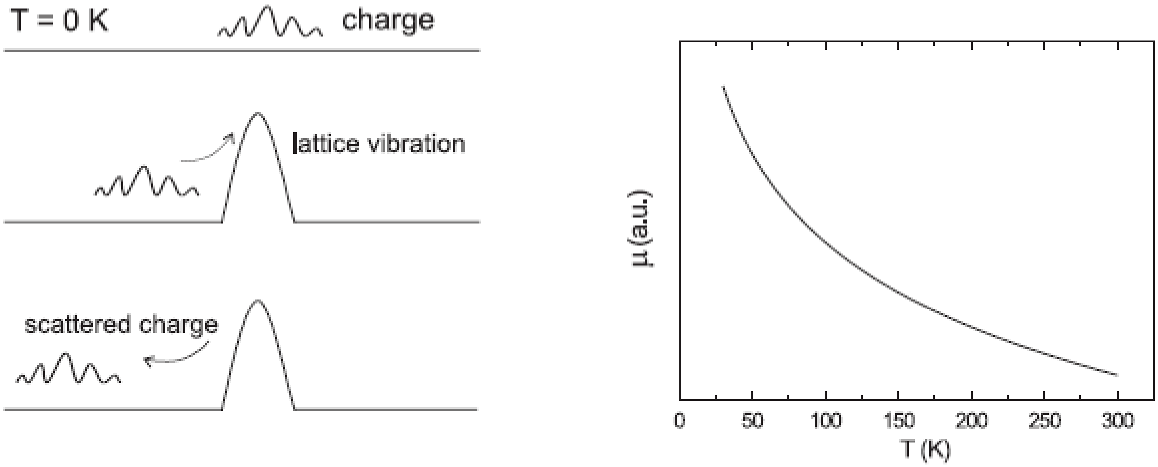

Figure 3-2: Band transport in a perfect crystal and thermal vibration scattering (left), schematic graph showing the decrease of the mobility as a function of increasing temperature (right)[8]

The lattice vibration of the crystalline and quasi-crystalline materials increases with temperature, which increases the lattice scattering of the charge carriers. Consequently the mobility decreases according to

$$\boldsymbol{\mu \propto T^{-n}} \qquad (3\text{-}7)$$

where n > 1

Inorganic semiconductors crystals have a wide bandwidth and narrow band gap because of the very strong covalent bonds between its components, which have an energy of about 76 Kcal mol^{-1} for the case of Si. Organic semiconductors crystals have a narrow bandwidth and wide bandgap because of the weak intermolecular interactions in organic semiconductors. These are mostly based on van der Waals forces in the very large class of neutral molecular crystals, or on a combination of van der Waals and local coulombic interaction in the minor class of ionic organic crystals. The intermolecular bond interaction energy is smaller than 10 Kcal mol^{-1}, which is close to the magnitude of vibrational energy of the molecules at or above room temperature. Also the crystalline quality is very poor compared to the inorganic semiconductors. [4,5,1]

3.3.2. Localized States and Hopping Transport

The periodicity of the crystalline structure is disturbed by the present of the defects even in a good crystal, and as the population of these defects increase the material start losing its crystalline structure to become domains of crystalline structure surrounded by grain boundaries. As these domains become smaller the structure changes to polycrystalline eventually reaching highly non crystalline or amorphous materials.

The rate of scattering increases with the number of defects. When the mean free path between scattering events becomes less than the intersite distance then the charge carrier is localized on a few atoms. Sometimes a charge carriers falls into a trap of a strongly localized state where it become immobile for a period of time until it escapes and traps again and so on. This is known as hopping transport between strongly localized states, which drops the carrier mobility to very low values $\mu << 1\ cm^2/V.s$ [4] as shown in figure 3-3

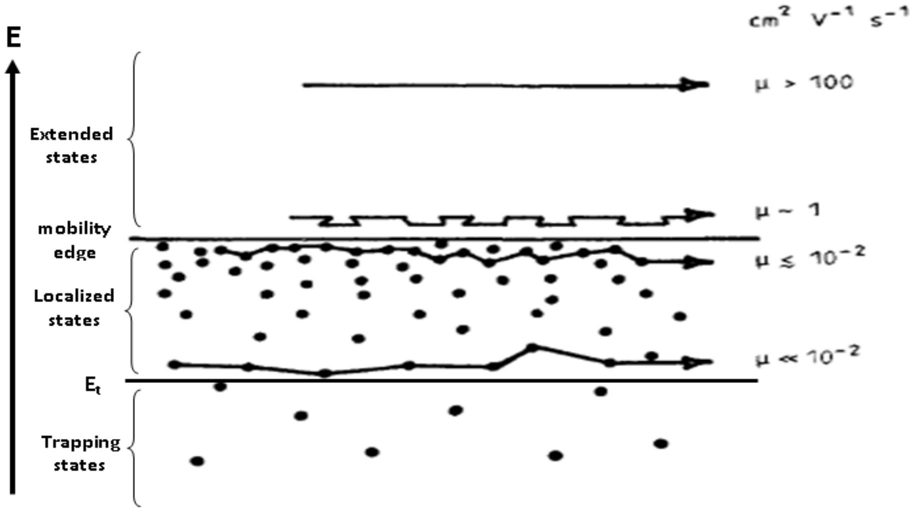

Figure 3-3: The variation of charge carrier mobility with the energy distribution of trap and an expectation of the mobility values according to energetic disorder.[9]

The electronic energy structure of well ordered crystalline semiconductors is well defined and consists of energy bands and energy gaps, while the electronic structure of very disordered materials can be treated as quasi continuous because of the presence of trap states within the energy gap. The organic semiconductor has discrete energy states because of the weak interactions between the molecules, however it retains some of the characteristic features of band structure, since the energy spectrum contains regions of high electron density of states and some of low electron density of states corresponding to the allowed and forbidden bands respectively. Note the density of states (DOS) is the concentration of the states per unit energy per unit volume. The relevant regions with high concentration are known as lowest unoccupied molecular orbital (LUMO) and highest occupied molecular orbital (HOMO) respectively. Similarly to the conventional amorphous semiconductor there are some energy levels separating the extended states from localized states which is known as the mobility edge as shown in figure 3-3. For an amorphous organic semiconductor the extended states are hardly observed and its density of states can be represented by a Gaussian distribution of localized molecular orbitals with a very narrow width. Charge transport occurs by hopping between localized molecular states, so a transport energy or escape energy level (E_t) is introduced, which is the energy of the mobility edge between the trap states and the hopping transport states as illustrated in figure 3-3 and figure 3-4(a).

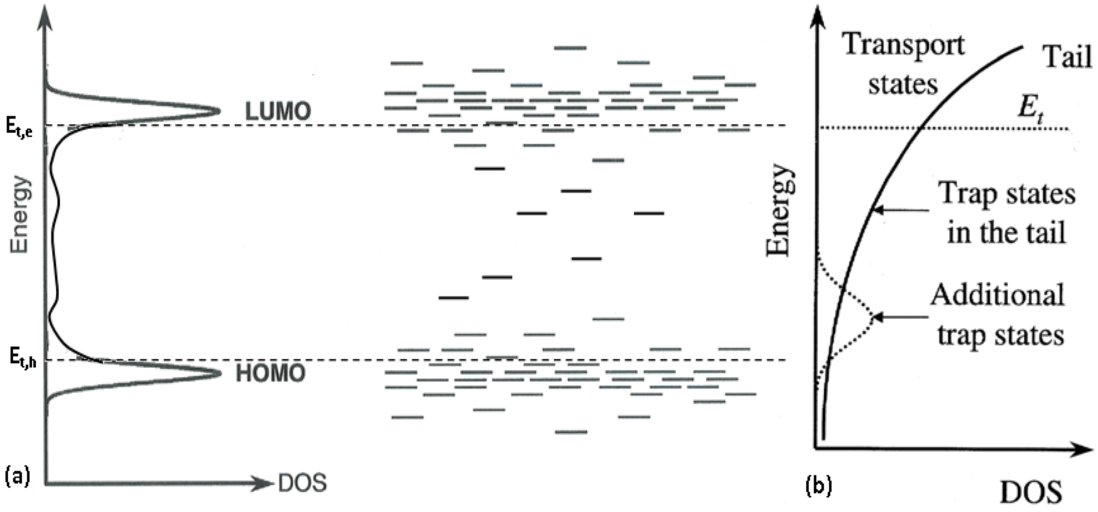

Figure 3-4: (a)Density of states distribution of HOMO/LUMO levels in disordered organic semiconductors, (b) enhancement of the tail region showing the trap states in the tail and the additional trap states and the transport states[10]

The electron transport energy level $E_{t,e}$ is located at the bottom of the LUMO level and the hole transport energy level $E_{t,h}$ at the top of the HOMO level. States below the electron transport energy level $E_{t,e}$ which are able to capture the electron are known as electron traps, and localized states above the hole transport energy level $E_{t,h}$ which capture the holes are known as hole traps. Therefore energy states between the two transport energies levels are trapped states. The density of states decreases when the energy moves away from the transport energy towards the centre on the gap. Most traps lie in the vicinity of the transport energy, the so-called tail region. The gap between the two transport energy levels can have additional deep trap states as shown in figure 3-4(b).[3,7,10,11]

The nature of the defects is different in organic semiconductors than in inorganic semiconductors because of the structural differences between them. For inorganic semiconductors the defects can be identified and controlled while it is more difficult to control them in organic semiconductors especially polymers. The defects in organic semiconductors can be classified as intrinsic or extrinsic. The extrinsic or chemical defect is a residual impurity from the synthesis or the thin film processing. If the HOMO or LUMO energy levels of the impurity molecule is positioned in the gap of the host molecules it forms a trap state. The intrinsic defect is a structural defect and includes any distortion of the structure such as a grain boundary, crystallography defect, chain end, conformation disorder, and bonding (oxidative) defect. The HOMO/LUMO energy levels are not only determined by chemical structure but are also influenced by the electronic polarization of the surrounding environment[10,12,13,14]. Hence the structural defect can locally affect the environment and form a trap.

The dominance of localized states in disordered semiconductors and the requirement of an activation energy E_{act} to jump from one localized trap state to another explains the correlation between the charge transport in amorphous organic semiconductors and the temperature. Therefore charge carrier mobility increases with temperature as illustrated schematically in figure 3-5 and with more detail in section 3.4 and in the discussion of results in section 3-6. Indeed some trap states at room temperature may become transport states at higher temperature.

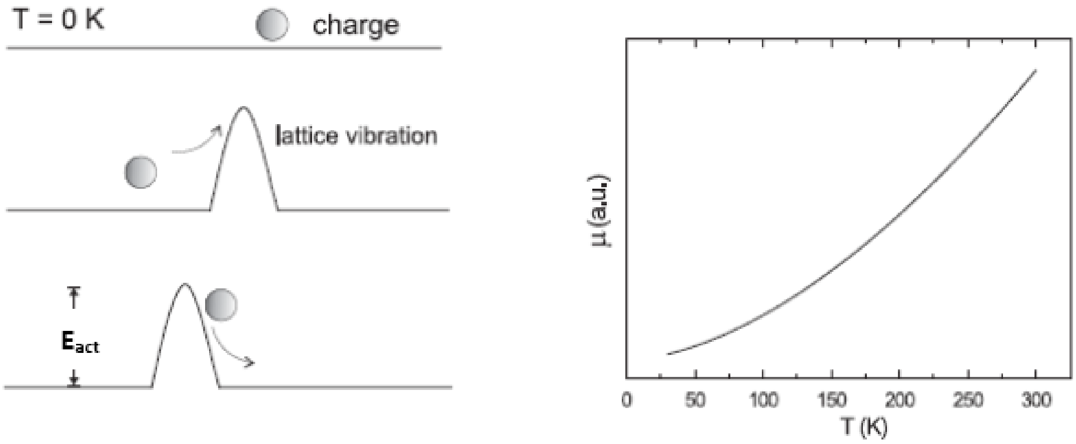

Figure 3-5: Hopping transport in disordered materials with localized carriers. Thermal vibration helps to overcome the activation barrier of energy E_b (left), schematic graph showing the increase of the mobility as a function of increasing temperature (right)[8]

3.4. Models of Hopping Transport

To date, many models have been developed to explain charge carrier transport in amorphous organic semiconductors based on energetic and positional disorder. These models were based and developed according to some experimental observations like the mobility dependence on the electric field, temperature, and many other factors. No single model can cover all of the factors affecting the charge transport mobility.

3.4.1. Poole-Frenkel Model

The Poole-Frenkel effect[15,16,17,18,19,20], which is also known as field-assisted thermal ionization, is a well known model to explain charge transport in semiconductors and its field and temperature dependence. This model was originally used for conventional semiconductors to explain the escape of the charge carriers from trapping centres into the conduction band under the influence of the applied field. This occurs via lowering of the barrier associated with their coulomb potential in the electric field direction by $\beta_{PF}E^{1/2}$as shown in figure 3-6. This predicts the field dependence of the mobility

$$\mu = \mu_o \exp\left(\frac{\beta_{PF}E^{1/2}}{k_B T}\right) \tag{3-8}$$

where $\beta_{PF} = (e^3/\pi\varepsilon\varepsilon_o)^{1/2}$ is the Poole-Frenkel coefficient, k_B is the Boltzmann constant, ε is the high-frequency dielectric constant of the insulator, ε_o is the permittivity of free space.

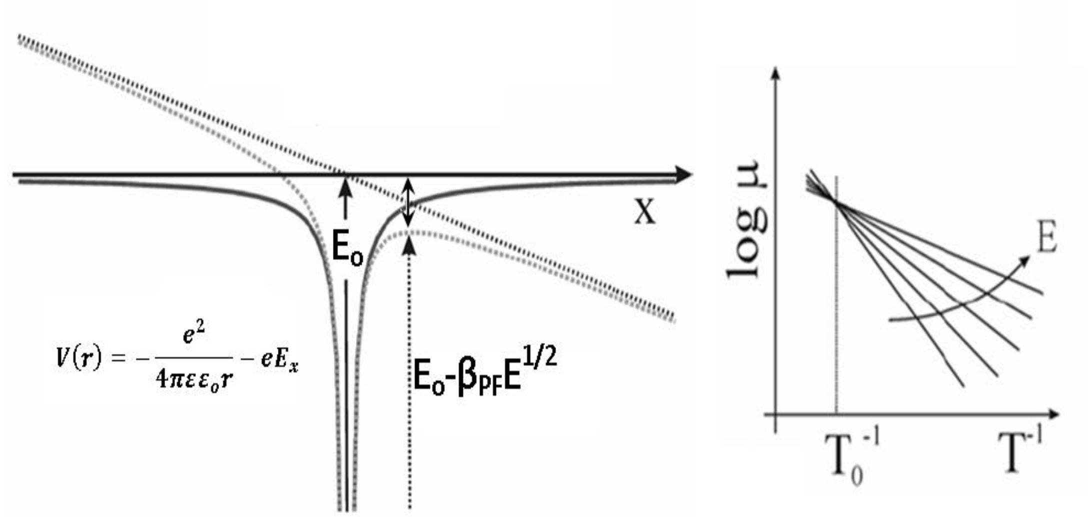

Figure 3-6: The lowering of the potential barrier of the localized charge carrier under the influence of the external electric field according to Poole-Frenkel model (left), the temperature dependence of the mobility for various electric field according to Gill's model (right)[21]

3.4.2. Gill Model

Similar results to the Poole-Frenkel model for the temperature and field dependence of the mobility were found by Gill in the case of molecular doped polymer TNF: PVK. The Gill's model gives an empirical relation for μ[22,23]

$$\mu = \mu_o \exp\left(-\frac{E_o - \beta_{PF}E^{1/2}}{k_B T_{eff}}\right) \tag{3-9}$$

where $\frac{1}{T_{eff}} = \frac{1}{T} - \frac{1}{T_o}$, E_o is the zero field activation energy, T is the sample temperature, and T_o is the temperature at which the extrapolated data intersect as shown in figure 3-6. This model has been used widely but it has some limitations, e.g. failure to relate the temperature and field dependence of the mobility to the disordered structure.

3.4.3. Gaussian Disorder Model (GDM)

The most important and comprehensive model for charge transport in organics semiconductors is the disorder formalism model developed by Bässler and coworkers[20, 24,25,26,23]. This formalism known as the Gaussian disorder model (GDM) is based on the absence of long-range order. All states are assumed to be localized and the DOS has a Gaussian energy distribution $\rho(\varepsilon)$ given by

$$\boldsymbol{\rho(\varepsilon) = (2\pi\sigma^2)^{-1/2}\exp\left(-\frac{\varepsilon^2}{2\sigma^2}\right)} \qquad (3\text{-}10)$$

where σ is the width of the Gaussian distribution of the energy hopping sites, The energy ε is measured relative to the centre of the DOS. Charge carriers injected into a site within the DOS tend to relax towards the tail states at quasi-equilibrium level; the energetic centre of the occupied (ODOS) is found at energy of $-\sigma^2/K_BT$ from the centre of DOS as illustrated in figure 3-7.

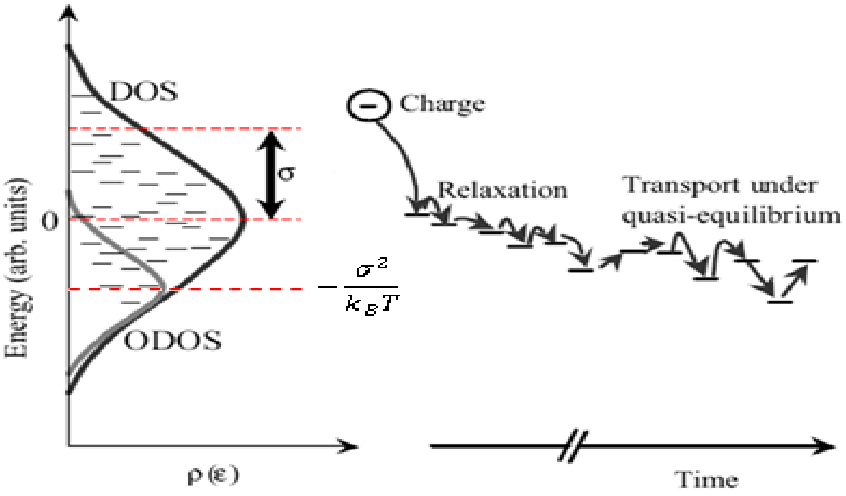

Figure 3-7: Schematic diagram of Gaussian distribution of the energetic hopping sites, illustrating the hopping transport of an injected charge carriers at a higher state and its relaxation to the equilibrium state of the occupied density of states ODOS.[27]

The Gaussian distribution formalism is the first key assumption of this model. The second one determine the jumping rate υ_{ij} between adjacent sites *i* and *j* of energy ε_i and ε_j respectively, and spatial separation R_{ij} using the Miller-Abrahams formalism[28]. This is the product of a frequency prefactor υ_o, the electronic wavefunction overlap factor and a Boltzmann factor for hopping upward in energy.

$$\boldsymbol{\upsilon_{ij} = \upsilon_o \exp\left(-2\gamma a \frac{\Delta R_{ij}}{a}\right) \exp\left(-\frac{\varepsilon_j - \varepsilon_i}{k_B T}\right); \quad \varepsilon_j > \varepsilon_i} \qquad (3\text{-}11)$$

where a is the average lattice distance or the localization length. γ is the charge carrier localization constant also known as the inverse wavefunction decay constant, with greater values corresponding to greater charge localization and a sharper decay of electron density with distance. The overlap parameter Γ=2γa quantifies the degree of electronic coupling between transport sites due to wavefunction overlap. $\Delta R_{ij} = |R_i - R_j|$.

The last exponential is for the upward hopping which requires an activation energy to overcome the energy barrier between the sites. However the downward hopping or hopping to the same energy have no need for activation energy even though some energy needs to be released as phonons to reach the other site. The relation becomes

$$\boldsymbol{\upsilon}_{\mathbf{ij}} = \boldsymbol{v_o}\mathbf{exp}\left(-\boldsymbol{\Gamma}\frac{\Delta\mathbf{R_{ij}}}{\mathbf{a}}\right) ; \qquad \boldsymbol{\varepsilon}_{\mathbf{j}} \leq \boldsymbol{\varepsilon}_{\mathbf{i}} \tag{3-12}$$

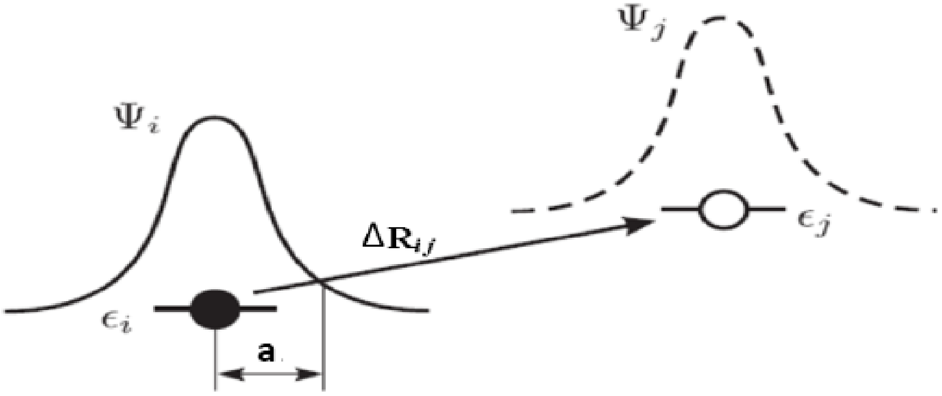

Figure 3-8: hopping transition between two localized state *i* and *j*. [3]

For Monte Carlo simulations, the energetic and positional disorder is specified using the previous assumption, with the degree of the energetic disorder given by the parameter σ/K_BT. The positional disorder is given by considering the wavefunction overlap parameter Γ to be the sum of the contribution from each site, $\Gamma_{ij} = \Gamma_i + \Gamma_j$. Each one can vary randomly in a Gaussian probability density of standard deviation $\delta\Gamma$. The variation of Γ was based on the variation of a and γ. The variance of Γ_{ij} is considered as positional parameter $\Sigma = (2\delta\Gamma)^{1/2}$ [24,20].

From the Monte Carlo simulation with zero applied field, it was found that the mobility dependence on the temperature is proportional to $(\sigma/K_BT)^2$ as shown in figure 3-9 and formulated as[24,20]

$$\boldsymbol{\mu}(\mathbf{E} = \mathbf{0}, \mathbf{T}) = \boldsymbol{\mu}_{\mathbf{o}}\ \mathbf{exp}\left[-\left(\frac{\mathbf{2\sigma}}{\mathbf{3K_BT}}\right)^{\mathbf{2}}\right] \tag{3-13}$$

where μ_o, the prefactor mobility, is the value of the zero field mobility projected to infinite temperature.

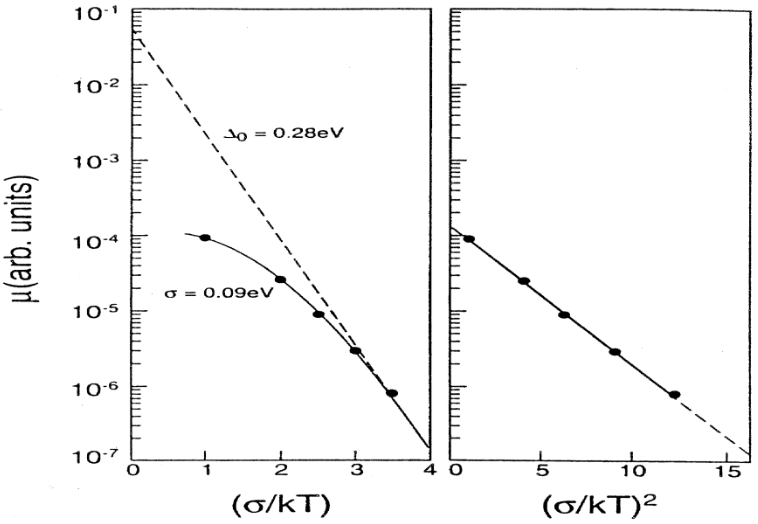

Figure 3-9: Simulation result for the dependence of the mobility on the energetic disorder parameter σ/K_BT where $\log(\mu)$ is plotted versus σ/K_BT and $(\sigma/K_BT)^2$ respectively [20]

The Monte Carlo simulation also shows that the electric field reduces the average barrier height for hopping to a higher energy site in the direction of the field. The effect of the field was examined using simulation by varying the degree of energetic disorder σ/K_BT and the positional disorder parameter Σ and monitoring the variation of the mobility with the field as shown in figure 3-10 and figure 3-11.

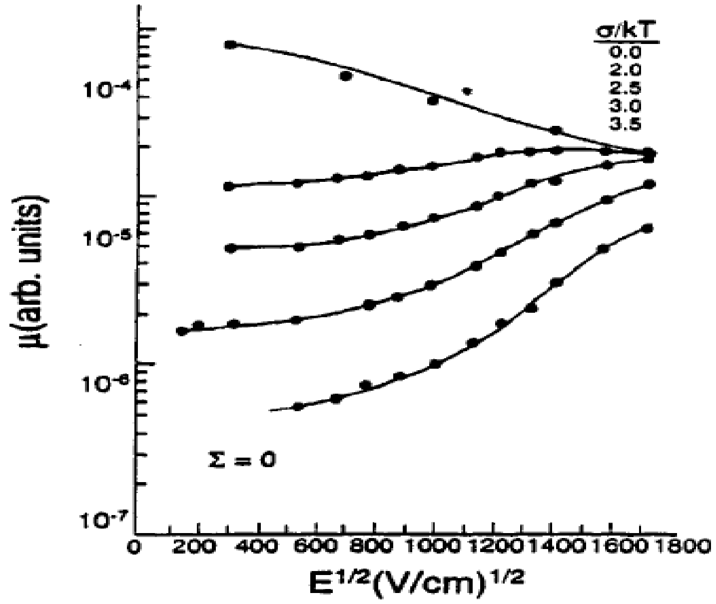

Figure 3-10: : Simulation result for the dependence of the mobility on the electric field for different values of σ/K_BT and absence of Σ [20]

Figure 3-10 shows the simulation result illustrating the dependence of the mobility on the field, the system is only subject to the variation of the energetic disorder

σ/K_BT as the positional disorder is eliminated by assuming Σ = 0. Generally we can see three different effects on the graph, at low field the mobility is saturated, at high field it increases following Poole-Frenkel behaviour ($ln\, \mu\, \alpha\, E^{1/2}$), and the third one is the effect of decreasing the energetic disorder parameter to zero ($\sigma/K_BT \rightarrow 0$): the gradient of the mobility decreases to a point where it become negative.

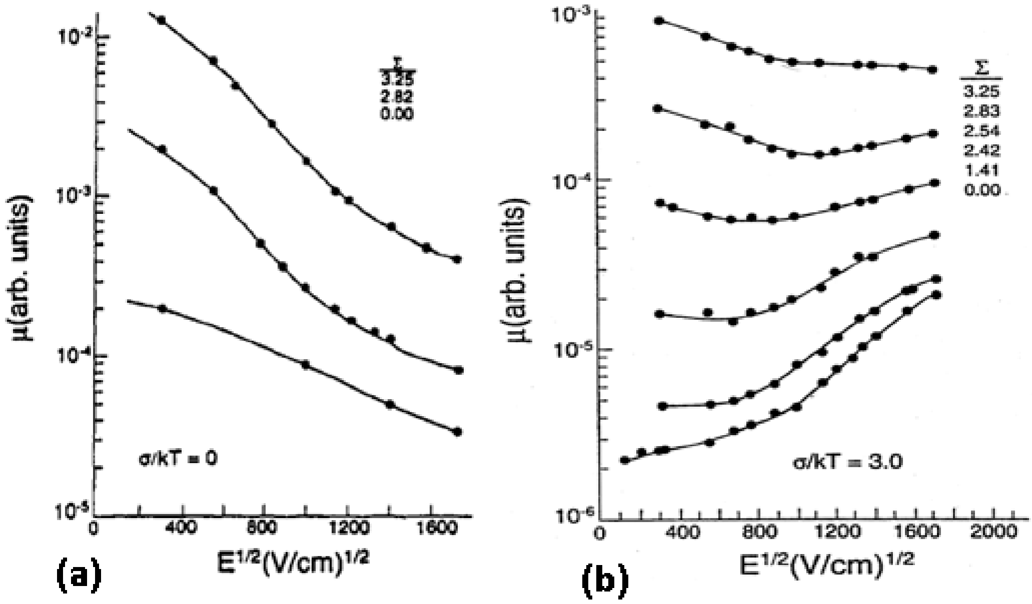

Figure 3-11: simulation result for the dependence of the mobility on the electric field for : (a) different values of Σ and absence of σ/K_BT,(b) both energetic and positional disorder with different values of Σ and fixed value for $\sigma/K_BT = 3$[20]

The effect of removing energetic disorder by letting $\sigma/K_BT = 0$ and varying the positional disorder parameter Σ is shown in figure 3-11(a). Over the entire range of the field the mobility decreases with an increase of field.

Figure 3-11(b) shows a superimposed disorder variable, where the energetic disorder is $\sigma/K_BT = 3$, and the positional disorder parameter Σ increases from zero. In this case there are two notable regions in the graph, low and high field regions, each with different variations in slope. Increasing the disorder parameter Σ decreases the slope in both regions until it becomes negative, in the high field region it becomes negative when $\Sigma > \sigma/K_BT$ while in the low field region it become negative for lower values of Σ. Following the Poole-Frenkel behaviour of ($ln\, \mu\, \alpha\, \beta E^{1/2}$), the slope $\beta = \partial\, ln\, \mu / \partial E^{1/2}$ decreases with the increase of Σ.

The negative electric field dependence is explained by Bässler[24]: the increase of the positional disorder increases the fluctuations in the electronic coupling between the charge transport sites. This fluctuation sometimes blocks some direct routes because of unfavourable coupling between the sites. However, it also create more options for faster routes with favourable coupling as shown in figure 3-12 where it is assumed that the electric field is in the A-D direction. The carrier following the favourable loop at some time needs to hop against the field giving higher barriers with an increase of the field, and consequently lower mobility values.

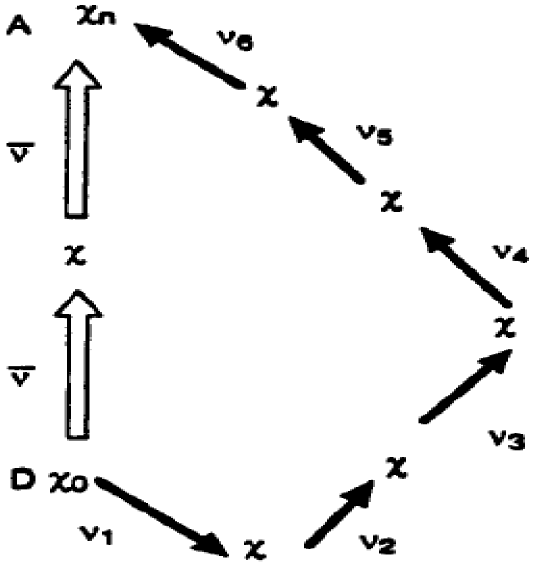

Figure 3-12: Schematic illustration of different route of charge carrier to follow under an influence of A-D direction electric field [20]

To obtain a formula relating the mobility to the temperature and the field μ(E,T) it is essential to know the dependence of the slope β with $\sigma/K_B T$ and Σ. Therefore the simulation result of β versus $(\sigma/K_B T)^2$ with variation of Σ is shown in figure 3-13. The result is a set of near parallel straight lines of slope C.

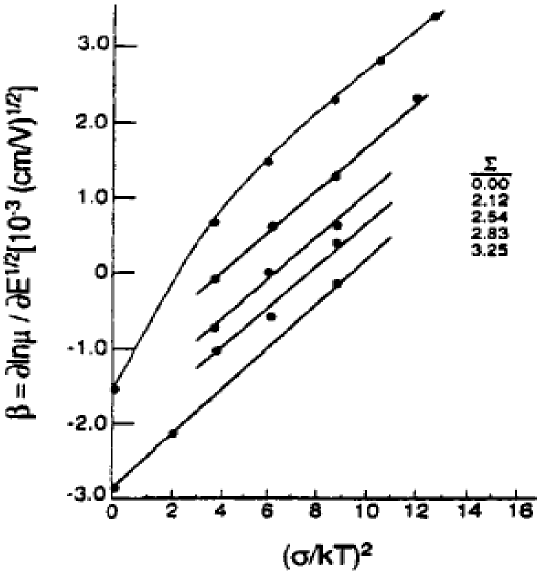

Figure 3-13: The variation of the slope β versus $(\sigma/K_BT)^2$ for different values of the positional disorder Σ.[20]

Incorporating the result in figure 3-13 and that in eq. 3-13 the mobility is expressed in terms of both the energetic and positional disorder parameters as

$$\boldsymbol{\mu(E,T) = \mu_o \exp\left[-\left(\frac{2\sigma_g}{3K_BT}\right)^2\right] \exp\left[C\left\{\left(\frac{\sigma_g}{K_BT}\right)^2 - \Sigma^2\right\}\sqrt{E}\right]} \; ; \quad \boldsymbol{\Sigma \geq 1.5} \qquad (3\text{-}14)$$

and

$$\boldsymbol{\mu(E,T) = \mu_o \exp\left[-\left(\frac{2\sigma_g}{3K_BT}\right)^2\right] \exp\left[C\left\{\left(\frac{\sigma_g}{K_BT}\right)^2 - 2.25\right\}\sqrt{E}\right]} \; ; \quad \boldsymbol{\Sigma} < 1.5 \qquad (3\text{-}15)$$

Where σ_g were used instead of σ to distinguished of σ_d in the next section. C is an empirical constant, which is expected to be dependent on the intersite hopping distance. Based on eq. 3-14 and eq. 3-15 the mobility and temperature dependence data can be used to determine the disorder parameters of σ_g, μ_o, Σ, and C. We discuss how this is done for one of our compounds in section 3.6.3.4.

3.4.4. Correlated Disorder Model (CDM)

As mentioned before the GDM model is the most important and comprehensive model to explain the charge transport in organic materials. However, it is not entirely accurate in accounting for all experimental data. For example it predicts a Poole-Frenkel dependence of the charge carrier mobility at only high electric field, higher than $3\text{x}10^5$ V/cm, while the experimental data show this behaviour down to electric field lower than 10^5V/cm[25,29,23,30]. Gartstein and Conwell argued in 1994 that the limitation of the GDM model came from the assumption that the energy sites are distributed independently with no correlations occurring over any length scales. They introduced a correlation between the energies of positionally close sites. For example this correlation can originate from a permanent charge dipole interaction with the spatially close sites. Based on the correlated media assumption, Novikov et al.[30,31] proposed the following empirical relation for the mobility dependence on the electric field and temperature.

$$\boldsymbol{\mu(E,T) = \mu_o \exp\left[-\left(\frac{3\sigma_d}{5K_BT}\right)^2\right] \exp\left[C\left\{\left(\frac{\sigma_d}{K_BT}\right)^{3/2} - \Gamma\right\}\sqrt{\frac{eRE}{\sigma_d}}\right]} \qquad (3\text{-}16)$$

where μ_o is the same as in GDM model and extracted in the same way. σ_d is the DOS width caused by the randomly positioned permanents dipoles. C was found to be 0.78 according to the Monte Carlo simulation by Novikov et al. assuming Γ to be 2. Γ characterizes the geometry disorder and depends on the transport site concentrations. A new term is introduced in CDM which is the intersite distance R. The extraction of the parameters is similar to the GDM model.

3.5. Mobility Measurement Technique (Time of Flight)

A number of experimental techniques has been developed to measure the charge carriers mobility, which can be divided in two groups[1,32,33], the electric transport methods such as time of flight (TOF), the space-charge-limited-current (SCLC), the field effect transistor (FET), the surface acoustic-electric travelling wave (SAW). The second group is the magnetic interaction methods such as Hall effect, magneto-resistance, and cyclotron resonance. Some of these techniques provide mobility data directly while others indirectly. These different techniques also provide different mobility results for the same material as a result of operating in different conditions such as the different carrier density, and the measurement direction. Therefore not all of these methods reflect the true intrinsic mobility.

3.5.1. Introduction

The time of flight (TOF) is a standard method for measuring the carrier mobility in materials with long dielectric relaxation times such as organic materials. It can be considered as the most conventional and successful experimental method for determining the mobility and studying charge transport phenomena. This technique has been developed and successfully applied to a wide range of crystalline and amorphous solids during the 1950s and 1960s. Kepler and LeBlanc were the first to apply this technique to organic materials in 1960.[34,35,20]

3.5.2. The Experiment Structure Terms and Conditions

The typical arrangement of the photocurrent TOF experiment is illustrated schematically in figure 3-14. Briefly, the principle of time of flight is based on applying a bias voltage to a sample sandwiched between two plate electrodes to get a uniform electric field, injecting charge carriers by photoexcitation which drift across the sample in a period of time known as transient time t_{tr} which can be measured from the extracted current in the external circuit.[3,35,20]

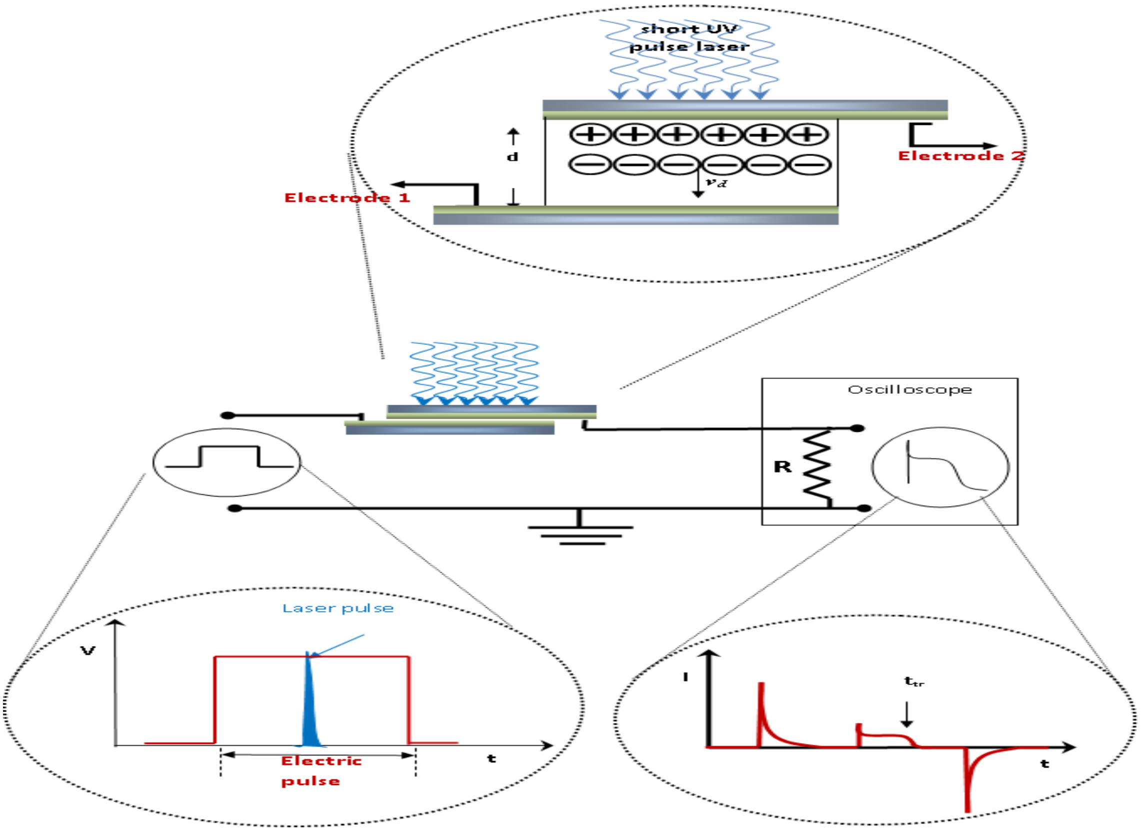

Figure 3-14: A typical experiment setup for TOF technique.

A sample of thickness d is placed between two electrodes; at least one of them needs to be semi-transparent for photoinjection. This is called the injection electrode, and the other one is the collecting or counter electrode. If a constant potential difference V is applied between the two electrodes they act as a parallel plate capacitor, where the charge Q builds up on the electrodes giving a capacitance of

$$\mathbf{C} = \frac{\mathbf{Q}}{\mathbf{V}} = \frac{\boldsymbol{\varepsilon\varepsilon_0}\mathbf{A}}{\mathbf{d}} \tag{3-17}$$

At this point and before the photoinjection using the pulse laser; the charge on each electrode is equal and opposite sign $Q_i = -Q_c$ creating a uniform electric field E between them of

$$\mathbf{E} = \frac{\mathbf{V}}{\mathbf{d}} \tag{3-18}$$

A sheet of charge carriers pairs is generated near the surface of the transparent electrode using a strongly absorbed pulse laser with short pulse duration t_{puls}, which should be much shorter than the carrier transit time ($t_{puls} << t_{tr}$) to ensure that all the transit occurs after the duration of the pulse. Also the laser wavelength is selected to ensure that light is absorbed in a thickness δ, which known as the penetration depth, much less than the sample thickness d ($\delta << d$). This guarantees that most of the charge carriers are generated close to the surface of the injection electrode and migrate across the sample freely.

The total photoinjected minority charge carriers, q, need to be much smaller than the capacitance charge of the sample, so $q << Q$. This condition is to keep a uniform electric field strength across the film, free from the effect of the injected charge. Violating this condition makes the electric field non-uniform and influenced by the space-charge. Also the transit of the drift current tail can become longer because of the attenuation of the travelling charge by the repulsion of the same charge causing an error in the transient time Δt as [36,37,4]

$$\frac{\Delta t}{t_{tr}} = \frac{q}{CV} \tag{3-19}$$

Under the influence of the applied electric field the generated electron-hole pairs split from each other, and according to the polarity of the electrodes, either electrons or holes are extracted immediately by reaching the exposed electrode. The opposite charge carrier drifts through the sample to the opposite electrode. As the carriers cross the sample to the counter electrode they generate a displacement current in the external circuit which can be recorded via a small resistance R in the external circuit. The time constant RC associated with the resistance R and the capacitance C is required to be much less than the transit time ($RC << t_{tr}$), which ensures the voltage source keeps the field across the sample constant and the drifting carrier sheet induces a constant current I(t) in the external circuit. This mode is known as current (differential) mode[37,20]. In the case of RC > t_{tr} the mode is known as voltage (integration) mode which will not be discussed as it is not part of our work.

3.5.3. Transient Current and Transient Time

In the ideal case where the charge carriers are assumed to move within the material with no distortion, the sheet of photoexited charge carrier pairs $(+q-q)$ is generated within an infinitesimal time close to the injecting electrode. Each pair of charge carriers splits into its components under the influence of the applied electric field E. The photocarriers with an opposite charge to the injection electrode are extracted immediately changing the injection electrode charge from Q_i to Q_i-q. The charge carriers of same sign as the injection electrode drift as a sheet moving together towards the counter electrode under the influence of the uniform electric field E with a constant drift velocity v_d until it reach the counter electrode at the time t_{tr} so

$$\mathbf{v_d}=\frac{\mathbf{d}}{\mathbf{t_{tr}}} \tag{3-20}$$

The charge of the electrodes changes with time. At the injection time $(t=0)$ the charge at the injection electrode is Q_i-q and at the counter electrode is Q_c. Within the period between $t=0$ to $t=t_{tr}$ the two electrodes try to reach the equilibrium so the charges move gradually in the external circuit between them creating a constant current I which has a flat plateau shape on the current time graph ($\frac{dI}{dt}=0$) and in the same time, the charge within the sample also moves to the counter electrode. At $t=t_{tr}$ the charges have completely moved; the charges on the injection electrode and counter electrode change to Q_i and Q_c+q respectively. When the charge sheet within the sample reaches the counter electrode, the oppositely charged carriers meet and recombine, so the current drops immediately to zero as shown in figure 3-15(a).

Therefore the transit time t_{tr} is considered as the time matching to the offset of the current.

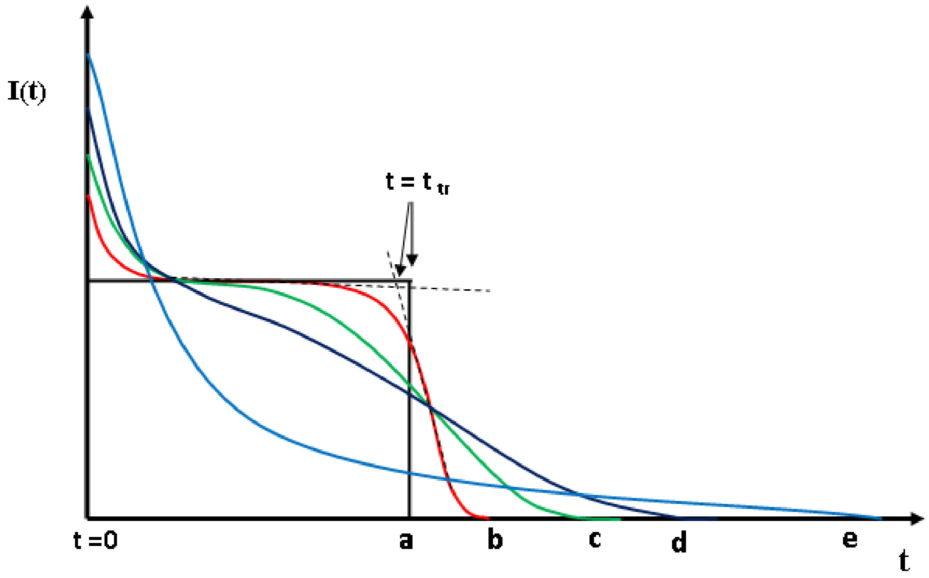

Figure 3-15 The transient current shape measured with TOF, where (a) is the ideal transient showing its transient time t_{tr} ; (b-e) transients deviated from the ideal shape as a result of the dispersivity of the material.

Using eq.(3-4), eq.(3-18) and eq.(3-20) we can relate the mobility μ to the transit time as

$$\mu = \frac{d^2}{V.t_{tr}} \tag{3-21}$$

The ideal case and the cases where we still observe the constant current characteristic plateau with a sharp drop in current representing the transit time t_{tr} are considered as non-dispersive transients as shown in figure 3-15(a,b) in this case the carrier moves with more or less constant drift velocity v_d across the sample[25].

As the disorder of the material increases by the presence of defect sources as explained in section (3-3-2), the constant current plateau begins to disappear and the photocurrent tail broadens gradually as a function of the disorder resembling the exponential decay in the case of strong dispersion of the sample. There is no clear offset marking the transit time. Therefore, t_{tr} can only be determined by plotting the time variation of the photocurrent in a double logarithmic representation, the inflection point of the graph is an indication of the first arrival time of the carrier packet at the counter electrode. The transit time is measured by the intersection of the asymptotes of the straight lines before and after the inflection point as shown in figure 3-16.

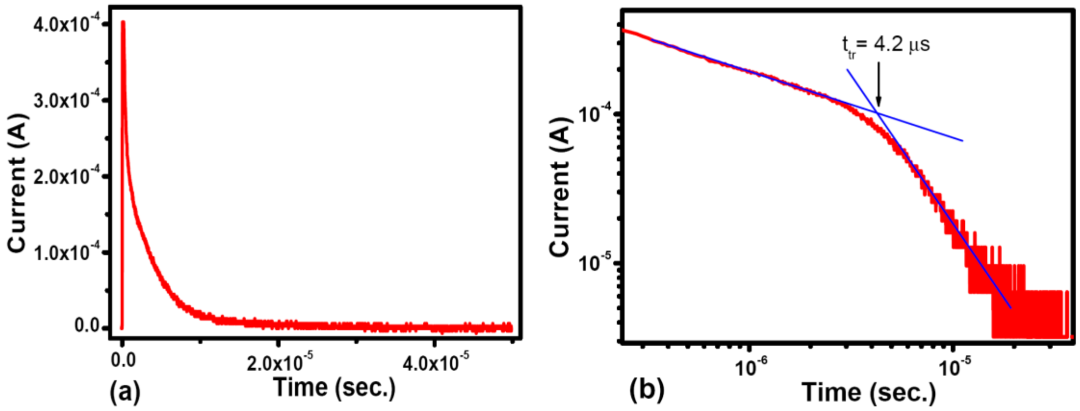

Figure 3-16: (a) The linear plot , (b) Double logarithmic plot showing the t_{tr} measurement of the dispersive photocurrent of compound 2.

3.5.4. Sample Preparation

Two types of samples were used for TOF: L.C. cells and spin coated thin films. The result of the two methods is different because of the different processing of the materials as it going to be shown in section 3.6.1.

3.5.4.1. Cells Method

3.5.4.1.1. Cell Preparation

Each cell consists of two (12x12mm) glass-ITO substrates. The ITO was etched using an acid etching technique to have an electrode of specific shape and small area as shown in figure 3-17. The electrodes have circular shape which is easily overlapped and to reduce the area of the electrodes in order to lower the RC time constant by reducing the capacitance (C) of the cell. The substrate surface is treated with plasma and cleaned before and after using detergent, water, acetone and Isopropanol.

Two substrates were glued together face to face with the two circular electrodes overlapping. The UV curable glue is mixed with spherical spacers of specific diameters (2, 3, 7µm). About one percent by volume of spacer to the glue was used in the mixture. If larger amounts of the spacers are used, the cell thickness between the two electrodes becomes uneven due to the possibility of double spacers. A very small amount of well mixed glue was applied to three sides of one glass-ITO substrate using a thin cleaned metal wire with a fine tip. The other substrate was gently rested on the glue as shown in figure 3-17.

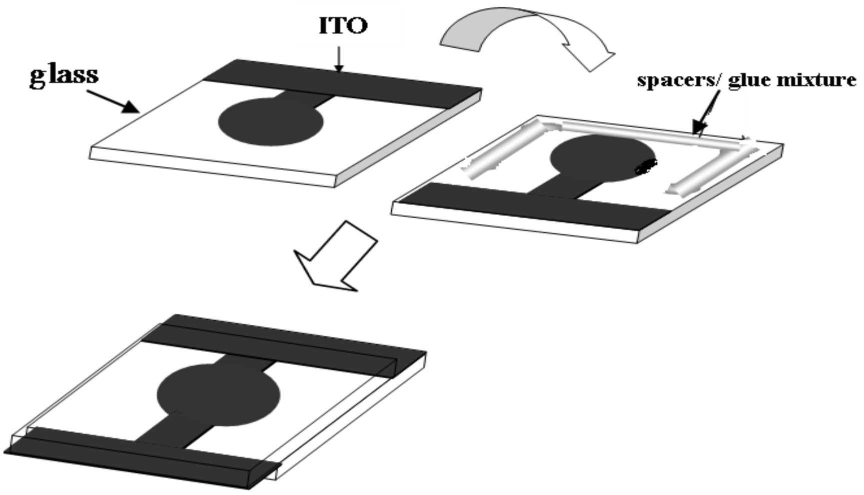

Figure 3-17: The cell Preparation process

The two substrates were held together at each side using metal clips, and then exposed to UV lamp for 15 minutes on each side of the cell. Glue was then used to seal the three sides of the cell perfectly, leaving one side open for the tilling.

3.5.4.1.2. Measuring the gap thickness of the cell

A normal cell consists of glass-ITO-air-ITO-glass. However for calculation of the cell’s gap we simplify this to be glass-air-glass as experiments have shown the difference in values obtained are within the measuring error confidence band. We used a simple white light interferometric method to obtain the cell gap (ITO to ITO). The light from a halogen lamp is coupled into one branch of a bifurcated, mixed optical fibre bundle, the composite end of which is positioned on top of and perpendicular to the cell. Light reflected from the cell is detected by an Ocean Optics spectrometer connected to the other branch of the fibre. Interference occurs between the two rays reflected from the upper glass-air interface and the lower air-glass interface of the cell gap illustrated in figure 3-18. Over the range of cells measured, the optical path difference is less than the coherence length of the white light source so a distinct interference pattern is observed. Rays C and D make no contribution as they are spatially incoherent due to relatively thick glass used in the cell (~1mm).

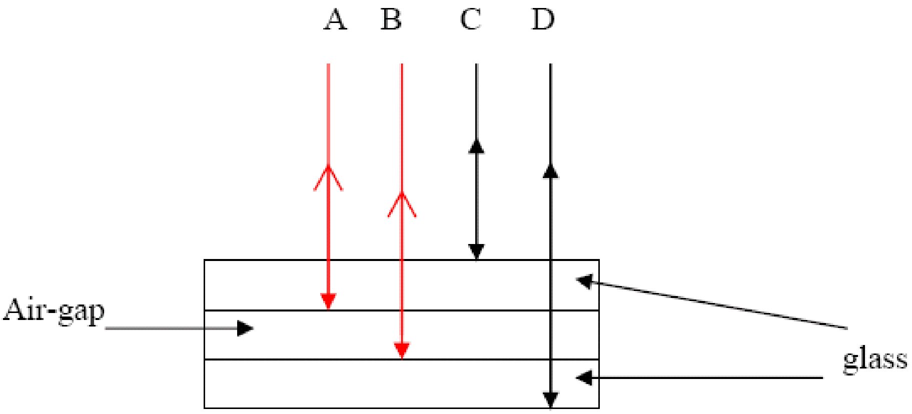

Figure 3-18 Ray diagram of incident and reflected light from a cell.

The cell gap can be obtained by calculation based on the periodicity of the wavelengths corresponding to maxima in reflected intensity. For a given peak A

$$\mathbf{n\lambda_n = 2n_o d} \tag{3-22}$$

where n is a positive integer, n_o is the refractive index of the air or any material filled in the gap, d is the thickness of the cell gap, λ is the wavelength of the light in vacuum. The m^{th} adjacent peak from peak A has wavelength λ_{m+n} ($\lambda_{m+n}<\lambda_n$) which given as

$$\mathbf{(m+n)\lambda_{m+n} = 2n_o d} \tag{3-23}$$

Therefore

$$\frac{m}{2n_o d} = \frac{1}{\lambda_{m+n}} - \frac{1}{\lambda_n} \tag{3-24}$$

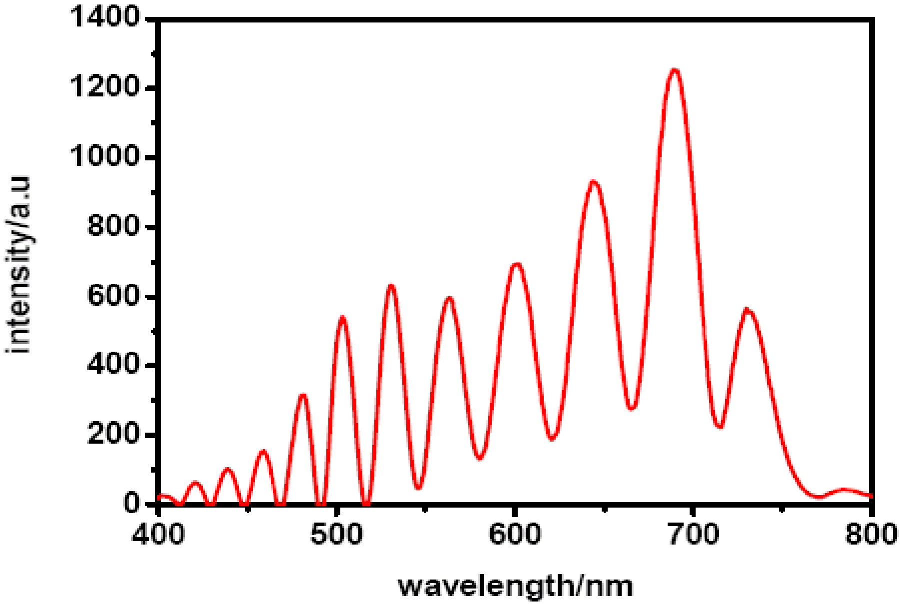

Figure 3-19 Typical interference patterns observed from the Ocean Optics.

Since the peak A at λ_n, can be chosen arbitrarily in an interference pattern, a programme is written to take the average value of d calculation using different peaks as starting points until all peaks are being considered. The program is written in Labtalk programming language under Origin 6.0. This method assumes that the variations of the Ocean Optics detector response with wavelength is insignificant compared with the variation of intensity of the fringes. A correction for these effects was made which confirmed that they are insignificant. Gordon Sowersby is thanked for writing the program.

3.5.4.1.3. The Cell Filling

The cell is placed on top of a controllable hot stage inside a vacuum chamber and the desired filling material is placed next to the opening of the cell. The chamber is evacuated and then flushed with nitrogen gas several times to ensure the nitrogen environment inside the chamber. It is finally evacuated to a pressure less than 0.1 torr. The temperature is elevated above the clearing point of the material which then becomes an isotropic liquid. The material spreads throughout the opening gap of the cell and flows into the cell under the influence of the capillary effect. After the material has filled at least one fifth of the cell, the vacuum chamber is flushed with nitrogen gas which provides pressure to completely fill the cell. The heater is turned off allowing it to cool down to room temperature at a material dependent rate. Any remaining compound is removed from the opening mechanically, and then carefully with an organic solvent to ensure the ITO is clean for contact. At this stage the sample is ready for the measurement using a special chamber with controllable hot stage and suitable contacts.

3.5.4.2. Spin coating method

3.5.4.2.1. Substrate preparation

Generally ITO coated glass (12x12mm, 13Ω/□) was used as the substrate. The substrates were cleaned following the general cleaning procedures mentioned elsewhere before acid etching, after acid etching, and after plasma treatment. Acid etching was done to remove about 2mm width from the ITO on the one side of the substrate in order to prevent short circuiting the device between the top aluminium electrode and the bottom ITO electrode. It also reduces the sample capacitance C via reducing the overlapping area of the electrodes as shown in figure 4-20.

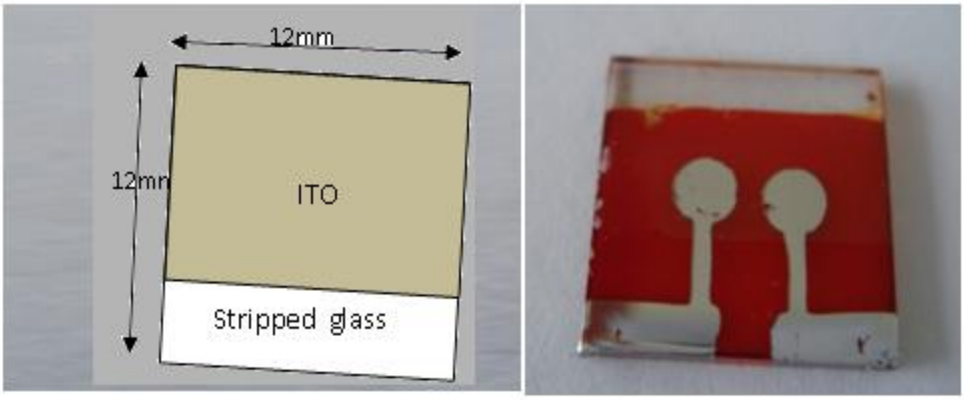

Figure 3-20: Photograph of a sample used for TOF measurement and drawing of the substrate showing the ITO on the glass.

3.5.4.2.2. Challenge and Development of Making Thick Film

A spin coating technique was developed to prepare samples because of the limitation of the cell technique, e.g. the components of blended samples do not fill the cell uniformly. Mobility measurements using TOF technique require samples of thickness larger than 1µm to fulfil the conditions of section 3.5.2 and to insure that the photocurrent is not created in the bulk of the sample. Therefore, the aim of this work was to obtain a thick film of ED and EA materials with a uniform smooth surface using the spin coating technique. Some challenges needed to be overcome. The film thickness was controlled with parameters such as the solution concentration, spin speed, and the evaporation speed which need to be balanced to get the optimum condition.

Firstly, a drop cast technique was used. The material was dissolved to a specific concentration in toluene and dropped on the substrate, leaving the solvent to evaporate. This is a good way to obtain a thick film. However the roughness of the film is very high, and was found to depend on the solvent evaporation rate of the sample controlled by fixing the temperature of the substrate. A wide range of substrate temperatures were used [110 °C, 100°C, 90 °C, 70 °C, 50 °C, 30 °C, RT] to control the evaporation rate. The roughness and uniformity of the film improved as the evaporation rate decreased (temperature go down). However, the film was still rough with room temperature solvent evaporation. Figure 3-21 shows an example of the surface profile for (50mg/ml) concentration of compound **2** in toluene and 70 ^{o}C evaporation temperatures obtained using the white light interferometer. The thickness of the film is 6.7 µm ±1.5 µm, and the surface is very rough with roughness RMS (Rq) of about 295nm.

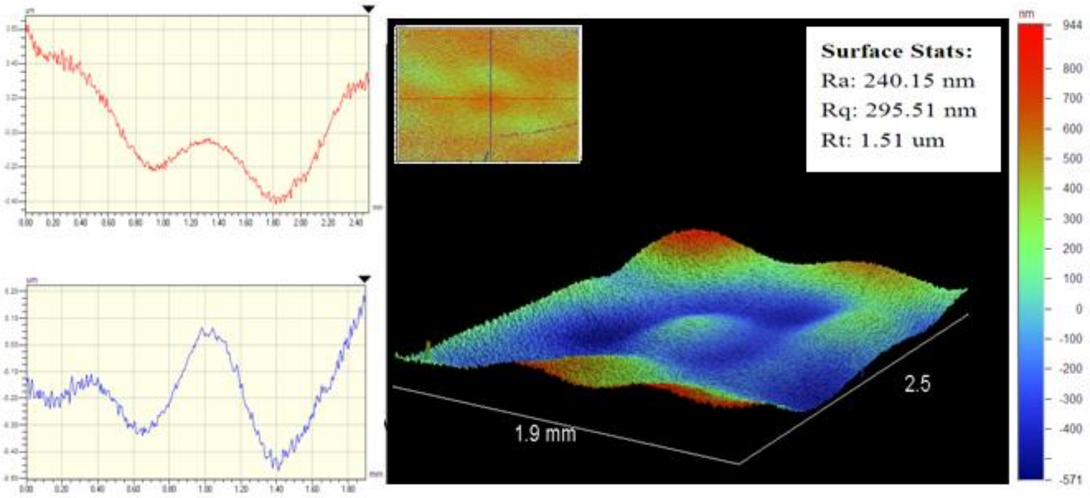

Figure 3-21: A white light interferometer surface profiling for thick film of compound 2 solvent evaporation was at 70^{o}C.

The concentration and the quantity of the drop cast solution was used to control the thickness of the film. The film become thicker as the concentration and quantity of the solution increases which is expected, however the surface remained rough.

Spin coating technique is the best way to produce smooth and uniform film, but the limitation of this technique is the film thickness is limited. The thickness increases with the decrease of the spin speed as shown in figure 3-22, up to a limit where the film roughness deteriorates as the spin speed goes down

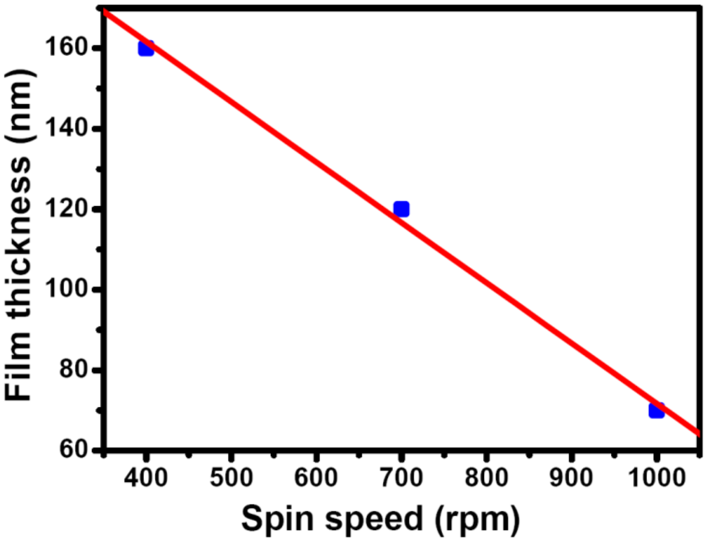

Figure 3-22: The film thickness of 17.5 mg/ml of compound 3 in toluene as function of the spin speed

Thicker films can be obtained using a higher solution concentration with the appropriate spin speed as shown in figure 3-23. Both films were spin coated from a toluene solution at a spin speed of 1000 rpm for 30s. The film thickness increased by a factor of ~2.3 to be 0.8 µm with doubling the concentration to 100mg/ml.

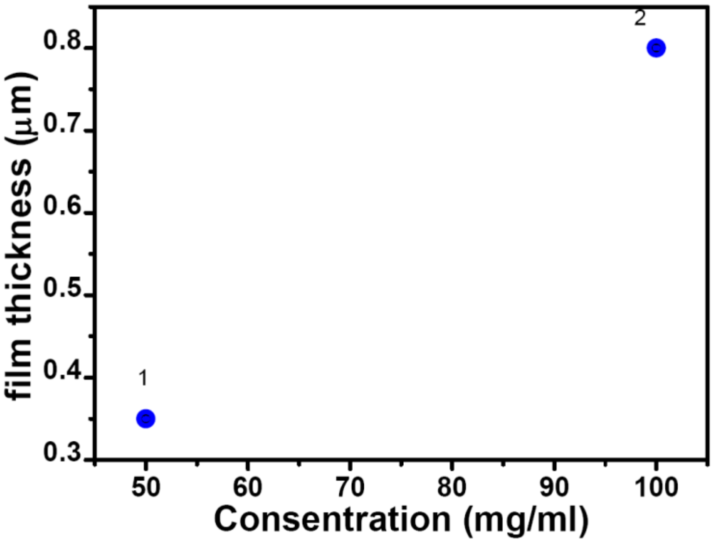

Figure 3-23: The effect of the solution concentration on the film thickness of compound 6 dissolved in toluene.

Increasing the concentration of the film is limited by the consumption of the material and the blocking of the filter. To overcome these constraints we increased the concentration of the solution by having a time period, the evaporation time, between the pouring of the solution onto the substrate and the spinning of it. There are two main advantages of having an evaporation time. The first one is that the concentration of the solution is increased which leads to an increase of the thickness up to 4 µm as shown in table 3-1 and figure 3-24. Secondly the film morphology is improved by giving the molecules longer time to arrange freely on the substrate

Table 3-1: The effect of the evaporation time on the solution concentration and consequently the film thickness of compound 2 in toluene.

sample	Material quantity (mg)	Solvent quantity (ml)	Solution initial concentration (mg/ml)	Evaporation time (min)	Spin speed (rpm)	Film thickness (µm)
1	15	0.1	100	0	1000	0.8
2	15	0.1	150	4	1000	1.7
3	20	0.1	200	3	1000	2
4	20	0.1	200	8	1000	4

However with these improvements of the film thickness some problems still need to be solved. First of all too much material (20mg) is still used. The filter gets blocked because of the high concentration. The evaporation speed is fast so that materials accumulate around the substrate. Finally the dust falls on the material from the surrounding environment during the evaporation period which can be seen in figure 3-24 as black spots.

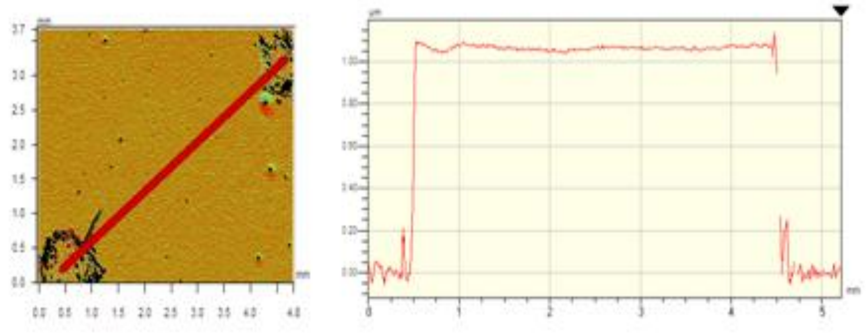

Figure 3-24: Surface profiling of thin film of 2 with a scratch marks to find its thickness of 1.05µm over 4mm, showing the uniformity of the film surface with some dust effects.

The sample was covered after pouring the solution on the substrate using a suitable sized beaker as shown in figure 3-25 to protect the sample and to make the environment solvent rich which slowed down the solvent evaporation, and so extended the evaporation time up to 45minutes. During this period the whole stage with the sample was tilted gently from time to time in each direction as illustrated to keep moving the solution on the substrate which prevented the accumulation of the material on the sides of the substrate

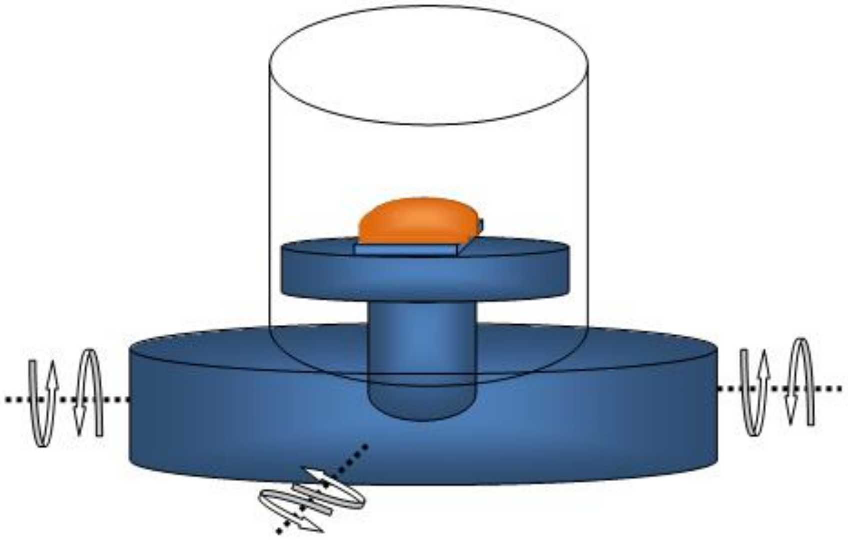

Figure 3-25: Drawing of spin coating stage showing the sample with the glass beaker cover.

In conclusion the conditions of making thick film vary slightly according to the physical property of the material, the substrate size, and the condition around the sample during the evaporation time. For optimum conditions, the solution concentration was about 10-20mg of the material - dependent on the material properties - dissolved in 0.2ml organic solvent, mostly toluene. The solution was dissolved very well and poured through a 0.2 µm filter onto the substrate on the spin coater stage, then covered by 250ml glass beaker for around 30 minutes, the spin speed was at 900rpm for 30s and acceleration of 590 r/m^2. The sample was kept under high vacuum over night to get rid of the trapped solvent. Because of the softness of the organic material, it is not recommended to dry a thick sample via annealing as the top surface becomes rough.

3.5.4.2.3. Deposition of to electrode

The spin-coated sample was then mounted above a shadow mask of two electrodes as shown in figure 3-20, inside the vacuum chamber ($<10^{-5}$mbar) for vapour deposition of the top electrodes. About 180nm thick Al was thermally evaporated onto the sample. All the sample fabrication was done in a nitrogen glovebox.

3.5.4.2.4. Measuring the film thickness

For the surface study and film thickness measurements the white light interferometer (Wyko NT1100) was used. A measurement sample is illustrated in figure 3-26. The instrument is a non-contact optical profiler, which uses two technologies to measure a wide range of surface heights. The phase-shift interferometry (PSI) mode is used to measure a smooth surface and small steps. The vertical scanning interferometry (VSI) mode measures rough surfaces and high steps up to several millimetres.

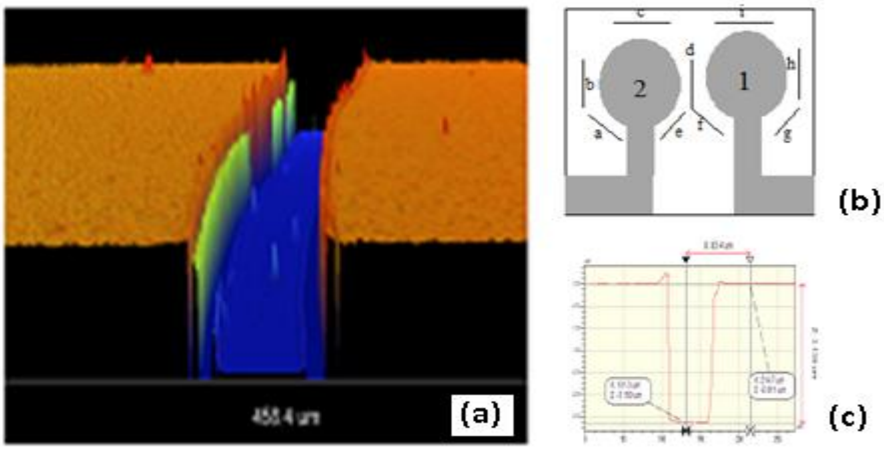

Figure 3-26: (a) A 3D white light interferometric profile of a thin film of compound 2 with a scratch mark to find its thickness of 3.2µm, (b) The positions of the various scratches around the electrodes, and (c) 2d profile of the scratch.

The sample was scratched several times around each electrode using a very fine needle as shown in figure 3-26(b). The measurements were averaged to find the mean and the standard error, which give an indication about the smoothness of the film around each electrode.

3.5.5. Experiment Setup

The instrumentation of TOF experiment is shown in figure 3-27 and consists of different instruments for different jobs.

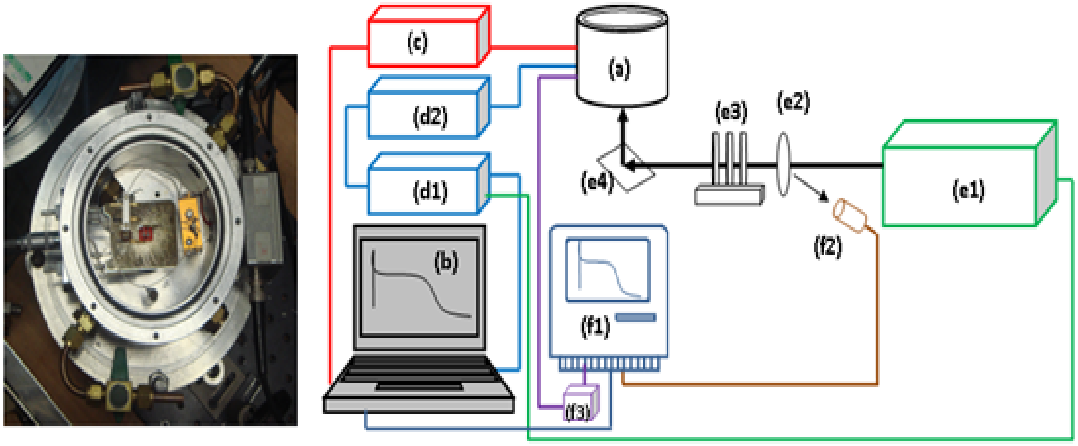

(i) (ii)

Figure 3-27: (i) photograph of the chamber showing the sample position on the hot stage. (ii) schematic diagram of the TOF experiment instrumentations showing the chamber (a), the computer with controlling program (b), the temperature controller (c), the function generator(d1), the amplifier (d2), the Nitrogen UV pulsed laser (e1), the laser beam alignment system of lens, neutral density filters and mirror (e2,e3,e4), the oscilloscope (f1), the avalanche photodiode (f2), the load resistance (f3).

A gas tight chamber (a) contains a heating stage with sample mount and positionable electrode contacts as shown in the image figure 3-27(i). A sample can be placed in the chamber either in an N_2 environment such as a glove-box or in a normal atmosphere then flushed out and filled with an inert gas via the two inlet/outlet pipes. A computer (b) with a Labview program controls the instrument and logs the data. The Linkam TP4 temperature controller (c) is used to set the temperature of the sample stage. A bias voltage controller consists of a waveform generator-Agilent 33120A (d1) and an amplifier (d2). A Laser Science Inc. VSL-337ND Nitrogen laser (e1) delivers a short pulse of 337nm wavelength and 6ns pulse duration. Lenses (e2) focus and steer the laser beam, whose intensity is controlled by (e3) neutral density filters. A mirror (e4) directs the laser beam onto the sample through a 0.049 cm^2 hole in the heating stage. The Tektronix TDS2012oscilloscope (f1) is connected to the sample via a switched load resistance and is triggered by an avalanche photodiode (APD) (f2) which is positioned to intercept some of the reflected laser beam. This trigger arrangement overcomes the uncertainty of the time lapse between the laser receiving a firing pulse and actually lasing.

Running the Labview program causes the following sequence of events to occur. The sample is first raised to the starting temperature after which the waveform generator-amplifier combination produces a number of positive bias voltage pulses which are applied to the sample. A firing pulse is also sent to the laser after a delay for the voltage across the sample to stabilize. The laser then fires and triggers the oscilloscope which collects and averages the current waveforms generated by the sample. This data is then stored on the computer and the pulse sequence is repeated with negative going pulse. For variable temperature scans the whole sequence is repeated with fixed temperature increments or decrements until the final temperature is achieved. Variable voltage fixed temperature scans are made in the same manner with the voltage changing between scan cycles. Provision is made for automatic or fixed setting of the oscilloscope vertical gain and also for the degree of signal averaging. Gordon Sowersby is thanked for setting up the control software.

3.6. Results and Discussion

3.6.1. Comparison of ToF Sample Preparation Methods

Two types of samples were used for TOF; L.C. cells and spin coated thin films as mentioned in section 3.5.4. The former one is recommended for the study of the single materials over the transition temperature range to show the variation of the mobility with temperature at the different phases. The second one is suggested for studying the materials in the same processing conditions of the devices which is not achievable with the other method such as the study of blend materials.

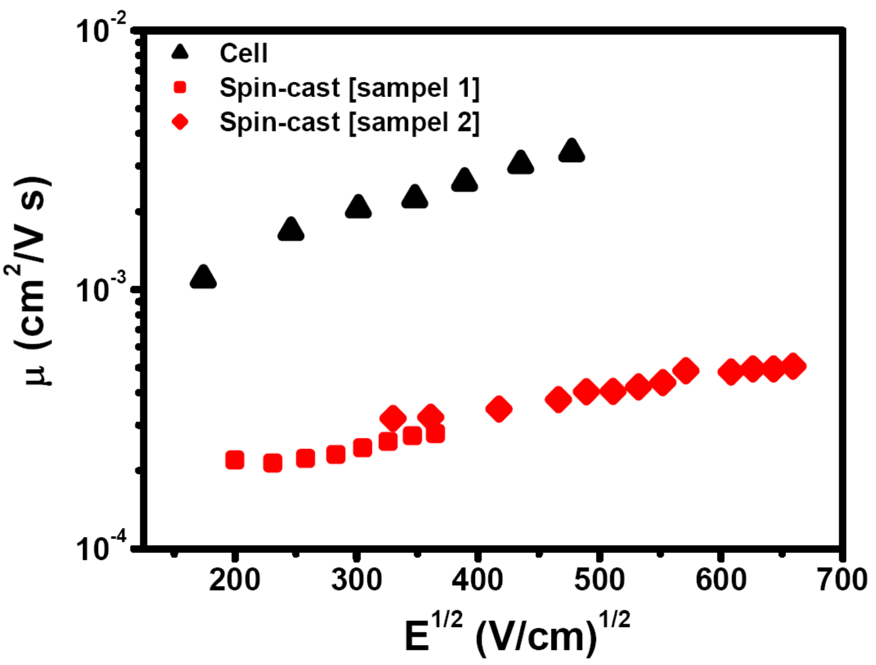

Figure 3-28: Hole mobility of compound 3 as function of electric field at room temperature using different sample preparation methods.

Figure 3-28 shows the room temperature mobility of samples of compound **3**, which were prepared using the two different preparation methods. The hole mobility using the cell configuration is significantly higher relative to the spin casting method, for example, at applied electric field of $1.1\text{x}10^5$ V/cm the mobility is $2.3\text{x}10^{-3}$ cm^2 V^{-1}s for cell method while for the spin casting it is $3.1\text{x}10^{-4}$ cm^2 V^{-1}s, which is about 7.5 times lower. This variation can be related to molecular order of the two samples; in the cell the sample is slowly cooled from the isotropic phase so it is more ordered than the spin cast sample which was not annealed to avoid thickness fluctuations[38].

The remaining samples discussed in this chapter use spin-cast method because of the need to have similar preparation methods for the mobility measurement and devices, and the difficulties of making well aligned cells.

3.6.2. Perylene Bisimide Derivatives as Electron Acceptor Materials

3.6.2.1. Introduction and Experimental Condition

One of the aims in the development of organic photonics and electronics is to meet the need for efficient n-type organic semiconductors i.e. electron acceptors characterized with high electron mobility and at the same time high electron affinity. These will lead to high efficiency devices such as OFETs, OLEDs and OPVs.

Perylene bisimide is one of the best known n-type organic semiconductors to date[39-43]. It exhibits excellent optical and electrochemical properties as shown in chapter two, together with outstanding chemical and photochemical stability. In addition some of Perylene bisimide derivatives show high electron mobility more than 0.1 $cm^2\ V^{-1}\ s^{-1}$ [44-51]. In the search for a new n-type organic semiconductors with good electronic properties and solution processability the chemistry branch of Organophotonics group in Hull university synthesized some novel Perylene bisimide derivatives with different functional groups linked at the two side imide group as illustrated in the previous chapter, it was hoped some of these compounds **9, 10, 11, 12, 13, 14, 15, 16** would be liquid crystalline aiming to improve the electron mobility.

In this section we study the charge transport mobility of these compounds aiming to correlate this result with the optical and electrochemical studies of chapter two to determine the usefulness of those derivatives as n-type semiconductor for use as electron acceptors for the organic solar cells which that will be discussed in the next chapters.

The TOF samples of these materials were prepared using the solution processing technique because of the difficulty in filling the cells due to the material characteristics. Depending on the chemical properties of the material we used different solvents, solvent quantities, material weight, and evaporation time as shown in table 3-2.

Table 3-2: The solution processing parameters and the film thickness of compounds 9, 11, 13, 15 and 16.

compound	solvent	Solvent quantity (ml)	Material quantity (mg)	Evaporation time (min)	Film thickness (µm)
9	toluene	0.15	11	25	0.9
11	toluene/chloroform	0.2/0.1	17	10	1.3
13	toluene	0.2	18	26	1.27
15	toluene	0.2	18	20	1.55
16	toluene/chloroform	0.1/0.1	17.6	10	1.87

For example we use toluene for compounds **9, 13** and **15** while for compounds **11** and **16** mixtures of toluene and chloroform were used with different ratios. Each solvent in the mixture is important to do a specific job. Toluene does not dissolve the compound very well but the chloroform does. However chloroform evaporates at a fast rate because of its low boiling point, so that toluene extends the evaporation time which is required for this technique. The amount of material used for each sample determines the sample thickness, as illustrated in the table 3-2. The quantity of compound **9** is small compared to the others because 18 mg of the material was originally used to make a film of reasonable thickness (~2.5µm) but resulted in the film having a number of cracks as shown in figure 3-29. Decreasing the quantity of the material helped create a thinner film with no cracks.

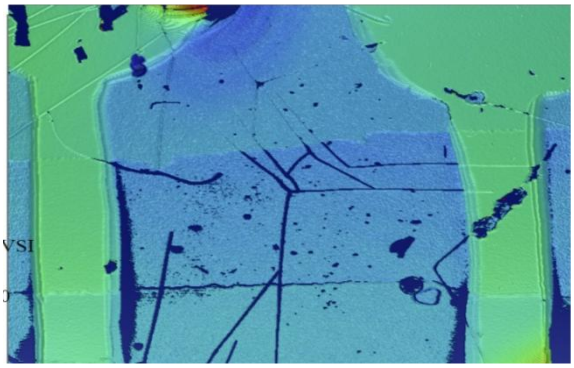

Figure 3-29: The cracks of compound 9 film as a result of the thickness of the film.

3.6.2.2. Applied Electric Field Mobility Dependence at Room Temperature

The perylene bisimide derivatives possess bipolar charge transport properties, which show transient photocurrents for electrons and holes as illustrated in figure 3-30 for compound **9** and appendix B for **11**, **13**, **15** and **16**. Compound **12** was very dispersive and there was no sign of the inflection to indicate the transit time.

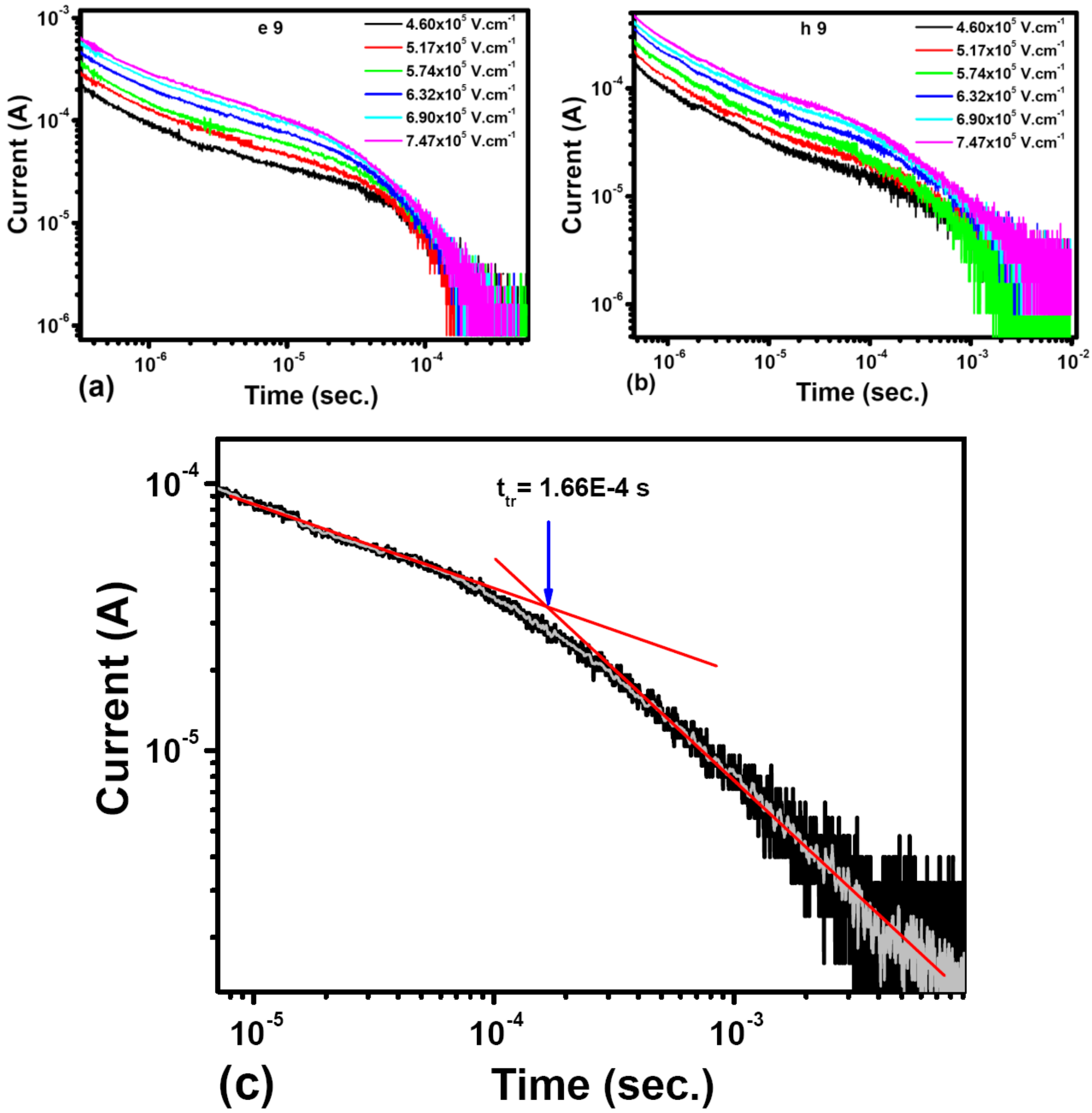

Figure 3-30: TOF photocurrent transients for a solution processed sample of compound 9 at room temperature with various applied electric field and fixed laser intensity, showing the variation of the transit time with applied electric field, where (a) is the electron photocurrent transient photocurrent, (b) the hole photocurrent transient photocurrent, (c) gives the hole photocurrent transient at applied electric field of 6.9 x10^5 V/cm showing the transit time measurements.

Figure 3-30(a,b) shows the electron and hole photocurrents of compound **9** at room temperature showing the variation of the photocurrent amplitude and transit time of both holes and electrons with applied electric field. Figure 3-30(c) shows an example of the double logarithmic transit time measurements of compound 9 at an applied field of 6.9 x10^5 V/cm.

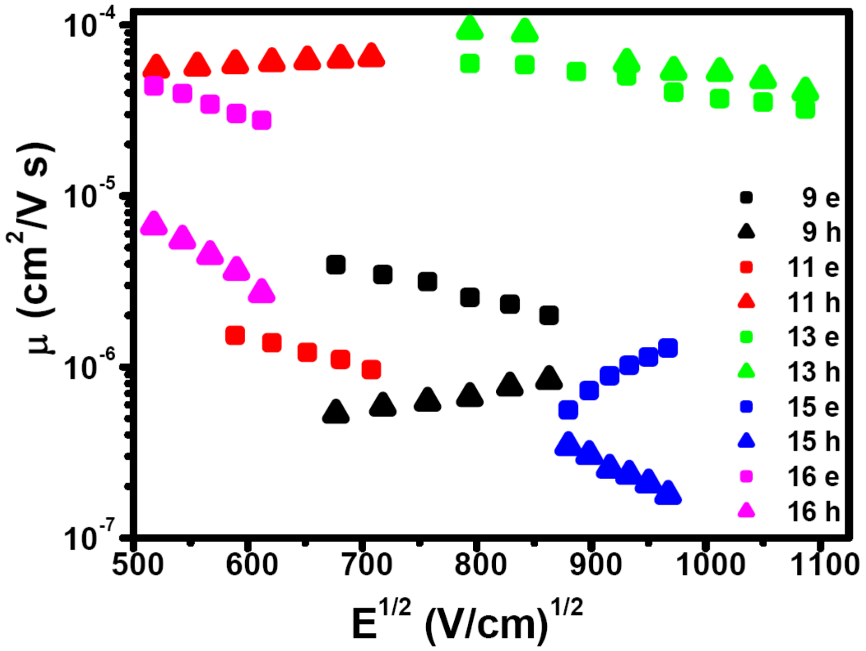

Figure 3-31: The variation of the electron and hole mobility as a function of the applied electric field at room temperature.

Figure 3-31 shows plots of the mobility versus the applied electric field for both electron and hole charge carriers for **9**,**11**,**13**,**15**, and **16** at room temperature. The variation of the electron and hole mobility with the applied electric field is different from one compound to another. The electron mobility of all compounds but one decreases with increased applied electric field. The hole mobility increases for compounds **9** and **11**. However for compound **15** the situation for both carriers is reversed, while for compounds **13** and **16** both electron and hole mobility decreases. The negative electric field dependence is explained in section 3.4.3 and occurs when the carrier following the favourable looped route at some time needs to hop against the field giving higher activation barriers with an increase of the field.

In the organic solar cell the EA material needs to be hole blocking and electron transporting, so we might expect that the electron mobility should be much higher than the hole mobility. The electron mobility is higher than the hole mobility for compound **9**, **15** and **16**. Compound **13** is ambipolar with almost equal electron and hole mobility, with hole transport probably occurring from the phenyl bifluorene groups on either side of the perylene. Compound **11** has two phenyl groups with a fluorene at both ends on the perylene and has a much higher hole mobility than the electron mobility.

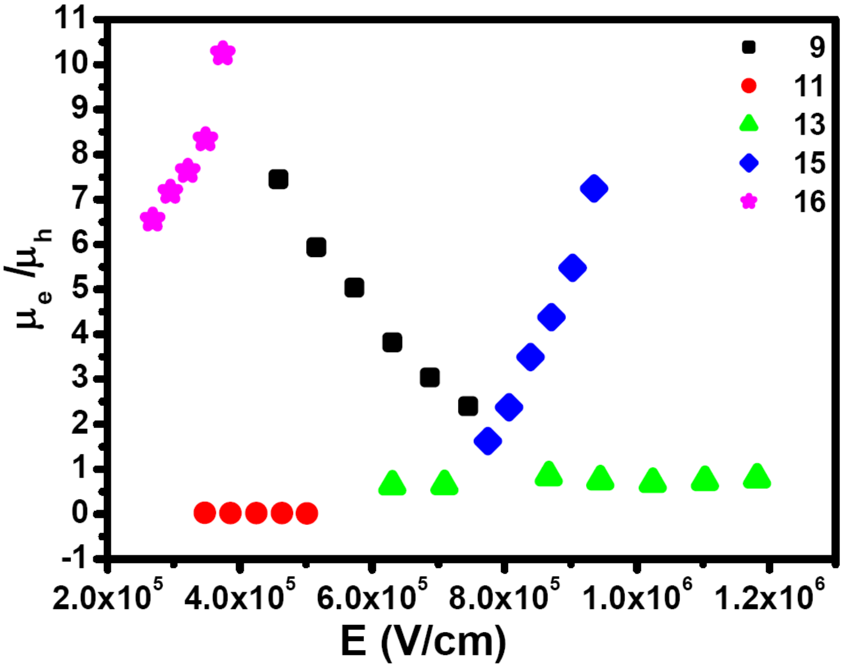

Figure 3-32: The relation between the electron/hole mobility ratio and the applied electric field.

Figure 3-32 shows the ratio of the electron mobility to the hole mobility (μ_e/μ_h) as a function of the applied electric field, which shows a very low variation for compounds **11** and **13**. The ratio increases with the increase of field for compounds **15** and **16**, while for compound **9** it showed an increase with a decrease of the field, which is an indication that this material is more efficient as n-type at low applied electric field – the range of the built in electric field of a photovoltaic (10^4-10^5V/cm)[52]. **16** also has a high ratio in the measurement range and so may also be a good candidate for the EA in a PV device.

3.6.2.3. Temperature Mobility Dependence with Fixed Applied Electric Field

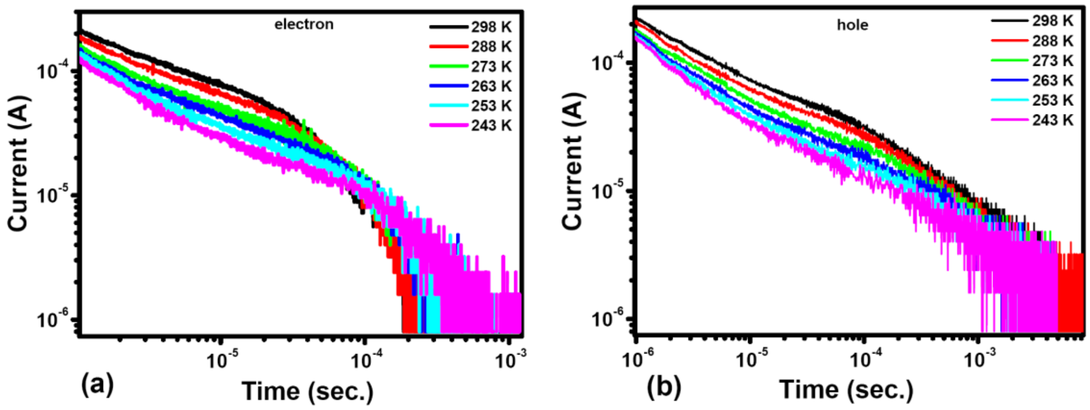

Figure 3-33: TOF transient photocurrent of compound 9 measured in 0.91µm thickness sample at different temperature and fixed applied electric field of 5.5x10^{5} V/cm,(a) electron photocurrent, (b) hole photocurrent.

Figure 3-33 shows the TOF photocurrent transients for a 0.9 µm thickness sample of compound **9** at a fixed applied electric field of 5.5x10^{5} V/cm and variable temperature for both electrons and holes. The photocurrent curves show clear temperature dependence with some variation between the electron and hole transients. The dispersion of the curve increases as the temperature goes down and it becomes more noisy, which indicates an increase in trapping because of the reduction in thermal energy. Also the temperature has a strong effect on the transit time, the electron and hole transit times increase from 4.34x10^{-5}s to 1.57x10^{-4}s and from 1.42x10^{-4}s to 5.76x10^{-4}s as the temperature reduce from 298 K to 243K respectively.

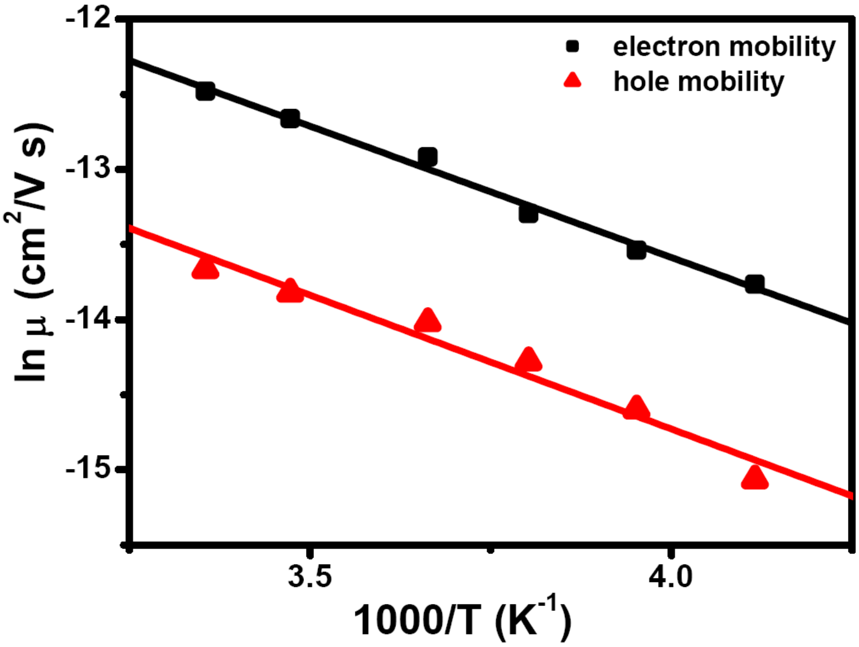

Figure 3-34: Temperature dependence of electron and hole mobility at fixed electric field of 5.5x10^5 V/cm.

Figure 3-34 shows the plot of the logarithm of the mobility versus the inverse temperature at fixed applied electric fields, where the lines indicate the best linear fit of the data. Following the Poole Frenkel model in section 3.4.1 the activation energy of the electrons and holes at the used applied electric field are 150 meV and 153 meV respectively. There is insufficient data for the more complete analysis discussed in section 3.6.3.3.

3.6.3. Liquid Crystals as Hole Transporting Materials

3.6.3.1. Introduction and Experimental Condition

The charge carrier mobility of the amorphous material is limited by molecular disorder to be in the order of 10^{-3} cm^{2}V^{-1}S^{-1} or less[53,54], which has a large influence on the organic devices performance. The discovery of the conjugated discotic and calamitic liquid crystal conductivity in 1993 and 1995 respectively helps to overcome this limitation with self-molecular alignment improving the mobility to be larger than 10^{-3} cm^{2}V^{-1}s^{-1} up to 0.1 cm^{2}V^{-1}s^{-1} [55].

Liquid crystal mesophases provide large self organized domains with highly ordered and close packed structures, which improve the intermolecular π orbitals overlapping, and support the hopping mechanism of the charge carrier between the closely spaced molecules (hopping sites). However the liquid crystals mesophases usually occur above room temperature. On cooling down to room temperature the large organized domains fragment to small polycrystalline domains separated by grain boundaries, which increase the charge trapping and attenuate the charge carrier mobility.

To retain the liquid crystals mesophase properties at room temperature reactive mesogens have been introduced[53,54,56]. These contain aromatic cores with semiconducting properties attached to two photoreactive polymerizable end groups via aliphatic spacers. The irradiation of thin films materials with UV light at the mesophase temperature cross-links the mesogens to form an insoluble crosslinked polymer network, which retains the molecular alignment on cooling. Some semiconducting reactive mesogens are nematic at room temperature. Other form nematic glasses on cooling from the nematic phase and can be cross-linked at room temperature. Smectic reactive mesogens have also been studied[53, 55].

The aim of this work is to study the effect of the reactive end groups with spacer on the charge carrier mobility, which show the dependence of the charge transport on the intermolecular separation. Compounds **1**, **2**, **3** and **4** are nematic glasses at room temperature with the same aromatic core but with different end groups as shown in table 2-1. Compound **1** has a methoxy end group, compound **2** has an alkoxy end group (-OC_8H_{17}), compound **3** and **4** have C_{10} alkoxy chain separating the aromatic core from the reactive end group, which is respectively a photoreactive diene-ester, and a photoreactive methyl methacrylate. Both of these can be photochemically polymerized to form a LC polymer network. These compounds show promising physical properties as donor materials for solar cells according to the cyclic voltammetry results in chapter two, as well as good chemical properties such as a good solubility in different organic solvents.

Table 3-3: The solution processing parameters and the film thickness of compounds 1,2,3,4.

compounds	solvent	Solvent quantity (ml)	Material quantity (mg)	Film thickness (µm)
1	toluene	0.15	15.3	3.67
2	toluene	0.2	16.3	1.5
3	toluene	0.15	20.3	3.75
4	toluene	0.15	12.5	1.69

The TOF samples of these materials were prepared using solution processing, where the processing conditions for each sample is illustrated in table 3-3. The common conditions for all these samples were the spin speed, acceleration, and time equal to 900rpm, 590 r/min^2 and 35s respectively. The evaporation time, the time between the pouring of the material on top of the substrate until starting the spin, is a key parameter because it is possible that the molecules arrange themselves in an efficient order because of the free movement in solution process for reasonable long time. The evaporation time varies from several minutes up to 40 minutes based on the surrounding environment such as the temperature.

3.6.3.2. Applied Electric Field Dependence at Room Temperature

Only hole transport was investigated for all these four compounds, because the electron photocurrent is suppressed, and seems to quench immediately after the photoexcitation, probably because of trapping[54].

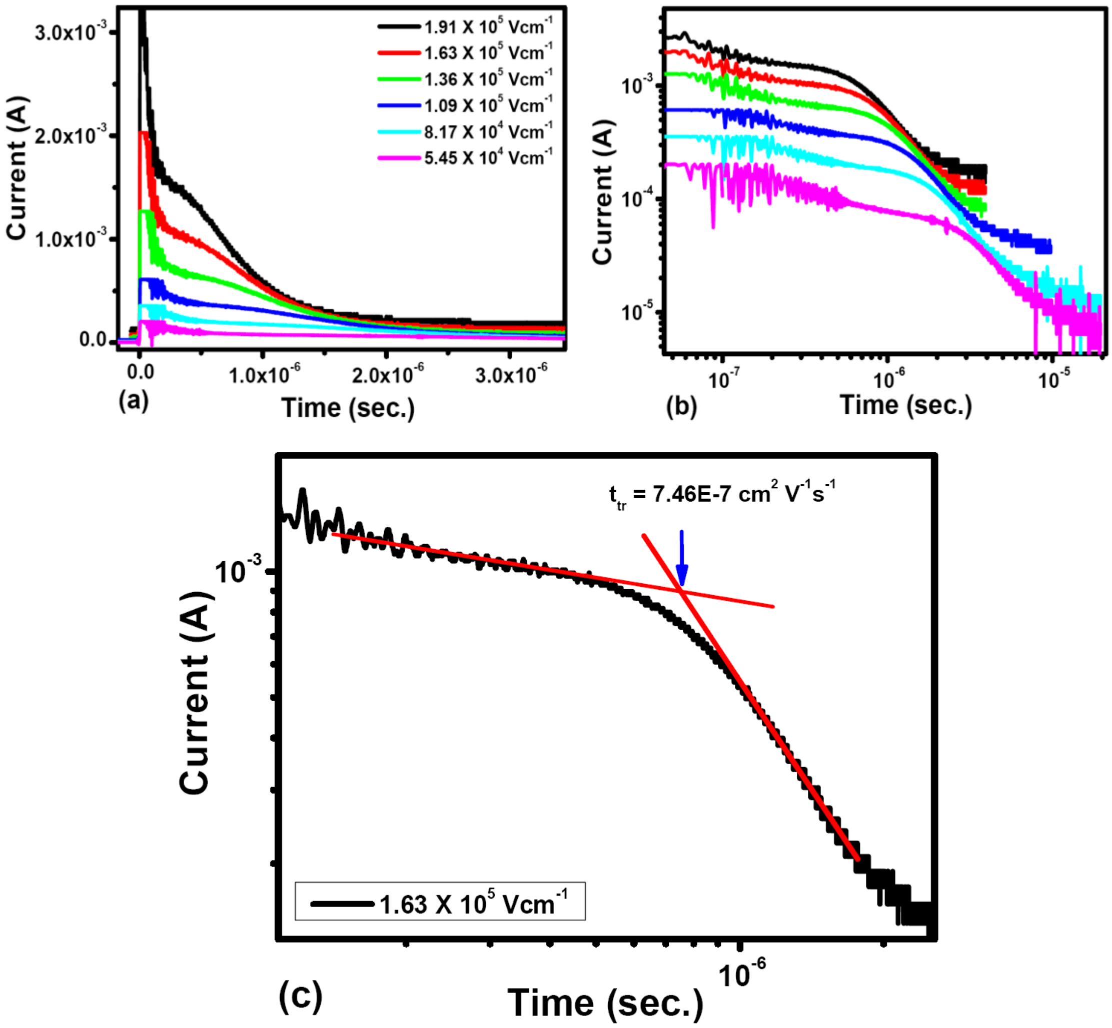

Figure 3-35: TOF hole transient photocurrent of compound 1 measured for 3.67µm thickness sample at different applied electric field and fixed temperature 328 K,(a) linear photocurrent plot, (b) double logarithmic photocurrent plot, (c) double logarithmic photocurrent plot at 1.63x10^{5} Vcm^{-1} showing the transient time measurement.

Figure 3-35(a,b) shows the linear and double logarithm plots of the hole photocurrents from a sample of thickness 3.67µm of compound **1** at temperature of 328 K with different applied electric field. The variation of the hole amplitude of the photocurrent and transit time is shown. Figure 3-35(c) illustrates an example of the transit time measurement from the inflection of the double logarithmic photocurrent curve, where the transit time decreases with the increase of the applied electric field.

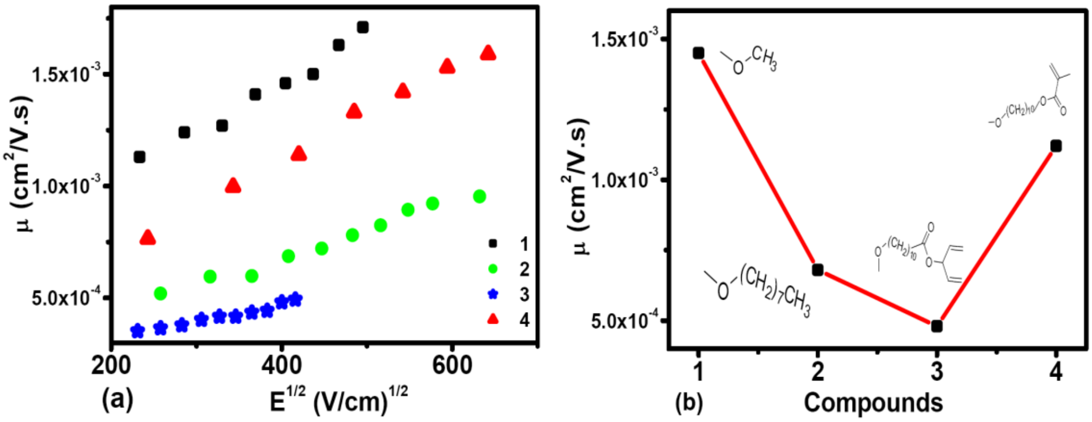

Figure 3-36: (a) The hole mobility for compounds 1, 2, 3, and 4 as a function of the applied electric field at room temperature. (b) The hole mobility of the compounds at room temperature and 1.6x10^{5} cmV^{-1} applied electric field.

Figure 3-36(a) shows plots of the hole mobility versus the square root of applied electric field at room temperature for compounds **1**, **2**, **3**, and **4**. The mobility of all these compounds increases with the applied electric field which agreed with Poole-Frenkel prediction ($\ln\mu\alpha\beta_{pf}E^{1/2}$).

Figure 3-36(b) shows the effect of the end group on the mobility. **1** has the simplest and shortest end group and shows the highest mobility, followed by **4** then **2** and the lowest one is **3.** In general, it has been shown that bulky end groups increases the intermolecular separation[57], which reduces the intermolecular π orbital overlapping as illustrated in figure 3-37. The end groups have different reductions of the mobility. The diene end group has the biggest effect because it has more bulky group which is expected to push the molecules apart because of the nematic order. This agrees with earlier work on smaller oligomers by Woon K.L. et al[58], and Baldwin R. J. et al[54].

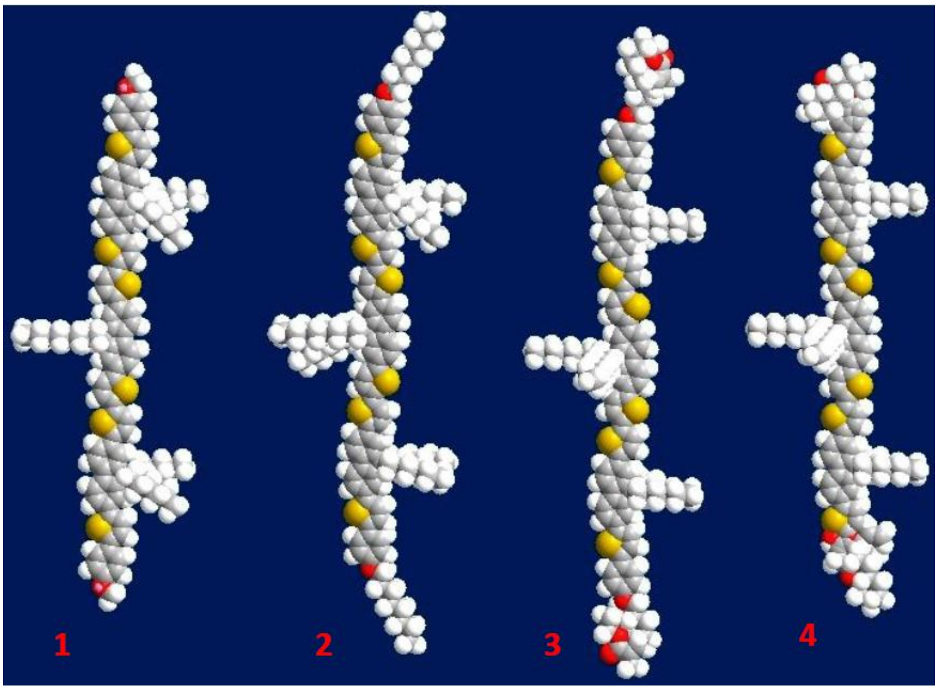

Figure 3-37: Illustration of conformation of compounds 1, 2, 3, and 4 obtained using MM2 optimization.

Figure 3-37 shows the depicted structures of compounds **1**, **2**, **3** and **4**, which are calculated by energy minimization using MM2 method on Chem-draw software. The calculations were carried out in the gas phase, where the intermolecular interaction was ignored. The global energy minimum is not guaranteed; therefore it may not represent the real structure of the molecules. However it gives an idea about the bulkiness of the diene end group of **3** relative to the methyl methacrylate group of **4**, also the alkyl chain in **2** extend more than the methyl methacrylate group of **4.** The structures show some agreement with the mobility measurements result.

3.6.3.3. Temperature Dependence of Mobility at Fixed Applied Electric Field

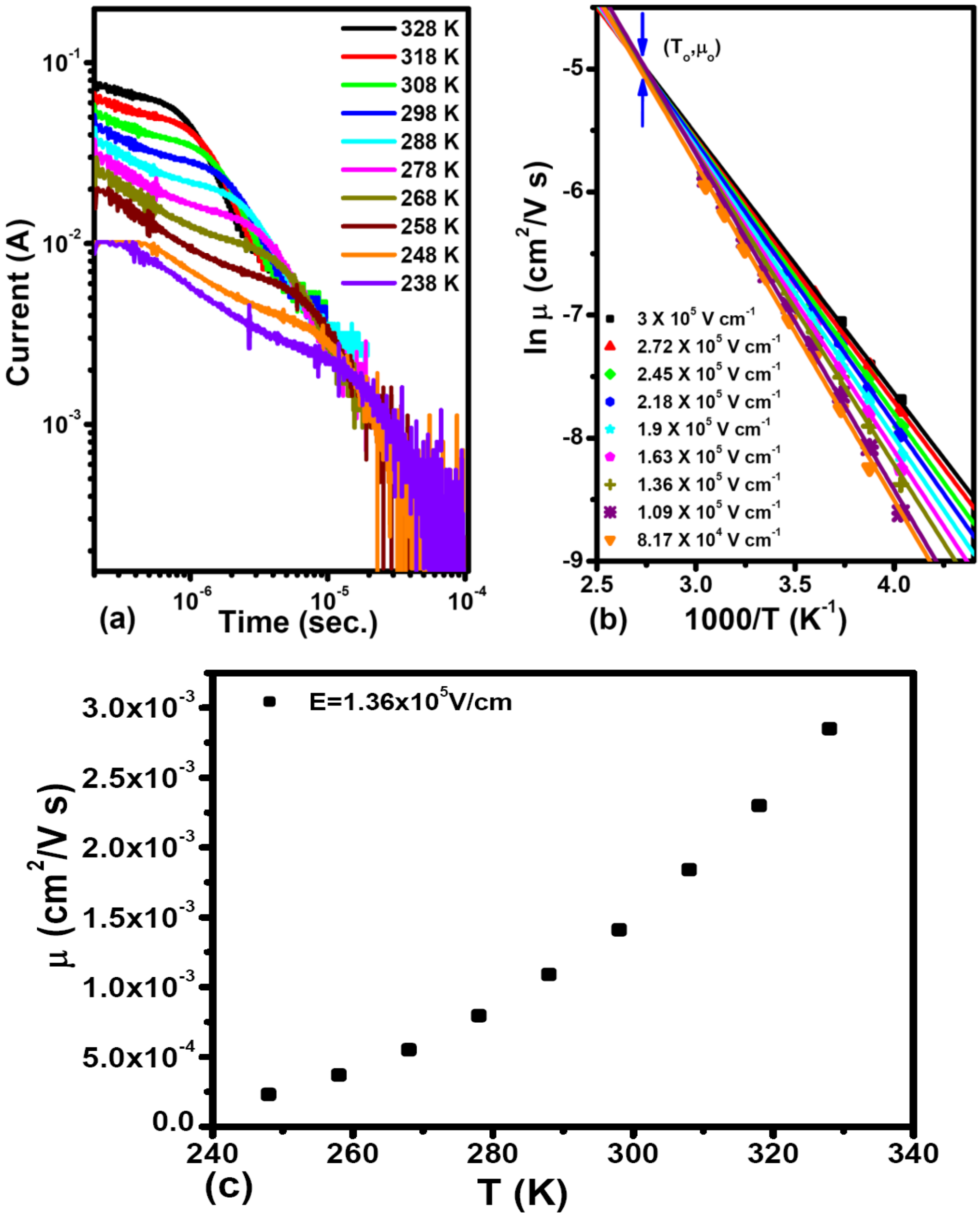

Figure 3-38: (a) TOF hole transient photocurrent of compound 1 measured with 3.67µm thick sample at different temperatures and a fixed applied field of 1.36x10^5 V.cm^{-1}, (b) Arrhenius plots of mobility of compound 1 for various applied electric fields. (c) The mobility variation with temperature at a fixed applied field of 1.36x10^5 V.cm^{-1}.

Figure 3-38(a) shows the hole transient photocurrent for a 3.67 µm thick sample of compound **1** at an applied electric field of 1.36x10^5 V/cm and variable temperature. The strong temperature effect on the photocurrent is very obvious with a shift toward higher current amplitudes and shorter transit times with the increase of the temperature. The hole transit time decreases from 1.76x10^{-5}s to 9.46x10^{-7}s as the temperature increases from 238 K to 328K and the photocurrent increases from 1.9 mA to 56 mA. Figure 3-38(c) show the variation of the mobility with temperature. The three figures indicate that hole transport in compound **1** is an activated process with an activation energy showing a hopping mechanism.

With the aim of measuring the activation energy of this material applying the Gill model given in section 3.4.2, we repeated the previous measurement at several applied electric fields. Arrhenius plots of the mobility at different applied electric field are shown in figure 3-38(b). The linear fits of the Arrhenius plots intercept at a common point which gives $T_o \approx 366$ K and $\mu_o \approx 6.75 \times 10^{-3}$ $cm^2V^{-1}s^{-1}$.

The slope of each Arrhenius plot at specific electric field gives the activation energy $E_{act}\,(1000K_B)^{-1}$at that field[59].

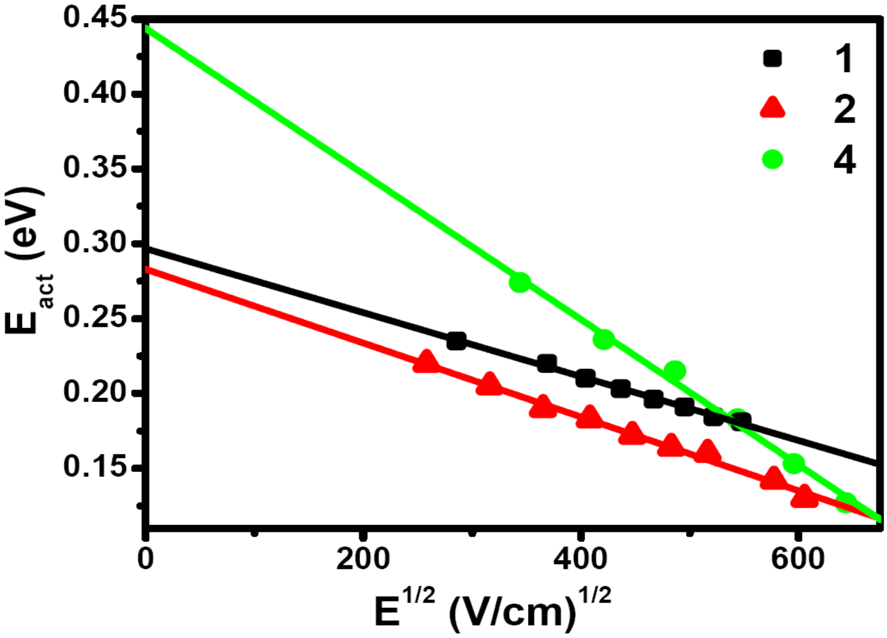

Figure 3-39: Gill model measurements of activation energy against the squared rout of applied electric field.

Figure 4-39 shows the plot of the activation energies against the square root of the applied field, where $E_{act} = E_o - \beta_{PF}E^{\frac{1}{2}}$. The zero field activation energy E_o where obtain from the intercept at zero field point and the Poole-Frenkel constant β_{PF} from the slope of the line. The Gill model parameters of all three compounds are extracted following the same method and tabulated in table 3-4.

Table 3-4: Gill model parameters of compounds 1, 2, and 4

compounds	1	2	4
E_o (eV)	0.297	0.283	0.444
β_{PF} (eV(V cm^{-1})$^{-1/2}$)	2.13 x10^{-4}	2.47x10^{-4}	4.86 x10^{-4}
T_o (K)	366	367	321
μ_o (cm^2 V^{-1} S^{-1})	6.75 x10^{-3}	2.45 x10^{-3}	2.4x10^{-3}

As explained before in section 3.4.1 the applied field influences charge carrier transport by lowering the barrier associated with their coulomb potential by $\beta_{PF}E^{1/2}$ in the electric field direction as shown in figure 3-6. This makes it easier for the charge carrier to be released from the localization centres supporting the hopping transport process. The activation energy of compound **4** is higher at zero field E_o than for the others but it shows a greater reduction with the applied electric field. Compound **1** is least affected by the electric field as shown by the lowest value of β_{PF}. The zero field activation energy of compound **1** is close to the P3HT of 0.29 eV measured by Mozir et al[59].

3.6.3.4. Disorder Model Analysis for Hole Transporting Reactive Mesogens

We use the Gaussian disorder model (GDM) and the correlated disorder model (CDM) in section 3.4.3 and section 3.4.4 to analyze the mobility measurements data of the four liquid crystals compounds. We aim to study the microscopic charge transport parameters of these materials and to investigate the effect of the end groups. The mobility measurement in section 3.6.3.1 was repeated at different temperatures and different applied electric fields for the four compounds.

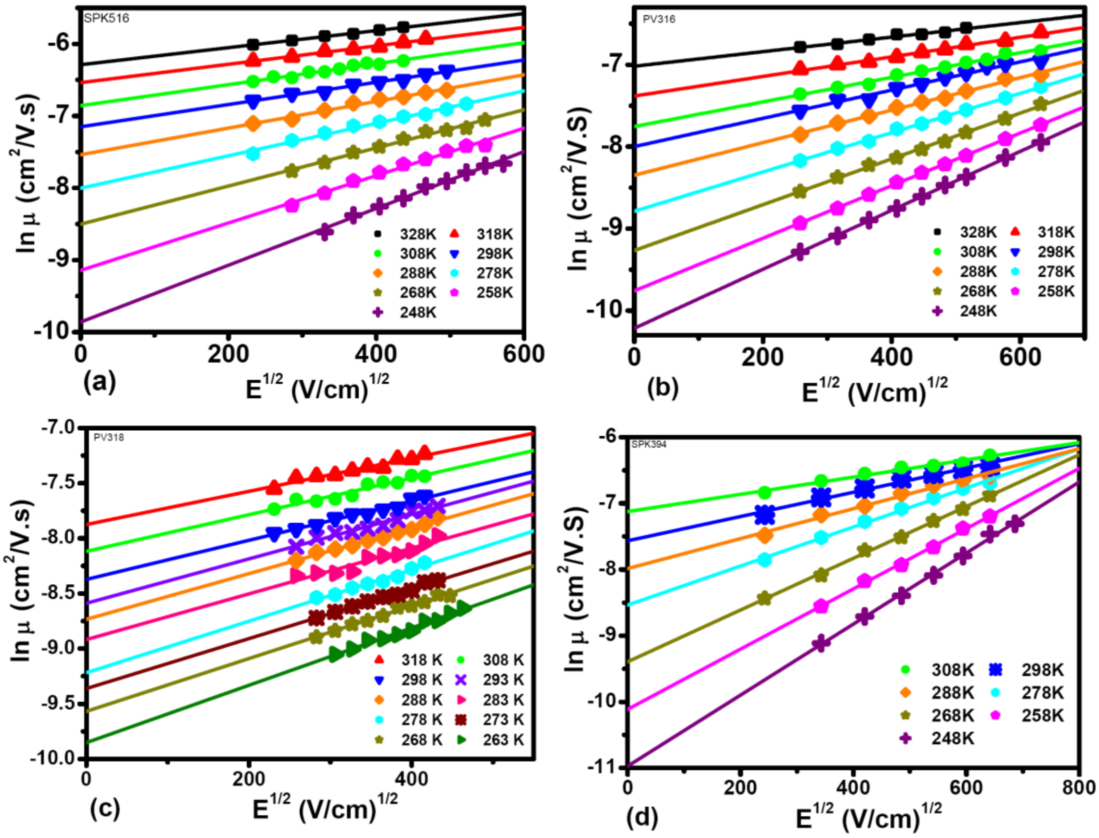

Figure 3-40: Electric field dependence of the mobility at different temperatures for compound 1 (a), compound 2 (b), compound 3 (c), and compound 4 (d).

Figure 3-40 shown the plot of the mobility versus the square root of the electric field follows the Poole–Frenkel-like behaviour with $\mu\ \alpha\ \beta_{PF} E^{1/2}$ with a positive slope β_{PF} at low temperature. As the temperature increases the slope decreases tending to become negative, as explained in section 3.4.3 by the Bässler model[24].

The zero field mobility at each temperature $\mu(E=0)]_T$ is obtained by extrapolating the linear fit of the field dependence of the mobility at each temperature as illustrated in figure 3-40 [25,26, 60]. At zero electric field eq. 3-14 and eq. 3-16 of the GDM and CDM models respectively become

$$\boldsymbol{\mu(0,T) = \mu_o\ exp\left[-\left(\frac{2\sigma_g}{3K_BT}\right)^2\right]} \tag{3-25}$$

$$\boldsymbol{\mu(0,T) = \mu_o\ exp\left[-\left(\frac{3\sigma_d}{5K_BT}\right)^2\right]} \tag{3-26}$$

Taking the logarithm of both sides gives

$$\boldsymbol{ln\,\mu(0,T)} = \left[-\left(\frac{2\sigma_g}{3K_B}\right)^2\right]\frac{1}{T^2} + \boldsymbol{ln\,\mu_o} \qquad (3\text{-}27)$$

$$\boldsymbol{ln\,\mu(0,T)} = \left[-\left(\frac{3\sigma_d}{5K_B}\right)^2\right]\frac{1}{T^2} + \boldsymbol{ln\,\mu_o} \qquad (3\text{-}28)$$

Plotting $\ln\mu(0,T)$ versus T^{-2} as shown in figure 3-41 gave the mobility prefactor μ_o from the intercept at $T^{-2} = 0$, and the energetic disorder parameters σ_g, σ_d of the slope of the fit based on eq. 3-27 and eq. 3-28.

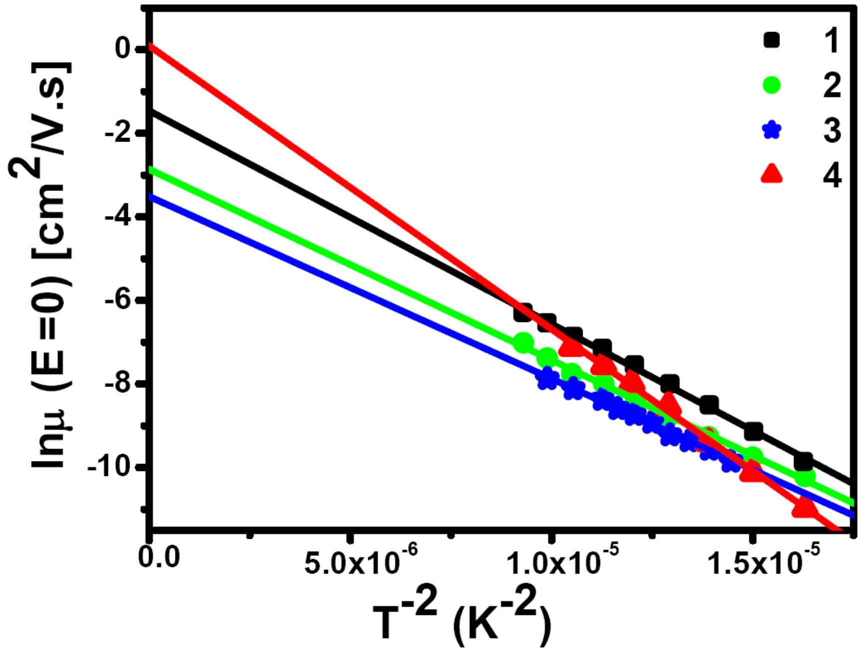

Figure 3-41: The temperature dependence of the zero field mobility gives the parameters μ_o, , σ_g and σ_d.

Figure 3-41 shows a linear relationship obtained for $ln\mu(E=0)$ versus T^{-2} for the four compounds as predicted in the GDM and CDM models. The mobility obtained for all the four compounds shows a good fit over a small temperature range of 248K to 328K. Published work on other materials shows deviation from linearity at low temperatures [59,61,25,62]. The low temperature deviation can be related to the transition of the charge transport from non-dispersive to dispersive at the deviation temperature [61,59]. Our lower temperature limit does not reach the deviation temperature.

Taking the logarithm of both sides of eq. 3-14 and eq. 3-16 gives

$$\boldsymbol{ln\,\mu(E,T) = ln\,\mu_o - \left(\frac{2\sigma_g}{3K_BT}\right)^2 + C\left\{\left(\frac{\sigma_g}{K_BT}\right)^2 - \Sigma^2\right\}\sqrt{E}} \tag{3-29}$$

$$\boldsymbol{ln\,\mu(E,T) = ln\,\mu_o - \left(\frac{3\sigma_d}{5K_BT}\right)^2 + C\left\{\left(\frac{\sigma_d}{K_BT}\right)^{3/2} - \Gamma\right\}\sqrt{\frac{eRE}{\sigma_d}}} \tag{3-30}$$

Taking the partial derivative of $\ln \mu(\mathrm{E}, T)$ with respect to $\sqrt{E}$ gives

$$\boldsymbol{\left.\frac{d\,ln\,\mu}{d\sqrt{E}}\right|_T = C\left(\frac{\sigma_g}{K_BT}\right)^2 - C\Sigma^2} \tag{3-31}$$

$$\boldsymbol{\left.\frac{d\,ln\,\mu}{d\sqrt{E}}\right|_T = C\left(\frac{\sigma_d}{K_BT}\right)^{3/2}\sqrt{\frac{eR}{\sigma_d}} - C\Gamma\sqrt{\frac{eR}{\sigma_d}}} \tag{3-32}$$

Eq. 3-31 and eq. 3-32 are used to estimate the positional and energetic parameters of GDM and CDM models as illustrated in figure 3-42.

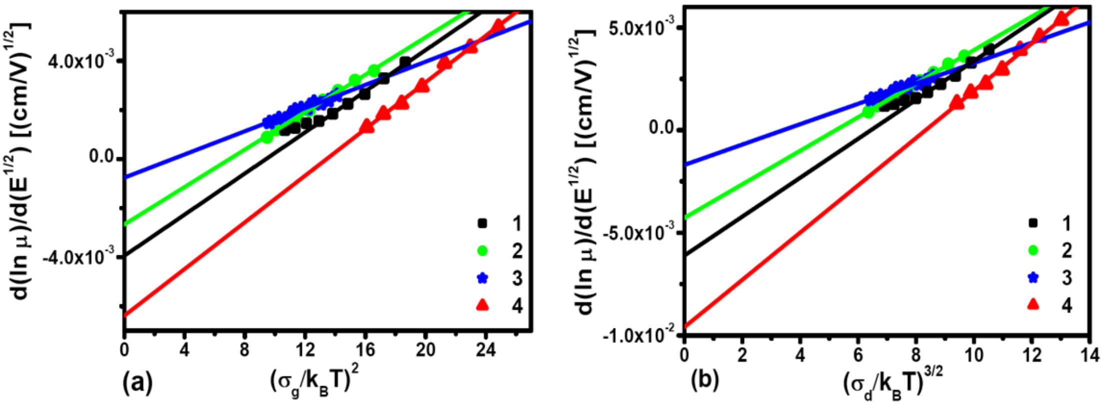

Figure 3-42: The field dependence gradients of the mobility versus, (a) the GDM model energetic disorder parameter $\boldsymbol{(\sigma_g/K_BT)^2}$, (b) the CDM model energetic disorder parameter $\boldsymbol{(\sigma_g/K_BT)^{3/2}}$

The positional disorder parameters Σ and C of the GDM model are extracted from the plot of the field dependence gradients of the mobility $\frac{d\ln\mu}{d\sqrt{E}}$ versus the energetic disorder parameter $(\sigma_g/K_BT)^2$ obtained from previous measurement as shown in figure 3-42(a). Similarly for the CDM model, the plot of the field dependence gradients of the mobility versus the energetic disorder parameter of $(\sigma_d/K_BT)^{3/2}$ is shown in figure 3-42(b). The positional disorder parameters Γ and R are extracted using 0.78 as the empirical constant C as mentioned in section 3.4.4.

The positional and energetic parameters relating to the two models are summarized in the table 3-5 for compounds **1- 4**.

Table 3-5: The GDM and CDM analysis parameters of compounds 1, 2, 3, and 4.

Compounds	Models	1	2	3	4
σ_g [meV]	GDM	92.3	87	85	106.5
C [(cm $V^2)^{1/2}$]		4.19 $\times 10^{-4}$	3.82×10^{-4}	2.36 $\times 10^{-4}$	4.76×10^{-4}
Σ		3.07	2.64	1.79	3.7
μ_o [$cm^2 V^{-1} s^{-1}$]	GDM/CDM	0.23	0.057	0.03	1.1
σ_d [meV]	CDM	102.6	97	95	118.3
R [nm]		1.57	1.06	0.38	2.57
Γ		6.44	5.22	3.4	8.34

The order of the mobility of the four compounds from highest is **1, 4**, **2** and **3**. All of the models' parameters decrease in the same sequence of compounds **4** > **1** > **2** > **3** showing a change in the order between **1** and **4**. However the parameters for compound **4** are all substantially higher than for the others.

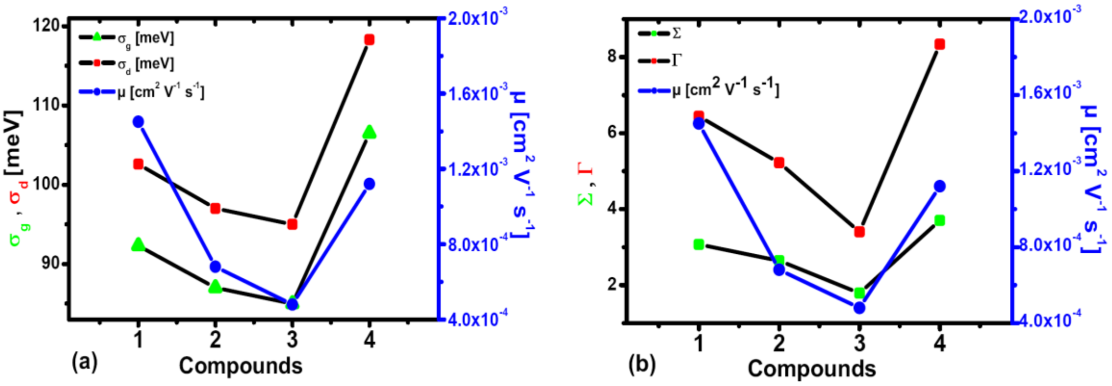

Figure 3-43: The variation of the energetic and positional parameters of GDM and CDM models (a) σ_g, σ_d , (b) Σ, Γ. The room temperature mobility is also shown.

Figure 3-43(a) shows the energetic parameters of the four compounds. The width of the Gaussian distribution of the energy sites correlates with the mobility. This is an unexpected result since a large distribution in energy site implies greater disorder. The positional disorder parameters correlate similarly with mobility. This is a more logical correlation since high positional disorder increases the chance of finding more loops for the charge to move through the material giving higher mobility. The zero field mobility μ_o follows the same sequence. We cannot explain why the parameters for compound **4** are anomalously high. This is related to the large value of μ_o obtained from figure 3-41for **4**. The disorder parameters must also be high since the mobility value of **4** is not correspondingly high over the temperature range measured. However, care must be taken when interpreting all these results because of the small field and temperature range used and the small variation of the mobility values.

3.6.4. Donor/Acceptor Blend Mobility Study

The active layer of the bulkheterojunction organic solar cells is a blend of donor-acceptor organic semiconductors as shown in chapter one. The charge transport within this layer is an important key factor for the optimization of the performance of organic solar cells

We choose compound **9** as our standard electron acceptor material. Compounds **1**, **2**, **3**, and **4** show good donor properties as discussed in chapter two and section 3.6.2 and section 3.6.3.

The TOF samples of these blends were prepared using the solution processing, where the common conditions for all samples are the solvent toluene and the spin speed, acceleration, and time which are 900rpm, 590 r/min^2 and 35s respectively. The processing conditions of each sample are illustrated in table 3-6.

Table 3-6: The solution processing parameters and the film thickness of the donor acceptors blends.

Blend compounds	Solvent quantity (ml)	Material quantity (mg/mg)	Evaporation time (min)	Film thickness (µm)	Laser intensity mJ/pulse [(µJ/cm2)/pulse]
2:9 (1:1)	0.3	8.1/8.1	45	1.5	4.94×10^{-4} [10]
2:9 (2:1)	0.2	10/5	30	2.1	4.94×10^{-4} [10]
3:9 (1:1)	0.2	7/7	30	0.98	5.93×10^{-4} [12]
4:9 (1:1)	0.2	8.7/8.7	30	3.49	5.93×10^{-4} [12]
4:9 (1:2)	0.2	5.2/10.4	27	2.14	5.93×10^{-4} [12]
4:9 (2:1)	0.2	12/6	31	2.55	4.61×10^{-4} [9.4]

The long evaporation time is important to support the phase separation of the two materials. The precipitation of the materials onto the ITO substrate is expected to be different based on the physical and chemical properties and the molecular weight of the materials. The laser intensity is controlled using neutral density filters before it hits the sample through a hole of area 0.049 cm^2 in the heating stage, which is considered to be the beam area. The striking thing about the laser intensity that it need to be reduced to very low values up to 9.4 ($\mu J.cm^{-2}$)/pulse to optimise the transient photocurrents. The average intensity used for TOF in blends is thirty, sixteen, fourteen and ten times less than the intensity used with the pristine compounds **9**,**3**, **2** and **4** respectively. This suggests that charge separation is significantly more efficient in blends.

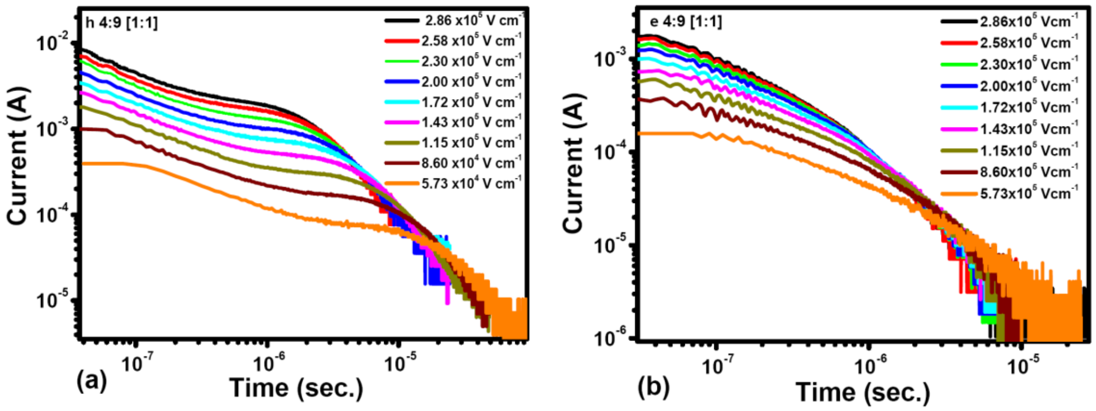

Figure 3-44: TOF hole photocurrent transients for blend of (1:1) ratio of compound 4 and 9 at room temperature and different applied electric field.

Figure 3-44 shows the hole and electron photocurrent transients of the blend of compound **4** as donor and compound **9** as acceptor in the ratio **1:1** at room temperature, it illustrates the strong applied electric field effect on photocurrent which increases in amplitude and decreases in transit time with an increase of field.

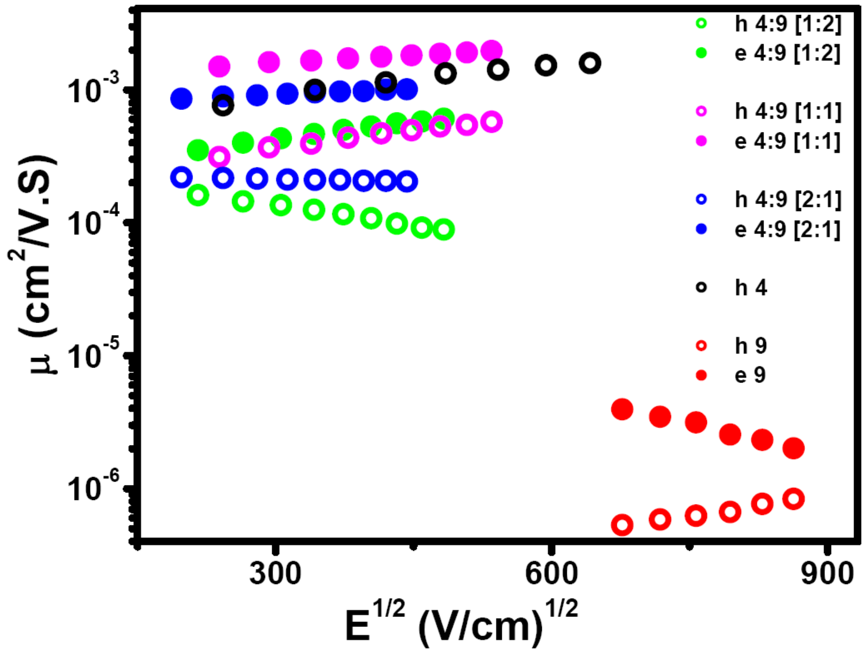

Figure 3-45: The electric field dependence of the mobility at room temperature for compound 4, and 9 and there blend with different ratio.

Figure 3-45 show the effect of the applied electric field on the mobility of the **4:9** blends with different ratios. In general, the electron mobility is higher than the hole mobility for all the ratios.

In relation to the pure donor/ acceptor materials, the hole mobility in blends is smaller than that of the pure donor and substantially larger than that of the pure acceptor. For example at 2x10^5 Vcm^{-1} applied field, the 1:1 blend hole mobility is about 4.84x10^{-4} $cm^2V^{-1}s^{-1}$, only 2.5 times smaller than the pure donor and about 1600 times bigger than that of the pure acceptor. The electron mobility in the blend is much greater than that of the acceptor, by about 200 times.

The ratio of the donor **4** to acceptor **9** has a strong effect on both the electron and hole mobility. The 1:1 ratio has the highest electron and hole mobility followed by 2:1 and then 1:2. The different blends show different variations of the hole and electron mobility with the field. The hole mobility of the pure compound **4** increases with the field, whilst for compound **9** there is a decrease of the electron mobility and an increase of the hole mobility with the field. For the 1:1 blend both electron and hole mobility increase with the field. Finally, for 1:2 and 2:1 ratios, the hole mobility decreases while the electron mobility increases with field.

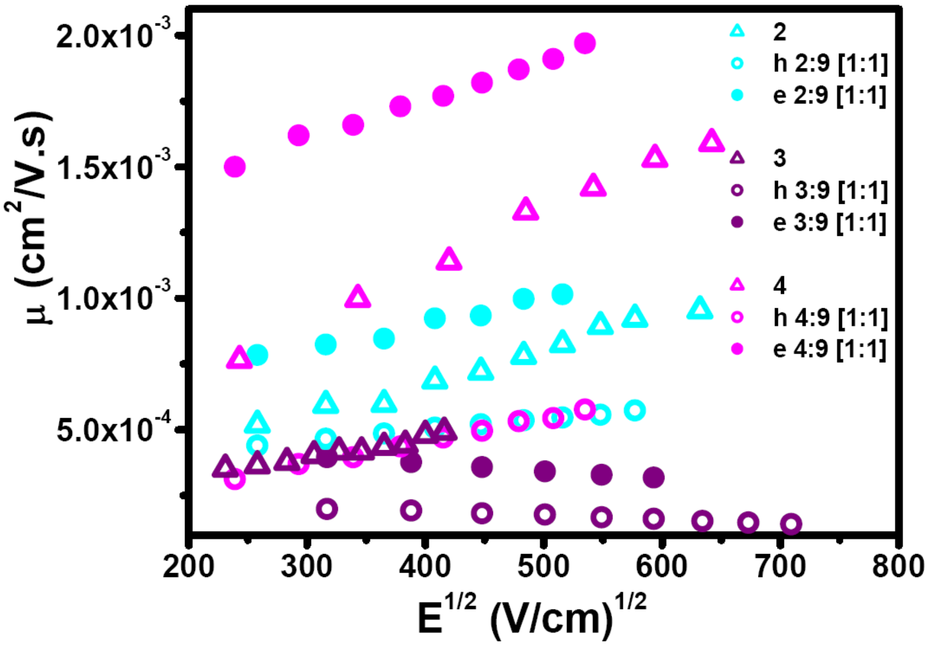

Figure 3-46: The electric field dependence of the mobility at room temperature for compound 2, 3, 4 and their 1:1 ratio blends with compound 9.

Figure 3-46 shows us the electric field dependence of mobility at room temperature for the blend of compound **2**, **3**, and **4** with **9** each with a 1:1 ratio. The field dependence of the hole mobility of the donor is also shown. The electron mobility of all blends is substantially higher than that of the pure acceptor and higher than the hole mobility of the same blend and the pure donor. As discussed earlier the hole mobility of all the blends is somewhat smaller than that of the pure donor.

The **4:9** blend has the highest electron and hole mobility followed by the **2:9** and finally the **3:9** blend. This follows the same arrangement of the pristine donors. The electron and hole mobility of the **4:9** and **2:9** blends show a positive field dependence whilst that of the **3:9** mixture has a small negative dependence.

3.7. Conclusion

TOF was the technique used to study the charge transport of organic semiconductors in this thesis. The samples were prepared in two different ways using the cell and spin casting. In the spin casting technique we did some optimisation to ensure a thick film with a flat and uniform surface.

We aimed to find good EDs and EAs to be used in the solar cells. Six of the perylene derivatives compounds were studied as EA materials, which are **9**, **11**, **12**, **13**, **15** and **16**. Compound **9** though not showing the highest electron mobility shows a good (μ_e/μ_h) ratio for low electric fields corresponding to the internal electric field of solar cell devices. Compound **16** also emerges as a promising EA. The other EAs contain donor-acceptor units and show ambipolar transport with hole mobility depending on the number of phenyl and fluorene groups attached to the perylene.

The effect of the reactive end group with spacer on the charge carrier mobility of EDs has been investigated. Results suggest that the mobility depends on the intermolecular separation. Four liquid crystal compounds **1**, **2**, **3** and **4** have been used. They form nematic glasses at room temperature with the same aromatic core but with different end groups. These compounds show promising hole transporting materials for solar cells. Compound **1** shows the highest mobility followed by **4**, **2** then **3**. Compounds **1** and **4** shows hole mobility $>10^{-3}cm^2V^{-1}s^{-1}$.

We applied the Gill model, to show that the mobility is an activated process, and the activation energy is field dependent, decreasing with increasing field. This supports the Poole-Frenkel model which describes the lowering of the potential barrier in the direction of the applied field making the hopping of the charge carriers easier.

We use the Gaussian disorder model (GDM) and the correlated disorder model (CDM) to analyze the mobility measurements data of the four liquid crystals compounds. The GDM and CDM model are applied to temperature and field dependent measurements. The aim was to study the microscopic charge transport parameters of these materials and to investigate the effect of the end groups on the charge mobility. Compounds **1**, **2** and **3** show correlation between the mobility measurements and the disorder parameters while compound **4** have anomalously high μ_o and disorder parameters.

Based on the need to correlate the charge transport of the ED/EA blend with PV devices, the electron and hole mobility were studied for blends of compound **9** as EA, and compounds **2**, **3**, and **4** as EDs with different ED: EA ratios. For all blends the hole mobility is lower than that of the pure ED. The electron mobility of the blends is 200 times higher than that of the pure EA. Possibly the acceptor morphology improves in the blend so that trapping is reduced. An alternative explanation is that the traps are saturated since the electron density is much higher in the blend than the pure acceptor.

The **4:9** blend gives the best mobility and the relatively small difference between electron and hole mobility is a promising feature for solar cells.

This result supports the cyclic voltammetry data in chapter which suggest **1**, **2**, **3**, and **4** as EDs and **9** as EA.

3.8. References

1 R. Farchioni and Giuseppe Grosso, *Organic electronic materials : conjugated polymers and low molecular weight organic solids*. (Springer, Berlin, 2001).

2 Charles Kittel, *Introduction to solid state physics*. (Wiley, New York ; Chichester, 1996), pp.xi, 673.

3 Sergei Baranovski, *Charge transport in disordered solids with applications in electronics*. (John Wiley, Chichester, 2006).

4 M. Pope and C. E. Swenberg, *Electronic processes in organic crystals and polymers*. (Oxford University Press, New York ; Oxford, 1999).

5 C. D. Dimitrakopoulos and D. J. Mascaro, "Organic thin-film transistors: A review of recent advances," IBM J. RES. & DEV. **45** (1), 11-27 (2001).

6 Jean-Pierre Colinge and C. A. Colinge, *Physics of semiconductor devices*. (Kluwer Academic, Boston, Mass. ; London, 2002), pp.xiii, 436 p.

7 Jasprit Singh, *Smart electronic materials : fundamentals and applications*. (Cambridge University Press, Cambridge, 2005), pp.xxii, 408 p.

8 Oana Diana Jurchescu, Molecular Organic Semiconductors for Electronic Devices, University of Groningen, 2006.

9 J. M. Marshall, "Carrier difusion in amorphous-seiconductors," Reports on Progress in Physics **46** (10), 1235-1282 (1983).

10 Wolfgang Brütting, *Physics of organic semiconductors*. (Wiley-VCH, Weinheim ; [Chichester], 2005), pp.xviii, 536 p.

11 J. Sworakowski, K. Janus, S. Nespurek et al., "Local states in organic materials: Charge transport and localization," IEEE Transactions on Dielectrics and Electrical Insulation **13** (5), 1001-1015 (2006).

12 T. P. Nguyen, "Defects in organic electronic devices," Physica Status Solidi a-Applications and Materials Science **205** (1), 162-166 (2008).

13 T. P. Nguyen, "Defect analysis in organic semiconductors," Materials Science in Semiconductor Processing **9** (1-3), 198-203 (2006).

14 N. I. Craciun, J. Wildeman, and P. W. M. Blom, "Universal arrhenius temperature activated charge transport in diodes from disordered organic semiconductors," Physical Review Letters **100** (5) (2008).

15 J. Frenkel, "On Pre-Breakdown Phenomena in Insulators and Electronic Semi-Conductors," Phys. Rev. **54** (8), 647 (1938).

16 S. D. Ganichev, E. Ziemann, W. Prettl et al., "Distinction between the Poole-Frenkel and tunneling models of electric-field-stimulated carrier emission from deep levels in semiconductors," Physical Review B **61** (15), 10361 (2000).

17 G. Pfister, "Hopping transport in a molecularly doped organic polymer," Physical Review B **16** (8), 3676 (1977).

18 John G. Simmons, "Poole-Frenkel Effect and Schottky Effect in Metal-Insulator-Metal Systems," Phys. Rev. **155** (3), 657 (1967).

19 L. B. Schein, A. Rosenberg, and S. L. Rice, "Hole transport in a molecular doped polymer: p-diethylaminobenzaldehyde-diphenyl hydrazone in polycarbonate," J. Appl. Phys. **60** (12), 4287-4292 (1986).

20 Paul M. Borsenberger and David S. Weiss, *Organic photoreceptors for xerography*. (Marcel Dekker, New York, 1998).

21 A.J. Mozer, Charge Transport and Recombination in Bulk Heterojunction Plastic Solar Cells Johannes Kepler University 2004.

22 W. D. Gill, "Drift mobilities in amorphous charge-transfer complexes of trinitrofluorenone and poly-n-vinylcarbazole," J. Appl. Phys. **43** (12), 5033-5040 (1972).

23 Guglielmo Lanzani, *Photophysics of molecular materials : from single molecules to single crystals*. (Wiley-VCH, Weinheim, 2006), pp.xvii, 583.

24 H. Bassler, "Charge transport in disordered organic photoconductors - A monte Carlo Simulation Study," Physica Status Solidi B-Basic Research **175** (1), 15-56 (1993).

25 T. Kreouzis, D. Poplavskyy, S. M. Tuladhar et al., "Temperature and field dependence of hole mobility in poly(9,9-dioctylfluorene)," Physical Review B **73** (23), 15 (2006).

26 R. U. A. Khan, D. Poplavskyy, T. Kreouzis et al., "Hole mobility within arylamine-containing polyfluorene copolymers: A time-of-flight transient-photocurrent study," Physical Review B **75** (3), 14 (2007).

27 A. Gadisa, Studies of Charge Transport and Energy Level in Solar Cells Based on Polymer/Fullerene Bulk Heterojunction, Linköping University, 2006.

28 A. Miller and E. Abrahams, "Impurity Conduction at Low Concentrations," Phys. Rev. **120** (3), 745 (1960).

29 S. V. Novikov, "Charge carrier transport in disordered organic matrices," Russian Journal of Electrochemistry **38** (2), 165-172 (2002).

30 S. V. Novikov, D. H. Dunlap, V. M. Kenkre et al., "Essential role of correlations in governing charge transport in disordered organic materials," Physical Review Letters **81** (20), 4472-4475 (1998).

31 S. V. Novikov and A. V. Vannikov, "Culster structure in the distribution of the electrostatic potential in a lattice of randomaly oriented dipoles.," Journal of Physical Chemistry **99** (40), 14573-14576 (1995).

32 N. Karl, "Charge carrier transport in organic semiconductors," SYNTHETIC METALS **133** (Sp. Iss. Sl), 649-657 (2003).

33 R. Dost, A. Das, and M. Gruel, "Time-of-flight mobility measurements in organic field-effect transistors," J. Appl. Phys. **104** (8) (2008).

34 R. G. Kepler, "Charge Carrier Production and Mobility in Anthracene Crystals," Phys. Rev. **119** (4), 1226 (1960).

35 B. Polischuk, S. O. Kasap, V. Aiyah et al., "The interrupted field time-of-flight transient photoconductivity technique for studying charge transport and trapping in high resistivity semiconductors" I. J. Electronics **76** (6), 1029-1041 (1994).

36 Evgenij Barsoukov and J. Ross Macdonald, *Impedance spectroscopy : theory, experiment, and applications*, 2nd ed. / edited by Evgenij Barsoukov, J. Ross Macdonald. ed. ([Chichester] : Wiley-Interscience, Hoboken, N.J., 2005), pp.xvii, 595 p.

37 J. Mort and D. M. Pai, *Photoconductivity and related phenomena*. (Elsevier, Oxf., 1976), p.0502p.

38 S. Droge, M. S. Al Khalifah, M. O'Neill et al., "Grazing Incidence X-ray Diffraction of a Photoaligned Nematic Semiconductor," Journal of Physical Chemistry B **113** (1), 49-53 (2009).

[39] F. Wurthner, "Perylene bisimide dyes as versatile building blocks for functional supramolecular architectures," Chemical Communications (14), 1564-1579 (2004).

[40] S. K. Lee, Y. B. Zu, A. Herrmann et al., "Electrochemistry, spectroscopy and electrogenerated chemiluminescence of perylene, terrylene, and quaterrylene diimides in aprotic solution," J. Am. Chem. Soc. **121** (14), 3513-3520 (1999).

[41] A. S. Lukas, Y. Y. Zhao, S. E. Miller et al., "Biomimetic electron transfer using low energy excited states: A green perylene-based analogue of chlorophyll a," J. Phys. Chem. B **106** (6), 1299-1306 (2002).

[42] M. J. Ahrens, M. J. Fuller, and M. R. Wasielewski, "Cyanated perylene-3,4-dicarboximides and perylene-3,4 : 9,10-bis(dicarboximide): Facile chromophoric oxidants for organic photonics and electronics," Chemistry of Materials **15** (14), 2684-2686 (2003).

[43] C. Li, J. Schoneboom, Z. H. Liu et al., "Rainbow Perylene Monoimides: Easy Control of Optical Properties," Chemistry-a European Journal **15** (4), 878-884 (2009).

[44] M. M. Ling, P. Erk, M. Gomez et al., "Air-stable n-channel organic semiconductors based on perylene diimide derivatives without strong electron withdrawing groups," Advanced Materials **19** (8), 1123-1127 (2007).

[45] B. Yoo, T. Jung, D. Basu et al., "High-mobility bottom-contact n-channel organic transistors and their use in complementary ring oscillators," Applied Physics Letters **88** (8) (2006).

[46] R. J. Chesterfield, J. C. McKeen, C. R. Newman et al., "Variable temperature film and contact resistance measurements on operating n-channel organic thin film transistors," J. Appl. Phys. **95** (11), 6396-6405 (2004).

[47] B. A. Jones, M. J. Ahrens, M. H. Yoon et al., "High-mobility air-stable n-type semiconductors with processing versatility: Dicyanoperylene-3,4 : 9,10-bis(dicarboximides)," Angewandte Chemie-International Edition **43** (46), 6363-6366 (2004).

[48] P. R. L. Malenfant, C. D. Dimitrakopoulos, J. D. Gelorme et al., "N-type organic thin-film transistor with high field-effect mobility based on a N,N-'-dialkyl-3,4,9,10-perylene tetracarboxylic diimide derivative," Applied Physics Letters **80** (14), 2517-2519 (2002).

[49] H. E. Katz, A. J. Lovinger, J. Johnson et al., "A soluble and air-stable organic semiconductor with high electron mobility," Nature **404** (6777), 478-481 (2000).

[50] P. Ranke, I. Bleyl, J. Simmerer et al., "Electroluminescence and electron transport in a perylene dye," Applied Physics Letters **71** (10), 1332-1334 (1997).

[51] C. W. Struijk, A. B. Sieval, J. E. J. Dakhorst et al., "Liquid crystalline perylene diimides: Architecture and charge carrier mobilities," J. Am. Chem. Soc. **122** (45), 11057-11066 (2000).

[52] H Hoppe, Johannes Kepler University Linz, 2004.

[53] M. O'Neill and S. M. Kelly, "Liquid crystals for charge transport, luminescence, and photonics," Advanced Materials **15** (14), 1135-1146 (2003).

[54] R. J. Baldwin, T. Kreouzis, M. Shkunov et al., "A comprehensive study of the effect of reactive end groups on the charge carrier transport within polymerized and nonpolymerized liquid crystals," J. Appl. Phys. **101** (2), 10 (2007).

[55] M. Funahashi and J. Hanna, "Impurity effect on charge carrier transport in smectic liquid crystals," Chemical Physics Letters **397** (4-6), 319-323 (2004).

[56] I. McCulloch, W. M. Zhang, M. Heeney et al., "Polymerisable liquid crystalline organic semiconductors and their fabrication in organic field effect transistors," Journal of Materials Chemistry **13** (10), 2436-2444 (2003).

[57] K. L. Woon, M. P. Aldred, P. Vlachos et al., "Electronic Charge Transport in Extended Nematic Liquid Crystals," Chemistry of Materials **18**, 2311-2317 (2006).

[58] K. L. Woon, M. P. Aldred, P. Vlachos et al., "Electronic charge transport in extended nematic liquid crystals," Chemistry of Materials **18** (9), 2311-2317 (2006).

[59] A. J. Mozer and N. S. Sariciftci, "Negative electric field dependence of charge carrier drift mobility in conjugated, semiconducting polymers," Chemical Physics Letters **389** (4-6), 438-442 (2004).

[60] H. Iino, J. Hanna, R. J. Bushby et al., "Hopping conduction in the columnar liquid crystal phase of a dipolar discogen," J. Appl. Phys. **100** (4), 4 (2006).

[61] Attila J. Mozer, Niyazi Serdar Sariciftci, Almantas Pivrikas et al., "Charge carrier mobility in regioregular poly(3-hexylthiophene) probed by transient conductivity techniques: A comparative study," Physical Review B **71** (3), 035214 (2005).

[62] S. Gambino, I. D. W. Samuel, H. Barcena et al., "Electric field and temperature dependence of the hole mobility in a bis-fluorene cored dendrimer," Organic Electronics **9** (2), 220-226 (2008).

4.

NANOSCALE MORPHOLOGY FOR ORGANIC SOLAR CELLS

4.1. Introduction

The morphology of an organic semiconductors active layer has a significant effect on its functionality in a wide range of organo-electronic applications such as light emitting diodes (OLEDs)[1,2], organic photovoltaics (OPVs)[3], and field effect transistors (OFETs).

As discussed in chapter one the power conversion efficiency of the solar cells depends on the following steps: (1) light absorption, (2) exciton diffusion and dissociation, (3) charge transport and collection. The thickness of the active layer (donor/acceptor) is required to be in the order of 100nm for efficient light absorption. However it is limited by the diffusion length of the exciton to be in the order of 10-20nm from the donor/acceptor interface[4]. After charge separation at the interface holes and electrons need to find suitable conductive path to their respective electrodes for collection.

Bilayer devices mainly satisfy the first and third step. However only a small fraction of the excitons produced, those in the vicinity of the interface are dissociated in to electrons and holes. Many designs for organic solar cells have targeted the nanoscale morphology to enlarge the donor/acceptor interface, where the donor/acceptor materials form a nanoscale interpenetrating network within the whole photoactive layer to ensure an efficient dissociation of excitons. The bulkheterojunction BHJ design shows one of the best power conversion efficiencies to date[5], with a good charge separation because of the large interface area. As the interface is dispersed throughout the bulk, most of the excitons are created within the exciton diffusion length. However the BHJ has demanding morphology requirements to ensure that the interpenetrated donor/acceptors network is bicontinuous to allow the two different charges to reach their respective electrode.

The blend film formed by solution processing is influenced by the spin coating process, which represents the quenched state of the solution and so produces a well mixed film even when this is not favorable thermodynamically[6,7]. The mixing of two different organic materials favors phase separation thermodynamically, with even near identical chemical structures. Demixing of the components has a large influence on the morphology of the film. A phase separated region with an interface between the electron donor/acceptor (ED/EA) blends components can develop, which is essential to improve charge separation of the OPV and charge recombination for some OLED devices, where these processes are predicted to occur at the interfaces between small domains of sub-micrometer size[8]. In the meanwhile, it is important to retain the connected pathways of each material to the right electrode, which requires to have one of the blend components (EA) appearing on the top surface of the active layer to be in contact with the top electrode. As more of the ED appears on the surface having a contact with the wrong electrode, the charge losses by recombination at the top electrode increase, and as a consequence the OPV performance is reduced.

The morphology of the photoactive blend layer can be controlled by several production parameters[1,4,9,10] before, during, and after the film formation: (i) substrate treatment has an influence on the sticking and dewetting of the components on the substrate surface. Its temperature during the film formation affects the drying time of the film, (ii) The spin coating solvent is chosen based on its ability to dissolve the components, and also on its volatility which influences the drying time during the film formation, (iii) The chemical structure of the blend material determines the solubility in the common organic solvents, the miscibility between the two components, their viscosity and the molecular weight, (iv) The relative proportions between the two components, (v) the solution concentration, (vi) the annealing temperature, and the annealing time. Demixing occurs at significantly higher temperatures than the glass transition temperature T_g of the compounds.

4.2. Atomic Force Microscope (AFM)

The surface topography and morphology of thin films can be imaged using different techniques such as scanning electron microscopy (SEM)[4,9,11], and transmission electron microscopy (TEM)[12,13]. However the invention of scanning probe microscopy (SPM) in early1980s[14] and the rapid development of this technique led it to become one of the most powerful tools for research especially in the field of materials, and more recently nanoscience and nanotechnology. Atomic force microscopy (AFM) or scanning force microscopy (SFM), scanning tunneling microscopy (STM), and scanning near field optical microscopy (SNOM) are members of the scanning probe microscopy (SPM) family. The operating principle of SPM techniques is to measure the interaction (attraction and repulsion forces) between a probe, which has an ultra-sharp tip, and the sample surface to obtain topographic or other physical information of the surface with very high resolution up to fractions of a nanometer, more than 1000 times better than the diffraction limited performance of an optical microscope[15,16].

The AFM has the following advantages. i) It offers very high resolution surface imaging, and provides information about the atomic and molecular arrangement with near atomic resolution in real space. ii) It can provide a three dimensional image of the sample surface. iii) Unlike the STM, it can image conducting and insulating samples where the tip to sample interactions are based on mechanical forces. iv) Unlike the SEM, it can image samples in various environments such as in air, liquids, at different temperature, and with different external conditions, which enables the monitoring of morphological changes with variation of time and condition. v) Samples can be measured directly without any complex preparation. vi) It provides information about physical properties such as elasticity, adhesion, hardness, friction, etc.

4.2.1. AFM Basic Operation Principles, and Measurements Modes

The basic operating principles of the AFM are the measurement of the inter-atomic force between the sample surface and a sharp probing tip. The tip is mounted on a soft leaf spring known as a cantilever as illustrated in figure 4-1(a). The changes in the height, Z direction, of the cantilever to keep the tip force constant provide the topographic measurement. The cantilever is usually mounted on a three axis piezo arrangement which controls the X, Y and Z axis movements.

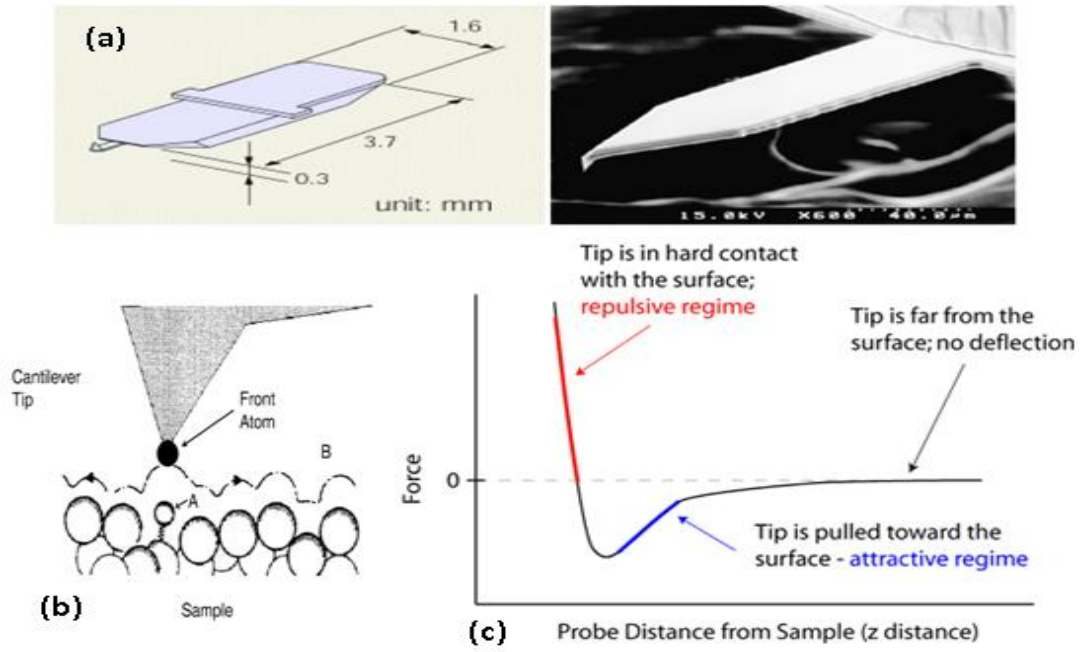

Figure 4-1: (a) Scaled drawing of AFM cantilever (left) and its tip viewed in the SEM (magnification 600 times)[6](right), (b) schematic diagram of a tip scanning a surface in atomic scale[17], (c) the variation of the inter-atomic force as function of the inter-atomic distance.[18]

As illustrated in figure 4-1(c), ignoring capillary effects, the inter-atomic forces contributing to the deflection of the cantilever usually depend on the short-range repulsive force and the long-range attractive van der Waals force whose affects are dependent on the inter-atomic distance between the tip and the sample surface. There are three basic measurement modes for the AFM based on the tip to surface distance: contact mode (C-AFM), non-contact mode (NC-AFM), and tapping mode (TM-AFM)[17,19,20].

In the C-AFM mode the tip makes physical contact with the sample, and the cantilever is bent according to the changes in topology as the tip is moved across the surface. Variations in the surface structure are obtained from the tip Z axis movement as the tip deflection is restored to a preset value by a servo mechanism. The inter-atomic force in this case lies in the repulsive region of the force distance curve as illustrated in figure 4-1(c), which is more efficient for atomic resolution imaging. The limitation of this mode is the substantial damage to the sample surface and the probe tip caused by the dragging motion of the tip and the adhesive forces between the tip and the surface.

In the NC-AFM mode the tip is quite close to the sample but has no contact with the sample, it is held on the order of 5-10 nm from the sample surface within the attractive region of the force distance surface. Stiffer cantilevers are used and can be made to oscillate in the frequency range 50-500 KHz, usually being driven by a piezo crystal to which the cantilever is fixed. The use of the stiff cantilever avoids the possibility of the cantilever sticking on contact with the surface. The force in this mode is quite low, on the order of pN (10-12 pN) which is several orders of magnitudes less than the contact mode. This mode has been developed to overcome the limitation of using the C-AFM with soft materials like organic thin films. The tip is kept at a preset distance from the surface by a feedback system, with an error signal derived from changes in the vibration amplitude or resonant frequency of the oscillating cantilever which causes the Z piezo to move in a direction to restore the cantilever amplitude to its preset value Figure 4-1(c). Again the topographic profile is obtained from this movement of the tip relative to the surface.

For TM-AFM mode a stiff cantilever is made to oscillate close to the sample, where the probe tip makes intermittent contact with the sample surface. Part of the oscillation extends into the repulsive regime. In this mode the cantilever is driven at a fixed frequency near resonance with large vibration amplitude with surface height measurements obtained from changes in the tip Z position as in NC-AFM mode whereby changes in amplitude of the oscillating cantilever provide error signals which are fed into the Z stage feedback system to preserve the tip to sample spacing. Fairly stiff cantilevers are typically used, as the tip can stick on the surface of soft materials. This mode is widely used to study soft materials because it is a compromise between C-AFM, giving high resolution with surface damage, and NC-AFM, with lower resolution and no surface damage, as it contacts the surface for a very short period to obtain high resolution images with reduced damage to the soft surface.

4.2.2. Instrumentation Structure

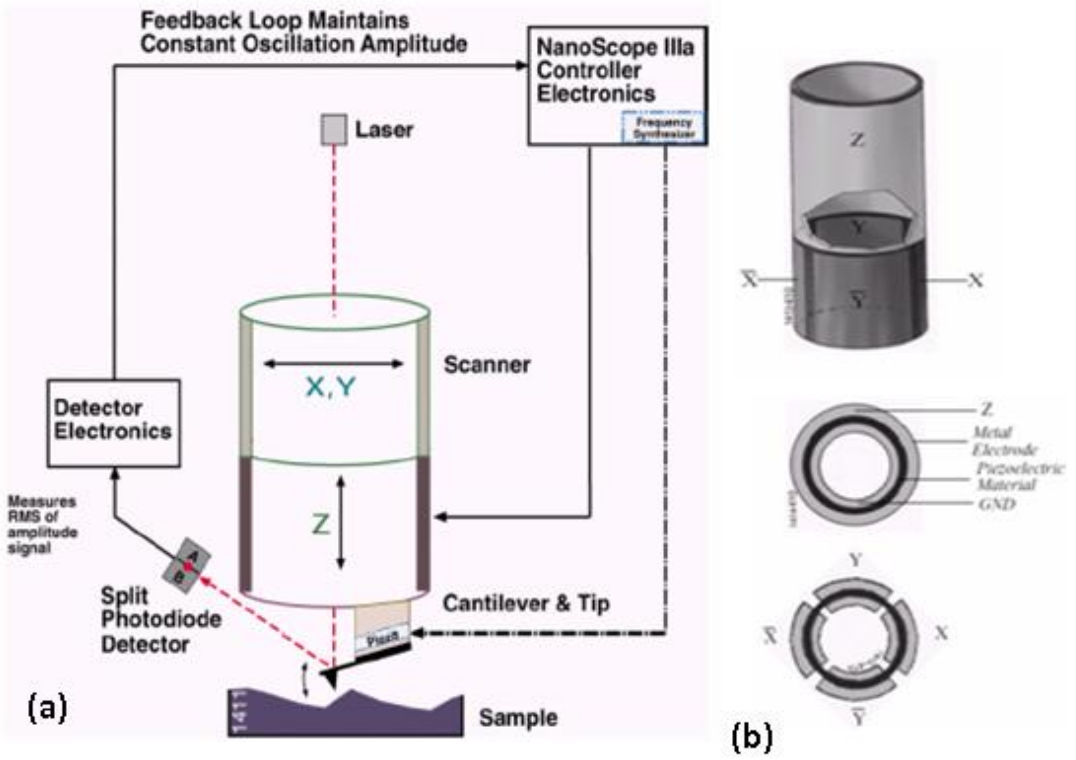

Figure 4-2: Schematic diagram showing the main components of AFM[6].

Figure 4-2 shows the basic arrangement of a typical AFM. The main components of the AFM are: (i) the force probe, a sharp tip mounted on a cantilever, which is deflected by changes in the surface topography as the tip is scanned across the surface. (ii) A sensor for the cantilever deflection, which is a laser beam reflected from the cantilever onto a split photodiode detector. (iii) A piezoelectric scanner to control the three dimensional movements of the tip as illustrated in figure 4-2(b), where it moves the tip on the x-y plane scanning close to or actually on the surface to and fro in parallel lines. It also controls the z-position of the tip on, or above, the sample surface to keep the deflection of the cantilever constant. (iv) A feedback system to control the cantilever deflection by applying a correction signal to the z-piezo of the scanner. (v) A computer to be used for data recording, analysis, and visualization, where the z-position of the tip is recorded as a function of x-y position. By analyzing this data we can obtain a topographical map of the sample surface. For NC-AFM and TM-AFM modes the cantilever is made to oscillate using one of several different methods such as a quartz piezo to excite the cantilever into oscillation, as shown in figure 4-2, or having the cantilever coated with magnetic material, which can be excited to oscillate by an alternating magnetic force produced by a coil underneath the sample or else mounted above the cantilever.

4.2.3. Phase Image and Nanoscale Demixing

As discussed in the introduction, it is important to have the EA components on the top surface, therefore investigating the surface compositions is an essential need to optimize the performance of electronics devices including OPV.

Atomic force microscopy allows an examination of the nanophase morphology of the blends. The topographic image shows little detail but the phase image shows clear evidence of nanoscale separation of the components of the blend[21,22]. The tip deforms stiffer sample surfaces to a lesser extent than more compliant surfaces, as the cantilever is oscillating at a specific frequency under a driving force, this frequency lags as the scanning cantilever goes over a more compliant surface compared to the stiffer surface. This is the phase lag, which can be related to the attractive and repulsive, or adhesive, forces at the interface and the sample's viscoelastic properties[21]. Therefore materials with different viscoeleastic properties have different phase lags. Lighter areas correspond to lower values of ϕ (less phase lag) and darker areas correspond to larger values (more phase lag). More viscous regions will appear darker in comparison to less viscous regions. So the light and dark regions indicate domains with different compositions. The degree of intermixing of the components in the mesoscale domains is unknown and could be obtained using scanning transmission X-ray microscopy (STXM)[8], photoconductive atomic force microscopy (pcAFM)[23], or atomic force photovoltaic microscopy (AFPM)[24].

4.3. Roughness parameters

Surface roughness measurement techniques, which are known as profiling methods provide a way to measure the surface data as a series of 2D traces which sense the height of the surface providing a quantitative surface profile Z_i in either X or Y direction as illustrated in figure 4-3, where L is the length of the surface profile along the x-direction. To provide an area profile many parallel traces are needed which can be combined to provide a 3D topographical measurement.

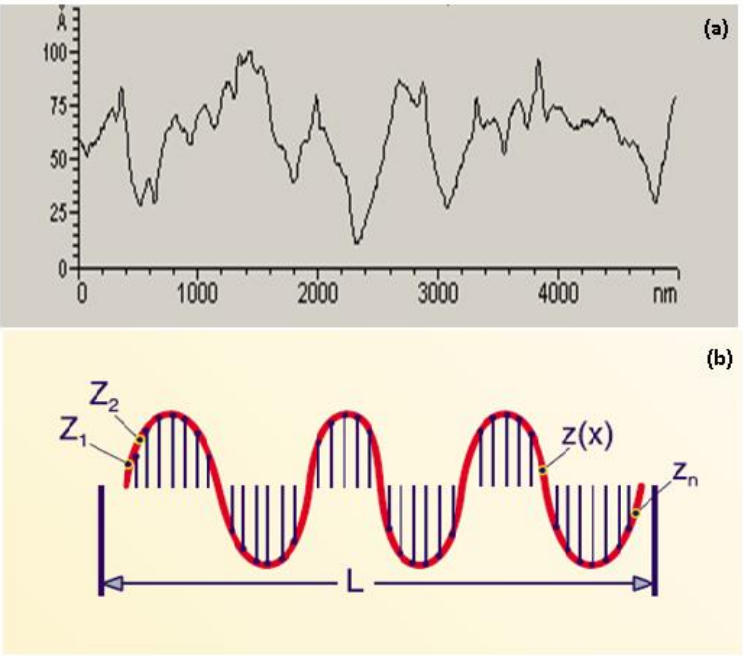

Figure 4-3: A surface roughness profile in x-direction Z(x)[25].

The best way to study and compare the surfaces roughness is to regard the waveform as being made up of amplitude (height) features and wavelengths, peak and troughs, spacing features, both independent of each other[17,26]. Several parameters are used as amplitude parameters such as the roughness average (R_a), the root mean square roughness (R_q), and the maximum profile peak height (R_p).

4.3.1. The Roughness Average (R_a)

The basic parameter for specification of roughness is the roughness average (R_a), which is the numerical average of the absolute values of the surface departures from the mean plane. It is given as[27,26]

$$\boldsymbol{R_a = \frac{1}{MN}\sum_{i=1}^{M}\sum_{j=1}^{N}|Z_{ij}|} \tag{4-1}$$

where M and N are the number of data points in the X and Y direction

respectively, and Z is the surface height relative to the reference mean plane. The roughness average gives no information on the spacing between the features or the shape of the surface irregularities.

4.3.2. The Root Mean Square (RMS)

The root mean square (RMS) roughness is the most widely used parameter for the specification of surfaces roughness and is much more valid statistically than R_a. It is obtained by squaring each height value in the dataset, then taking the square root of the mean as[25]

$$\boldsymbol{R_q = \sqrt{\frac{1}{MN}\sum_{i=1}^{M}\sum_{j=1}^{N}Z_{ij}^2}} \tag{4-2}$$

RMS is limited in the detection of differences in spacing; however the RMS is more sensitive to peaks and valleys than average roughness because height values are squared in calculation.

4.3.3. Fourier Analysis and Power Spectral Density (PSD)

To obtain spatial frequency information from the surface topography data it is converted to the frequency domain using a 2D Fourier transform. This process decomposes the data into an array of frequency components which are easier to manipulate for this purpose than the original data format. The Fourier transform is based on the Fourier series principle which assumes that any periodic function f(x) on the interval λ can be decomposed into a sum of simple sine and cosine functions of the form *sin(nx)* and *cos(nx)* as shown in figure 4-4. The periodic function *f(x)* can be represented as[28]

$$\boldsymbol{f(x) = \frac{a_o}{2} + \sum_{n=1}^{\infty} a_n \cos nkx + \sum_{n=1}^{\infty} b_n \sin nkx} \qquad (4\text{-}3)$$

where a_o, a_n, b_n are called Fourier coefficients of the function *f(x)* and the process to determine these coefficients is known as Fourier analysis. The coefficients are

$$\boldsymbol{a_o = \frac{2}{\lambda}\int_0^{\lambda} f(x)dx} \qquad (4\text{-}4)$$

$$\boldsymbol{a_n = \frac{1}{\lambda}\int_0^{\lambda} f(x)\cos(nx)dx \qquad n \geq 0} \qquad (4\text{-}5)$$

$$\boldsymbol{b_n = \frac{2}{\lambda}\int_0^{\lambda} f(x)\sin(nx)dx \qquad n \geq 1} \qquad (4\text{-}6)$$

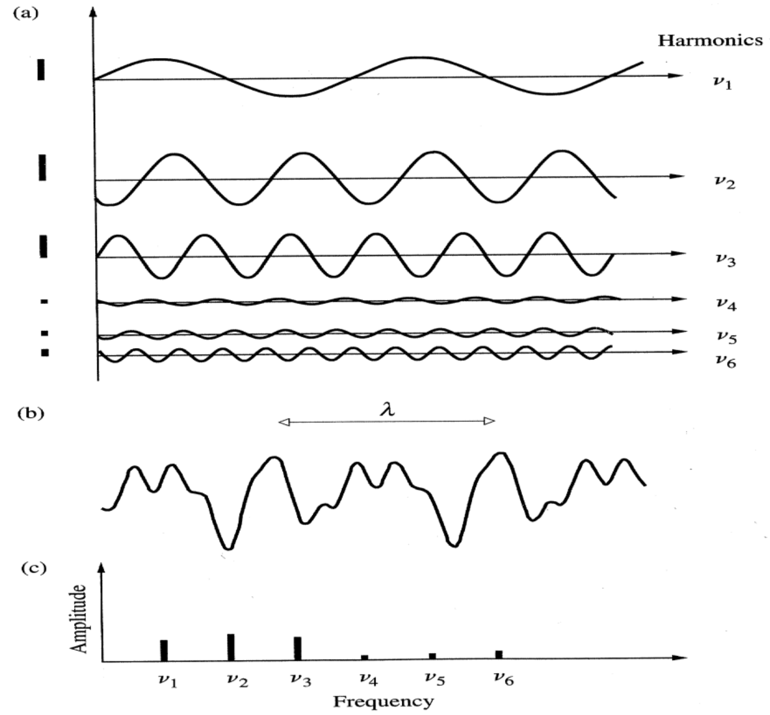

Figure 4-4: periodic function f(x) on the interval λ and its decomposition sine and cosine functions[28].

The function to be transformed can be either continuous or discrete, and also periodic or aperiodic. Hence the Fourier transform can be classified to four categories[29]: Fourier series (periodic-continuous), Fourier transform (aperiodic-continuous), Discrete time Fourier transform (DTFT) (aperiodic-discrete), Discrete Fourier transform(DFT) (periodic-discrete).

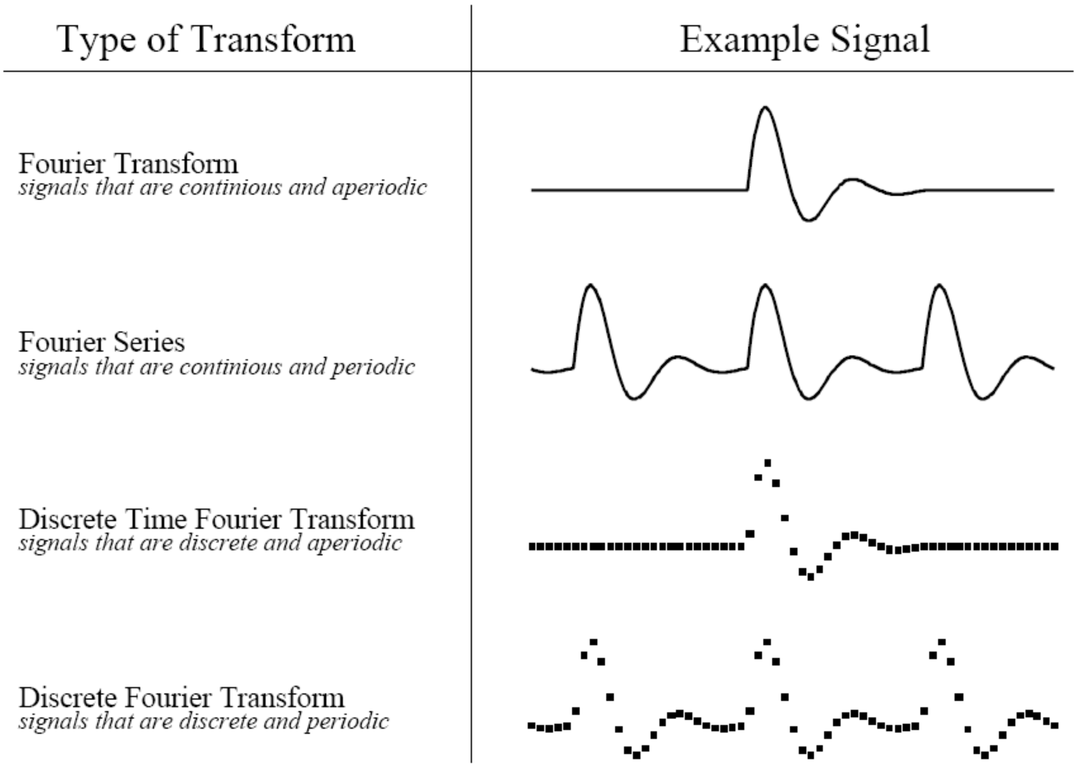

Figure 4-5: Illustration of the four Fourier transforms[29].

The DTFT represents the surface topography, when it consists of a set of finite number of discrete data points synthesizing a signal that is aperiodic. It is impossible for the DTFT to be calculated using the computer algorithm unlike the DFT which operates on discrete signals that repeat themselves in a periodic fashion from negative to positive infinity. The DFT finds the frequency content of such a limited collection of data. Therefore the periodicity can be invoked using the digital signal processing DSP, in order to be able to use the DFT[29].

For computational ease a modified form of the DFT is usually utilised. This is the fast Fourier transform (FFT), which significantly reduces the number of arithmetic operations involved in the calculations when using large data sets.

The discrete Fourier transform can be given as[26]

$$\boldsymbol{F(k) = \frac{1}{N}\sum_{n=0}^{N-1} f(n) exp\left(\frac{-2\pi i}{N} nk\right) \quad n = 0, \ldots., N-1} \tag{4-7}$$

The power spectral density (PSD) decomposes the measured surface profile into its component spatial frequencies (*f*) using Fourier analysis. The PSD is the square of the transform as a function of the spatial frequency. The PSD function calculates the power spectral densities for each horizontal (X) or vertical (Y) line in the data, and then averages over all the X or Y profile. L is the scan length, assumed to be equal in *x* and *y* direction, f_x and f_y is the spatial frequency for *x* and *y* directions respectively, N is the number of the measured data points, assumed to be equidistantly spaced in *x*, *y* direction at distances $\Delta x, \Delta y = L/N$. The 1-D PSD is given as[30]

$$\boldsymbol{PSD(f_x) = L\left[\frac{1}{N}\sum_{m=1}^{N} Z(x_m). exp\,(-2\pi i. x_m f_x)\right]^2} \tag{4-8}$$

The 2-D PSD is given as

$$\boldsymbol{PSD(f_x, f_y) = L^2\left[\frac{1}{N^2}\sum_{n=0}^{N}\sum_{m=0}^{N} Z(x_m, y_n)\, exp\left\{-2\pi i\left[(x_m.f_x) + \left(y_n.f_y\right)\right]\right\}\right]^2} \tag{4-9}$$

where $x_m = m.\frac{L}{N}$, $y_n = n.\frac{L}{N}$, the spatial frequency f_x, f_y takes a discrete range of values $f_x, f_y = \frac{1}{L}, \frac{2}{L}, \ldots..\frac{N}{2L}$, and $i = \sqrt{-1}$.

The PSD as a function of spatial frequency evaluates the in-plane spatial periods of the surface texture which gives some indication of the film morphology. PSD gives complementary information about the surface to the RMS which gives the out of plane characterization, and the amplitude distribution of the roughness which gives more statistical roughness.

For further analysis of the PSD as function of the spatial frequency, the frequency scale is divided into three regions as shown in figure (4-6). (i) The lowest frequency region (< 0.01 nm^{-1}), corresponds to domains larger than 100nm. (ii) The middle spatial frequency region (> 0.01 nm^{-1}, < 0.05 nm^{-1}), corresponds to domains between 20nm and 100nm respectively. (iii) The highest spatial frequency region (>0.05 nm^{-1}), describes the domains smaller than 20nm.

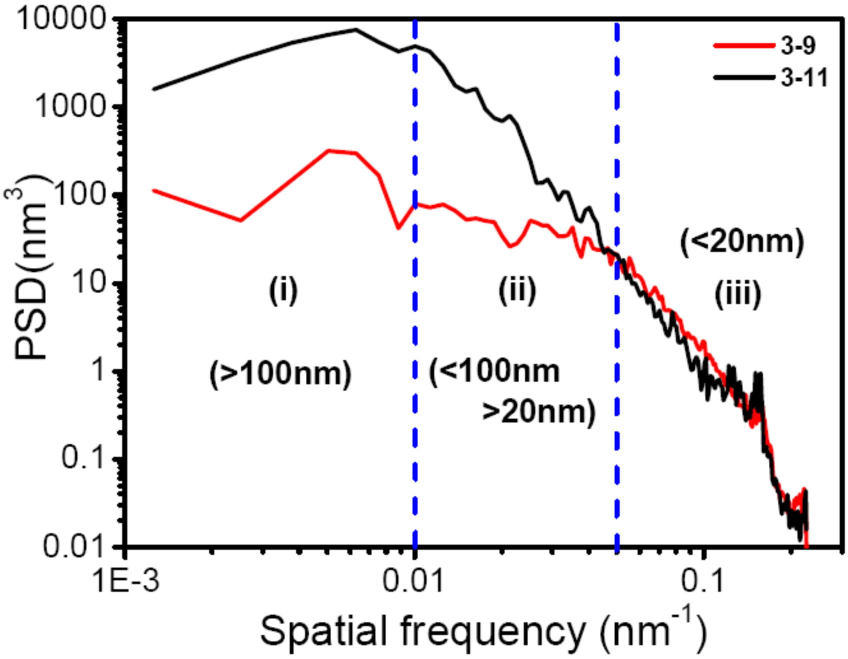

Figure 4-6: Power spectral density versus radial spatial frequency of 3:9 and 3:11 blends defining the analysis regions.

4.4. Results and Discussion

In this chapter we study the morphology of thin films of nematic EDs blended with a range of EAs, which are liquid crystalline or amorphous. Most of the blends form LC glasses at room temperature and we show that they phase separate on a nanometre scale level. The study was to investigate the effect of the chemical structure of EDs and EAs, the casting solvents and the annealing temperature on the nanoscale morphology. The results of this chapter will be correlated to the PV device performance in the next chapter to evaluate the suitability of the various acceptors, donors, solvents, and annealing temperatures for photovoltaic blends.

4.4.1. The Effect of Functional Groups for Perylene Bisimide Derivatives

Perylene bisimide is one of the best known n-type organic semiconductors, and it exhibits good electrical and optical properties to be an efficient EA. In this section **9,11,13,16** are some perylene derivatives with different functional groups which have been investigated as EA with compound **3** as ED.

Samples of the different blends were produced using identical processing conditions, which are also identical to the photovoltaic devices processing, for correlation with the solar cells’ performance in the next chapter. The devices were fabricated on Indium Tin Oxide (ITO) coated glass (13Ω/□) substrates. The substrates were first plasma etched and coated with a polystyrene sulphonate/polyethylene dioxythiophene (PSS/PEDOT, Baytron P VP. AI 4083). The PSS/PEDOT layer was spin-coated onto the ITO surface at 4000 rpm spin speed and 2000 rpm^2 acceleration with a spin duration of 30 seconds, to form a uniform layer. The substrate was then placed on a temperature controlled hot stage and cured at 120 ^{o}C for 30 min to evaporate the water, followed by 220 ^{o}C for 5 min to thermally polymerize the PEDOT. Finally the temperature was ramped to room temperature at a cooling rate of 10^{o}C/min. The devices were prepared by spin casting at 2000 rpm for 30s a solution of different ED and EA pairs in the ratio of 1:1 by weight in toluene (15 mg ml^{-1}) on the substrates. The films were then annealed at 120 °C for 60 mins.

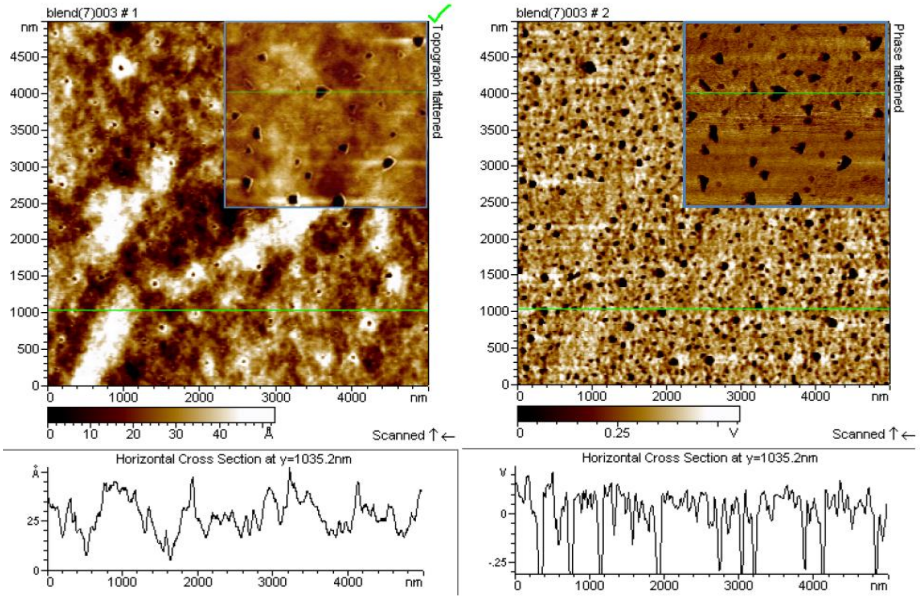

Figure 4-7: AFM images (topographic on left; phase on right) of a thin film of the 1:1 blend of 3:16. The investigated area is 5µm×5µm, and 1µm×1µm in the box at the right side corner.[1]

Figure 4-7 shows the topography and phases image of a **3:16** blended thin film of 5µm×5µm and 1µm×1µm areas. The cross sections taken through both images are shown and the rms, height distribution and PSD were measured. The topographic image shows some pinholes with little other detail. However the phase image shows clear evidence of nanoscale separation of the components of the blend as mentioned before in section 4.2.3.

---

[1] ** Indicates that experimental measurements were made by Dr. C. Lei. Analysis was done by me.

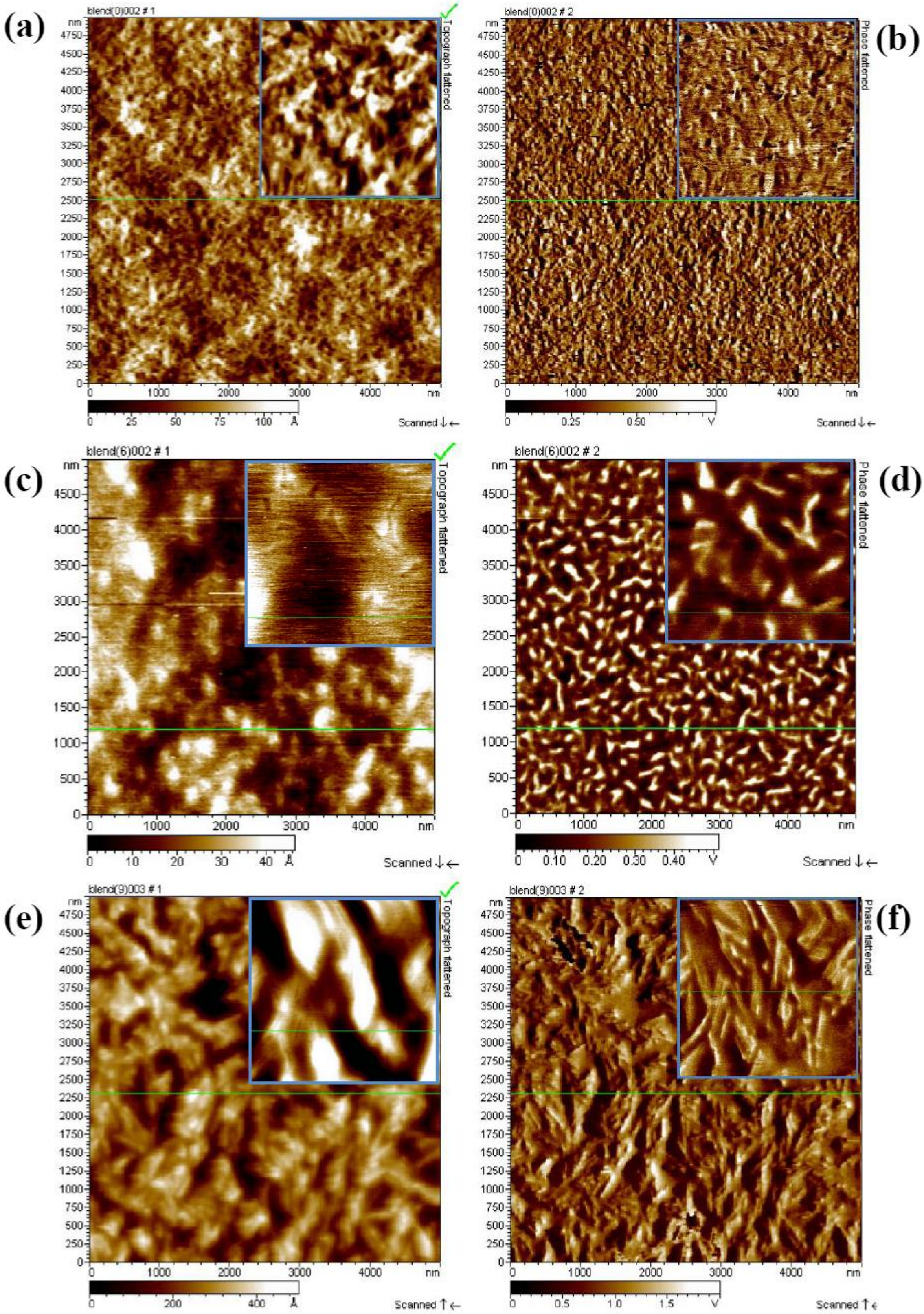

Figure 4-8: AFM images (topographic on left; phase on right) of a thin toluene casted film of the 1:1 different blends of 3 as ED. The EA was (a,b) 9, (c,d) 13, (e,f) 11. The investigated area is 5μm×5μm, and 1μm×1μm in the box at the right top corner.**

Figure 4-7 and figure 4-8 show the topography and phase images of 5μm×5μm and 1μm×1μm areas of the four blends of **3** with **16, 9, 13, 11** in order. The **3:9** blend shows phase separation with low contrast, possibly because the domains are better intermixed. The **3:16** blend has fine structure with low contrast and many pinholes. The **3:11** blend shows elongated domains with low contrast. The **3:13** blend shows fine structure with a clear contrast between two different domains, which is illustrated clearly in the phase image.

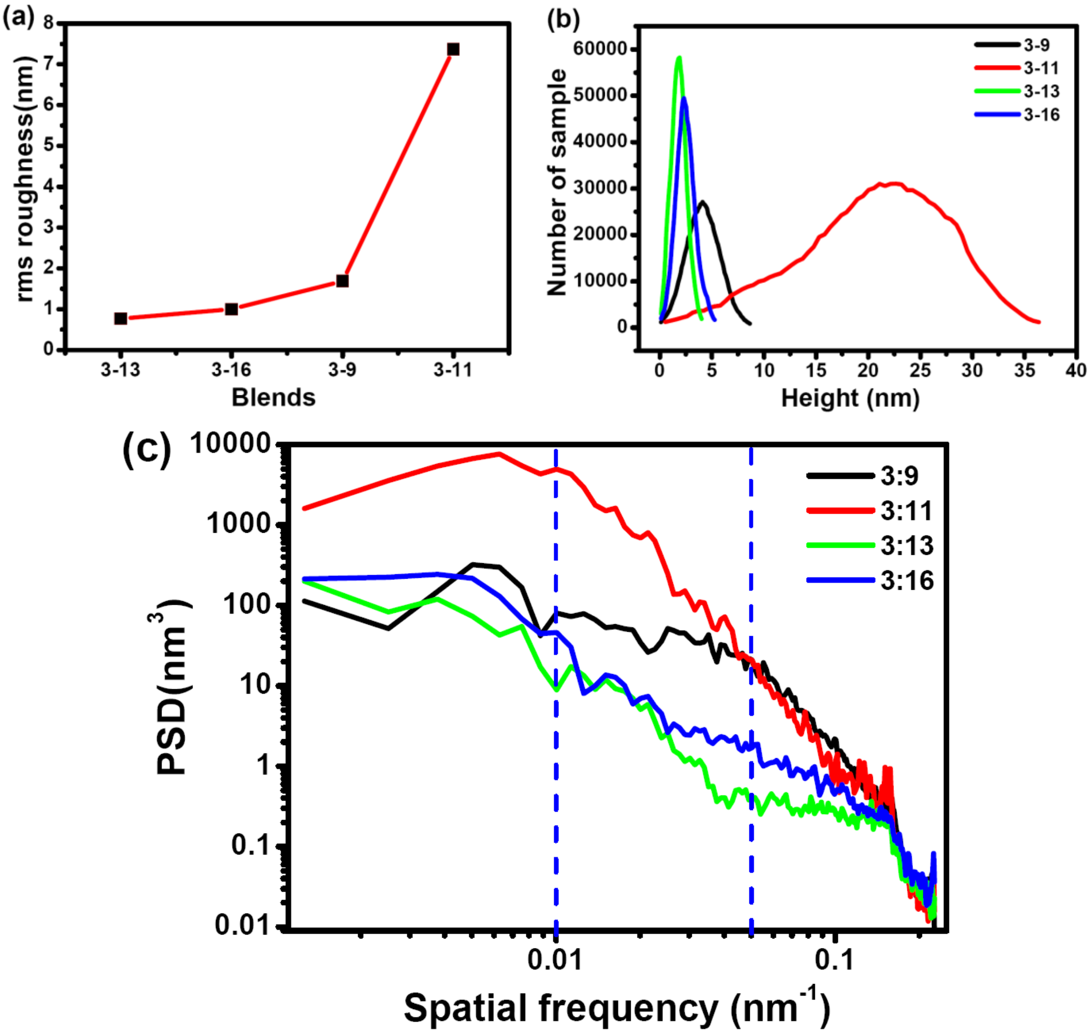

Figure 4-9: Surface roughness analysis for the four blends,(a) rms roughness, (b) height distribution, (c) PSD as a function of spatial frequency.

Figure 4-9(a, b, c) shows the rms roughness, height distribution, and PSD respectively, which illustrates the variation of the nanoscale morphology as a function of the acceptor compounds, confirming what is shown visually in figure 4-7 and figure 4-8. The rms values are 0.77nm, 1nm, 1.69 nm for blends **3:13, 3:16** and **3:9** respectively, however the blend **3:11** shows a dramatic increase in the roughness to 7.37

nm. The height distribution also follows the same sequence of change, where the peaks of height distribution are at 1.9nm, 2.3nm, 4.1nm, and 22.7nm. and the height variation is of the order of 4nm, 5.3nm, 8.7nm, and 36.4nm respectively.

The PSD as a function of spatial frequency for the **3:11** blend shows the highest amplitude in the spatial frequency range regions (i) and (ii), corresponding to large domain size of (>20 nm). However for the fine structure (< 20nm) of region (iii) blend **3:9** provides a larger PSD amplitude. Blends **3:13** and **3:16** show lower PSD amplitudes over the full frequency range.

Blend of **3:11** is crystalline at room temperature and forms a nematic liquid crystal phase over 270 ^{o}C, **3:9**, **3:13** and **3:16** are nematic glasses at room temperature. This may explain the rough morphology of **3:11** relative to the others.

This result indicates the poor nanoscale morphology of **3:13** and **3:16** and the rough nanoscale morphology of **3:11** in contrast with **3:9**, which shows relatively high spatial frequencies, which will be related to PV devices performance in the next chapter.

4.4.2. The Effect of Casting Solvent on the Nanoscale Morphology

A critically important factor determining the nanoscale morphology of the blend thin film is the variation in solubility of the components of the blend in the casting solvent. Walheim and coworkers[7] show that solution processing of compounds with different solubility results in the formation of surface features such as pinholes or bumps, where the size of these features is based on the solubility of each compound and the variation between the solubility of the two compounds. During and after spin coating the more soluble compound contains more solvent than the less soluble one. Therefore, at the moment when the less soluble compound evaporates all its contained solvent, the more soluble one is still swollen with the solvent, and the film is relatively flat. Going further in the evaporation leads to collapse of the more soluble region after losing its solvent content. If it is dominant on the surface bumps, of the less soluble compounds appear, and if the less soluble one is dominant on the surface, pinholes containing the more soluble compound characterize the surface as illustrated on figure 4-10.

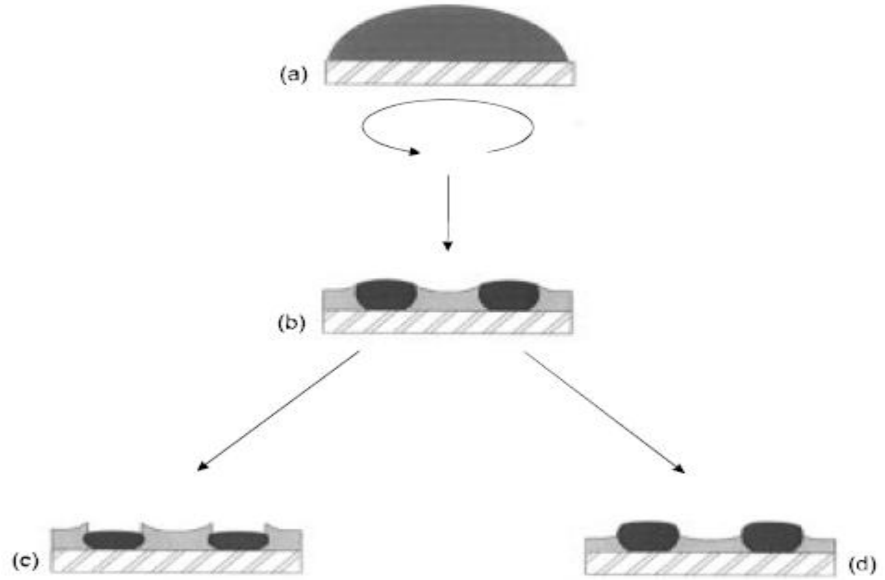

Figure 4-10: Schematic illustration of the formation of the topographic structure during and after spin coating process, (a) before spin coating the blend compounds mixed very well, (b) shortly after spin coating, (c,d) the pinhole and bump creation after complete drying[7].

In this study we aim to find the best common solvent to work with our EDs and EAs, which dissolve both compounds efficiently with low solubility variation between the blend compounds. Therefore samples of the same blend were produced using identical processing conditions to the previous section while, varying the casting solvents. Solution of **3** as ED and **11** as EA in the ratio of 1:1 by weight were spin-coated in different solvents (15 mg ml^{-1}). The solvents used were toluene, chloroform and chlorobenzene with boiling points 111^{o}C, 61^{o}C and 132^{o}C respectively.

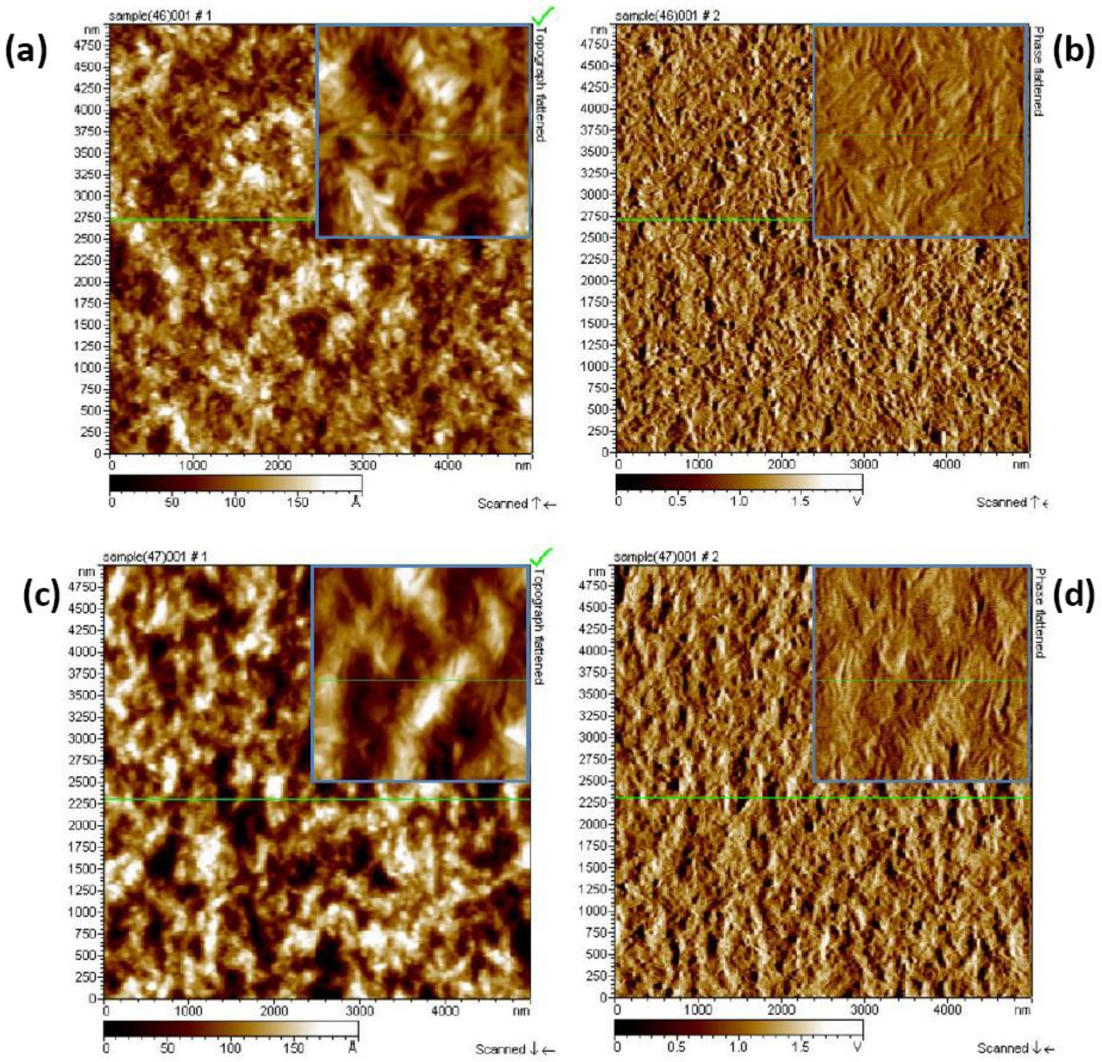

Figure 4-11: AFM images (topographic on left; phase on right) of a thin film of the 1:1 different blends of 3 as ED and the 11 as EA using different solvents of (a,b) chloroform, (c,d) chlorobenzene. The investigated area is 5µm×5µm, and 1µm×1µm in the box at the right side corner.**

Figure 4-8(e,f) and figure 4-11 show the topography and phase images of 5µm×5µm and 1µm×1µm areas of the three blends of **3** with **11** using toluene, chloroform, and chlorobenzene as solvents.

The surface structure with toluene as casting solvent contains elongated domains with low contrast and horizontal dimensions of the order of 500nm. From the phase image the low contrast of the image indicates that the top materials have similar mechanical stiffness and adhesion properties, which can be explained by assuming the two materials have similar mechanical properties, or that one of the two materials is embedded and enveloped within the elongated features. In contrast the surface of chloroform and chlorobenzene cast samples contain smaller height elongated domains, with fine structure and low contrast, the horizontal dimensions of the cross section of these domains is in order of 200nm.

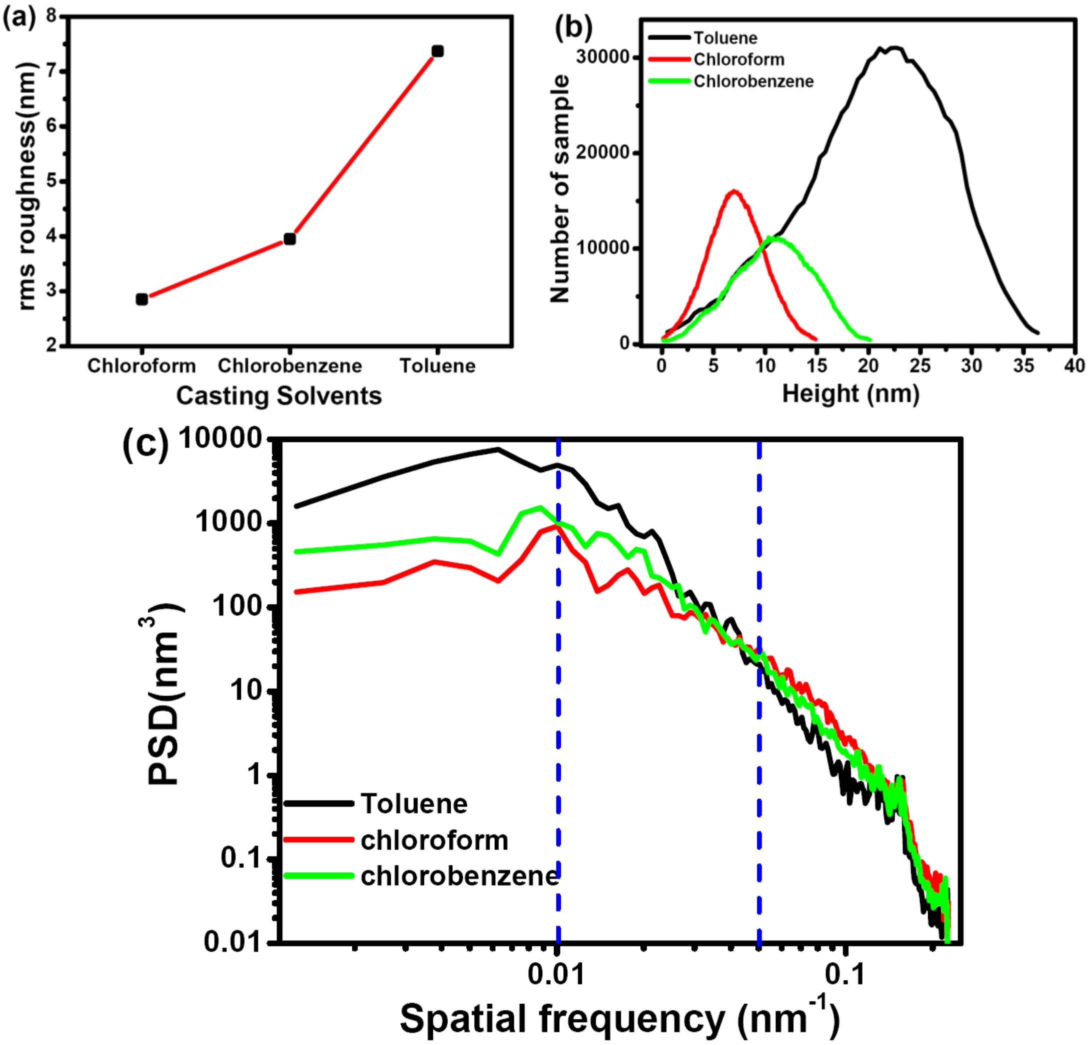

Figure 4-12: Surface roughness analysis for 3:11 blends using different solvents,(a) rms roughness, (b) height distribution, (c) PSD as a function of spatial frequency.

Figure 4-12(a, b, c) shows the rms roughness, height distribution, and PSD respectively which illustrates the variation of the nanoscale morphology as a function of the acceptor compounds, also it confirms what is shown visually in figure 4-8(e,f) and figure 4-11. The rms values were 2.85nm, 3.95nm, 7.37nm for blends cast with chloroform, chlorobenzene, and toluene respectively. Height distribution also follows the same variation order, where the peaks of height distribution were at 7nm, 10.3nm, and 22.7nm. The height variation was of the order of 14.9nm and 20.1nm, and 36.4nm respectively.

The PSD as a function of spatial frequency for the toluene cast blend shows highest amplitude over the first two highest frequency regions (i) and (ii), whilst it start to drop rapidly in the region (ii), whereas the chloroform cast sample shows the lowest. In the high spatial frequency range (iii) indicating fine structure, the toluene cast PSD amplitude was lower compared to the chloroform casting film. Chlorobenzene casting shows amplitude located in between the two other solvent PSD curves.

The coarser structure of the toluene cast samples is due to it low solubility for compound **11** in contrast to compound **3**. However chloroform and chlorobenzene dissolve both compounds efficiently. Chloroform evaporates quickly compared to chlorobenzene and toluene which results in quenching and fixing the molecules in non-equilibrium positions before they align themselves and phase separate. This is noticeable by comparing the 1µm x 1µm images in Figure 4-8(e,f) and figure 4-11, where the elongated domain regions are smaller with large variation in direction in neighbouring domains. Chlorobenzene and toluene tend to align in similar directions in neighbouring domains.

4.4.3. The Effect of the Spacers and End Groups on the Nanoscale Morphology

1, 3 and **4** are nematic liquid crystals with the same aromatic core. **1** has methoxy terminal groups, whilst **3** and **4** are reactive mesogens, which can be photochemically polymerized to form a LC polymer network, with the help of alkyl chain spacers linked to diene end groups for **3** and methacrylate end groups for **4** as illustrated in table 2-1. The optical and electrical properties of these compounds were studied in the previous two chapters, and show good ED properties. Therefore, in this section the nanoscale morphology of the blends of these three compounds as ED, with **9** as EA have been investigated. Chlorobenzene was used as casting solvent based on results from the previous section, which agrees with the literature[31].

Blends of the three ED and **9** as EA were produced with a ratio of 1:2 by weight using identical processing conditions to the previous sections. The devices were prepared by spin casting a solution of the blends in chlorobenzene (15 mg ml^{-1}) to evaluate the suitability of the various donors for photovoltaic blends.

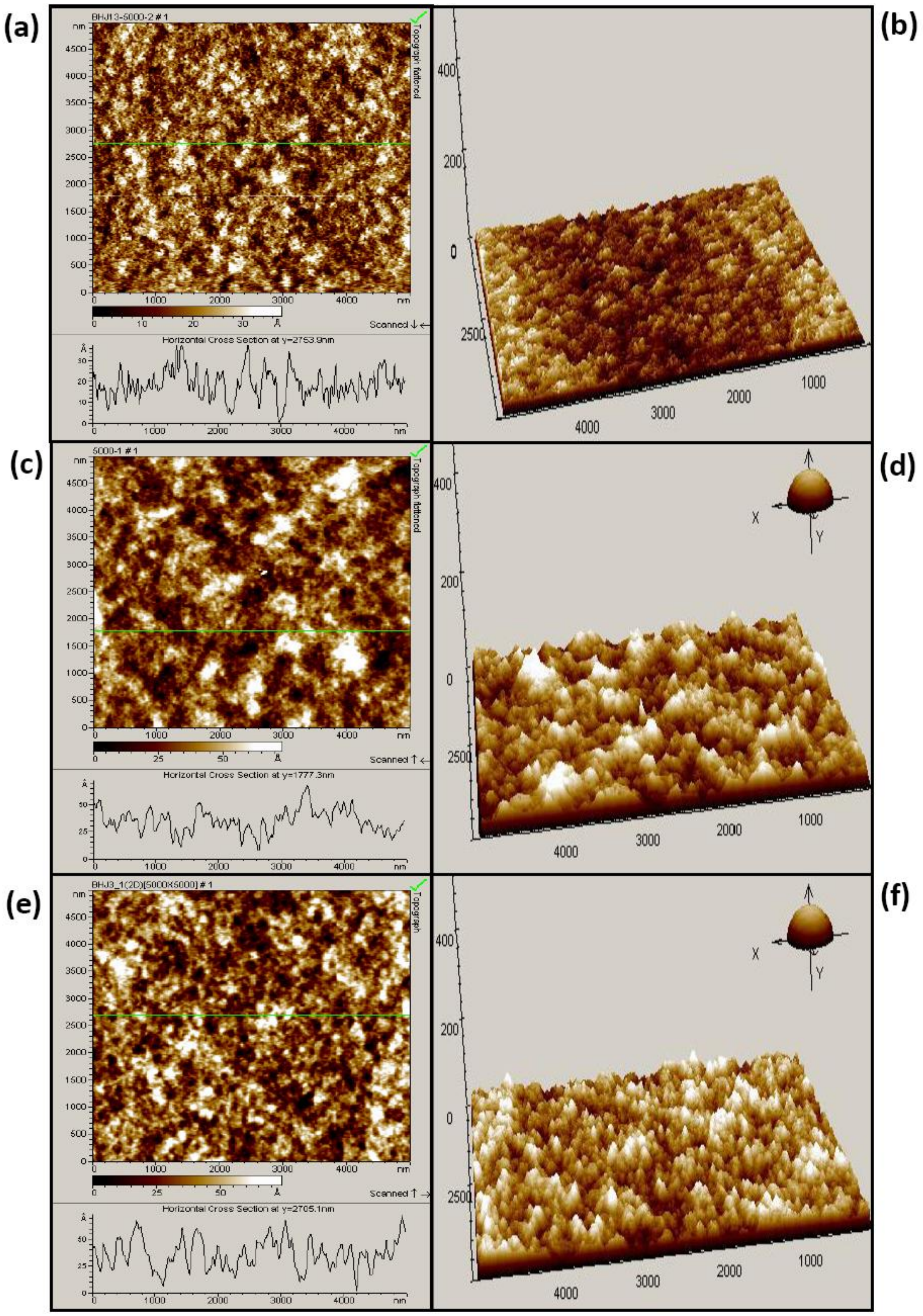

Figure 4-13: AFM topographic images (2D on left with cross section; 3D on right) of a thin film of the 1:2 different blends of 1, 3, and 4 as EDs with 9 as EA using chlorobenzene as coasting solvent ,(a,b) 1:9, (c,d) 3:9,(e,f) 4:9 the investigated area is 5μm×5μm.

Figure 4-13 show 2D and 3D topographic images of 5μm×5μm areas for the blends of **3, 4,** and **1** with **9** respectively, where the size, height, and shape features reflect the variation in the nanoscale morphology of the surface of the blended thin film based on the chemical structure of the donors. As the scale of the images is identical, visually the surface morphology of the blends **1:9**, **3:9** and **4:9** goes from the fine structure to rough respectively.

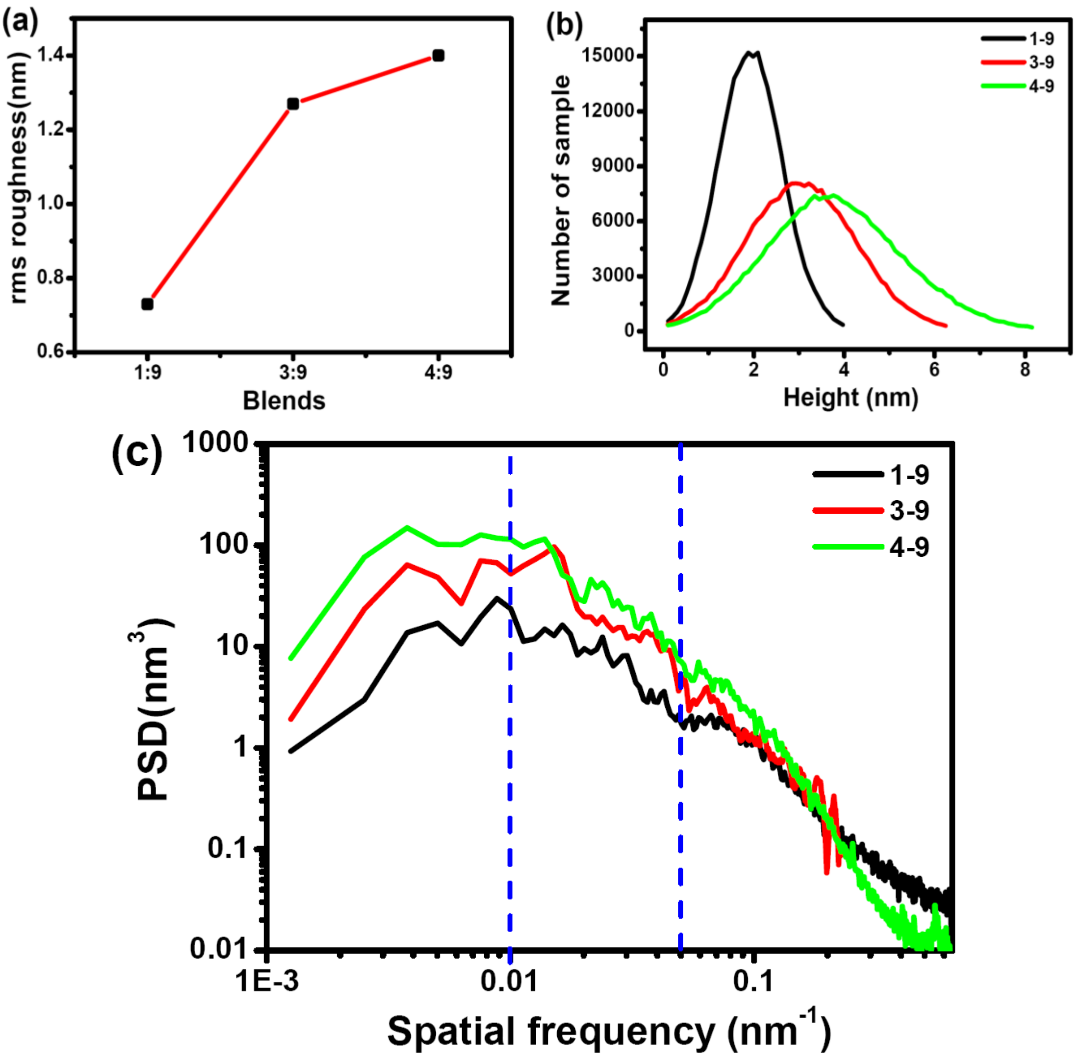

Figure 4-14: Surface roughness analysis for the three blends,(a) rms roughness, (b) height distribution, (c) PSD as a function of spatial frequency.

The visual observations of the nanoscale morphology as a function of the donor compounds are confirmed in Figure 4-14 which shows the rms roughness, height distribution, and PSD respectively. The rms values are 0.73nm, 1.27nm and 1.4nm for blends **1:9**, **3:9**, and **4:9** respectively. The height distribution also follows the same trend, with the peaks in the height distribution at 2nm, 2.9nm, and 3.8nm, and the height variation at about 4nm, 6.2nm and 8nm respectively.

The PSD as a function of spatial frequency for the **3:9** and **4:9** blends relative to **1:9** blend show higher values in the first and second spatial frequency regions (i, ii), whereas at higher spatial frequency region (iii) it becomes relatively lower. The PSD amplitude of **4:9** is somewhat higher relative to **3:9** in the first two regions (i, ii). This result indicates rough nanoscale morphology for **3:9** and **4:9** in contrast to **1:9**, which will be related to PV devices performance in the next chapter.

4.4.4. The Effect of Annealing Temperature on the Nanoscale Morphology

The Annealing temperature is a second key factor to control the nanoscale morphology of the blend thin film which helps to increase the intermixing of the two components. The annealing duration is another important parameter[7,32].

Therefore, samples of identical blends were produced using identical processing conditions to the previous sections whilst varying the annealing temperature (RT, 50°C, 100°C, 120°C, 150°C, 200°C) for fixed duration of 60 mins and cooling rate of 10 °C/min. The devices were prepared by spin casting a solution of **1** as ED and **9** as EA in the ratio of 1:2 by weight in chlorobenzene (15 mg ml^{-1}). The critical temperatures in the annealing temperature range for the phase separation of this blend are the glass transition temperature of **1** at 80°C, the melting point of **9** at 274°C, as well as the boiling point of the casting solvent at 132°C.

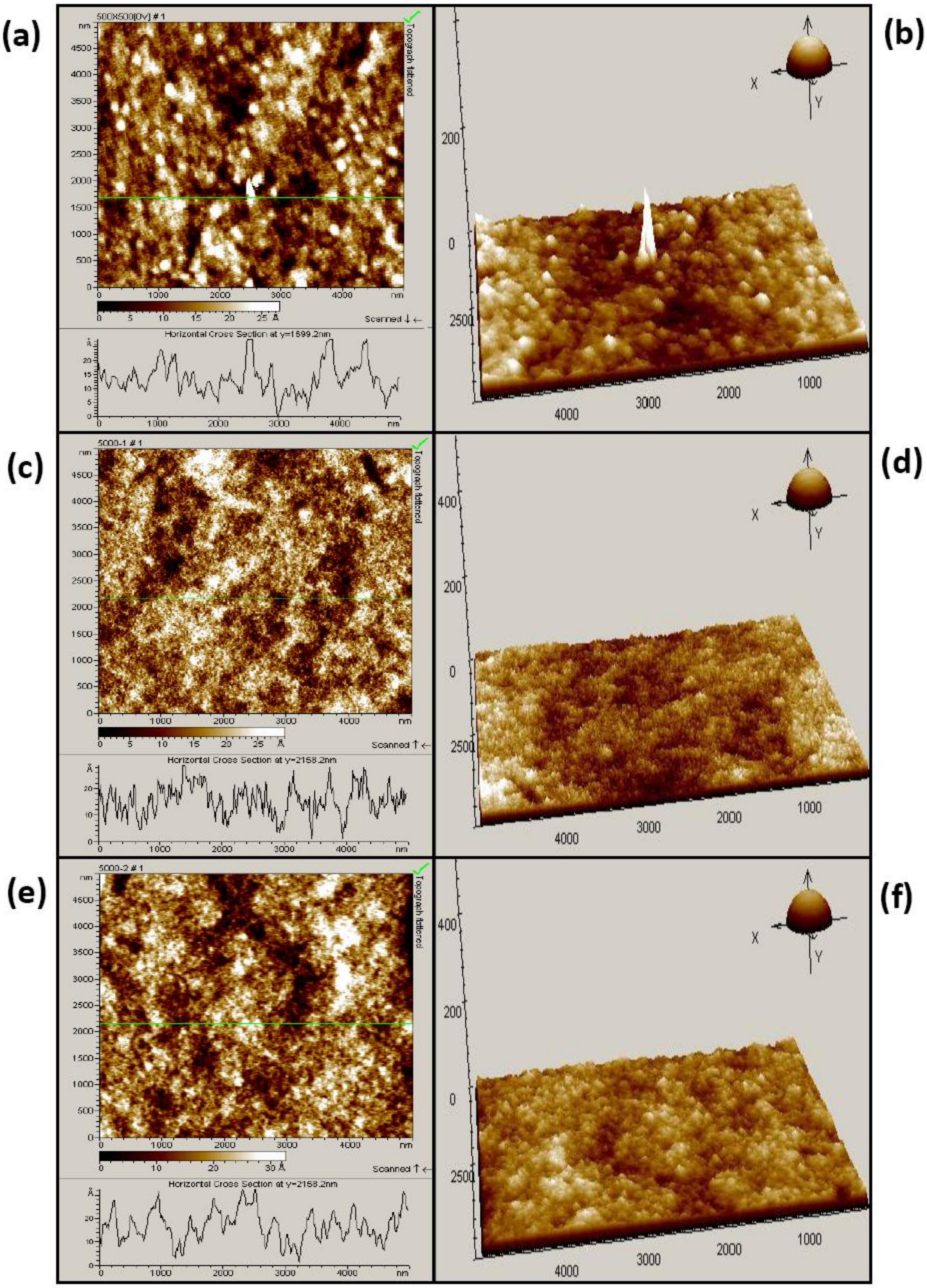

Figure 4-15: AFM topographic images (2D on left with cross section; 3D on right) of a thin film of the 1:2 different blends of 1 as ED with 9 as EA using chlorobenzene as coasting solvent, at different annealing temperature (a,b) RT, (c,d) 50^{o}C, (e,f) 100^{o}C, the investigated area is 5μm×5μm.

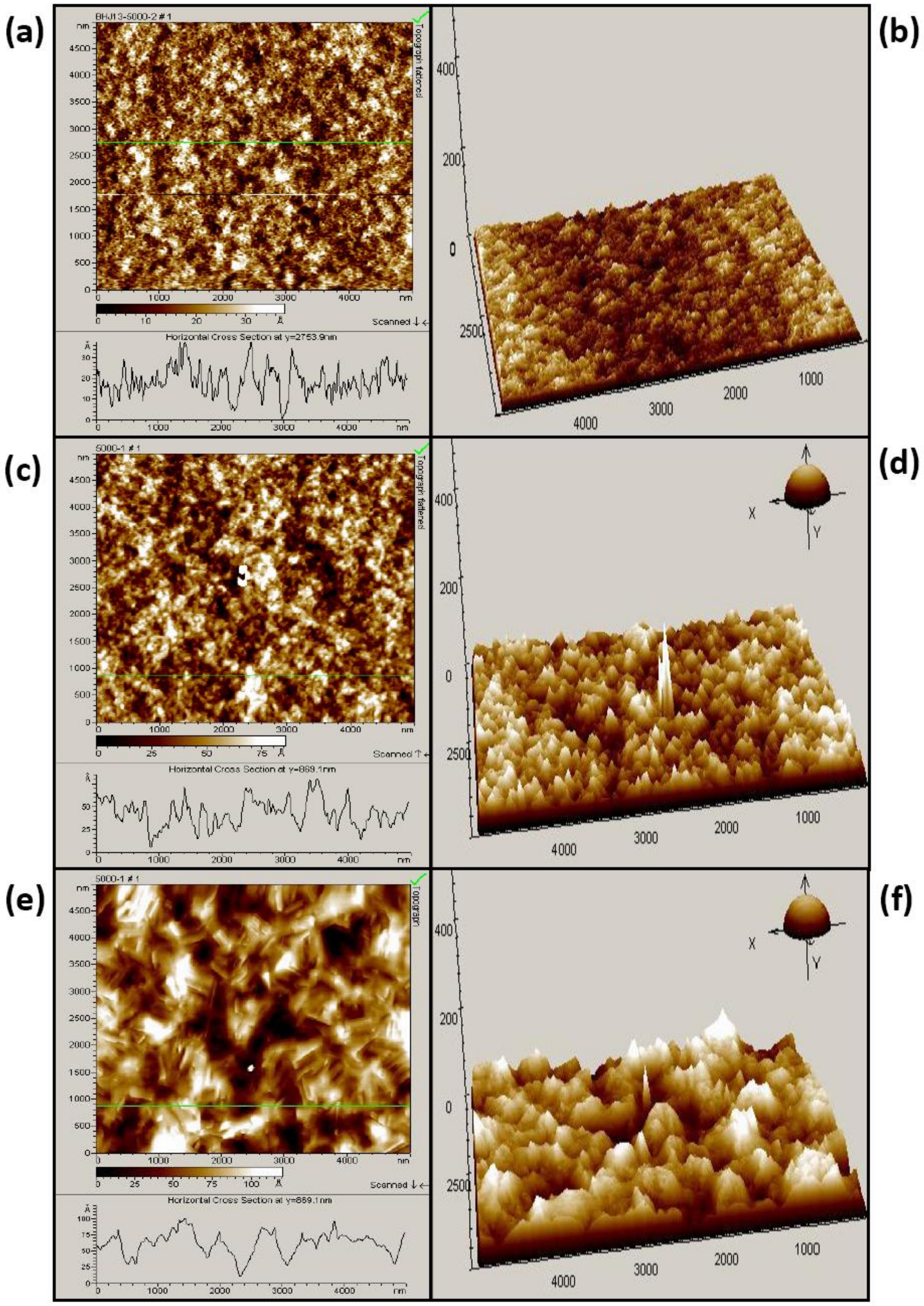

Figure 4-16: AFM topographic images (2D on left with cross section; 3D on right) of a thin film of the 1:2 different blends of 1 as ED with 9 as EA using chlorobenzene as coasting solvent, at different annealing temperature (a,b) 120°C, (c,d) 150°C, (e,f) 200°C, the investigated area is 5µm×5µm.

Typical development of the films with annealing temperature is shown in Figure 4-15 and figure 4-16, which represent 2D and 3D topographic images of 5μm×5μm areas for **1**:**9** blends following different annealing temperatures. Immediately after spin coating, generally the films appeared smooth, after annealing at different temperatures the surface started to roughen as the annealing temperature increases.

Figure 4-15(a,b) shows the RT sample, dried after spin coating using a vacuum for one hour. There are some lumps coming out of the surface possibly because one of the compounds is more soluble in the solvent than the other. After spin coating it is still swollen with the solvent which evaporated later, that lower the height of its regions relative to the other material, giving the lumps. Annealing at 50^{o}C below the three critical annealing temperatures has a smaller affect on the surface morphology and phase separation. A smooth film with low contrast is shown. At 100^{o}C the temperature is past the glass transition temperature of compound **1** so it shows some freedom to move and diffuse which shows the appearance of some low height features. As the temperature increases to become higher or closer to the critical points the features size and height increase and the surface becomes rougher, because of the greater freedom of the molecules to move and diffuse.

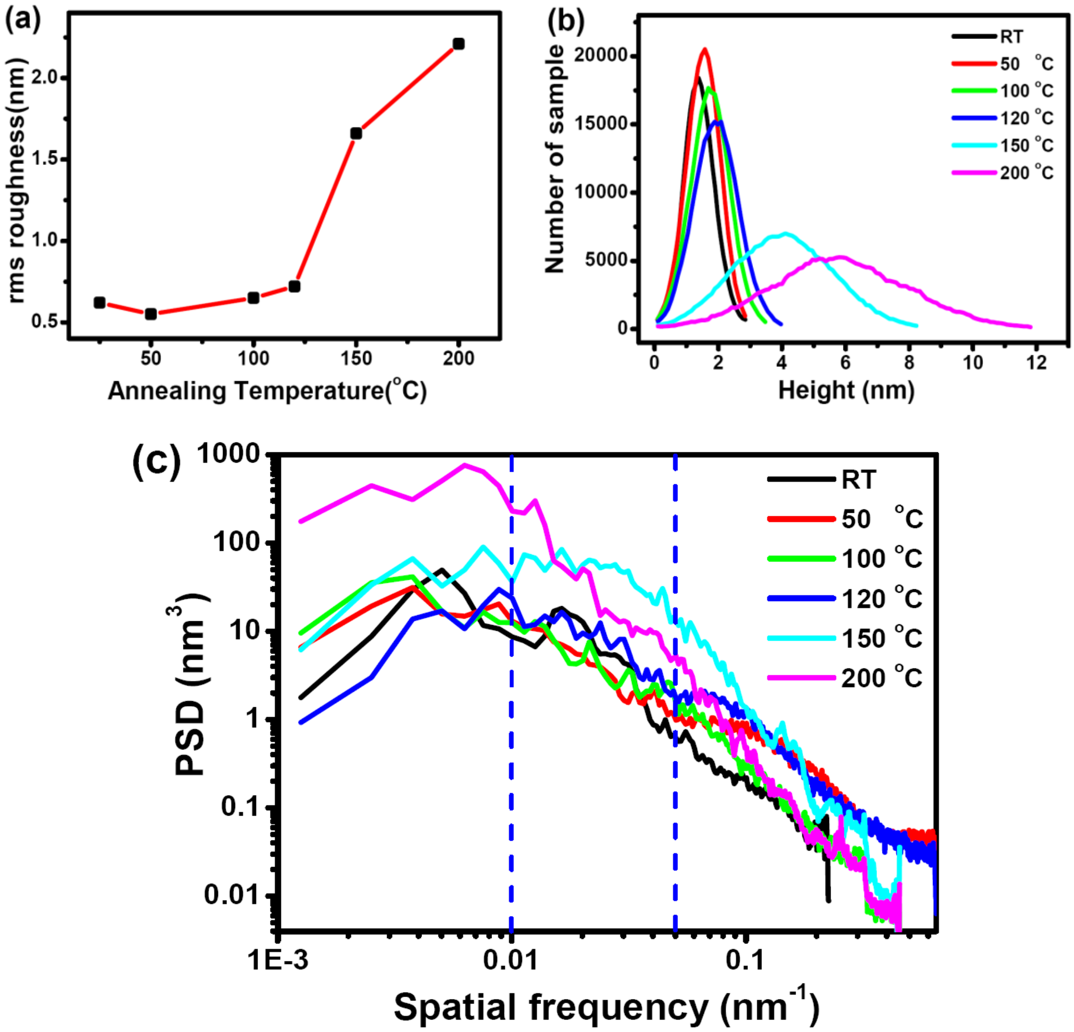

Figure 4-17: Surface roughness analysis for the six blends,(a) rms roughness, (b) height distribution, (c) PSD as a function of spatial frequency.

Figure 4-17 shows the corresponding rms roughness, height distribution, and PSD respectively which illustrate the variation of the nanoscale morphology as a function of annealing temperature. It confirms what is shown visually in Figure 4-15 and figure 4-16. The rms values are 0.62nm, 0.55nm, 0.65nm, 0.72nm, 1.66nm, 2.21nm for RT (vacuum), 50^{o}C, 100^{o}C, 120^{o}C, 150^{o}C, and 200^{o}C annealing temperatures respectively, which shows the rms roughness increase following the temperature increase except for RT (vacuum) which shows a higher rms values compared to 50^{o}C.

The height distribution peaks are 1.4nm, 1.6nm, 1.7nm, 2.1nm, 4.1nm, and 6nm and so increase in order with temperature. Similarly the height variations follows the same increase with temperature and are 2.8nm, 2.8nm, 3.5nm, 4nm, 8.2nm, and 11.8nm respectively.

Annealing at 200^{o}C gives the roughest structure. This has the highest PSD amplitude over the first region (i), followed by the sample annealed at 150^{o}C with 10 fold less. The 120 ^{o}C annealed sample has the lowest PSD amplitude in this region. In the region (ii) the PSD of the 200^{o}C sample starts dropping to become less than that of the 150^{o}C sample while the PSD of the 120^{o}C sample become slightly higher than that from the other temperatures (RT,50^{o}C,100^{o}C). In the region (iii), corresponding to a fine structure, the sample annealed at 150^{o}C has the highest PSD up to the first quarter of this region where the samples annealed at 120^{o}C and 50^{o}C took over, and they do not decay as quickly as those at 100 ^{o}C, 150 ^{o}C, 200 ^{o}C and RT.

4.5. Conclusion

Nematic liquid crystals with a fluorene-thiophene structure in combination with a range of perylene-based compounds were shown in the previous chapter as promising materials for good electron-donating and electron-accepting pairs for PV blend devices. We show here that the thin film nanoscale morphology and phase separation of the ED/EA blends are affected by the chemical structures of EDs and EAs, the casting solvents and the annealing temperature of the film.

Four different perylene-based compounds were investigated as EAs in combination with **3** as ED in blends of 1:1 ratio to correlate the blend nanoscale morphology to the acceptor chemical structure and to nominate the most promising one to be used in the further investigation. The blends with **9**, **11**, **13** and **16** as EAs show large variations in surface nanoscale morphology. However the **3:9** blend has the smallest domain sizes, suggesting that **9** as EA might give better charge separation. Unfortunately, the blends with LC EAs **11** and **13** have quite different morphology.

Three solvents were investigated to find their suitability to assist nanoscale morphology with good phase separation. The solvents were toluene, chloroform and chlorobenzene. Toluene did not dissolve all our compounds as efficiently as the other two which limits its ability to mix the blend components. Chloroform and chlorobenzene were good solvents. However chloroform evaporates faster which results in fixing the components before phase separation happened. Therefore the chlorobenzene shows the best performance.

Three different nematic liquid crystals with the same fluorene-thiophene aromatic structure were investigated as EDs in combination with **9** as EA in blends of 1:2 ratio to correlate the blend nanoscale morphology to the donors chemical structure, as they have different terminals end groups. The EDs were **1**, **3** and **4** and the corresponding blends show some variation in surface nanoscale morphology. However the **1:9** blend has the finest in-plane structure, which can be related to the small phase separated domains, suggesting that it might give better charge separation.

The annealing temperature was investigated to find the suitable temperature to form an intermixed network of EDs and EAs with nanoscale morphology and phase separation. Blends of **1:9** in the mixing ratio of 1:2 were used, which were annealed at temperatures of RT, 50 ^{o}C, 100 ^{o}C, 120 ^{o}C, 150 ^{o}C and 200^{o}C. The blend annealed at 120 ^{o}C showed a relatively large number of small domains from the PSD analysis.

There were wide variations in the amplitude surface roughness among samples studied so it will be interesting to check for any correlation with PV performance in the next chapter.

4.6. References

[1] E. Moons, "Conjugated polymer blends: linking film morphology to performance of light emitting diodes and photodiodes," Journal of Physics-Condensed Matter **14** (47), 12235-12260 (2002).

[2] M. Voigt, J. Chappell, T. Rowson et al., "The interplay between the optical and electronic properties of light-emitting-diode applicable conjugated polymer blends and their phase-separated morphology," Organic Electronics **6** (1), 35-45 (2005).

[3] C. H. Lei, M. S. Al Khalifah, M. O'Neill et al., "Calamitic liquid crystal blends for organic photovoltaics - art. no. 705214," Organic Photovoltaics Ix **7052**, 5214-5214 (2008).

[4] H. Hoppe and N. S. Sariciftci, "Morphology of polymer/fullerene bulk heterojunction solar cells," Journal of Materials Chemistry **16** (1), 45-61 (2006).

[5] B. Kippelen and J. L. Bredas, "Organic photovoltaics," Energy & Environmental Science **2** (3), 251-261 (2009).

[6] H Hoppe, Johannes Kepler University Linz, 2004.

[7] S. Walheim, M. Boltau, J. Mlynek et al., "Structure formation via polymer demixing in spin-cast films," Macromolecules **30** (17), 4995-5003 (1997).

[8] C. R. McNeill, B. Watts, L. Thomsen et al., "Nanoscale quantitative chemical mapping of conjugated polymer blends," Nano Letters **6** (6), 1202-1206 (2006).

[9] H. Hoppe, T. Glatzel, M. Niggemann et al., "Efficiency limiting morphological factors of MDMO-PPV : PCBM plastic solar cells," Thin Solid Films **511**, 587-592 (2006).

[10] H. J. Snaith and R. H. Friend, "Morphological dependence of charge generation and transport in blended polyfluorene photovoltaic devices," Thin Solid Films **451**, 567-571 (2004).

[11] V. Djara and J. C. Bernede, "Effect of the interface morphology on the fill factor of plastic solar cells," Thin Solid Films **493** (1-2), 273-277 (2005).

[12] W. U. Huynh, J. J. Dittmer, W. C. Libby et al., "Controlling the morphology of nanocrystal-polymer composites for solar cells," Advanced Functional Materials **13** (1), 73-79 (2003).

[13] J. J. M. Halls, C. A. Walsh, N. C. Greenham et al., "Efficient photodiodes from interpenetrating polymer networks," Nature **376** (6540), 498-500 (1995).

[14] J. Loos, "The art of SPM: Scanning probe microscopy in materials science," Advanced Materials **17** (15), 1821-1833 (2005).

[15] S. H. Cohen and Marcia L. Lightbody, *Atomic force microscopy/scanning tunneling microscopy 3*. (Kluwer Academic/Plenum Publishers, New York ; London, 1999), pp.viii, 210 p.

[16] http://en.wikipedia.org/wiki/Atomic_force_microscope.

[17] K. C. Khulbe, C. Y. Feng, and T. Matsuura, *Synthetic polymeric membranes : characterization by atomic force microscopy*. (Springer, Berlin ; London, 2008), pp.xvii, 197 p.

[18] http://www.nanoscience.com/education/AFM.html.

[19] S. Morita, *Roadmap of scanning probe microscopy*. (Springer, Berlin, 2007), pp.xvii, 201 p. : ill. ; 225 cm.

[20] S. Amelinckx, *Handbook of microscopy : applications in materials science, solid-state physics and chemistry*. (VCH, Weinheim ; Cambridge, 1997), pp.xxv,p540-986.

[21] W. W. Scott and B. Bhushan, "Use of phase imaging in atomic force microscopy for measurement of viscoelastic contrast in polymer nanocomposites and molecularly thick lubricant films," Ultramicroscopy **97** (1-4), 151-169 (2003).

[22] C. H. Lei, K. Ouzineb, O. Dupont et al., "Probing particle structure in waterborne pressure-sensitive adhesives with atomic force microscopy," Journal of Colloid and Interface Science **307** (1), 56-63 (2007).

[23] D. C. Coffey, O. G. Reid, D. B. Rodovsky et al., "Mapping local photocurrents in polymer/fullerene solar cells with photoconductive atomic force microscopy," Nano Letters **7** (3), 738-744 (2007).

[24] B. J. Leever, M. F. Durstock, M. D. Irwin et al., "Spatially resolved photocurrent mapping of operating organic photovoltaic devices using atomic force photovoltic microscopy," APPLIED PHYSICS LETTERS **92**, 013302 (2008).

[25] T Vorburger and J Fu, "In the rough," spie's oemagazine, 31-34 (2002).

[26] D. J. Whitehouse and D. J. Handbook of surface metrology Whitehouse, *Handbook of surface and nanometrology*, Rev. and expanded ed. ed. (Institute of Physics Publishing, Bristol, 2003), pp.xx, 1150 p.

[27] *WYKO surface profilers technical reference manual.* (1999).

[28] Eugene Hecht, *Optics*, 4th ed., International ed. ed. (Addison-Wesley, San Francisco ; London, 2002), pp.vi, 698 p.

[29] Steven W. Smith, *The scientist and engineer's guide to digital signal processing*. (California Technical, San Diego, Calif., 1997), pp.xiv, 626 p.

[30] R. Gavrila, A. Dinescu, and D. Mardare, "A power spectral density study of thin films morphology based on AFM profiling.," Romanian journal of information science and technology **10** (3), 291-300 (2007).

[31] S.E. Shaheen, C.J. Brabec, and N.S. Sariciftci, "2.5% efficient organic plastic solar cells," Applied Physics Letters **78** (6), 841 (2001).

[32] H. Wang and R. J. Composto, "Thin film polymer blends undergoing phase separation and wetting: Identification of early, intermediate, and late stages," Journal of Chemical Physics **113** (22), 10386-10397 (2000).

5. DEVICE FABRICATION AND CHARACRARIZATION

5.1. Device Fabrication

The general configuration of solar cell devices, fabricated in this thesis, is illustrated in figure 5-1; showing cells consisting of several layers. The preparation processing and fabrication of each layer will be detailed in the following sections.

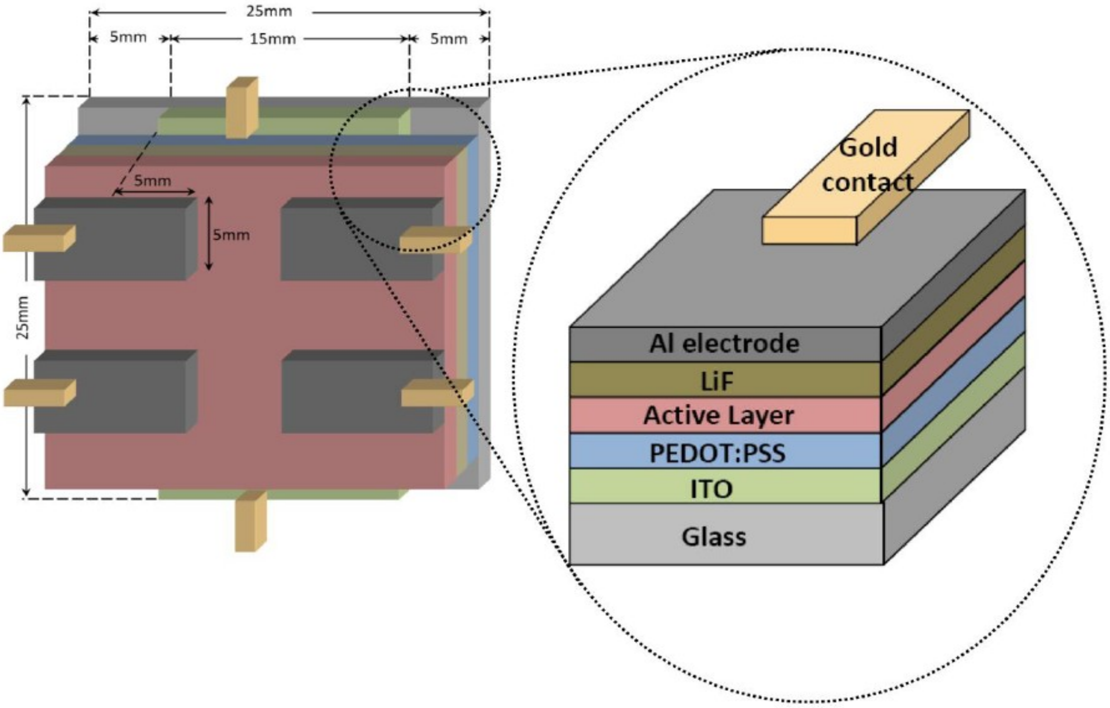

Figure 5-1: The device configuration of an organic PV solar cell with an undefined organic active layer where light is absorbed and charge is separated.

5.1.1. Preparation of the Substrate and Bottom Electrode

The device properties such as device reliability and stability are not only dependent on the properties of components of the active organic layers, but also affected by each layer of the device and also the interfaces between these layers. The bottom electrode is one of the key factors to consider for the optimization of the solar cell performance.

The PV cells were fabricated on a 150 nm thick layer of indium tin oxide (ITO) commercially pre-coated onto a glass substrate having sheet resistance of 13 $\Omega/\square$ and supplied cut into 25mm squares. The substrate was first cleaned by immersion in an ultrasonic bath using the following liquids, times and temperatures: (i) detergent (SVC 150) for 30min at 60^{o}C, (ii) de-ionized water for 15min at 60^{o}C, repeated twice to remove the detergent from the substrate. (iii) acetone 15min at RT, (iv) isopropyl alcohol 15min at RT, followed by blowing dry with nitrogen gas. Photolithography with an acid etch was used to remove a 5mm strip of ITO from two sides of the substrates in order to prevent any contact between the top and bottom electrodes. The substrates were sonicated twice in acetone followed by a repeat of the initial cleaning processes to remove the remaining photo resist material, used in the etching process.

Because of the morphology of the interface between the ITO and the active material, together with contaminants on the ITO surface, a barrier is formed which inhibits hole transport from the active layer to the external circuit. This barrier height affects the I–V characteristics of the device[1]. It is proven that the work function of the ITO is affected by the modification and treatment of its surface[2,3,4,5,6]. In addition, ITO-induced degradation mechanisms, which cause release of oxygen from the electrode, can lead to the creation of trapping centres. Many techniques have been attempted to modify the ITO surface in order to optimize the interface morphology and remove the contaminants from the ITO surface which reduce the hole-transport barrier. The most effective method appears to be O_2 plasma treatment[7].

The plasma treatment subjects the surface of the ITO to bombardment with large ions. This smoothes the surface by abrading the peak features and also causes the release of trapped contaminants, a lot of which adhere to the ITO making further cleaning a necessity. Cleaning was accomplished by sonicating the substrate in water, then acetone and finally isopropyl alcohol, 10min for each process at RT. Water is good for removing the hydrophilic contaminants while acetone removes the organic and the hydrophobic materials (sometimes a stronger organic solvent is used). The final use of the isopropyl alcohol is to get rid of the residual water and acetone. The substrates are then blown dry using nitrogen gas before being moved to the glove box admittance chamber, where they are placed under vacuum for a while to dry out any remaining solvent, after which they are introduced into the glove box nitrogen environment where cell fabrication takes place.

5.1.2. Preparation of PEDOT: PSS Layer

The poly(3,4-ethylenedioxythiophene) PEDOT is an organic polymer material with good electronic conductivity, optical clarity and environmental stability, properties required for successful opto-electronic devices[8,9]. However it is infusible and insoluble, and so is difficult to process in a thin film form by either wet or dry processing techniques. A new type of PEDOT, doped with poly(styrenesulfonate) (PSS), is water soluble. PEDOT:PSS is used to increase the work function of the ITO electrode and also acts as a physical barrier to many defect sites known to be present in ITO[8,10,11].

Commercially prepared PEDOT: PSS (Baytron P VP. AI 4083) in water based solution was sonicated at RT for 5min in order to dissolve any clumps within the solution. Immediately after plasma treatment and cleaning of the ITO the PEDOT:PSS was spin-coated onto the ITO surface at 4000 rpm spin speed and 2000 rpm^2 acceleration with a spin duration of 30 seconds, to form a uniform layer. The substrate was then placed on a temperature controlled hot stage and cured at 120 ^{o}C for 30 min to evaporate the water, followed by 220 ^{o}C for 5 min to thermally polymerize the PEDOT. Finally the temperature was ramped to room temperature at a cooling rate of 10^{o}C/min.

5.1.3. Preparation of the Bulkheterojunction Active Layer

The active layer of a PV device can be configured as double layers, bulk heterojunction (BHJ) etc. as discussed in section 1.8.

For BHJ configuration, measured amounts of electron-acceptor and donor materials were mixed in a sample tube to give the desired weight percent of the mixture. This was then dissolved in an organic solvent (e.g. toluene). The solution was spin cast at 2000 rpm spin speed and 560rpm^{2} acceleration for 30s on top of the PEDOT: PSS layer, applied using a syringe fitted with a 0.02 µm filter to remove un-dissolved large particles in the solution. The substrate was then placed on a hot stage and annealed typically at 120^{o}C for 1hr which caused the solvent to evaporate and improved the morphology of the interface between layers. After annealing, the sample was cooled to room temperature at a fixed rate of 10^{o}C/min.

5.1.4. Preparation of Top Electrode by Vapor Deposition

Electrode fabrication was carried out inside a vacuum vapour deposition unit equipped with a quartz crystal film thickness monitor that was used to determine the thickness of the films and the deposition rate. The sample was placed inside the vacuum chamber and mounted upside down above a shadow mask with cut-outs for the four electrodes, as shown in figure 5-2. The chamber was then evacuated to ~$3x10^{-7}$ Torr. A layer of LiF about 0.6nm thick was vapor deposited onto the sample, followed by deposition of around 80nm of Al to form the top electrode. The LiF was used to enhance transport of electrons to the external circuit by reducing the height of the electron barrier between the top layer and the Al electrode.

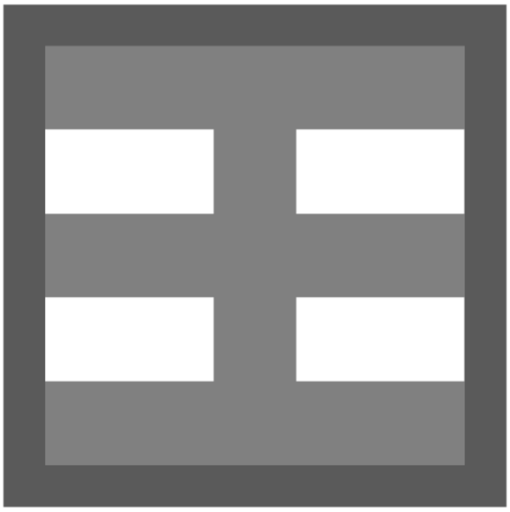

Figure 5-2: The top electrode shadow mask

5.1.5. Preparation of the Device for Characterization

All the previous fabrication steps were carried out in a nitrogen environment inside a glove box as the organic compound suffers degradation and trapping sites can be created in the presence of oxygen and moisture, especially during the heating and cross-linking processes. To allow measurements outside the glovebox, the devices were mounted in a sealed test chamber equipped with a quartz window, and a glass to metal seal, with feed-throughs for the electrical connections. A mounting frame with spring loaded clips held the devices in place against contacts, for the ITO electrode, and four contacts touching the Al electrodes,

5.2. Devices Characterisation:

5.2.1. J-V Curve

As we mentioned in section 1-5 solar cells have a rectifying behaviour like diodes. The solar cell admits current in the forward bias direction (V>0) and blocks the current when reverse biased (V<0) in the dark as shown in figure 1-14. Under illumination the curve is shifted due to an increase in the current, caused by the addition of the induced photocurrent, in the 3rd and 4th quadrant. The J-V curve was plotted on a log scale, which is a useful method to characterize solar cells, as it can be used to measure most of the solar cell's parameters such as: (i) the open circuit voltage V_{oc}, (ii) the short circuit current density J_{sc} (A/cm^2) as shown in figure 5-3.

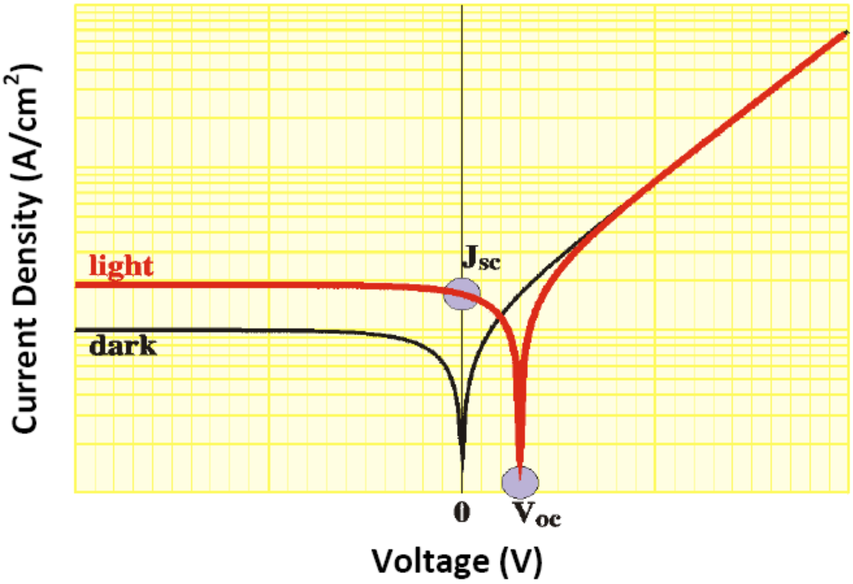

Figure 5-3: The J- V curve in log scale, which can be used to measure I_{sc} and V_{oc} as shown.

The electric power density in the output circuit can be calculated as P = JV (mW/cm^2), where the maximum power point P_{max} is the maximum value of JV within the voltage range between zero and V_{oc}. The solar cell fill factor FF, the power conversion efficiency PCE (%), and the external quantum efficiency EQE, mentioned in section 1.5.3 can be measured using eq. 1-12, eq. 1-13, and eq. 1-14 respectively.

The series resistance R_s and the shunt resistance R_{sh} is measured using the (J-V) curve plotted using a linear scale as illustrated in section 1.4.2.

5.2.2. Photocurrent versus Wavelength

The photocurrent varies with the wavelength of the incident light depending on the energy gap between HOMO and LUMO of the active materials as explained in section 1.5.1. Most of the organic materials absorb in the UV and short wavelength end of the visible spectrum, while the aim is to cover the full solar spectrum and to shift the absorption towards, and into, the infrared. A plot of the photocurrent versus wavelength is important in understanding the effective wavelength range of the device for operation as a solar cell.

From the photocurrent curve we can measure the external quantum efficiency (EQE) as a function of wavelength (λ) using eq.1-14. The optical power density of the incident light, P_o (λ) is obtained by measuring the light power of one wavelength of the spectrum and then using the calibration curve of the light source to compute power at other wavelengths.

5.2.3. Intensity Dependence of Solar Cells Parameters

We change the light intensity, P_o, by means of an array of interchangeable optical neutral density filters, with different transmission. The photovoltaic parameters are obtained for different light intensities in order to study the affect of the variation of light intensity on the electrical properties of a solar cell.

5.3. Experimental Setup

The experimental setup used in this work for the current-voltage (I-V) characterization and photocurrent spectral measurements is illustrated in figure 5-4.

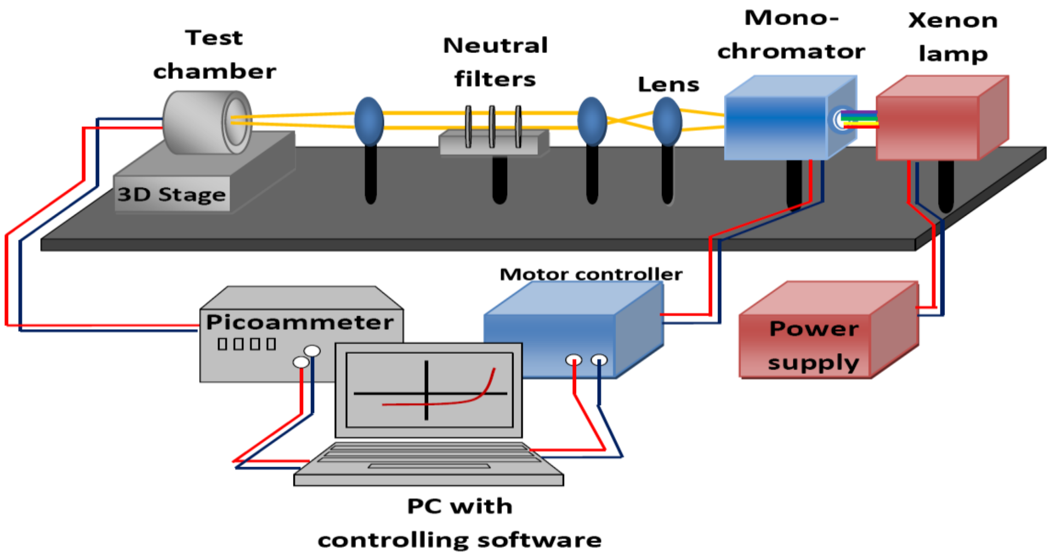

Figure 5-4: schematic diagram of the measurements set up

A voltage waveform generator (incorporated in the computer) supplies voltage to the device, the current through it being measured by a picoammeter, also attached to the computer. The data is displayed and saved using home written software.

A Xenon lamp (Bausch & Lomb) with its power supply was used as an illumination source, as it provides high light intensity and also emits a continuous spectrum, ranging from ultraviolet through visible to infrared. A motorized monochromator (Bausch & Lomb) was used to vary the wavelength of the light for photocurrent spectrum measurement. The monochromator is connected to a computer based controller with software to control wavelength selection.

A set of lenses collimates the light and focuses it, perpendicular to the chamber, to cover almost all the active area of the selected device (the overlapping area between the top and bottom electrodes), which is about 25mm^2. A power meter (Coherent Fieldmaster) is used to measure the power of the illumination, with selected neutral density filters inserted in the collimated light path to control the light intensity. The test chamber, enclosing the device, was mounted on top of an adjustable 3D stage, which was used for focusing the light on the selected active area.

5.4. Results and Discussion

As discussed in chapter one the power conversion efficiency of the solar cells depends on; (i) light absorption and exciton production, (ii) exciton diffusion and dissociation, and (iii) charge transport and collection.

The synthetic chemistry branch of the Organophotonics group at Hull University synthesized a set of organic conjugated materials to be used as electron donors (EDs) and electron acceptors (EAs) for organic photovoltaic devices (OPV) in the search for good materials to fulfill the above criteria. The compounds they produced have been studied extensively in the last three chapters based on energy levels and optical properties, charge transporting properties, and morphological properties respectively. The most promising materials are discussed in this chapter as the active materials in BHJ solar cells. The processing conditions are varied to find the optimal condition. The performance of the solar cells is then related to the nanoscale morphology of the active layer.

Table 2-1 shows the chemical structure of the materials used in this thesis. Compounds **1, 3** and **4**, which are nematic liquid crystals with the same aromatic core have been chosen to be EDs. **1** has methoxy terminal groups, whilst **3** and **4** are reactive mesogens, which can be photochemically polymerized to form a LC polymer network, with the help of alkyl chain spacers linked with diene end groups for **3** and methacrylate end groups for **4.** Compounds **9, 11, 13** and **16** are perylene bisimide derivatives with different functional groups. These have been chosen to be used as EAs. Table 2-1 shows the transition temperatures of these compounds. Compounds **1, 3** and **4** are nematic LCs with no detectable melting point. They form long-lived nematic glasses at room temperature on rapid cooling of a thin film from the isotropic liquid. Compound **13** exhibits a monotropic smectic C liquid crystal and forms a metastable supercooled LC phase in a thin film for room temperature processing. Compound **11** forms a nematic phase at high temperature, above a very high melting point, whereas compounds **9** and **16** do not exhibit observable liquid crystalline phases and just melt at 274 °C and 182 °C, respectively.

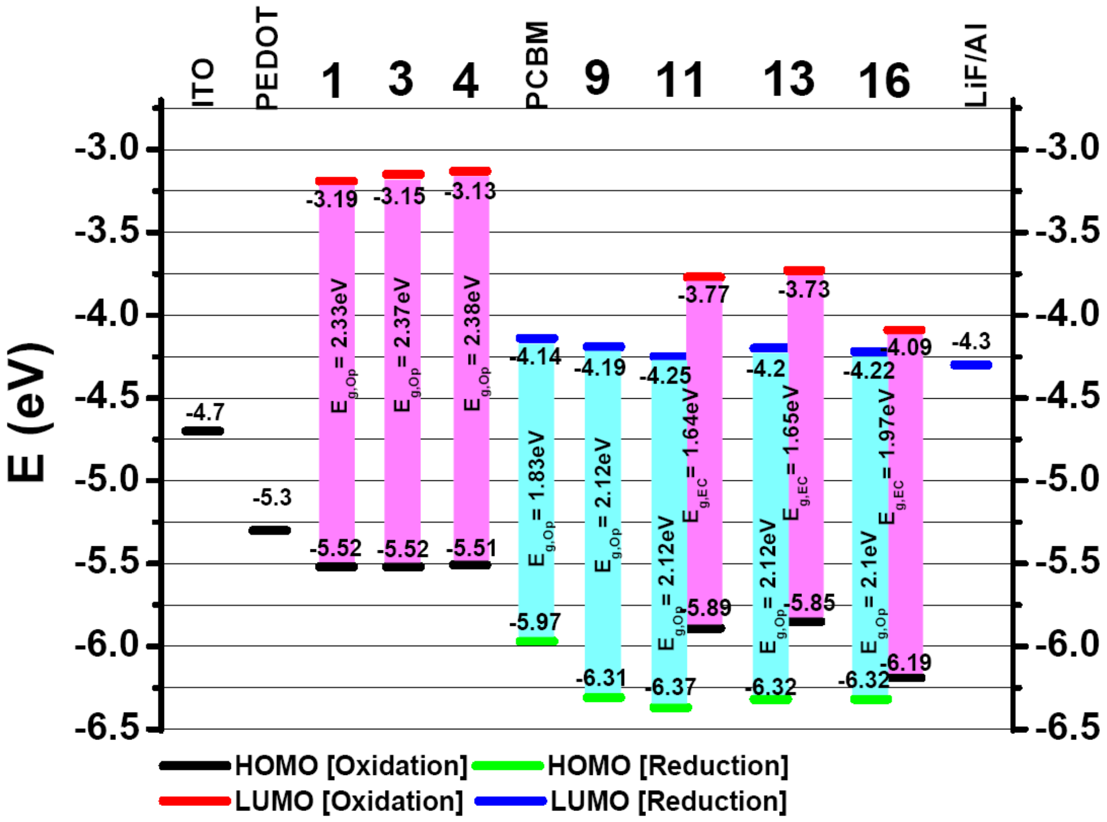

Figure 5-5: The energy levels of compounds 1, 3, 4, PCBM, 9,11,13,16 incorporated with the work function of the ITO, PEDOT: PSS, and LiF/Al.

Figure 5-5 shows the HOMO and LUMO energies of the nominated materials as EDs, and EAs in comparison with PCBM. The energies depend on the chemical structure of the aromatic core of the molecules, so compounds **1, 3** and **4** have the same HOMO, the low value of which 5.52 eV confirms their stability (below the air oxidation level), and suitability as the electron-donating species in the OPV blend. The LUMO values measured using the reduction onset of compounds **9, 11, 13** and **16** are similar, between 4.19 eV and 4.25 eV, which confirms their suitability as EA for the OPV devices, whilst the LUMO values measured using the oxidation onset are 3.73, 3.77 and 4.09 eV for **13, 11,** and **16** respectively, **9** however could not be measured because it has a high oxidation energy which is out of the range of the experimental setup used for measurements.

The frontier orbital energy offset between the EDs and the EAs is an important electrical characteristic of the OPV. The LUMO offset is in the range 1eV - 1.12eV, with the HOMO offset in the range 0.79 eV – 0.8 eV. The difference between the HOMO of **1, 3** and **4** and the LUMO of **9, 11, 13** and **16** is in the range 1.27 eV - 1.32 eV, which determine the maximum limit of the open circuit voltage V_{oc} as shown in eq. 2-2. This energy difference is smaller than the energy of the absorption band-edge of the materials, around 2.38 eV for **1, 3**, **4** and 2.12 eV for **9, 11, 13** and **16** making charge separation at the donor-acceptor interface thermodynamically favorable, resulting in the electron being located in the LUMO level of acceptor material and the hole in the HOMO of the donor.

Following the dissociation of the charges, good transport properties are required for the electrons in the EAs and holes in the EDs to be collected at their respective electrodes. The electron mobility of compounds **1, 3** and **4** could not be measured as shown in chapter 3, however the hole mobility of **1** is the highest of the three EDs and is $1.45\text{x}10^{-3}$ $\text{cm}^2\text{V}^{-1}.\text{s}^{-1}$ at room temperature and $1.6\text{x}10^5\text{cm.V}^{-1}$ applied electric field, followed by **4,** and **3** respectively. These compounds have the same core, with structural difference in the terminal end groups as mentioned before, so the mobility variations can be related to the effect of the terminal end groups on the molecular packing and morphology.

For compounds **9, 11, 13** and **16,** both the hole and electron mobility were found. In chapter three we introduced the ratio of electron mobility to hole mobility (μ_e/μ_h) as a function of the applied electric field as illustrated in figure 3-34. Compounds **11** and **13** show a very small variation with field compared to **16** where the ratio increases with an increase of the applied electric field. **9** shows an increase with a decrease of the applied electric field, which indicates this material to be more efficient as n-type at lower applied electric field – in the range of the built in electric field of 10^4-10^5 V/cm.

The mobility of the blends **9:3** and **9:4** have been investigated using different weight ratio as illustrated in figure 3-44 and 3-45. The blends show very large increase of the electron and hole mobility compared to **9** and a smaller decrease in the hole mobility compared to **3** and **4** as pristine compounds. The TOF charge photoinjection of the blends shows a large improvement, as it require a very low power laser pulse compare to the pristine compounds, up to thirty times less as discussed in section 3.6.4, which suggest that the charge separation is significantly more efficient in blends.

Finally the morphology of the active layer is expected to have an influence on the optical and electrical properties as well as the OPV devices power conversion process. As discussed in chapter one, distributed interfaces are needed to maximize charge separation. These can be formed in phase-separated blends of electron-donor compounds (EDs) and electron acceptor compounds (EAs) with continuous paths to the respective electrode. It is critically important to optimise the grain size of the blend to maximize carrier collection and avoid recombination. Too intimate mixing results in electron-hole recombination before collection at the electrode, whereas the exciton recombines before separation, if the grain size is too coarse. Optimised grain sizes have been obtained in polymers by appropriate choice of solvent and casting conditions[12] and in low-molar-mass materials by annealing of a co-evaporated blend[13].

In this chapter single layer blends are prepared for PV devices and their performance is correlated with nanoscale morphology, based on the nanoscale morphology investigation in the previous chapter.

5.4.1. The Evaluation of Perylene Bisimide Derivatives as Electron Acceptors for OPV Devices

Photovoltaic devices of different blends were produced using identical processing conditions as illustrated in section 5.1. Compound **3** was used as ED for all blends, the EAs **9, 11, 13** and **16** were studied to evaluate their suitability for photovoltaic blends, based on their functional group. The devices' active layers were prepared by spin casting a solution of different ED and EA pairs in the ratio of 1:1 by weight in toluene (15 mg ml^{-1}) on the substrates. The films were then annealed at 120 °C for 60 mins.

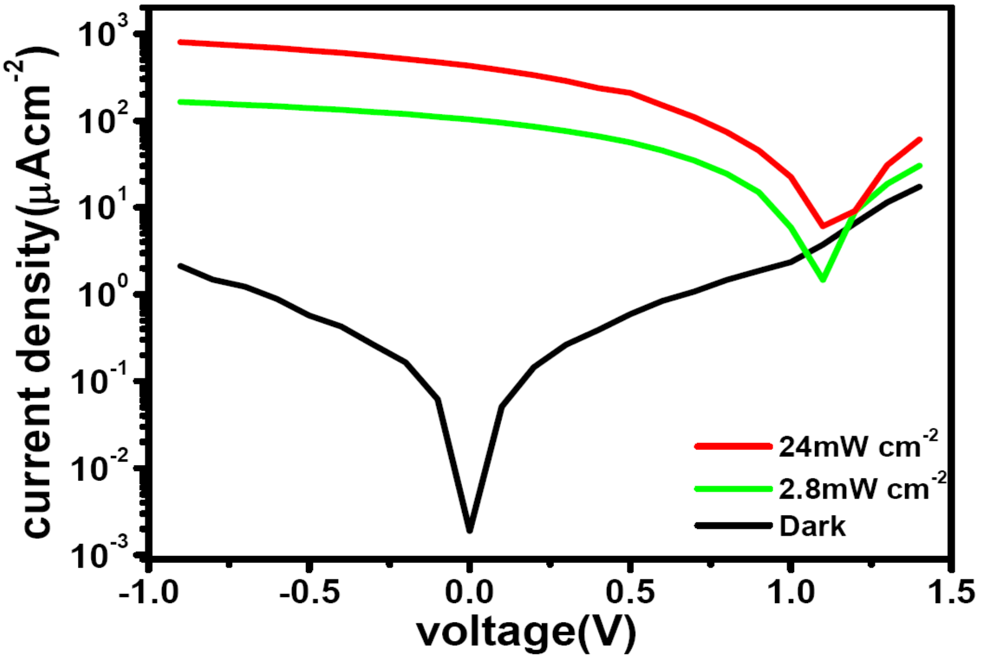

Figure 5-6: The current density versus voltage of the photovoltaic device incorporating a thin film of a 1:1 blend of 3 and 9. The labels give the irradiance in mW cm^{-2} of the input light source of wavelength 470 nm.**

Figure 5-6 shows current-voltage characteristics of a PV device made from a blend of **3** and **9** in the dark and on irradiation at 470 nm, the peak of the photocurrent action spectrum. The photocurrent and the open circuit voltage, V_{oc}, change with input irradiance as will be detailed in section 5.4.1.4. The maximum V_{oc} value of 1.15 V approaches the limit of 1.32eV, equal to the energy difference between the HOMO and LUMO energies of the electron-donor and acceptor. The power conversion efficiency (PCE) was 0.43 % when the input irradiance is 24 mW.cm^{-2}.

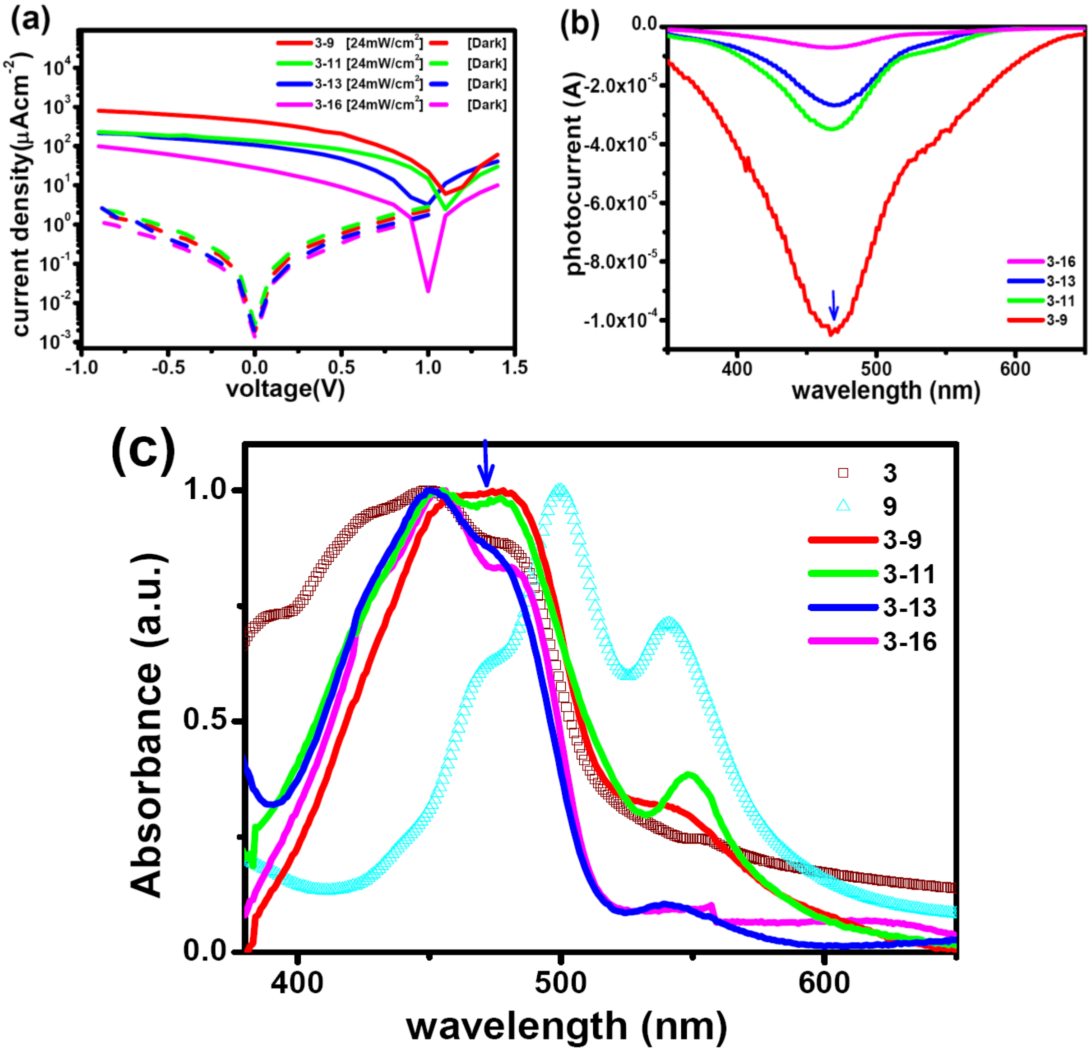

Figure 5-7: (a) The current density versus voltage for the different photovoltaic devices consisting of 1:1 blends of the materials specified in the inset labels, where the irradiance of the input light source of wavelength 470 nm is 24mW cm^{-2}, b) Photocurrent action spectra for the devices, c) Absorption spectra of thin films of blends prepared using identical conditions to those in devices. The arrow marks the excitation wavelength, which gives maximum photocurrent.**

Figure 5-7(a) shows the current-voltage characteristics of a PV device made from the four blends in the dark and on irradiation at 470 nm with an input irradiance of 24mW cm^{-2}. Figure 5-7(b) shows the photocurrent action spectrum for the four devices illustrating the peak of the photocurrent action to be around 470nm wavelength. Figure 5-7(c) shows the absorption spectra of the thin film blends prepared similarly to those used in the PV devices, as well as the absorption spectra of **3** and **9,** where **9** shows similar absorption features to the other EAs. The photocurrent peaks at 470nm wavelength for all devices and the photocurrent action spectra match fairly closely the absorption spectra of the blends. The peaks of the absorption spectra occur at the overlapping region of the blend components. The blends **3:9** and **3:11** absorb more in the red region and show the highest solar cell performance respectively.

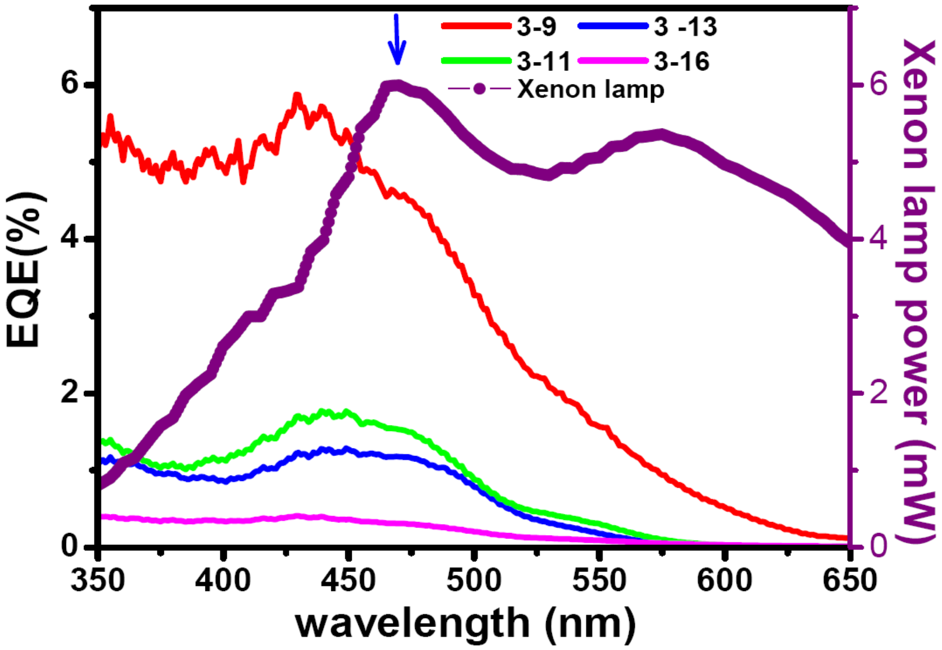

Figure 5-8: The external quantum efficiency for the different photovoltaic devices consisting of 1:1 blends of the materials specified in the inset labels. The power spectrum of the input light source is also shown.

Figure 5-8 shows the external quantum efficiency EQE of the four blends as a function of the incident light wavelength incorporated with the power spectra of the xenon lamb light source. The EQE shows higher values in the shorter wavelengths with low light power, then decreases gradually just before the maximum light power peak. From 450nm the EQE mirrors the absorption spectrum of the ED suggesting that donor absorption generates more current than acceptor absorption.

Table 5-1: Performance parameters for the PV blend devices on excitation with 24 mW.cm^{-2} at 470 nm

Blend compounds	V_{oc} (V)	J_{sc} mA cm^{-2}	P_{max} mW cm^{-2}	FF	EQE (%)	PCE (%)
3:9	1.15	0.428	0.104	0.211	4.5	0.43
3:11	1.1	0.138	0.041	0.27	1.53	0.17
3:13	1	0.106	0.024	0.227	1.18	0.1
3:16	1	0.028	0.0047	0.168	0.31	0.02

Table 5-1 summarises the performance of the PV devices with different EAs. The best solar cell performance is obtained with **9** as EA, and the performance of the devices using the other EAs decreases in the order **11** > **13** > **16**.

Charge separation depends on the HOMO and LUMO energy alignment. As shown in figure 5-5, the LUMO energies of the EAs are similar, so the thermodynamics of charge separation cannot explain the difference in device performance. **11** and **13** show ambipolar transport.

Both charge separation and transport depend on molecular packing and the spatial scale and geometry of the phase separation of ED and EA blends, investigated in section 4-4-1. The poor performance of the **3:16** device may be explained by the large numbers of pinholes in the thin film which may act as carrier traps. The superior performance of the **3:9** blend device in comparison to the **3:13** and **3:11** devices may be explained by the morphology. The distribution of domain sizes of the **3:9** device shown by the PSD is more homogeneous with higher values for the domain sizes less than 20nm compared to the others. The **3:11** blends both have much coarser features. The phase contrast between the domains of **3:13** is greater than that of the **3:11** blend which indicates the appearance of the two compounds on the top surface. This implies that phase separation is more complete in the former, which may explain its poorer PV performance compared to the **3:11** blend.

Another possible explanation for the relatively poor performance of devices with **11** and **13** relate to the donor-acceptor nature of these compounds. The difference between the HOMO (oxidation) of ED and EA is relatively low and hole transport in the EA is efficient. Hence there is a relatively high probability of hole transfer to the EA and subsequent recombination of holes and electrons in the EA. Note that the electron mobility of **16** is very good which does not correlate with device performance.

5.4.2. The Effect of Casting Solvent on the BHJ Solar Cell Performance

Photovoltaic devices of different blends were produced using identical processing conditions as in the previous section but with a variety of solvents, **3** was the ED for all blends and **11** was the EA. The active layer were prepared by spin casting a solution of ED and EA in the ratio of 1:1 by weight of different solvents on the substrates to evaluate the suitability of the various solvents for photovoltaic blend. Toluene, chloroform, and chlorobenzene (15 mg ml^{-1}) the solvents used. The films were then annealed at 120 °C for 60 mins.

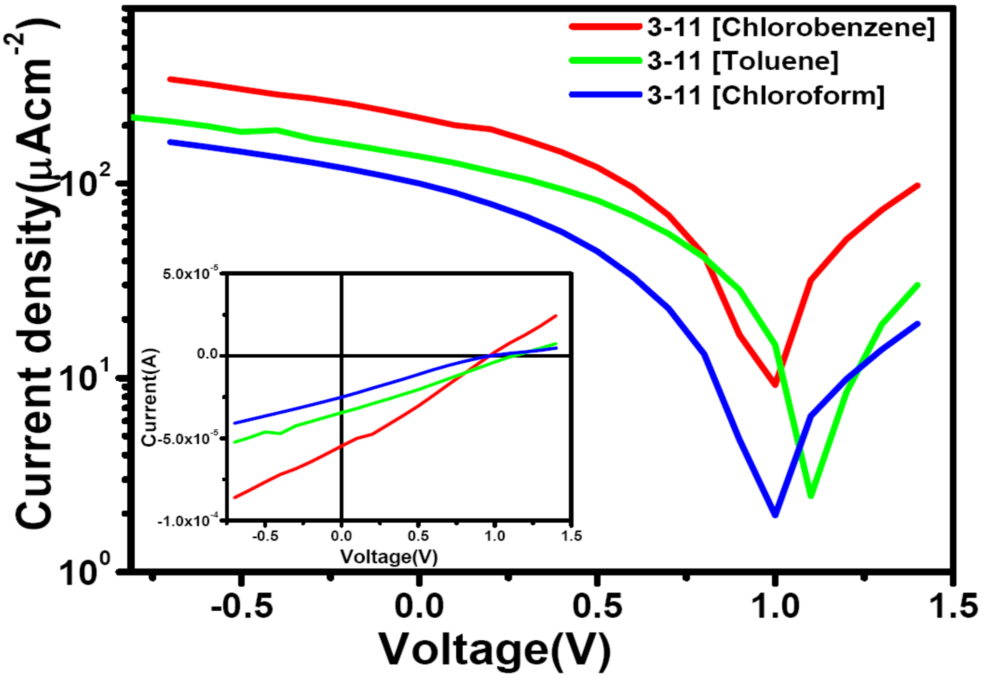

Figure 5-9: The current density versus voltage of the photovoltaic device incorporating a thin film of a 1:1 blend of 3 and 11 using different solvents.**

Figure 5-9 shows the current-voltage characteristics of the **3:11** blend devices using different solvents and irradiated at 470 nm. The power conversion efficiency (PCE) is 0.25, 0.17 and 0.09 % for chlorobenzene, toluene, and chloroform devices respectively when the input irradiance is 24 mW.cm^{-2}. The other PV parameters of J_{sc}, P_{max}, FF, and EQE vary in the same way as shown in table 5-2 apart from the V_{oc} which was higher with the toluene compare to other solvents.

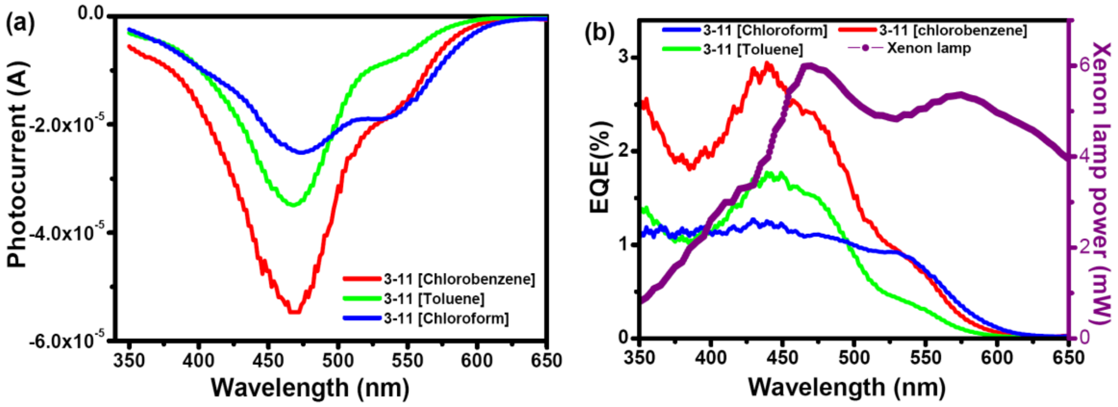

Figure 5-10: a)The Photocurrent action spectra for the different photovoltaic devices incorporating a thin film of a 1:1 blend of 3 and 11 using different solvents specified in the inset labels, b) The external quantum efficiency for the devices.**

Figure 5-10(a) shows the photocurrent action spectrum of PV devices made using the three different solvents with an input irradiance of 24mW cm^{-2}. The peaks of the photocurrent action spectra are around 470nm. Figure 5-10(b) shows the external quantum efficiency EQE of the three blends as a function of the incident light wavelength incorporated with the power spectrum of the xenon lamb. The EQE of the blends shows a similar spectral trend as before.

Table 5-2: Performance parameters for the 3:9 PV blend devices using different solvent on excitation with 24 mW.cm^{-2} at 470 nm.

Solvents	V_{oc} (V)	J_{sc} mA cm^{-2}	P_{max} mW cm^{-2}	FF	EQE (%)	PCE (%)
Chlorobenzene	1	0.219	0.061	0.278	2.41	0.25
Toluene	1.1	0.138	0.041	0.27	1.53	0.17
Chloroform	1	0.1	0.0226	0.226	1.1	0.09

Table 5-2 tabulates the performance parameters of the devices fabricated with different solvents. The chlorobenzene cast device shows the best solar cell performance, followed by toluene then chloroform devices.

As we are using the same blend compounds, the variation of the solar cells' performance can be related to the variation of the nanoscale morphology of the thin films produced with different casting solvents. The molecular packing and phase separation of ED and EA blends is affected by the solubility of the compounds in the solvent and the speed of solvent evaporation from the thin film, as discussed in section 4.4.2.

The sample cast from toluene shows elongated domains with high surface roughness and large domain sizes. In contrast the chlorobenzene cast film has low roughness and a higher concentration of fine domains less than 20 nm. This can be related to the lower performance of the toluene devices compared to the chlorobenzene one. However chloroform also shows fine structure, but as illustrated in the previous chapter the chloroform evaporates quickly compared to chlorobenzene and toluene, which results in quenching and fixing the molecules in non-equilibrium positions before they can self-assemble and phase separate.

The poor performance of the toluene device compared to the chlorobenzene one can be related to the too coarse grain size, which causes the excitons to recombine before charge separation is achieved. Possibly the non ideal intermixing of EDs and EAs using chloroform results in more recombination centers for electrons and holes before collection at the electrode.

5.4.3. The Effect of Spacers and End Groups on the BHJ Solar Cell Performance

Photovoltaic devices of different blends were produced using identical processing conditions as in the previous sections. **1, 3,** and **4** were compared as EDs for different blends with **9** as EA, since it is the best of the different acceptors. The active layers of the devices were prepared by spin casting a mixture of different ED and EA pairs in the ratio of 1: 2 by weight in the best solvent, Chlorobenzene (15 mg ml^{-1}), onto the substrates. The films were then annealed at 120 °C for 60 mins.

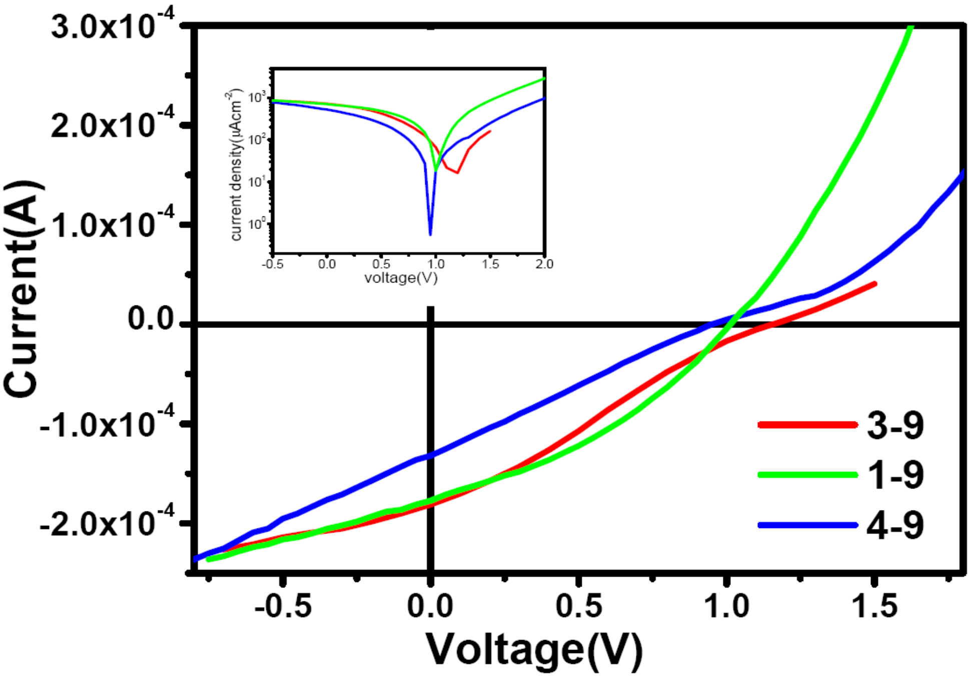

Figure 5-11: The current density versus voltage of the photovoltaic device incorporating a thin film of a 1:2 blend of 1,3 and 4 as ED and 9 as EA in chlorobenzene. The inset shows the same plots on a semi-log scale.

Figure 5-11 shows current-voltage characteristics of the three PV blend devices at 470 nm. The power conversion efficiency (PCE) is 1.14, 0.96 and 0.55 % for the devices with EDs **1, 3,** and **4** respectively when the input irradiance is 22 mW.cm^{-2}, **3:9** has the highest J_{sc} and V_{oc}, whereas **1:9** has the best rectifying properties with a higher P_{max} and FF. The performance of device **4:9** was inferior to that of the other devices as shown in table 5-3.

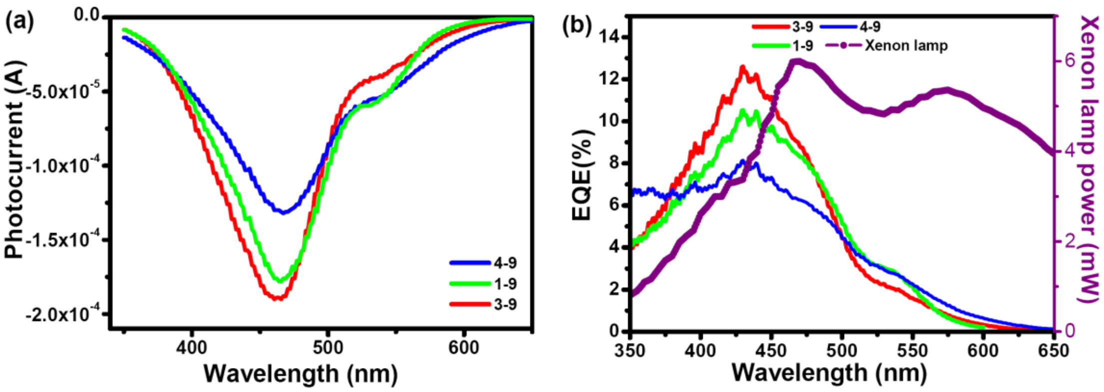

Figure 5-12: a) The Photocurrent action spectra for the different photovoltaic devices incorporating a thin film of a 1:2 blend of the materials specified in the labels, b) The external quantum efficiency of the devices.

Figure 5-12(a) shows the photocurrent action spectrum of PV devices made from the three blends, with an input irradiance of 22 mW.cm^{-2}, illustrating the peaks of the photocurrent action to be around the wavelength of 466nm. Figure 5-12(b) shows the external quantum efficiency EQE of the three blends as a function to the incident light wavelength incorporated with the power spectrum of the xenon lamb. The EQE of all the blends peaks at a wavelength of 430nm. The performance parameters of the devices are tabulated in table 5-3.

Table 5-3: Performance parameters for the PV devices on excitation with 22 mW.cm^{-2} at 466 nm.

Blend compounds	V_{oc} (V)	J_{sc} mA cm^{-2}	P_{max} mW cm^{-2}	FF	EQE (%)	PCE (%)	R_s KΩ	R_{sh} KΩ
1:9	1	0.708	0.252	0.356	8.31	1.14	2.5	11.2
3:9	1.2	0.724	0.214	0.246	8.8	0.96	3.9	10.5
4:9	0.95	0.528	0.124	0.247	6.3	0.55	11.4	7.6

The **1:9** blend show the best performance, and the performance of the EDs decreases in the order **1** > **3** > **4**. Interestingly, although the EQE of **3:9** is better than **1:9**, its PCE is poorer because of its poor fill factor.

Compound **1** shows the lowest R_s followed by **3** then with a large difference **4**. Compound **1** also shows the highest R_{sh} followed by **3** and then **4**. This order of the series and shunt resistances explain the drop of the FF in **3** and **4** in relative to **1**. The drop of the J_{sc} of **4** can be correlated to the high R_{sh} relative to **1** and **3**.

The variation of the solar cells performance of the blends follows the same trends as the nanoscale morphology parameters investigated in section 4.4.3 in the previous chapter. As the devices performance decrease in the order **1:9** > **3:9** > **4:9**, the surface roughness increases for the blends, with the rms equal to 0.73nm , 1.3nm, 1.4nm respectively, the height distribution peaking at 2nm, 2.9nm, 3.8nm, and the height variation of the order of 4nm, 6.2nm, 8.1nm. Also the domain size study shows that in the region where the domain size is larger than 20 nm, **4:9** has the highest PSD followed by **3:9** with similar values, while **1:9** has the lowest PSD. However in the region with domains smaller than 20 nm, the PSD of **3:9** and **4:9** has decayed more to become less than that of **1:9**. The mobility of the **1:9** blend was not studied, while both the electron and hole mobility of the **4:9** blend was significantly higher than the **3:9** blend, both measured with a 1:1 ratio. There is no correlation with PV devices performance. Therefore, the performance of the solar cells can be related to the nanoscale morphology as the three compounds have the same aromatic core and the only difference is the spacers and the end groups as previously explained. The terminal aliphatic chains of **3** and **4** are more bulky than that of **1**. This influences the morphology of the blends and surface roughness. The roughest sample gives the worst performance.

5.4.4. The Effect of Annealing Temperature on the BHJ Solar Cell Performance

Photovoltaic devices were fabricated with different blends using identical processing conditions as in the previous section. Compound **1** was used as ED and **9** as EA for all the blends in order to evaluate the affect of various annealing temperature on the photovoltaic blends.

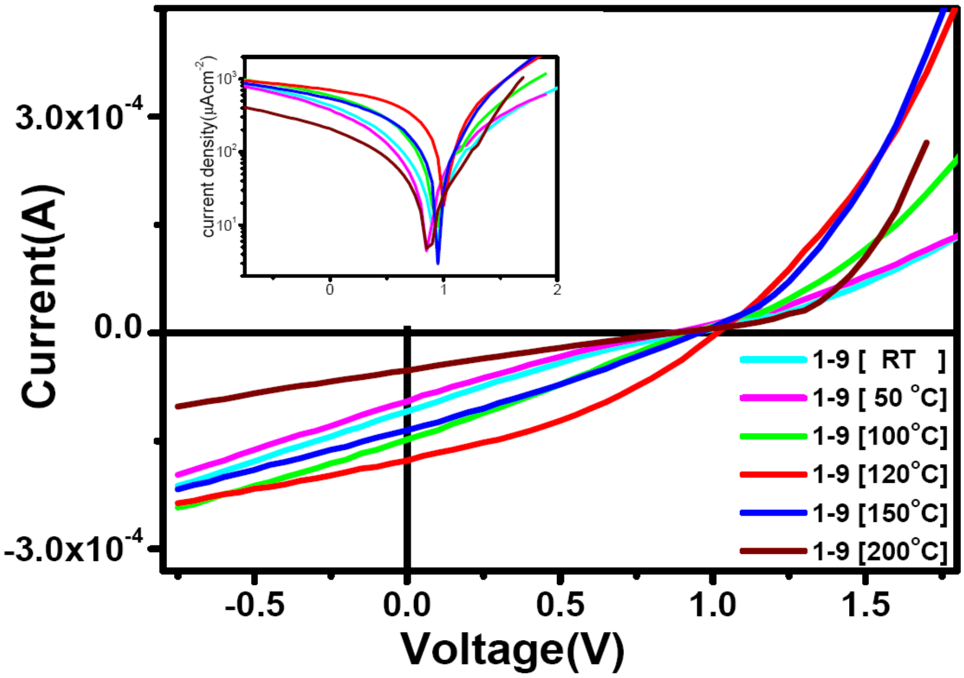

Figure 5-13: The current density versus voltage of the photovoltaic devices incorporating a thin film of a 1:2 blend with 1as ED and 9 as EA in chlorobenzene. The devices were annealed at different temperature for 60mins. The input light source irradiance was 22 mW cm^{-2} at a wavelength of 466 nm.

Figure 5-13 shows current-voltage characteristics of the PV blend devices with an input irradiance of 22 mW.cm^{-2} at 466 nm wavelength, the peak of the photocurrent action spectrum. It is obvious from the I-V curves that the solar cell performance parameters are affected by the annealing temperature. The J_{sc}, FF, and P_{max} were influenced more than the V_{oc} which only varied between 0.85 and 1V. These have a large influence on the power conversion efficiencies (PCE) which are 0.4, 0.32, 0.65, 1.14, 0.65 and 0.19 % when annealing at RT, 50, 100, 120, 150, 200°C respectively, as shown in table 5-4.

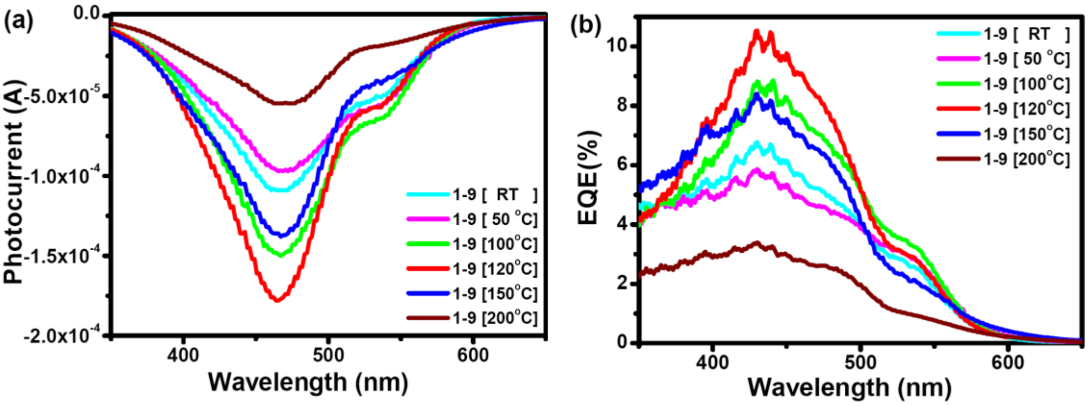

Figure 5-14: a)The Photocurrent action spectra for the different photovoltaic devices incorporating a thin film of 1:2 blends of 1as ED and 9 as EA in chlorobenzene. The devices were annealed at different temperature for 60mins, b) The external quantum efficiency for the different annealed devices.

Figure 5-14(a) and figure 5-14(b) show the photocurrent action spectra and the EQE spectra of PV devices fabricated with different annealing temperatures. The action spectra peaks at 466nm. Interestingly at wavelengths longer than 500nm where the EA contributes more to absorption, the photocurrent curves of the devices show some change in the order, for example the EQE of the 100°C annealed device become higher than that of the 120°C device.

Table 5-4: Performance parameters for the 1:9 blend PV devices with different annealing temperatures, on excitation with 22 mW.cm^{-2} at 466 nm.

Annealing Temperature	V_{oc} (V)	J_{sc} mA cm^{-2}	P_{max} mW cm^{-2}	FF	EQE (%)	PCE (%)
RT	0.95	0.436	0.0875	0.21	5.21	0.4
50	0.85	0.381	0.0713	0.22	4.61	0.32
100	0.95	0.592	0.144	0.256	7.1	0.65
120	1	0.708	0.252	0.356	8.31	1.14
150	0.95	0.54	0.143	0.278	6.55	0.65
200	0.85	0.21	0.043	0.24	2.6	0.19

Table 5-5 tabulates the performance of PV devices with different annealing temperature. Annealing the device at 120°C provided the best performance as also illustrated in figure 5-15. The different parameters change similarly with annealing temperature apart from the FF at 50 °C, which increases relative to that at RT while all the other parameters decrease.

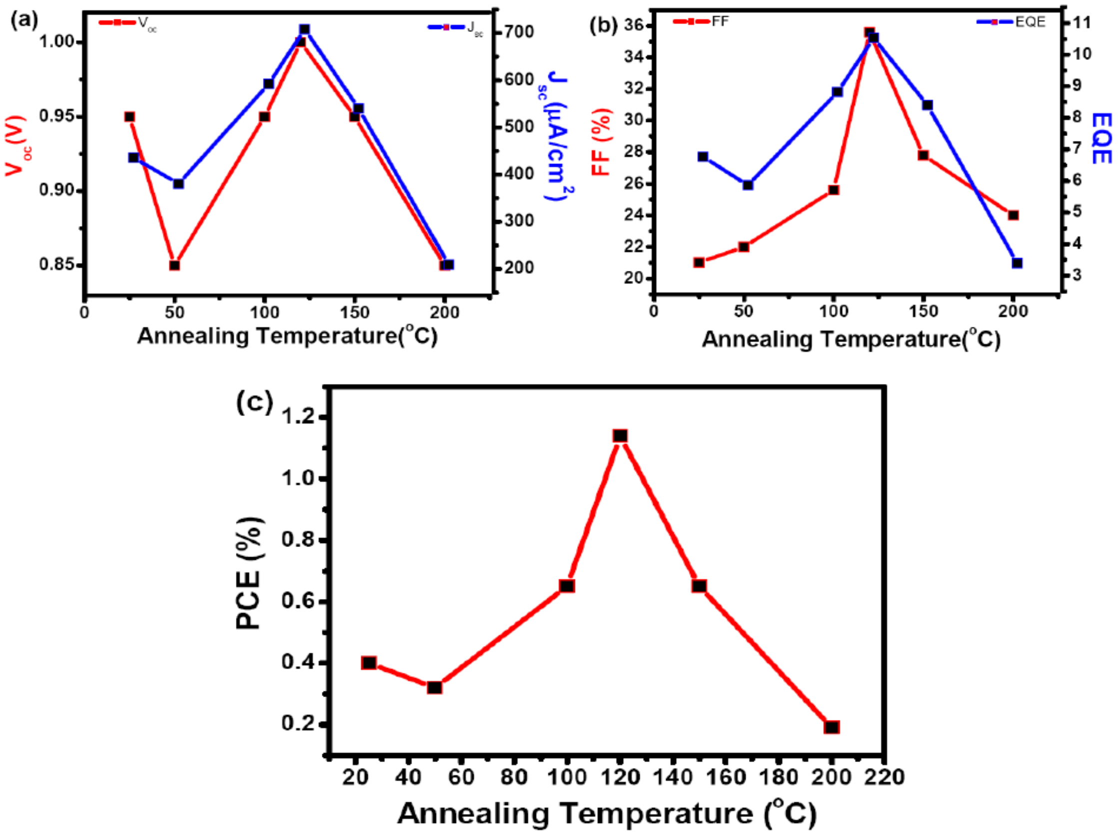

Figure 5-15: Comparison of the solar cells" performance parameters as function of annealing temperature.

The variation of the solar cell performance parameters as a function of the annealing temperature can be related to the nanoscale morphology of the interpenetrating network of the ED and EA compounds. Mixing the blend materials efficiently before spin casting produces an intimate mixing of the cast film without substantial phase separation resulting in many electron-hole recombination sites before collection in the electrodes.

The following analysis assumes tiny isolated grains of each component after spin casting. The annealing of the active layer at temperatures less than the glass transition temperature of the blend components, results in a limited movement of the molecules, giving a limited phase separation of the compounds as illustrated in figure 5-16(a) for 50°C. The glass transition temperature is 80°C for **1**, while **9** has only a melting point at 274°C. As the annealing temperature passes the glass transition temperature of one of the compounds, the molecules become more mobile, which stimulates the phase separation of the compounds to increase gradually with the increase of the annealing temperature building up the grain sizes as illustrated in figure 5-16 (b,c). Note above T_g compound **1** is a nematic LC. As the temperature becomes closer to the melting point of one of the compounds (218 °C for **1**) the phase separation process becomes much faster, and the grain sizes become larger tending to be isolated from the other compound or being in contact with the wrong electrode as illustrated in figure 5-16 (d). Therefore, as the grain size becomes too coarse, the excitons recombine before separation, deteriorating the solar cells' performance.

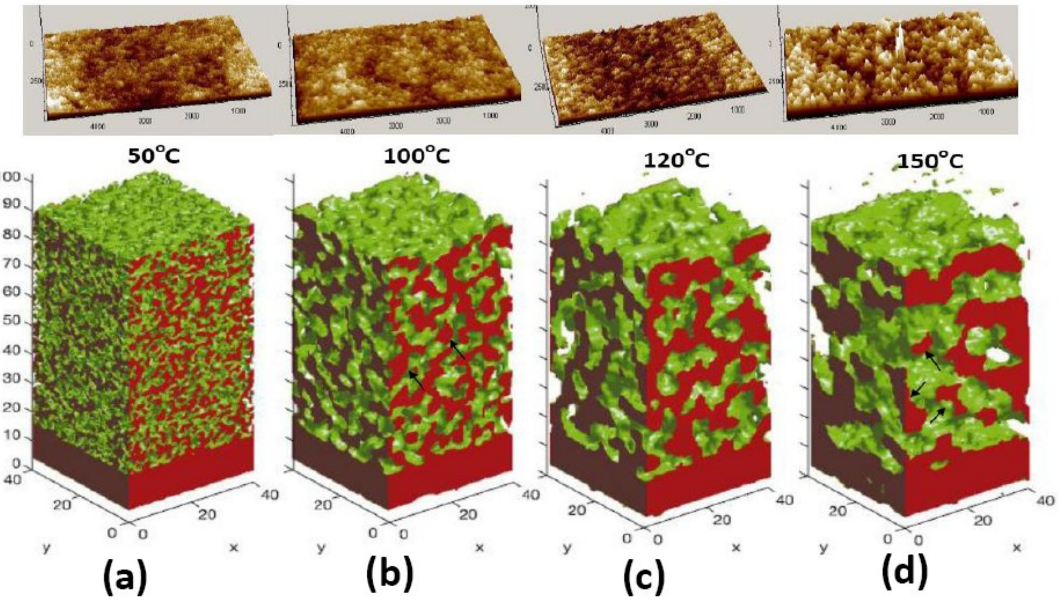

Figure 5-16: (top)AFM 3D images of the surface topography of different annealing temperature, (bottom) the simulated effects of the annealing temperature of the phase separation of the blend compounds[13].

5.4.5. The Effect of Light Intensity on the BHJ Solar Cell Performance

The **1-9** blend PV devices were characterized at different light intensities to evaluate the effect of light intensity on performance. The light intensity was controlled using an array of interchangeable optical neutral density filters, with different transmission as illustrated in section 5.2.3.1.

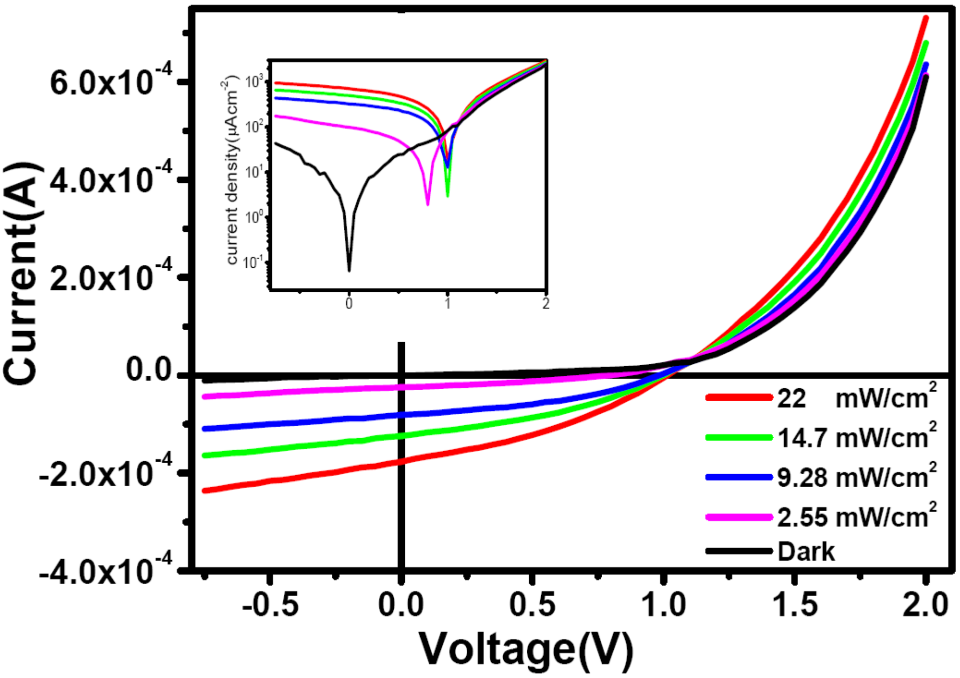

Figure 5-17: The current density versus voltage of the photovoltaic device incorporating a thin film of a 1:2 blend of 1as ED and 9 as EA in chlorobenzene, the device was annealed at 120 ^{o}C for 60mins. The inset labels the irradiance in mW cm^{-2} of the input light source of wavelength 466 nm.

Figure 5-17 shows current-voltage characteristics of the 120^{o}C annealed PV blend device in the dark and on irradiation with 22, 14.7, 9.28, 2.55mW.cm^{-2} intensities at 466 nm. The photocurrent varies significantly with the input irradiance. However the open circuit voltage has fixed values at all intensities apart from the lowest one.

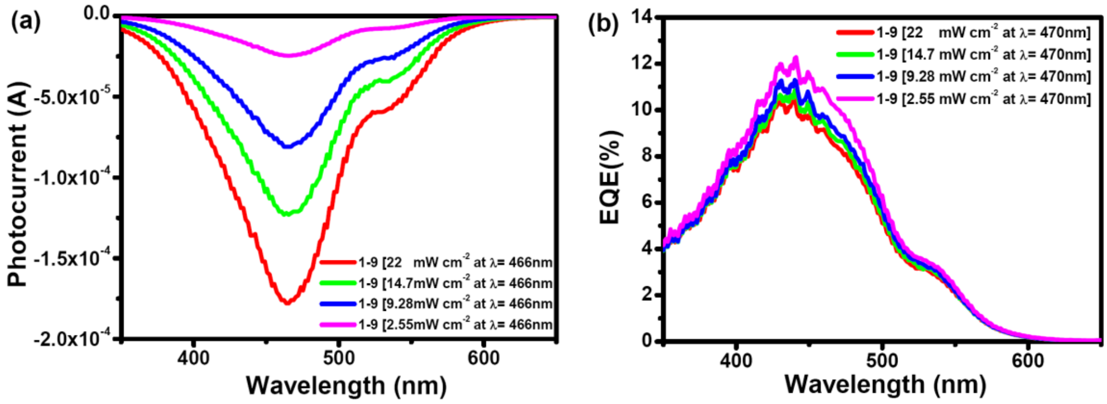

Figure 5-18: a)The Photocurrent action spectra for a photovoltaic device incorporating a thin film of a 1:2 blend of 1as ED and 9 as EA in chlorobenzene, the device was annealed at 120°C for 60mins, The light intensity was varied as specified in the inset labels, b) The external quantum efficiency of the device with different light intensities.

Figure 5-18(a) shows the variation in the photocurrent action spectrum of the PV device annealed at 120°C at different irradiance, illustrating the peaks of the photocurrent to be around the wavelength of 466nm. Figure 5-18(b) shows the external quantum efficiency EQE of the PV device as a function of the incident light wavelength. The EQE shows a small variation with intensity. At higher intensity the probability of electron-hole recombination increases so that the EQE decreases.

Table 5-5: Performance parameters for the 1:9 blend PV device annealed at 120°C, on varying the irradiance at 466 nm

Light intensity (mW cm^{-2})	V_{oc} (V)	J_{sc} mA cm^{-2}	P_{max} mW cm^{-2}	FF	EQE (%)	PCE (%)
22	1	0.708	0.252	0.356	8.58	1.14
14.7	1	0.496	0.183	0.369	8.88	1.24
9.28	1	0.324	0.126	0.389	9.27	1.35
2.55	0.8	0.098	0.025	0.32	10.25	0.99

Table 5-5 tabulates the PV device performance of the 120°C annealed device with the different irradiances at wavelength 466nm. V_{oc} is 1 V with no variation for all irradiances apart from 2.55mW.cm^{-2}, where it drops to 0.8V, which as a consequence changes the variation order of FF and PCE with reference to the EQE.

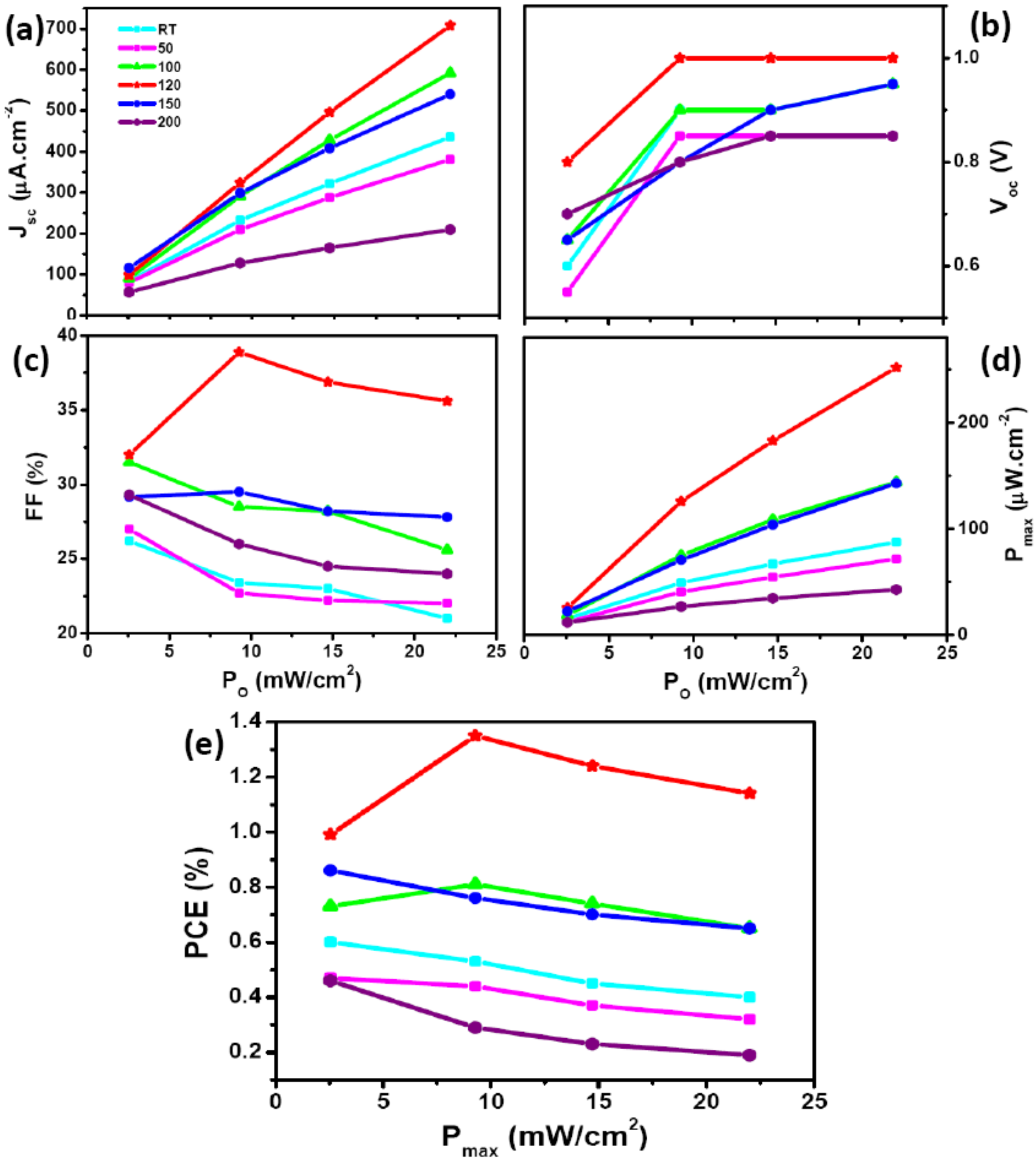

Figure 5-19: The power conversion efficiency as function of the light intensity and the annealing temperature.

Figure 5-19 shows the variation of the performance parameters as a function of the light intensity for **1:9** blend PV devices with different annealing temperatures. There is some correlation between the PV performance and the morphology (see section 4.4.4) with annealing temperature. Annealing at 120°C gives the best PV performance and produces a smooth sample with relatively small domains. The sample annealed at 200

^{o}C is very rough with large domains and shows the worst PV performance. Interestingly the sample annealed at 150^{o}C shows relatively good PV performance but has high roughness. This may be related to its large proportion of domains <100nm. Interestingly the sample annealed at RT is slightly better than that annealed at 50^{o}C.

The current is negatively influenced by the recombination. Therefore the plot of the short circuit density current J_{sc} as a function of light intensity P_o in double logarithmic scale can be used to predict the recombination properties, where J_{sc} follows the power law dependence $J_{sc} = P_o^b$ [14]. The charge carriers losses in the absorber bulk are dominated by monomolecular recombination in the case of nearly linear dependence with b≈1, while pure bimolecular recombination follows the square root dependence with b=0.5. The different annealing temperatures change the nanoscale morphology of the ED/EA, so changing the network paths of the charge carriers to the respective electrode, which influences the recombination of the charge carriers via adding or removing some trapping centres.

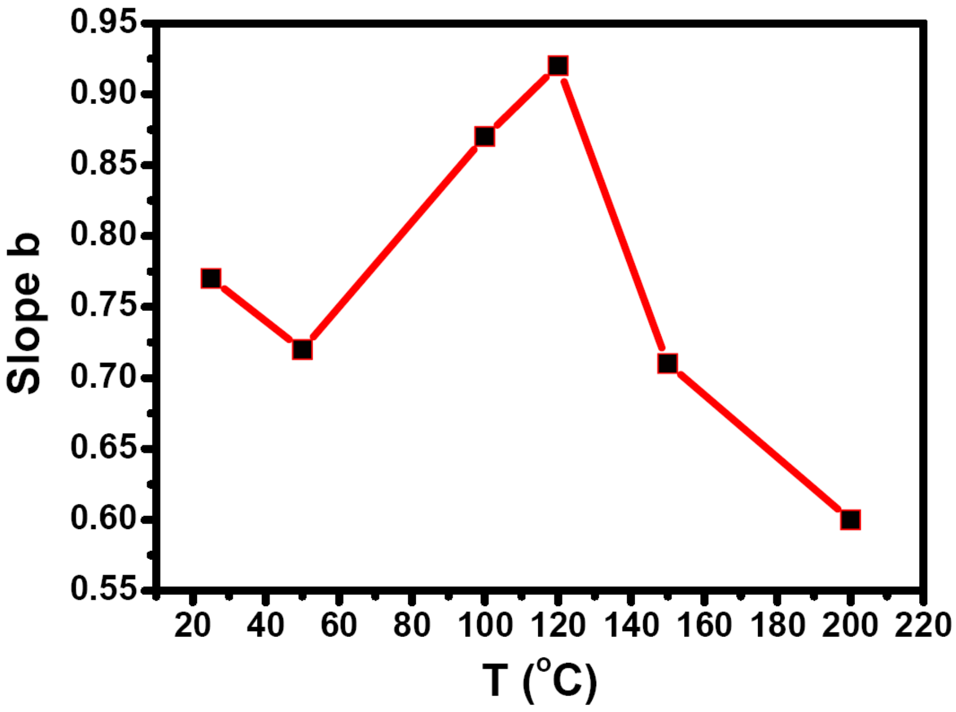

Figure 5-20: The variation the power law slope with the annealing temperature.

Figure 5-20 shows the variation of the power law slope with annealing temperature indicating a change in the dominant recombination type. The samples annealed at 120^{o}C shows a high level of phase separation and the slope is 0.92 indicating that monomolecular recombination is dominant with a small contribution from bimolecular. As the roughness and domain sizes increase for the 150^{o}C and 200^{o}C annealed samples the bimolecular recombination contribution increases.

5.5. Conclusion

Different EAs were tested in PV devices blended with the ED **3**. **9** was found to be the best EA and shows good charge transport and the finest scale intermixing in blends. Compounds **11** and **13** have donor-acceptor components showing good hole as well electron transport. This and/or the relatively coarse morphology of the **3:11** and **3:13** blends may explain their relatively poor performance.

Chlorobenzene is found to be the best solvent for PV devices. The three donors **1**, **3** and **4** with the same aromatic core and different terminal aliphatic polymerisable groups were compared in PV devices. Devices incorporating **1** showed the best performance which correlates with blend morphology rather than charge transport.

Finally we show the importance of choosing the optimum annealing temperature to optimise blend morphology and the PV device performance.

5.6. References

1 A. Sharma, A. Haldi, W. J. Potscavage et al., "Effects of surface modification of indium tin oxide electrodes on the performance of molecular multilayer organic photovoltaic devices," Journal of Materials Chemistry **19** (30), 5298-5302 (2009).

2 S. Besbes, H. Ben Ouada, J. Davenas et al., "Effect of surface treatment and functionalization on the ITO properties for OLEDs," Materials Science & Engineering C-Biomimetic and Supramolecular Systems **26** (2-3), 505-510 (2006).

[3] F. Steuber, J. Staudigel, M. Stossel et al., "Reduced operating voltage of organic electroluminescent devices by plasma treatment of the indium tin oxide anode," Applied Physics Letters **74** (23), 3558-3560 (1999).

[4] A. Sharma, A. Haldi, P. J. Hotchkiss et al., "Effect of phosphonic acid surface modifiers on the work function of indium tin oxide and on the charge injection barrier into organic single-layer diodes," Journal of Applied Physics **105** (7) (2009).

[5] A. Sharma, P. J. Hotchkiss, S. R. Marder et al., "Tailoring the work function of indium tin oxide electrodes in electrophosphorescent organic light-emitting diodes," Journal of Applied Physics **105** (8) (2009).

[6] J. S. Kim, J. H. Park, J. H. Lee et al., "Control of the electrode work function and active layer morphology via surface modification of indium tin oxide for high efficiency organic photovoltaics," Applied Physics Letters **91** (2007).

[7] I. M. Chan, W. C. Cheng, and F. C. Hong, "Enhanced performance of organic light-emitting devices by atmospheric plasma treatment of indium tin oxide surfaces," Applied Physics Letters **80** (1), 13-15 (2002); M. Utsumi, N. Matsukaze, A. Kumagai et al., "Effect of UV treatment on anode surface in organic EL displays," Thin Solid Films **363** (1-2), 13-16 (2000).

[8] I. Yoo, M. Lee, C. Lee et al., "The effect of a buffer layer on the photovoltaic properties of solar cells with P3OT : fullerene composites," Synthetic Metals **153** (1-3), 97-100 (2005).

[9] Y. Kim, A. M. Ballantyne, J. Nelson et al., "Effects of thickness and thermal annealing of the PEDOT:PSS layer on the performance of polymer solar cells," Organic Electronics **10** (1), 205-209 (2009).

[10] L. S. C. Pingree, B. A. MacLeod, and D. S. Ginger, "The changing face of PEDOT : PSS films: Substrate, bias, and processing effects on vertical charge transport," Journal of Physical Chemistry C **112** (21), 7922-7927 (2008).

[11] H. J. Snaith, H. Kenrick, M. Chiesa et al., "Morphological and electronic consequences of modifications to the polymer anode 'PEDOT : PSS'," Polymer **46** (8), 2573-2578 (2005).

[12] S.E. Shaheen, C.J. Brabec, and N.S. Sariciftci, "2.5% efficient organic plastic solar cells," Applied Physics Letters **78** (6), 841 (2001).

[13] P. Peumans, S. Uchida, and S. R. Forrest, "Efficient bulk heterojunction photovoltaic cells using small smallmolecular-weight organic thin films," Nature **425** (6954), 158-162 (2003).

[14] I. Riedel, J. Parisi, V. Dyakonov et al., "Effect of temperature and illumination on the electrical characteristics of polymer-fullerene bulk-heterojunction solar cells," Advanced Functional Materials **14** (1), 38-44 (2004).

6. CONCLUSION

6.1. Review of Results

This thesis aims to study and evaluate some novel LCs and amorphous organic conjugated materials to be used as EDs and EAs for PVs. More than 30 homemade organic semiconductor compounds were investigated. These compounds help the understanding of the influence of some well known active groups and elements on the optical and charge transport properties and the performance of PV devices.

The CV experiment and the UV/VIS spectrometer were used to estimate the HOMO/LUMO energy levels and the optical and electrical energy gaps ($E_{g,op}$,$E_{g,elc}$) of the materials. Perylene materials, some with donor-acceptor properties, were characterised as EAs. All have similar LUMO energy coming from the accepting moiety of the molecule (perylene). There is significant variations in the HOMO properties coming from the donating moiety (phenyl and fluorene aromatic substituent), which causes a discrepancy between the optical and electrochemical measurement of E_g. Carbazole compounds are disappointing as functional groups with the perylene. Although they modify the HOMO energy, the oxidation is irreversible.

Liquid crystal compounds with a fluorene-thiophene structure were identified as potential EDs to form good D/A pairs in combination with the nine perylene based compounds as EAs, with suitable ΔE ($HOMO_D$-$LUMO_A$) to be used for PV's.

TOF was used to study the charge transport of organic semiconductors in this thesis. Six of the perylene derivatives compounds, **9**, **11**, **12**, **13**, **15** and **16**, were studied as EA materials. Compound **9** though not showing the highest electron mobility shows a good (μ_e/μ_h) ratio for low electric fields corresponding to the internal electric field of solar cell devices. The other EAs contain donor-acceptor units and show ambipolar transport with hole mobility depending on the number of phenyl and fluorene groups attached to the perylene.

We studied how the reactive end group with spacer affected the charge carrier mobility of EDs using four fluorene-thiophene structures, compounds **1**, **2**, **3** and **4**, with the same aromatic core but with different end groups. They form nematic glasses at room temperature. Results suggest that the mobility depends on the intermolecular separation. These compounds show promising hole transporting properties for solar cells. Both compounds **1** and **4** shows hole mobility $>10^{-3}cm^2V^{-1}s^{-1}$.

The electron and hole mobility were studied for blends of compound **9** as EA, and compounds 2, **3**, and **4** as EDs with different ED: EA ratios. For all blends the hole mobility is lower than that of the pure ED. The electron mobility of the blends is 200 times higher than that of the pure EA. The **4:9** blend gives the best mobility followed by 2:9 then **3:9**. The ED: EA ratios are shown to influence the mobility measurements**.**

The thermal activation of charge transport in the liquid crystals is illustrated by applying the Gill model to compound **1**, **2** and **4**. The result showed that the activation energy is field dependent. It decreases with increasing field, which follows the Poole-Frenkel model expectation of lowering the potential barrier in the direction of the applied field and so making the hopping of the charge carriers easier. The Gaussian disorder model (GDM) and correlated disorder model (CDM) were used to analyze the mobility data of the four liquid crystals ED compounds. Compounds **1**, **2** and **3** show good correlation between the mobility and the disorder parameters, while compound **4** has anomalously high μ_o and disorder parameters.

We show that the thin film nanoscale morphology and the phase separation of the ED/EA blends depend on the chemical structures of EDs and EAs, the casting solvents and the annealing temperature of the film. Both amorphous and liquid crystal EAs were studied. There is a big variation in domain size and roughness depending on the EA. Blends incorporating compound **9** have the smallest domain sizes with no odd features, although the domain size of **16** is smaller, it show large number of pin holes. Morphology is quite different for blends with LC compounds **11** and **13**. This suggests that devices with **9** as EA might give better charge separation.

Three liquid crystal of the same aromatic core and different terminals end groups were investigated as EDs in blends. The surface roughness of the blended thin film is minimum and its phase separation finest when the ED component has short terminal aliphatic groups rather than long polymerisable chains. The solvents were found to be an important player in controlling the nanoscale morphology and the phase separation of the ED/EA blends. Toluene, chloroform and chlorobenzene were investigated with chlorobenzene showing the best performance. The annealing temperature was found to be significant in controlling the nanoscale morphology and the phase separation of an intermixed network of the ED/EA blends. Any change of the blend materials and ratio requires different annealing conditions for the optimum phase separation.

We successfully demonstrated PV performance using blends of our novel EDs and EAs. The amorphous material **9** was the best EA, possibly because it has poor donor properties or because it produces the finest domain features. The annealing temperature was very important to optimise the solar cells performance by optimisation of the phase separation. The LC EAs have disappointing performance, maybe because of their donor-acceptor nature. The ED with the shortest terminal end groups gives best result.

The device performance fully correlates with the blend nanoscale morphology; the blend with the smallest domains gives best PCE. The best device is the **1:9** blend which has a monochromatic PCE of 1.14% as illustrated in table 6-1. This is relatively poor compared to the state of the art of 5.1% (broad band) using a P3HT:PCBM blend published by A. J. Heeger and coworkers[1].

Table 6-1: Comparison of our best device with P3HT: PCBM blend published by A. J. Heeger and coworkers.

Blend compounds	Voc (V)	Jsc mA cm-2	FF	PCE (%)	Measurement condition
1:9	1	0.708	0.36	1.14	Monochromatic light [466nm] 22 mW cm-2
P3HT:PCBM	0.63	9.5	0.68	5.1	AM 1.5G 100 mW cm-2

The V_{oc} of our devices is very good, which can be correlated to the large ΔE ($E_{D,HOMO}$-$E_{A,LUMO}$). The FF and J_{sc} are poor which can be correlated to the low photon harvesting because of the high ED energy gap of 2.33eV, and maybe traps from impurities as well as recombination at the layers interfaces and low mobility of the ED and EA, which reflected in the high R_s of 625 Ω cm^2 compared to 7.9 Ω cm^2 in reference paper[1].

6.2. Future work

This work has led to improved understanding of the correlation between aromatic substituent and semiconducting and optical properties. We can apply these results to design new organic semiconductors to be used as EDs and EAs for OPV.

The nanoscale morphology of the ED/EA blend phase separation needs to be improved using new methods. Dichlorobenzene is a promising solvent to be investigated. The morphology can be controlled with cross linking the blend since there is a photo-induced phase separation between photopolymerisable and non-photopolymerisable blend components during cross linking[2]. This is an important point of research which can be investigated in the future.

The interface between the electrodes and the organic materials is very important to control the R_s. Annealing the device after the evaporation of the top electrode improved the interface[1]. The annealing promotes Al diffusion increasing the interface or chemical reaction formation [C-Al or C-O-Al] which could lead to strong contacts and increased contact area[1].

The mobility measurement was carried out at RT without annealing after spin coating resulting in morphology which maybe different than the devices. Similar preparation and measurement conditions should be used for the TOF and PV samples for improved correlation of the blends' mobility and the solar cells' performance.

6.3. References

1 W. Ma, C Yang, X. Gong et al., "Thermally stable, efficient polymer solar cells with nanoscale control of the interpenetrating network morphology," Advanced Functional Materials **15**, 1617-1622 (2005).

2 M. Carrasco-Orozco, W. C. Tsoi, M. O'Neill et al., "New Photovoltaic Concept: Liquid-Crystal Solar Cells Usinga Nematic Gel Template," Advanced Materials **18**, 1754-1758 (2006).

Appendix A

Cyclic Voltammograms

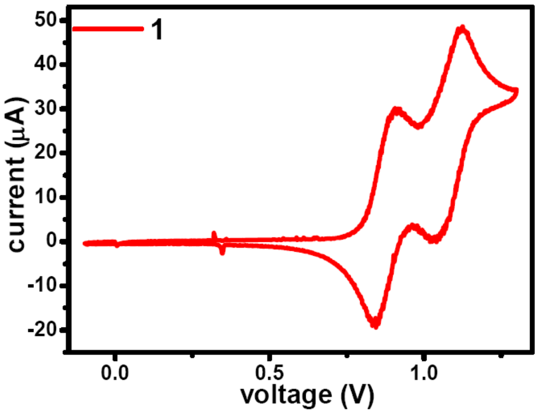

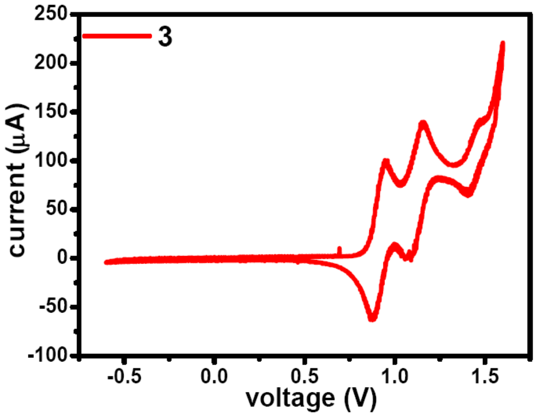

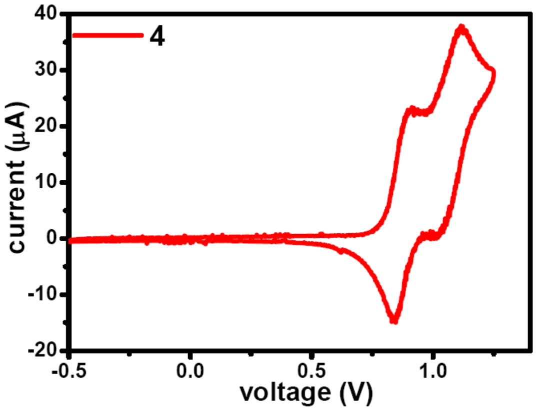

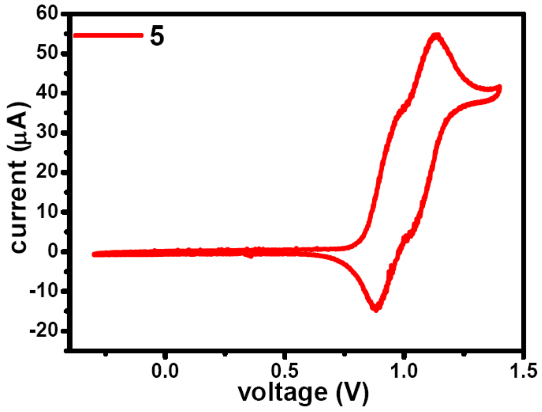

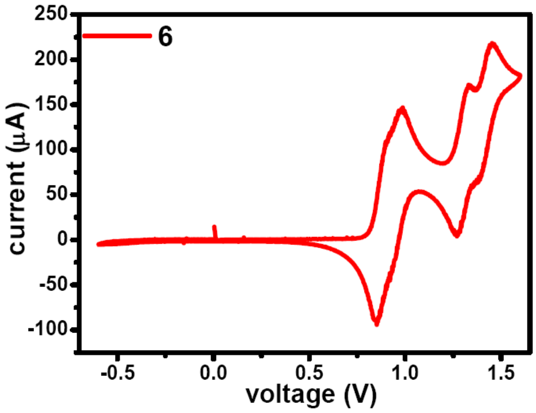

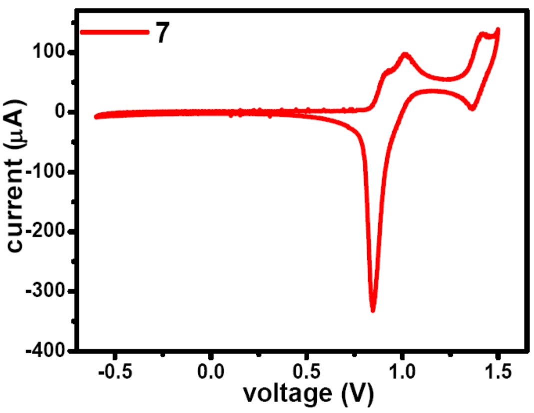

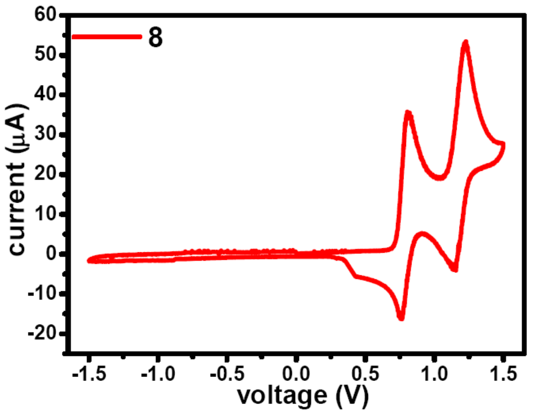
8
current (μA)
60
50
40
30
20
10
0
-10
-20
-1.5
-1.0
-0.5
0.0
0.5
1.0
1.5
voltage (V)

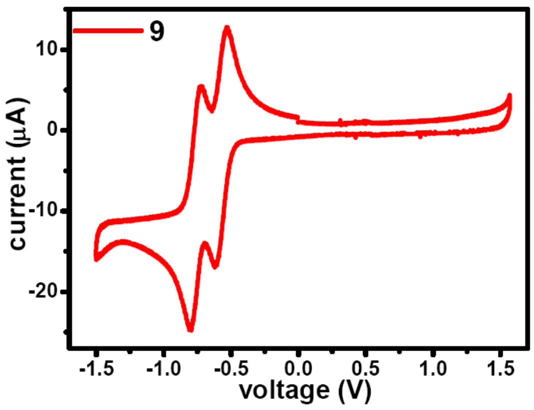
9
current (μA)
10
0
-10
-20
-1.5
-1.0
-0.5
0.0
0.5
1.0
1.5
voltage (V)

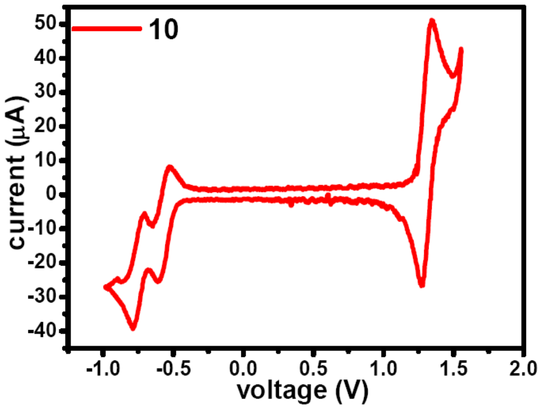
10
current (μA)
50
40
30
20
10
0
-10
-20
-30
-40
-1.0
-0.5
0.0
0.5
1.0
1.5
2.0
voltage (V)

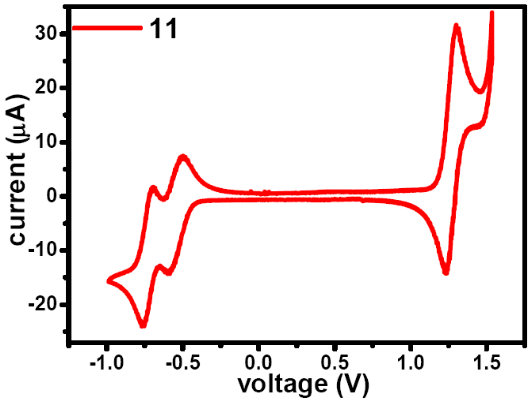
11
current (μA)
30
20
10
0
-10
-20
-1.0
-0.5
0.0
0.5
1.0
1.5
voltage (V)

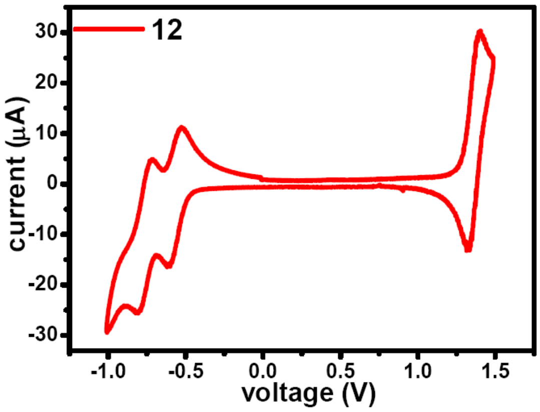
12
current (μA)
30
20
10
0
-10
-20
-30
-1.0
-0.5
0.0
0.5
1.0
1.5
voltage (V)

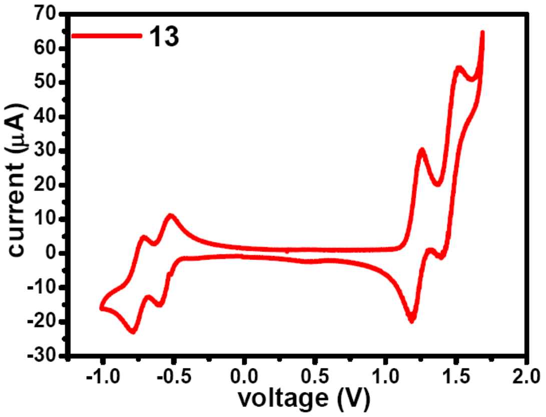
13
current (μA)
70
60
50
40
30
20
10
0
-10
-20
-30
-1.0
-0.5
0.0
0.5
1.0
1.5
2.0
voltage (V)

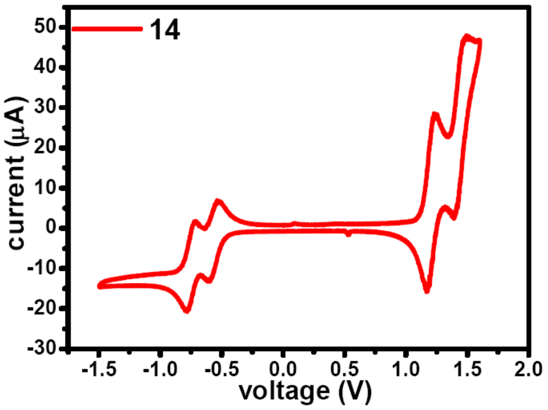
14
current (μA)
50
40
30
20
10
0
-10
-20
-30
-1.5
-1.0
-0.5
0.0
0.5
1.0
1.5
2.0
voltage (V)

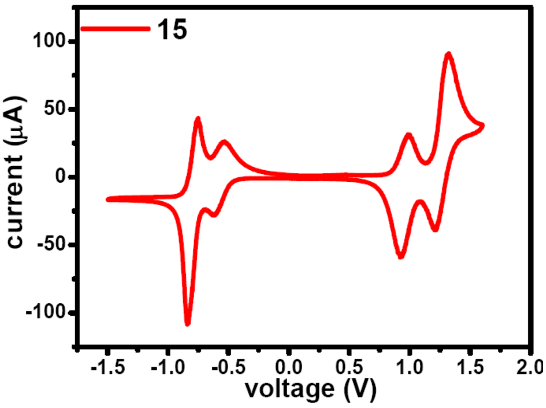
15
current (μA)
100
50
0
-50
-100
-1.5
-1.0
-0.5
0.0
0.5
1.0
1.5
2.0
voltage (V)

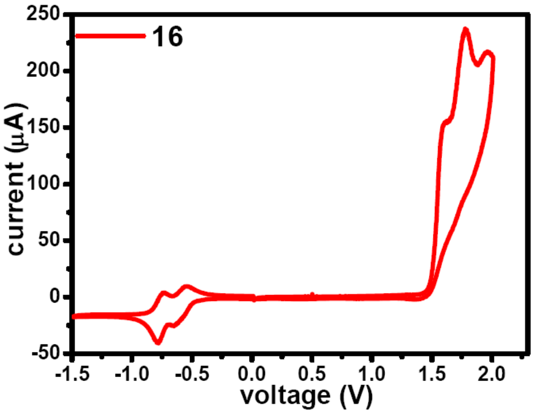
16
current (μA)
250
200
150
100
50
0
-50
-1.5
-1.0
-0.5
0.0
0.5
1.0
1.5
2.0
voltage (V)

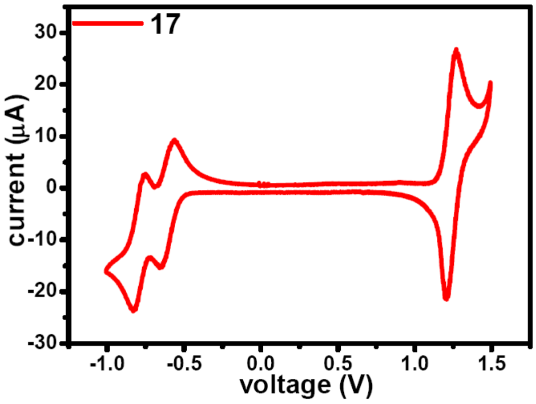
17
current (μA)
30
20
10
0
-10
-20
-30
-1.0
-0.5
0.0
0.5
1.0
1.5
voltage (V)

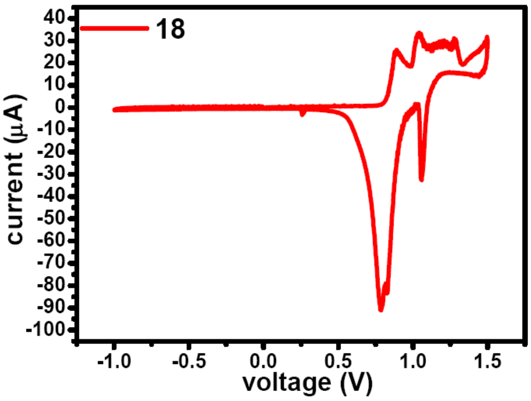
18
current (μA)
40
30
20
10
0
-10
-20
-30
-40
-50
-60
-70
-80
-90
-100
-1.0
-0.5
0.0
0.5
1.0
1.5
voltage (V)

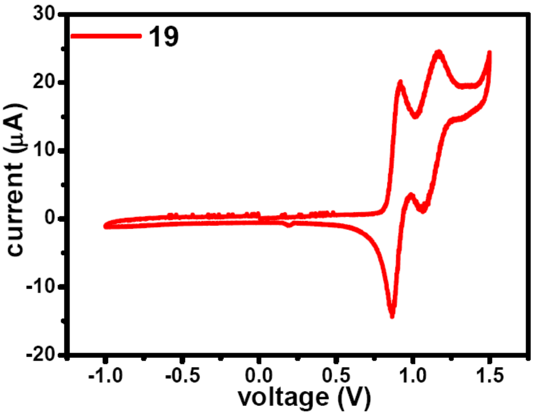
19
current (μA)
30
20
10
0
-10
-20
-1.0
-0.5
0.0
0.5
1.0
1.5
voltage (V)

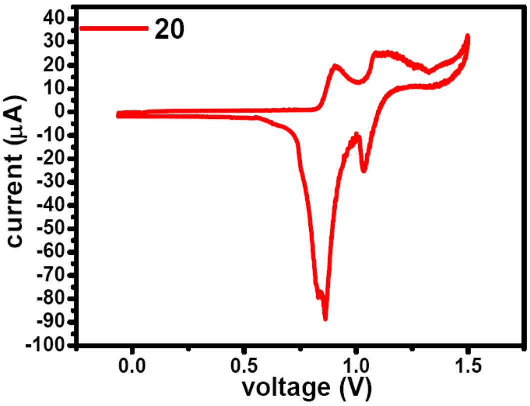
20
current (μA)
40
30
20
10
0
-10
-20
-30
-40
-50
-60
-70
-80
-90
-100
0.0
0.5
1.0
1.5
voltage (V)

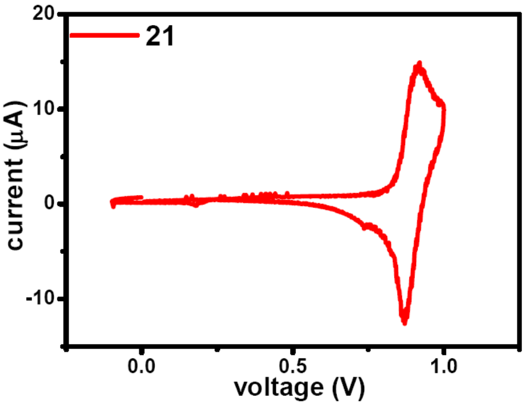
21
current (μA)
20
10
0
-10
0.0
0.5
1.0
voltage (V)

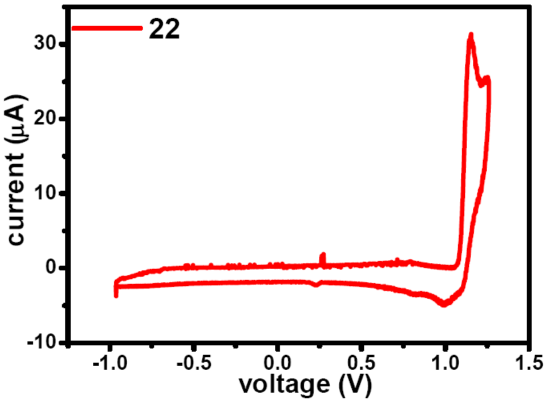
22
current (μA)
30
20
10
0
-10
-1.0
-0.5
0.0
0.5
1.0
1.5
voltage (V)

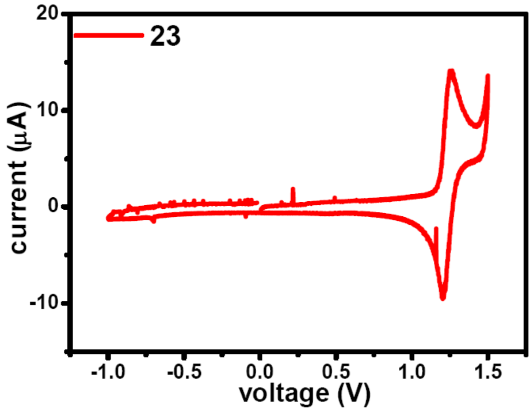
23
current (μA)
20
10
0
-10
-1.0
-0.5
0.0
0.5
1.0
1.5
voltage (V)

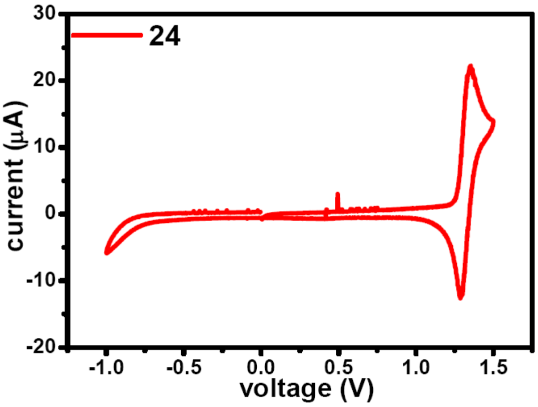
24
current (μA)
voltage (V)
30
20
10
0
-10
-20
-1.0
-0.5
0.0
0.5
1.0
1.5

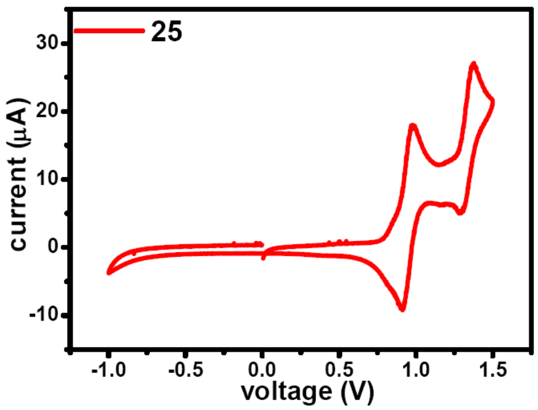
25
current (μA)
voltage (V)
30
20
10
0
-10
-1.0
-0.5
0.0
0.5
1.0
1.5

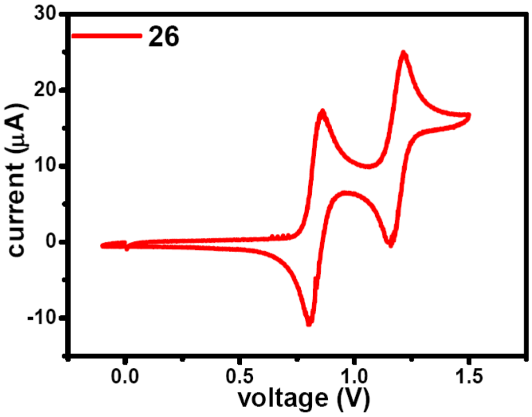
26
current (μA)
voltage (V)
30
20
10
0
-10
0.0
0.5
1.0
1.5

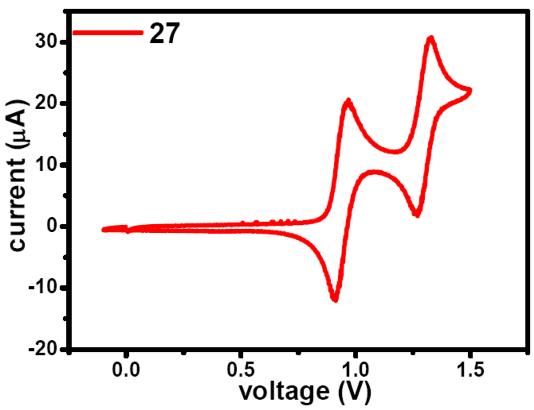
27
current (μA)
voltage (V)
30
20
10
0
-10
-20
0.0
0.5
1.0
1.5

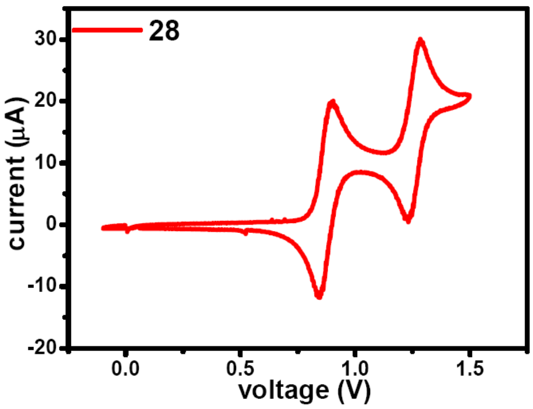
28
current (μA)
voltage (V)
30
20
10
0
-10
-20
0.0
0.5
1.0
1.5

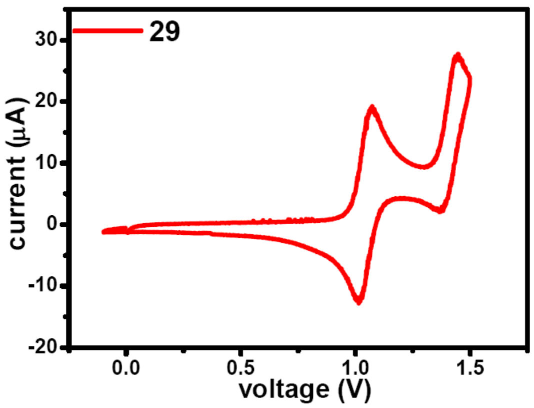
29
current (μA)
voltage (V)
30
20
10
0
-10
-20
0.0
0.5
1.0
1.5

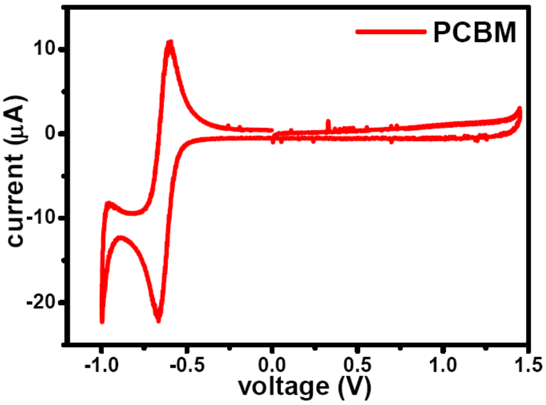
PCBM
current (μA)
voltage (V)
10
0
-10
-20
-1.0
-0.5
0.0
0.5
1.0
1.5

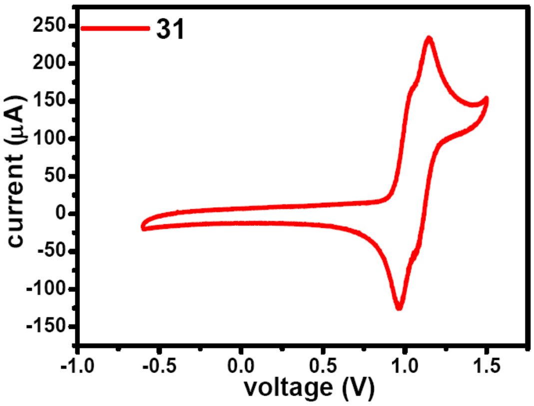
31
current (μA)
voltage (V)
250
200
150
100
50
0
-50
-100
-150
-1.0
-0.5
0.0
0.5
1.0
1.5

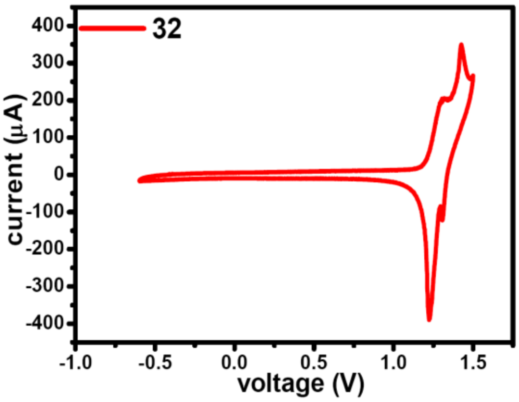
32
current (μA)
400
300
200
100
0
-100
-200
-300
-400
-1.0
-0.5
0.0
0.5
1.0
1.5
voltage (V)

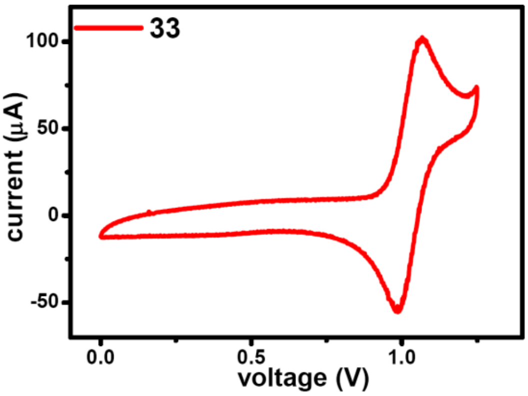
33
current (μA)
100
50
0
-50
0.0
0.5
1.0
voltage (V)

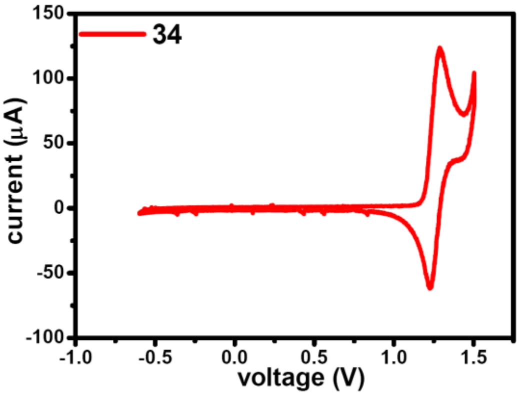
34
current (μA)
150
100
50
0
-50
-100
-1.0
-0.5
0.0
0.5
1.0
1.5
voltage (V)

Appendix B

Transient Photocurrent

I. Acceptors Compounds

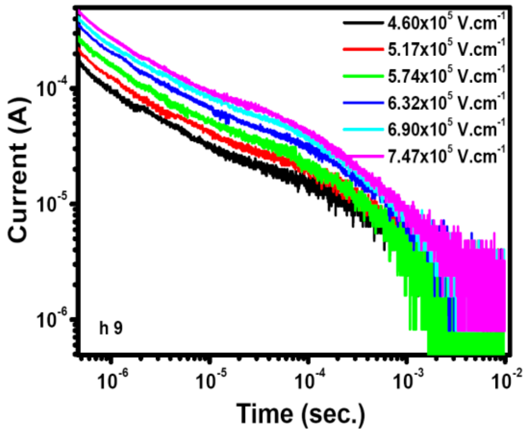

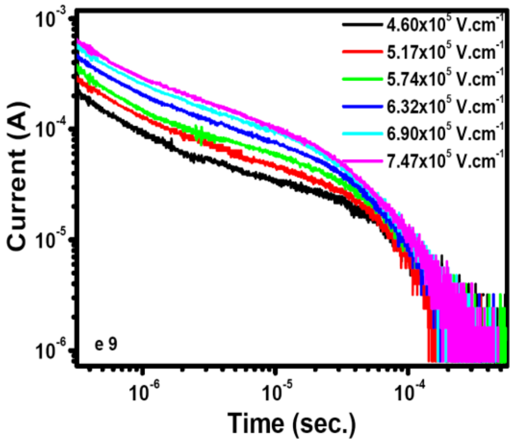

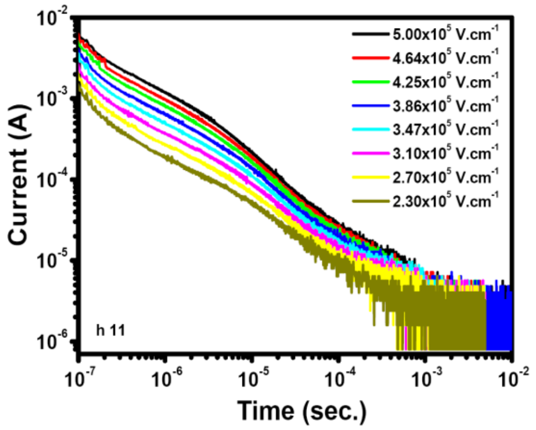

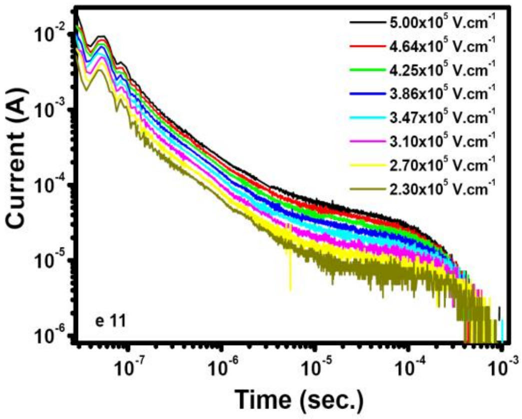

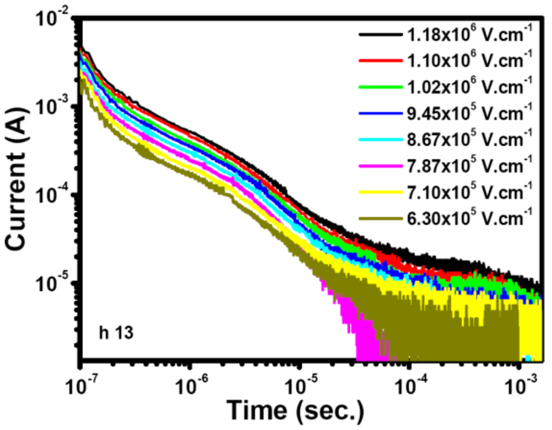

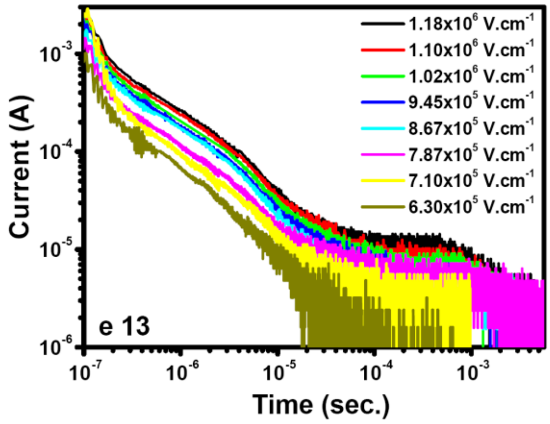

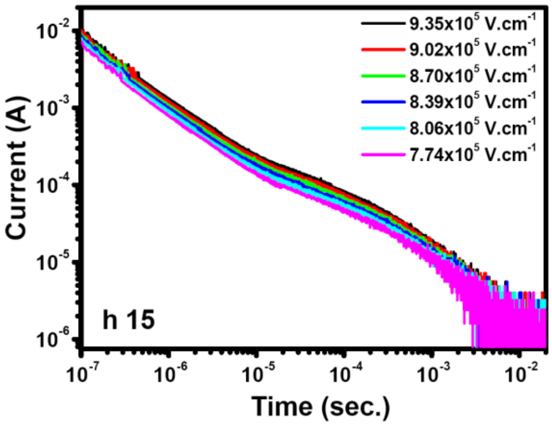

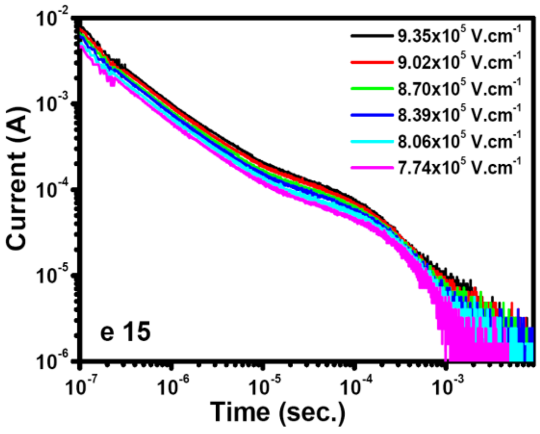

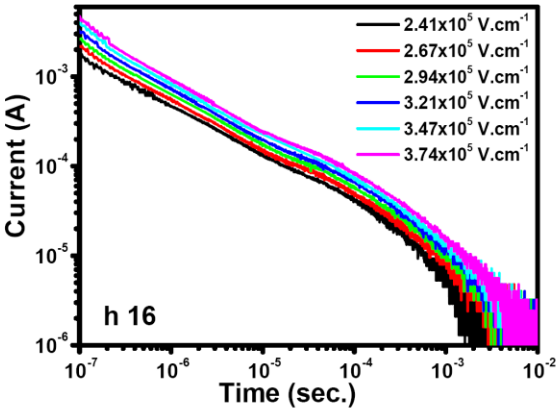

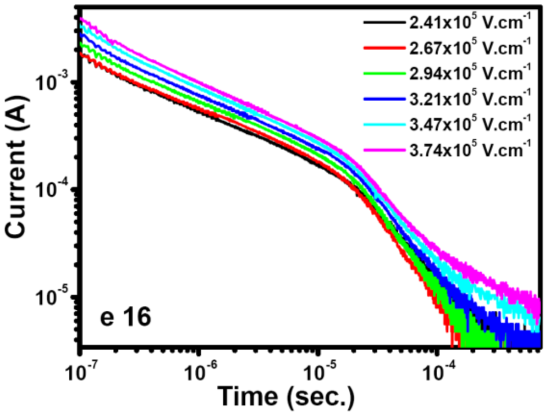

II. Donor Compounds

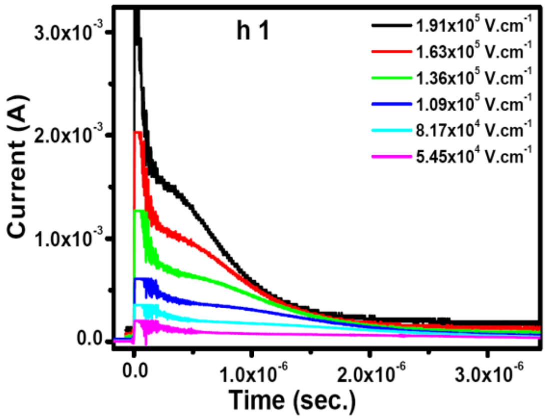

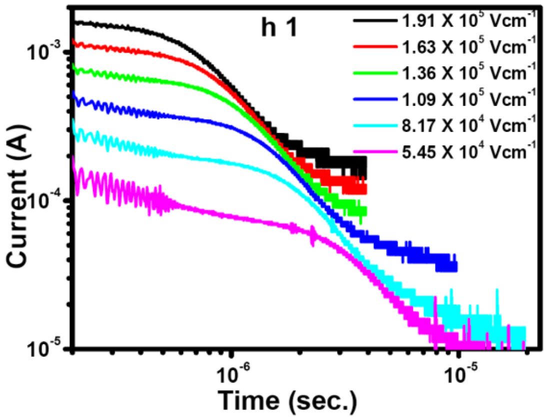

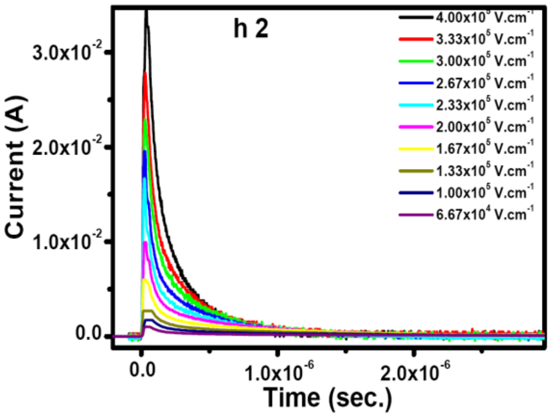
h 2
Current (A)
$3.0\text{x}10^{-2}$
$2.0\text{x}10^{-2}$
$1.0\text{x}10^{-2}$
0.0
0.0
$1.0\text{x}10^{-6}$
$2.0\text{x}10^{-6}$
Time (sec.)
$4.00\text{x}10^{5}$ V.cm^{-1}
$3.33\text{x}10^{5}$ V.cm^{-1}
$3.00\text{x}10^{5}$ V.cm^{-1}
$2.67\text{x}10^{5}$ V.cm^{-1}
$2.33\text{x}10^{5}$ V.cm^{-1}
$2.00\text{x}10^{5}$ V.cm^{-1}
$1.67\text{x}10^{5}$ V.cm^{-1}
$1.33\text{x}10^{5}$ V.cm^{-1}
$1.00\text{x}10^{5}$ V.cm^{-1}
$6.67\text{x}10^{4}$ V.cm^{-1}

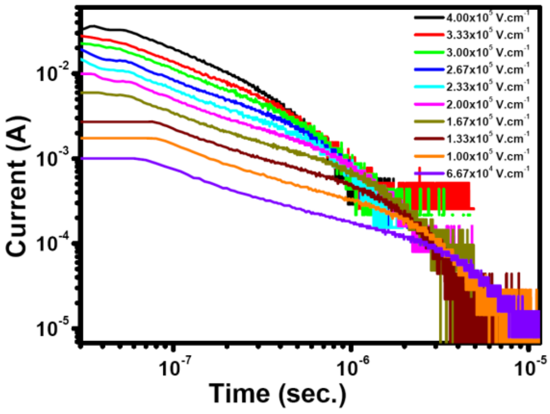
Current (A)
10^{-2}
10^{-3}
10^{-4}
10^{-5}
10^{-7}
10^{-6}
10^{-5}
Time (sec.)
$4.00\text{x}10^{5}$ V.cm^{-1}
$3.33\text{x}10^{5}$ V.cm^{-1}
$3.00\text{x}10^{5}$ V.cm^{-1}
$2.67\text{x}10^{5}$ V.cm^{-1}
$2.33\text{x}10^{5}$ V.cm^{-1}
$2.00\text{x}10^{5}$ V.cm^{-1}
$1.67\text{x}10^{5}$ V.cm^{-1}
$1.33\text{x}10^{5}$ V.cm^{-1}
$1.00\text{x}10^{5}$ V.cm^{-1}
$6.67\text{x}10^{4}$ V.cm^{-1}

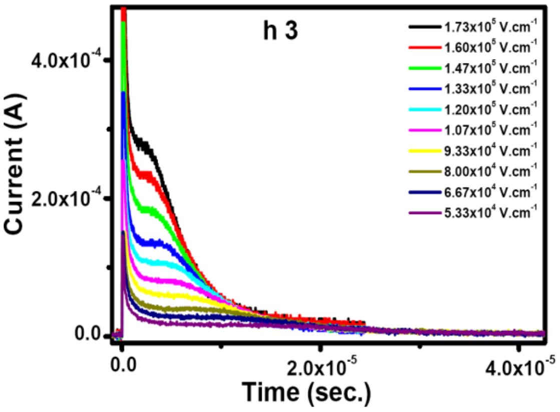
h 3
Current (A)
$4.0\text{x}10^{-4}$
$2.0\text{x}10^{-4}$
0.0
0.0
$2.0\text{x}10^{-5}$
$4.0\text{x}10^{-5}$
Time (sec.)
$1.73\text{x}10^{5}$ V.cm^{-1}
$1.60\text{x}10^{5}$ V.cm^{-1}
$1.47\text{x}10^{5}$ V.cm^{-1}
$1.33\text{x}10^{5}$ V.cm^{-1}
$1.20\text{x}10^{5}$ V.cm^{-1}
$1.07\text{x}10^{5}$ V.cm^{-1}
$9.33\text{x}10^{4}$ V.cm^{-1}
$8.00\text{x}10^{4}$ V.cm^{-1}
$6.67\text{x}10^{4}$ V.cm^{-1}
$5.33\text{x}10^{4}$ V.cm^{-1}

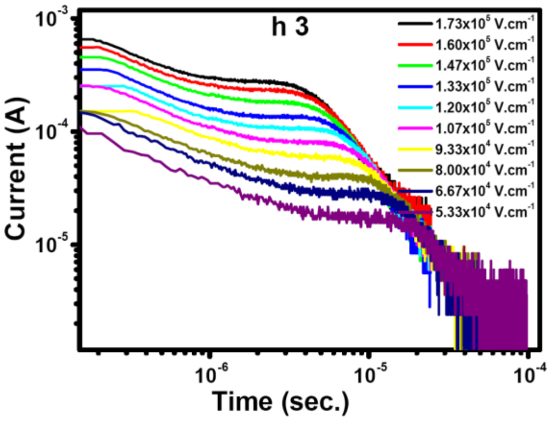
h 3
Current (A)
10^{-3}
10^{-4}
10^{-5}
10^{-6}
10^{-5}
10^{-4}
Time (sec.)
$1.73\text{x}10^{5}$ V.cm^{-1}
$1.60\text{x}10^{5}$ V.cm^{-1}
$1.47\text{x}10^{5}$ V.cm^{-1}
$1.33\text{x}10^{5}$ V.cm^{-1}
$1.20\text{x}10^{5}$ V.cm^{-1}
$1.07\text{x}10^{5}$ V.cm^{-1}
$9.33\text{x}10^{4}$ V.cm^{-1}
$8.00\text{x}10^{4}$ V.cm^{-1}
$6.67\text{x}10^{4}$ V.cm^{-1}
$5.33\text{x}10^{4}$ V.cm^{-1}

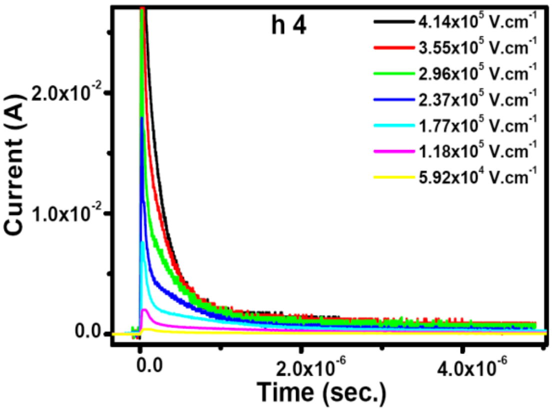
h 4
Current (A)
$2.0\text{x}10^{-2}$
$1.0\text{x}10^{-2}$
0.0
0.0
$2.0\text{x}10^{-6}$
$4.0\text{x}10^{-6}$
Time (sec.)
$4.14\text{x}10^{5}$ V.cm^{-1}
$3.55\text{x}10^{5}$ V.cm^{-1}
$2.96\text{x}10^{5}$ V.cm^{-1}
$2.37\text{x}10^{5}$ V.cm^{-1}
$1.77\text{x}10^{5}$ V.cm^{-1}
$1.18\text{x}10^{5}$ V.cm^{-1}
$5.92\text{x}10^{4}$ V.cm^{-1}

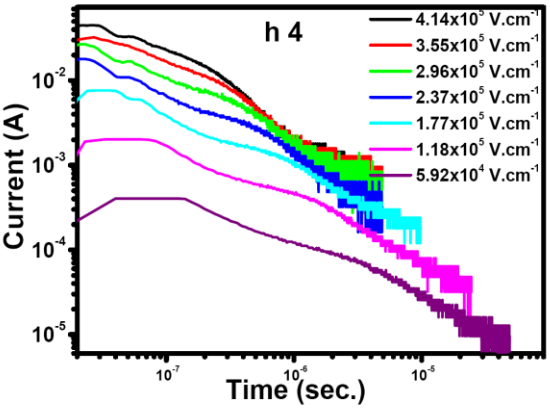
h 4
Current (A)
10^{-2}
10^{-3}
10^{-4}
10^{-5}
10^{-7}
10^{-6}
10^{-5}
Time (sec.)
$4.14\text{x}10^{5}$ V.cm^{-1}
$3.55\text{x}10^{5}$ V.cm^{-1}
$2.96\text{x}10^{5}$ V.cm^{-1}
$2.37\text{x}10^{5}$ V.cm^{-1}
$1.77\text{x}10^{5}$ V.cm^{-1}
$1.18\text{x}10^{5}$ V.cm^{-1}
$5.92\text{x}10^{4}$ V.cm^{-1}

III. Donor/Acceptors blends

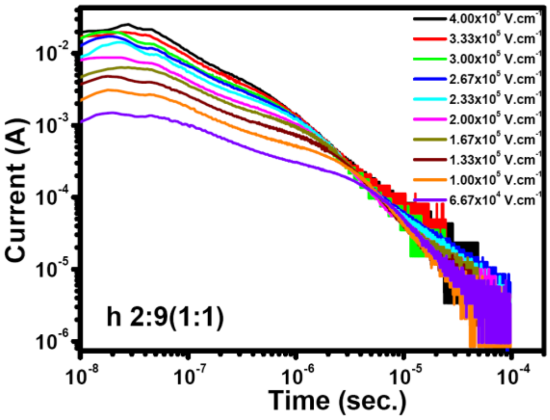

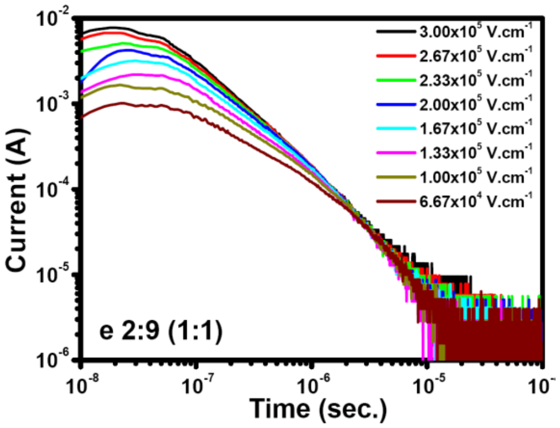

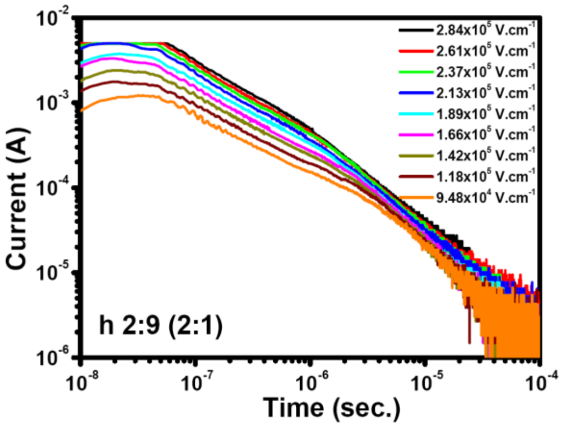

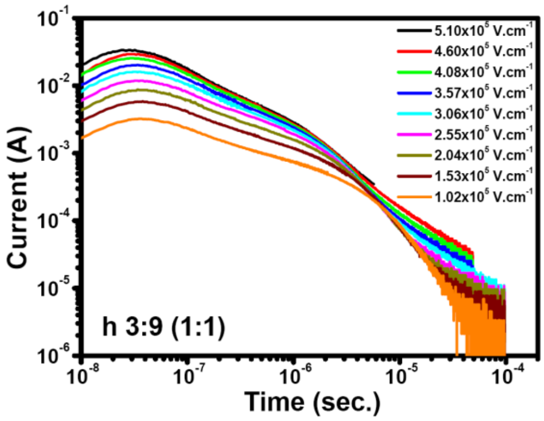

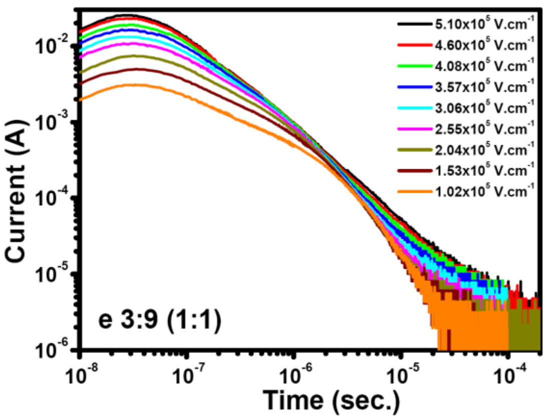

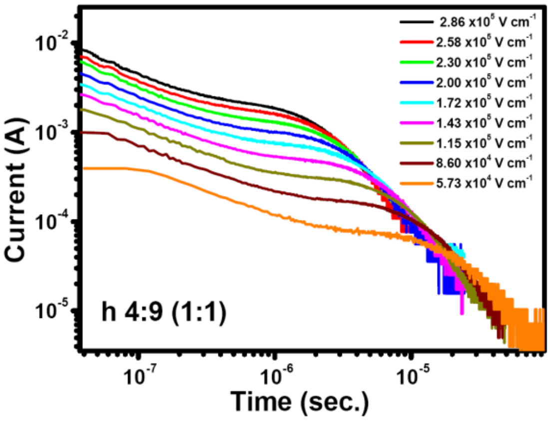

2.86 x10^5 V cm^{-1}
2.58 x10^5 V cm^{-1}
2.30 x10^5 V cm^{-1}
2.00 x10^5 V cm^{-1}
1.72 x10^5 V cm^{-1}
1.43 x10^5 V cm^{-1}
1.15 x10^5 V cm^{-1}
8.60 x10^4 V cm^{-1}
5.73 x10^4 V cm^{-1}
h 4:9 (1:1)
Current (A)
Time (sec.)

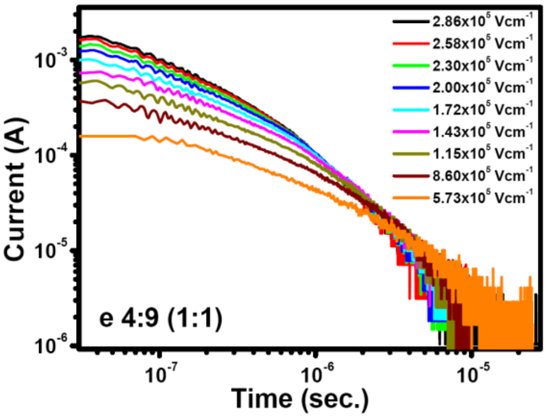

2.86x10^5 Vcm^{-1}
2.58x10^5 Vcm^{-1}
2.30x10^5 Vcm^{-1}
2.00x10^5 Vcm^{-1}
1.72x10^5 Vcm^{-1}
1.43x10^5 Vcm^{-1}
1.15x10^5 Vcm^{-1}
8.60x10^5 Vcm^{-1}
5.73x10^5 Vcm^{-1}
e 4:9 (1:1)
Current (A)
Time (sec.)

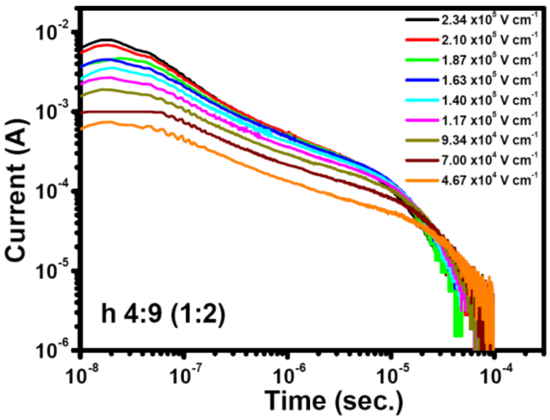

2.34 x10^5 V cm^{-1}
2.10 x10^5 V cm^{-1}
1.87 x10^5 V cm^{-1}
1.63 x10^5 V cm^{-1}
1.40 x10^5 V cm^{-1}
1.17 x10^5 V cm^{-1}
9.34 x10^4 V cm^{-1}
7.00 x10^4 V cm^{-1}
4.67 x10^4 V cm^{-1}
h 4:9 (1:2)
Current (A)
Time (sec.)

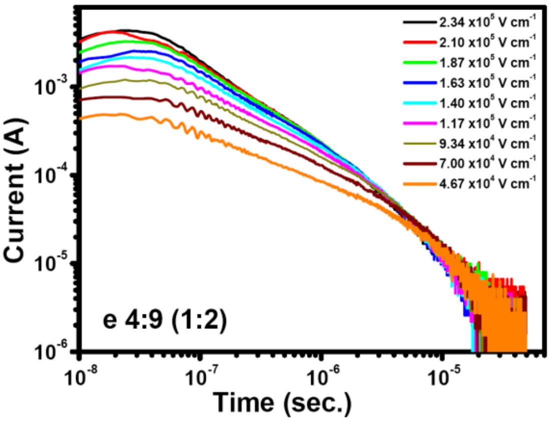

2.34 x10^5 V cm^{-1}
2.10 x10^5 V cm^{-1}
1.87 x10^5 V cm^{-1}
1.63 x10^5 V cm^{-1}
1.40 x10^5 V cm^{-1}
1.17 x10^5 V cm^{-1}
9.34 x10^4 V cm^{-1}
7.00 x10^4 V cm^{-1}
4.67 x10^4 V cm^{-1}
e 4:9 (1:2)
Current (A)
Time (sec.)

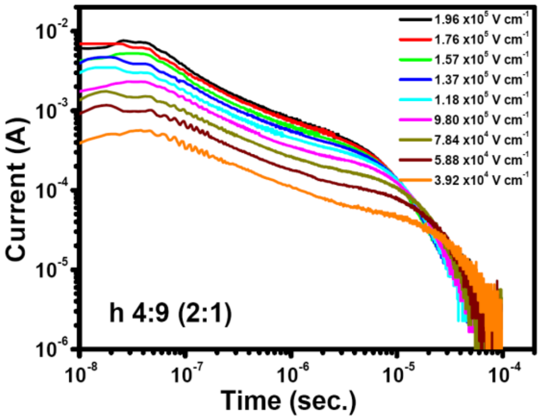

1.96 x10^5 V cm^{-1}
1.76 x10^5 V cm^{-1}
1.57 x10^5 V cm^{-1}
1.37 x10^5 V cm^{-1}
1.18 x10^5 V cm^{-1}
9.80 x10^5 V cm^{-1}
7.84 x10^4 V cm^{-1}
5.88 x10^4 V cm^{-1}
3.92 x10^4 V cm^{-1}
h 4:9 (2:1)
Current (A)
Time (sec.)

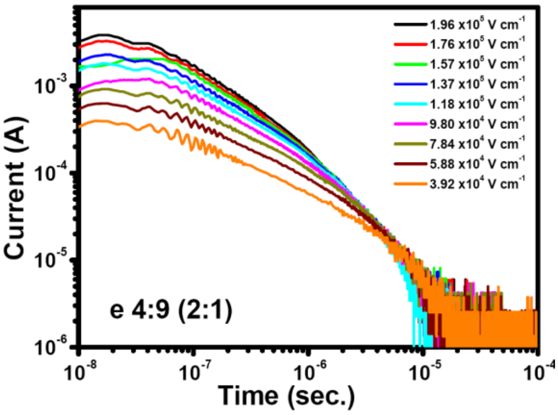

1.96 x10^5 V cm^{-1}
1.76 x10^5 V cm^{-1}
1.57 x10^5 V cm^{-1}
1.37 x10^5 V cm^{-1}
1.18 x10^5 V cm^{-1}
9.80 x10^4 V cm^{-1}
7.84 x10^4 V cm^{-1}
5.88 x10^4 V cm^{-1}
3.92 x10^4 V cm^{-1}
e 4:9 (2:1)
Current (A)
Time (sec.)

Appendix C

Publications and Presentations

Publications

1 C. H. Lei, M. S. Al Khalifah, M. O'Neill et al., "Calamitic liquid crystal blends for organic photovoltaics - art. no. 705214," Organic Photovoltaics Ix **7052**, 5214-5214 (2008).

2 S. Droge, M. S. Al Khalifah, M. O'Neill et al., "Grazing Incidence X-ray Diffraction of a Photoaligned Nematic Semiconductor," Journal of Physical Chemistry B **113** (1), 49-53 (2009).

Presentations

1 Liquid Crystaline electron-donors and acceptors for charge transport and photovoltaics

Manea S. Al Khalifah, Chunhong H. Lei, Mary O’Neill, Matthew P. Aldred, Stuart P. Kitney, Panagiotis Vlachos, Stephen M. Kelly.

Exitonic Solar Cell Conference, University of Warwick, UK, September 2008

2 Calamatic liquid crystal blends for organic photovoltaics

Chunhong H. Lei, Manea S. Al Khalifah, Mary O’Neill, Matthew P. Aldred, Stuart P. Kitney, Panagiotis Vlachos, Stephen M. Kelly.

Exitonic Solar Cell Conference, University of Warwick, UK, September 2008